PCCP

PERSPECTIVE

View Article Online
View Journal | View Issue

Cite this: *Phys. Chem. Chem. Phys.*, 2016, **18**, 15482

Tracing the origins of transient overshoots for binary mixture diffusion in microporous crystalline materials†

Rajamani Krishna

Received 7th January 2016,
Accepted 16th May 2016

DOI: 10.1039/c6cp00132g

www.rsc.org/pccp

Separation of mixtures using microporous crystalline materials is normally achieved by exploiting differences in the adsorption strengths of the constituent species. The focus of the current investigation is on diffusion-selective separations that exploit differences in intra-crystalline diffusivities of guest molecules. A number of experimental investigations report overshoots in intra-crystalline loadings of the more mobile species during transient mixture uptake. Analogous overshoots in fluxes occur for mixture permeation across thin microporous membrane layers. The attainment of supra-equilibrium loadings is a common characteristic of diffusion-selective separations; this allows the over-riding of adsorption selectivities. The primary objective of the current investigation is to demonstrate that the Maxwell–Stefan diffusion formulation, using chemical potential gradients as driving forces, is capable of providing a quantitative description of the temporal and spatial overshoots found in diverse experimental studies. The origins of the overshoots can be traced to thermodynamic coupling effects that emanate from sizable off-diagonal contributions of the matrix of thermodynamic correction factors. If thermodynamic coupling effects are neglected, the overshoots are not realized. It is also demonstrated that while the transport of the more mobile partner is uphill of its loading gradient, its transport is downhill the gradient of its chemical potential. The deliberate exploitation of uphill diffusion to achieve difficult separations is highlighted.

1. Introduction

Microporous adsorbents such as zeolites, carbon molecular sieves, metal–organic frameworks (MOFs), and zeolitic imidazolate frameworks (ZIFs) have potential in a variety of applications such as CO_2 capture, natural gas purification, and O_2/N_2 separations.[1–3] Such separations are commonly conducted in fixed bed adsorbers.[4] The fixed bed devices are operated in a cyclical manner with adsorption and desorption cycles; the operations are intrinsically transient in nature, *i.e.* the concentrations in the bulk fluid phase, and within the particles, vary both with distance along the adsorber, z, and time, t.[4–7] Most commonly, the separation performance in a fixed-bed adsorber is dictated by the adsorption equilibrium of mixtures. Intra-particle diffusion limitations cause distended breakthrough characteristics and usually lead to diminished separation effectiveness.[2,7] However, there are some instances where diffusional effects over-ride the influence of adsorption equilibrium of mixtures and are the prime drivers of separations.[3,4,8,9]

For the separation of O_2/N_2 mixtures using LTA-4A, LTA-5A, or NaX, the adsorption selectivity is in favor of N_2 due to the larger permanent quadrupole moment of N_2 compared to that of O_2.[9,10] This implies that an adsorption based process would selectively adsorb N_2, and pure O_2 can be produced in the adsorption cycle.[11,12] For production of purified N_2, it is desirable to selectively adsorb O_2. Selectivity towards O_2 can be achieved by choosing a LTA-4A zeolite or a carbon molecular sieve (CMS).[9–13] Due to its smaller cross-sectional dimension, 3.1 Å for O_2, compared to 3.3 Å for N_2, the intra-particle diffusivity of O_2 is significantly higher than that of N_2 in both LTA-4A and CMS.[9,11–13] Due to the significantly lower diffusivity of N_2 purified N_2 breaks through earlier in a fixed bed adsorber and can be recovered to the purified form during the initial stages of transient breakthroughs.[2,4,9]

Another example is the separation of N_2/CH_4 mixtures, which is important in the context of natural gas upgrading because the presence of N_2 reduces the heating value. Some

---

Van 't Hoff Institute for Molecular Sciences, University of Amsterdam, Science Park 904, 1098 XH Amsterdam, The Netherlands. E-mail: r.krishna@contact.uva.nl; Fax: +31 20 525 5604; Tel: +31 20 627 0990

† Electronic supplementary information (ESI) available: Details of (a) pure component isotherm fits, (b) modelling of the adsorption equilibrium of mixtures, (c) calculation of thermodynamic correction factors, (d) Maxwell–Stefan diffusion equations for describing transient uptake of mixtures, and (e) methodology for simulation of transient uptake, membrane permeation, and transient breakthroughs in fixed beds. Video animations of the transient development of loadings within particles, and across membranes. These animations provide some "feel" of spatio-temporal overshoots in loadings during transient uptake and membrane permeation. See DOI: 10.1039/c6cp00132g

natural gas reserves contain up to 20% N_2; reduction to less than about 2% is required in order to meet the pipeline specifications for natural gas. For most known adsorbents, the adsorption selectivity favors CH_4 that has a higher polarizability.[9,10] A practical approach is to rely on diffusion selectivities by using microporous adsorbents such as the LTA-4A zeolite and Ba-ETS-4.[14–16] The cross-sectional dimension of CH_4 is 3.7 Å, which is higher than that of N_2 (3.3 Å); consequently, the diffusivity of N_2 is significantly higher in LTA-4A and Ba-ETS-4. Purified natural gas can be recovered during the early stages of transient breakthroughs in fixed-bed adsorbers packed with LTA-4A and Ba-ETS-4.[2,7]

A common characteristic of diffusion selective separations is that the transient mixture uptake within a porous particle exhibits overshoots in the loading of the more mobile component. The experimental data of Chen *et al.*[13] for the transient uptake of the O_2/N_2 mixture within a CMS particle show an overshoot for the more mobile O_2; see Fig. 1a. For the transient uptake of N_2/CH_4 mixtures, overshoots in the loading of the more mobile N_2 have been reported for the LTA-4A zeolite;[14] see Fig. 1b. The experimental data of Titze *et al.*[17] for the transient uptake of *n*-hexane(*n*C6)/2-methylpentane(2MP) mixtures in MFI zeolite crystals, exposed to an equimolar binary gas mixture at constant total pressure (=2.6 Pa), show a pronounced overshoot in the uptake of the more mobile linear isomer *n*C6; supra-equilibrium loadings of *n*C6 are attained during the transient approach to equilibrium; see Fig. 1c.

The experimental data of Saint-Remi *et al.*[18] for the transient uptake of ethanol/1-propanol mixtures within SAPO-34 crystals, the structural analogs of CHA zeolites, are shown in Fig. 1d. The more mobile ethanol exhibits a pronounced overshoot in the transient uptake, exceeding the final equilibrated loading.

In more recent experimental investigations using interference microscopy (IFM), Binder *et al.*[19] and Lauerer *et al.*[20] have monitored the uptake of CO_2 and C_2H_6 within the crystals of the DDR zeolite exposed to a bulk gas phase consisting of 1 : 1, 2 : 1, and 3 : 1 CO_2/C_2H_6 mixtures. In all three sets of experiments, supra-equilibrium CO_2 loadings are attained during transient equilibration. A significant aspect of the Binder and Lauerer experiments is that both the spatial loadings (along the radial direction of crystal; see Fig. 2a and b) and spatial-averaged uptake (see Fig. 3a–c) of guest molecules have been monitored. Their experiments show overshoots, both spatial and temporal, in the loadings of the more mobile CO_2. For example, the radial profile of 2 : 1 CO_2/C_2H_6 mixtures (Fig. 2a) shows that the CO_2 peaks migrate to the crystal interiors as time progresses; the magnitude of the peaks decreases until equilibration.

In all the above mentioned sets of uptake experiments, with diverse guest/host combinations, the attainment of supra-equilibrium loadings signals uphill diffusion.[21]

Diffusion-selective separations can also be achieved in membrane constructs, by allowing the feed mixture to permeate through thin microporous films. Such membrane devices are normally operated under steady-state conditions. Experimental data on the transient permeation of CH_4/nC_4H_{10},[22] H_2/nC_4H_{10},[23] nC_4H_{10}/iso-C_4H_{10},[24] *n*C6/2MP,[25] *n*C6/2,3-dimethylbutane (23DMB),[25] benzene/*p*-xylene,[26] *m*-xylene/*p*-xylene,[27] and *o*-xylene/*m*-xylene/*p*-xylene[27] mixtures across MFI membranes show overshoots in the flux of the more mobile partners during the transient approach towards steady-state.

The primary objective of this article is to demonstrate that the spatial and temporal overshoots in the afore-mentioned sets of uptake and membrane experiments can be modelled quantitatively using the Maxwell–Stefan (M–S) diffusion formulation.[7,21] The secondary objective is to show that while the more mobile species experiences transport uphill of the gradient of its molar loading, it is downhill of the gradient of its chemical potential.

The ESI† accompanying this publication provides details of fitting of pure component isotherms, modelling of mixture adsorption equilibrium, calculations of chemical potential gradients, solution of the partial differential equations describing intra-crystalline diffusion, and details of simulations of transient uptake, membrane permeation, and fixed-bed breakthroughs.

Rajamani Krishna

Rajamani Krishna is a Professor at the University of Amsterdam in the Netherlands. His current research focus is on adsorption and diffusion in nanoporous crystalline materials. He has published two text books (one of these has been translated into Chinese), 450 peer-reviewed journal articles, and holds several patents. A complete list of his research contributions can be found on Google Scholar: http://scholar.google.nl/citations?user=cKqtQ0MAAAAJ&hl=en. According to the latest statistics on Google scholar, his publications have been cited more than 26 000 times, with an h-index of 85. He is the recipient of the prestigious 2013 ENI award for his research theme Improving Process Technologies with Molecular Insights.

2. The Maxwell–Stefan formulation for micropore diffusion

The key to modelling overshoots in transient mixture diffusion lies in the appropriate choice of driving forces for the diffusion of the constituent species. Within microporous materials, the guest molecules exist in the adsorbed phase, and the Gibbs adsorption equation[28] in differential form is

$$A\mathrm{d}\pi = \sum q_i \mathrm{d}\mu_i \tag{1}$$

The quantity A on the left side of eqn (1) is the surface area per kg of framework, with units of m^2 per kg of the framework of the crystalline material; q_i is the molar loading of component i in the adsorbed phase with units moles per kg of framework; μ_i is the molar chemical potential of component i. The spreading pressure, π, has the same units as surface tension, *i.e.* N m^{-1};

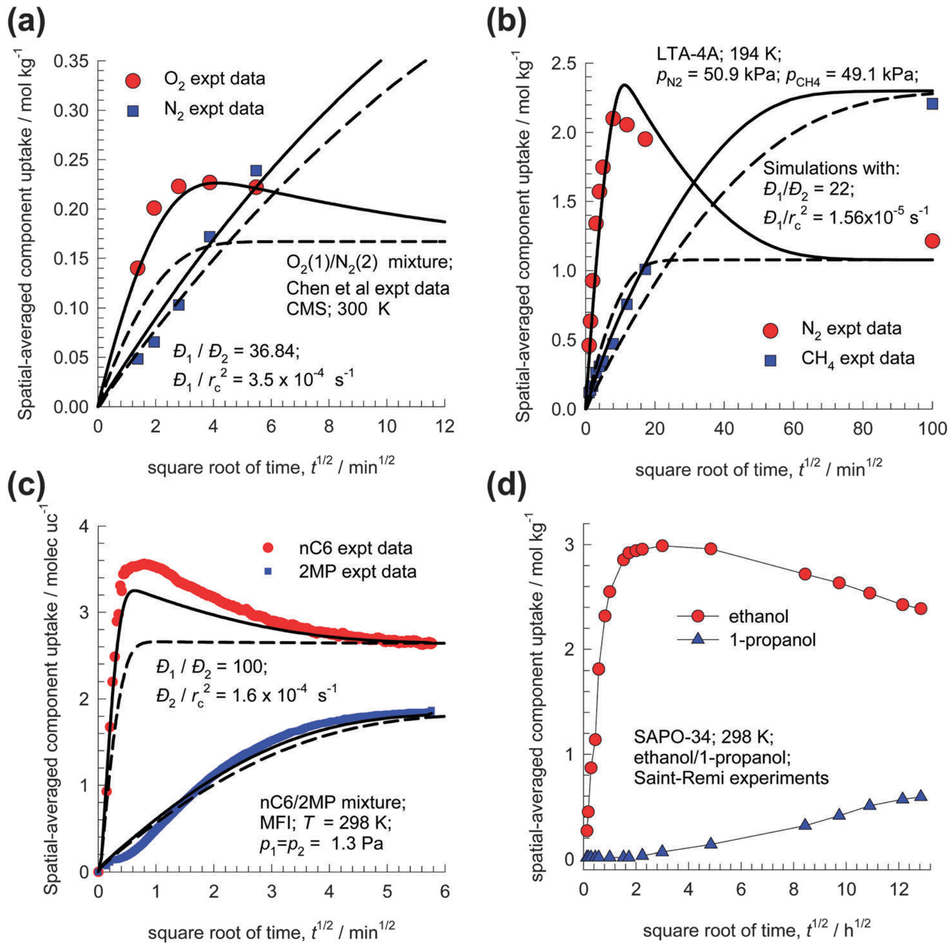

Fig. 1 (a) Experimental data of Chen *et al.*[13] for the spatial-averaged transient uptake of the $O_2(1)/N_2(2)$ mixture in a carbon molecular sieve (CMS) at 300 K exposed to binary gas mixtures at partial pressures p_1 = 109.6 kPa; p_2 = 432.56 kPa. (b) Experimental data of Habgood[14] on the transient uptake of the $N_2(1)/CH_4(2)$ mixture within LTA-4A crystals, exposed to binary gas mixtures at 194 K and partial pressures p_1 = 50.9 kPa; p_2 = 49.1 kPa. (c) Experimental data (Run 1) of Titze *et al.*[17] for the transient uptake of *n*C6/2MP mixtures in the MFI zeolite. (d) Experimental data of Saint-Remi *et al.*[18] for the transient uptake of ethanol/1-propanol mixtures within SAPO-34. The continuous solid lines are based on the flux eqn (11). The dashed lines are the calculations using the uncoupled flux eqn (16). Further simulation details are provided in the ESI.†

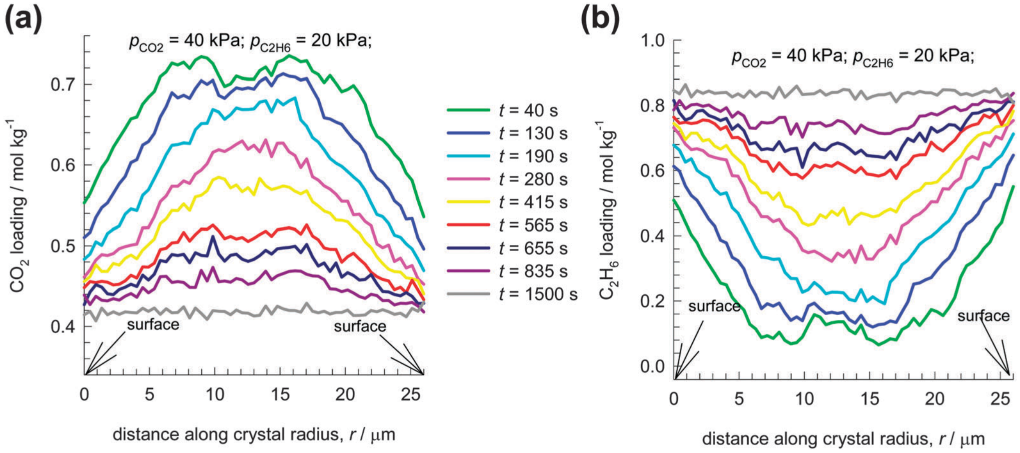

Fig. 2 (a and b) Experimental data of Binder and Lauerer[19,20] for the transient development of molar loadings of (a) $CO_2(1)$, and (b) $C_2H_6(2)$ along the radius of the DDR crystal monitored at different times from the start of the uptake. In the bulk gas phase 298 K, p_1 = 40 kPa, p_2 = 20 kPa.

indeed, the spreading pressure is the negative of the surface tension.[29]

For describing the unary transport of bound moisture in wood, Babbitt[30,31] suggested the use of the gradient of the

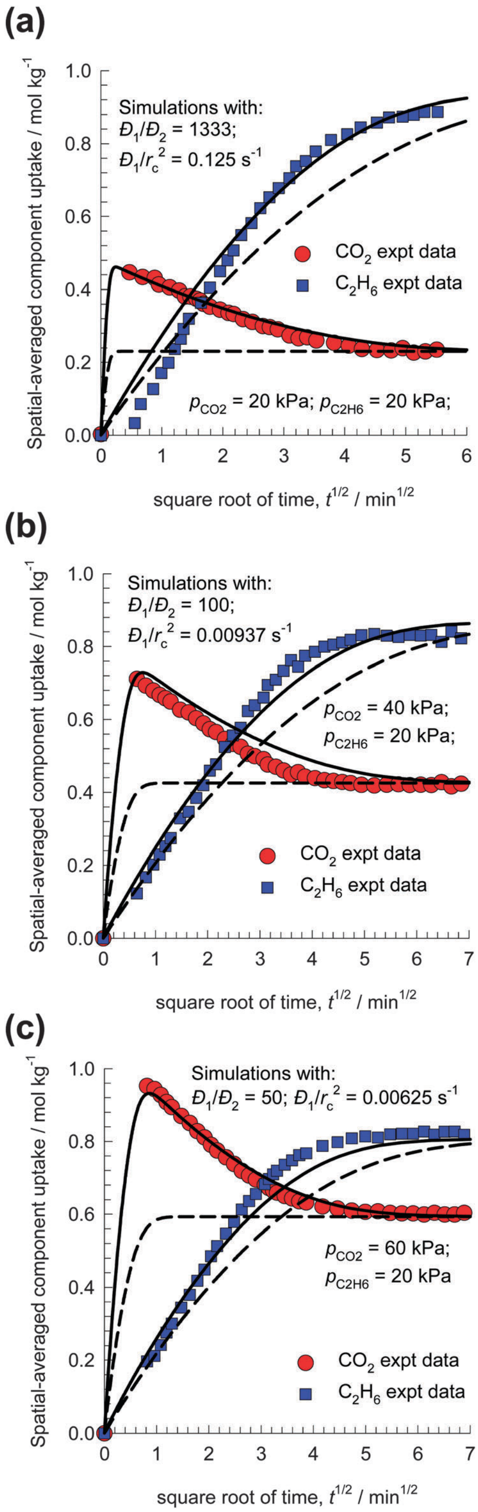

Fig. 3 (a–c) Experimental data of Binder and Lauerer[19,20] (indicated by symbols) for the spatial-averaged transient uptake of (a) 1 : 1 (b) 2 : 1, and (c) 3 : 1 $CO_2(1)/C_2H_6(2)$ gas mixtures within crystals of the DDR zeolite. The continuous solid lines are based on the flux eqn (11). The dashed lines are the calculations using the uncoupled flux eqn (16). Further simulation details are provided in the ESI.†

spreading pressure $\partial\pi/\partial r$ as thermodynamically correct driving force. Essentially, he postulated that the force exerted per mole of adsorbate, $-(A/q_i)(\partial\pi/\partial r)$, is balanced by friction, or drag, between the mobile adsorbates and the material surface

$$-\frac{A}{q_i}\frac{\partial\pi}{\partial r} = \frac{RT}{Đ_i}u_i \qquad (2)$$

where u_i is the velocity of motion of the adsorbate with respect to the framework material. The unary diffusivity $Đ_i$, with the units $m^2\ s^{-1}$, is interpreted as an inverse drag coefficient between the adsorbate and the surface. If we define N_i as the number of moles of species i transported per m^2 of the crystalline material per second

$$N_i \equiv \rho q_i u_i \qquad (3)$$

where ρ is the framework density with units of kg m^{-3}, we obtain the flux relation

$$-\rho\frac{A}{RT}\frac{\partial\pi}{\partial r} = \frac{N_i}{Đ_i} \qquad (4)$$

In view of eqn (1), the Babbitt eqn (4) is equivalent to the Maxwell–Stefan (M–S) formulation,[7,21,32] commonly written for unary diffusion in the form

$$-\rho\frac{q_i}{RT}\frac{\partial\mu_i}{\partial r} = \frac{N_i}{Đ_i} \qquad (5)$$

The use of chemical potential gradients as appropriate driving forces has also been emphasized in the classic text of Ruthven.[28]

In extending eqn (5) to describe binary mixture diffusion in micropores, we need to include interactions between the guest species. The M–S equations[32–35] are usually written in the following form:

$$\begin{aligned} -\rho\frac{q_1}{RT}\frac{\partial\mu_1}{\partial r} &= \frac{x_2N_1 - x_1N_2}{Đ_{12}} + \frac{N_1}{Đ_1}; \\ -\rho\frac{q_2}{RT}\frac{\partial\mu_2}{\partial r} &= \frac{x_1N_2 - x_2N_1}{Đ_{12}} + \frac{N_2}{Đ_2} \end{aligned} \qquad (6)$$

The diffusivities $Đ_1$ and $Đ_2$ retain the same physical significance as for unary diffusion; these are inverse drag coefficients of the respective species experienced with the material surface. Indeed, a persuasive advantage of the M–S formulation over the Onsager formulation is that the $Đ_i$ often retains the same magnitude and loading dependence characteristics as the corresponding unary micropore diffusivities.[32,33,36] $Đ_{12}$ is the exchange coefficient representing interaction between component 1 and component 2. At the molecular level, the $Đ_{12}$ reflects how the facility for the transport of species 1 correlates with that of species 2. For mesoporous materials with pores in the 20 Å to 100 Å size range the values of the exchange coefficient $Đ_{12}$ are nearly the same as the binary fluid phase M–S diffusivity, $Đ_{12,fl}$, over the entire range of pore concentrations.[32,33,37,38] Procedures for the estimation of the $Đ_{12,fl}$ are available in Poling *et al.*,[39] and therefore this provides a convenient starting point for the estimation of the $Đ_{12}$. For microporous materials, the exchange coefficients $Đ_{12}$ are lower than the corresponding values of $Đ_{12,fl}$ by a factor that depends on the pore size, connectivity and topology.[32,33,37,38] Alternative Maxwell–Stefan formulations for mixture diffusion in microporous materials are available in the literature;[5,40–42] these use occupancies $\theta_i = q_i/q_{i,\mathrm{sat}}$ instead of the adsorbed phase mole fractions, x_i; for further details see the ESI.†

For microporous crystals in equilibrium with an ideal gas mixture, $\frac{\partial \mu_i}{\partial r} = RT\frac{\partial \ln p_i}{\partial r} = RT\frac{1}{p_i}\frac{\partial p_i}{\partial r}$. The gradients in the chemical potential can be related to the gradients of the molar loadings, q_i, by defining thermodynamic correction factors Γ_{ij}

$$\frac{q_i}{RT}\frac{\partial \mu_i}{\partial r} = \sum_{j=1}^{2}\Gamma_{ij}\frac{\partial q_j}{\partial r}; \quad \Gamma_{ij} = \frac{q_i}{p_i}\frac{\partial p_i}{\partial q_j}; \quad i,j = 1,2 \tag{7}$$

The thermodynamic correction factors Γ_{ij} can be calculated by differentiation of the model describing the adsorption equilibrium of mixtures. Generally speaking, the Ideal Adsorbed Solution Theory (IAST) of Myers and Prausnitz[29] is the preferred method for estimation of the adsorption equilibrium of mixtures, especially for cases in which the saturation capacities of the constituents are largely different.[43,44] The IAST may however fail in the case of segregated adsorption and occurrence of molecular clustering. In special cases, the mixed-gas Langmuir model

$$\frac{q_i}{q_{i,\mathrm{sat}}} = \theta_i = \frac{b_i p_i}{1 + b_1 p_1 + b_2 p_2}; \quad i = 1,2 \tag{8}$$

may be of adequate accuracy. If eqn (8) is used to describe the adsorption equilibrium of mixtures, the elements Γ_{ij} can be calculated explicitly from

$$\Gamma_{ij} = \delta_{ij} + \left(\frac{q_{i,\mathrm{sat}}}{q_{j,\mathrm{sat}}}\right)\frac{\theta_i}{1-\theta_1-\theta_2}; \quad i = 1,2 \tag{9}$$

Combining eqn (6), and (7) we obtain[32–34]

$$\begin{pmatrix} N_1 \\ N_2 \end{pmatrix} = -\frac{\rho}{1 + \frac{x_1 Đ_2}{Đ_{12}} + \frac{x_2 Đ_1}{Đ_{12}}} \times \begin{bmatrix} Đ_1\left(1 + \frac{x_1 Đ_2}{Đ_{12}}\right) & \frac{x_1 Đ_1 Đ_2}{Đ_{12}} \\ \frac{x_2 Đ_1 Đ_2}{Đ_{12}} & Đ_2\left(1 + \frac{x_2 Đ_1}{Đ_{12}}\right) \end{bmatrix} \begin{bmatrix} \Gamma_{11} & \Gamma_{12} \\ \Gamma_{21} & \Gamma_{22} \end{bmatrix} \begin{pmatrix} \frac{\partial q_1}{\partial r} \\ \frac{\partial q_2}{\partial r} \end{pmatrix} \tag{10}$$

The ratios $Đ_1/Đ_{12}$, and $Đ_2/Đ_{12}$ quantify the degrees of correlations.[32,34] As an illustration, Fig. 4 shows Molecular Dynamics (MD) data on $Đ_1/Đ_{12}$ for equimolar binary $H_2(1)/CH_4(2)$ mixtures in a variety of host materials. The data are compared as a function of the total pore concentration, $c_t = (q_1 + q_2)/V_p$ where V_p is the accessible pore volume.[37] For any guest/host combination, $Đ_1/Đ_{12}$ is seen to increase as the pore concentration increases; this implies that correlation effects are expected to be stronger at higher pressures. We consider correlation effects to be strong when $Đ_1/Đ_{12} > 1$; $Đ_2/Đ_{12} > 1$; this scenario holds for mixture diffusion in mesoporous materials, one-dimensional (1D) channel structures (*e.g.* MgMOF-74), intersecting channels (*e.g.* MFI, BEA zeolite), and "open" structures (*e.g.* NaX zeolite, CuBTC, IRMOF-1) consisting of large cages separated by wide windows. Strong correlation effects cause slowing-down of more-mobile-less-strongly-adsorbed molecules by tardier-more-strongly-adsorbed-partner species.[32,34]

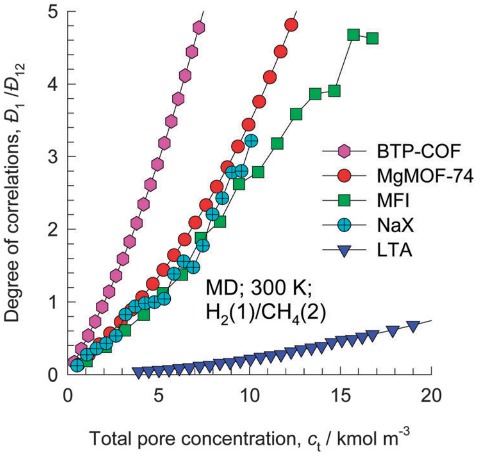

Fig. 4 MD simulation data for the degree of correlations, $Đ_1/Đ_{12}$, for the diffusion of equimolar binary $H_2(1)/CH_4(2)$ mixtures at 300 K in a variety of host materials, as a function of the total pore concentration, $c_t = (q_1 + q_2)/V_p$.

Conversely, when $Đ_1/Đ_{12} \ll 1$; $Đ_2/Đ_{12} \ll 1$, correlation effects are of negligible importance. This scenario holds for materials such as LTA, ZIF-8, CHA, DDR, and ERI that consist of cages separated by windows in the 3.4–4.2 Å size range.[32–34,45] Molecules jump one-at-a-time across the narrow windows, and the assumption of negligible correlations is justified; in this scenario, eqn (10) simplifies to yield[7,21]

$$\begin{aligned} N_1 &= -\rho Đ_1 \frac{\partial(\Gamma_{11}q_1 + \Gamma_{12}q_2)}{\partial r}; \\ N_2 &= -\rho Đ_2 \frac{\partial(\Gamma_{21}q_1 + \Gamma_{22}q_2)}{\partial r} \end{aligned} \tag{11}$$

The quantities $\Gamma_{11}q_1 + \Gamma_{12}q_2$, and $\Gamma_{21}q_1 + \Gamma_{22}q_2$ have the units mol kg^{-1} and may be regarded as the "thermodynamically corrected" measures of component loadings of components 1 and 2. The intra-crystalline fluxes N_1, and N_2 are, respectively, proportional to the gradients of these corrected loadings. Round *et al.*[46] were the first to use eqn (11) to model transient uptake in zeolites and provide a theoretical basis for transient overshoots. Eqn (11) has also been used by Brandani *et al.*[47] to interpret co- and counter-diffusion of benzene and xylenes in MFI zeolites.

Depending on the specific guest/host combination that is under consideration, either eqn (10) or (11) is used to describe the fluxes for binary mixture diffusion. The theoretical framework is valid for any type of microporous material, such as zeolites, MOFs, ZIFs or activated carbon. For ordered crystalline materials, molecular simulations may be used as guidelines for determining the diffusivities and adsorption equilibrium.[7]

3. Transient CO_2/C_2H_6 mixture uptake in DDR crystals

We begin with modeling of the CO_2/C_2H_6 mixture uptake in DDR zeolite crystals with the objective of simulating the Binder and Lauerer experiments.[19,20] DDR is a cage-type zeolite with 278 Å^3 sized cages separated by narrow windows with dimensions 3.65 Å × 4.37 Å; see Fig. S12–S14 of the ESI.† Molecular Dynamics (MD) simulations[34,45,48,49] have established that CO_2 molecules jump lengthwise across the windows. The cross-section dimension of a CO_2 molecule is 3.03 Å, significantly lower than that of C_2H_6 that has a cross-section of 3.76 Å; see Fig. S15 (ESI†). Using MD simulations[1,34,45,48] as guidelines, we anticipate the diffusivity of CO_2 to be about 1–3 orders of magnitude higher than that of C_2H_6. Inter-cage hopping of guest molecules in DDR occurs one-at-a-time across windows; *i.e.* the molecular jumps are not correlated,[34,45,48] and eqn (11) is the appropriate flux expression to use.

The accuracy of the use of the mixed-gas Langmuir model (8) to describe the adsorption equilibrium of the CO_2/C_2H_6 mixture in DDR is established by comparison with calculations using the Ideal Adsorbed Solution Theory (IAST);[29] see Fig. S17 (ESI†). The agreement between the mixed-gas Langmuir and IAST model is good because of the limited range of loadings considered. Consequently, eqn (9) is used to determine the elements Γ_{ij}. Fig. 5 presents calculations of Γ_{ij}, expressed as a function of total mixture loading, q_t, for the 3 : 1 ratio of partial pressures of $CO_2(1)$ and $C_2H_6(2)$ in the gas phase. The off-diagonal elements Γ_{12}, and Γ_{21} become increasingly important with increased mixture loadings, q_t. In particular, it is noteworthy that the ratio Γ_{12}/Γ_{11} gets progressively closer to unity as the mixture loading, q_t, increases. This implies that thermodynamic coupling effects are of particular significance for the uptake of CO_2 from CO_2/C_2H_6 gas mixtures.

For transient mixture uptake under conditions of finite loadings, eqn (7) and (9) imply that the chemical potential gradient of species i is influenced by the gradients in the loading of both species in the mixture; this influence is termed thermodynamic coupling. Thermodynamic coupling is always of importance for mixture uptake in microporous materials under conditions of finite loadings.

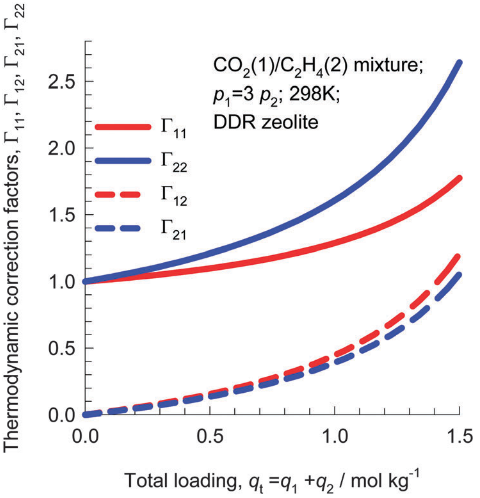

Fig. 5 Elements of the matrix of thermodynamic correction factors Γ_{ij} as a function of total mixture loading, q_t, calculated using the mixed-gas Langmuir model for binary $CO_2(1)/C_2H_6(2)$ mixture adsorption in DDR for the 3 : 1 ratio of partial pressures in the gas phase. In these calculations the total gas pressure, p_t, was varied from 1 to 100 kPa.

For most crystal geometries, model representation as an equivalent sphere is an acceptable approximation for modelling transient uptake.[28] The hexagonal-shaped crystals of DDR zeolites, used in the Binder and Lauerer[19,20] experiments, are modelled as spherical crystals of radius r_c. The radial distribution of molar loadings, q_i, is obtained from a solution of a set of differential equations describing the uptake[7,28]

$$\frac{\partial q_i(r,t)}{\partial t} = -\frac{1}{\rho}\frac{1}{r^2}\frac{\partial}{\partial r}\left(r^2 N_i\right) \tag{12}$$

The fluxes N_i, in turn, are related to the radial gradients in the molar loadings by eqn (11). At time t = 0, *i.e.* the initial conditions, the molar loadings $q_i(r,0)$ at all locations r within the crystal are uniform (zero loadings). For all times $t \geq 0$, the exterior of the crystal is brought into contact with a bulk gas mixture at partial pressures $p_i(r_c,t)$ that is maintained constant till the crystal reaches thermodynamic equilibrium with the surrounding gas mixture.

$$t \geq 0;\ q_i(r_c,t) \text{ in equilibrium with the initial values } p_i(r_c,t) \tag{13}$$

At any time t, during the transient approach to thermodynamic equilibrium, the spatial-averaged component loadings within the crystallites of radius r_c are calculated by integrating over the volume of the crystal

$$\bar{q}_i(t) = \frac{3}{r_c^3}\int_0^{r_c} q_i(r,t)r^2\mathrm{d}r \tag{14}$$

The experimental $\bar{q}_i(t)$ data of Binder and Lauerer[19,20] with 1 : 1, 2 : 1, and 3 : 1 CO_2/C_2H_6 gas mixtures are indicated by the symbols in Fig. 3, panels a, b, and c. For each data set, the parameters $Đ_1/r_c^2$, and $Đ_2/r_c^2$ were chosen to get a good match with the experiments; the simulation results with use of eqn (11) are shown by the continuous solid lines in Fig. 3. The fitted values of $Đ_1/r_c^2$, and $Đ_2/r_c^2$, appear to correlate with the corresponding loadings, q_1, and q_2, in the adsorbed mixture at final equilibration; see Fig. 6. The overshoots in the spatial-averaged CO_2 loadings in all three experimental campaigns are captured adequately by the M–S model eqn (11), in conjunction with the fitted diffusivity values.

In the Henry regime of adsorption, where the fractional occupancies are vanishingly small, we have the special case where elements of the matrix of thermodynamic factors Γ_{ij} are equal to the Kronecker delta

$$\theta_i \to 0;\quad \Gamma_{ij} \to \delta_{ij};\quad \frac{q_i}{RT}\frac{\partial \mu_i}{\partial r} \to \frac{\partial q_i}{\partial r};\quad i,j = 1,2 \tag{15}$$

In this scenario of negligible thermodynamic coupling, eqn (11) reduces to yield the uncoupled flux relations

$$N_i = -\rho Đ_i \frac{\partial q_i}{\partial r};\qquad i = 1,2;\ \text{neglecting thermodynamic coupling} \tag{16}$$

The simulation results neglecting thermodynamic coupling effects are indicated by the dashed lines in Fig. 3, panels a, b, and c. In this scenario, the overshoots in the spatial-averaged

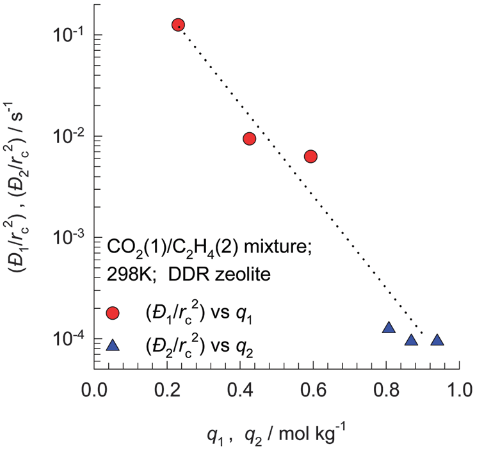

Fig. 6 The dependence of the diffusivities $Đ_1/r_c^2$, and $Đ_2/r_c^2$ for CO_2(1), and C_2H_6(2) in DDR on the corresponding component loadings, q_1, and q_2, in the adsorbed phase at equilibrium.

CO_2 loadings disappear. The inescapable conclusion to be drawn is that thermodynamic coupling effects are the root cause of the transient overshoots of the more mobile species in binary mixture uptake in DDR crystals.

Fig. 7a and b present the simulation results for the transient development of component loadings along the radius of the DDR crystal (center, $r = 0$; surface of crystal, $r = r_c$) monitored at different times for uptake from 2 : 1 CO_2/C_2H_6 gas mixtures; analogous data for 1 : 1, and 3 : 1 CO_2/C_2H_6 gas mixtures are provided in Fig. S25 and S27 (ESI†). Video animations of transient development of spatial loadings have been uploaded in the ESI;† these animations provide some feel of the spatio-temporal overshoots experienced by CO_2 during transient uptake.

The CO_2 peak migrates from the surface regions to the crystal interiors as time progresses, in qualitative agreement with the corresponding experimental profiles in Fig. 2a. Despite the fact that the values of $Đ_1/r_c^2$, and $Đ_2/r_c^2$ are fitted to match the spatial-averaged $\bar{q}_i(t)$, we should not expect a one-to-one correspondence in the data on the $q_1(r,t)$, and $q_2(r,t)$; this is because of the use of a spherical geometry to model the hexagonal DDR crystals employed in the experiments. Due to the presence of surface barriers, the experimentally determined surface loadings change with time. However, in our simulations instantaneous equilibration at the surface is assumed; consequently, there are quantitative differences in the radial profiles obtained in the two sets. The spatial overshoot of CO_2 loadings is a clear indication of uphill transport. In order to determine

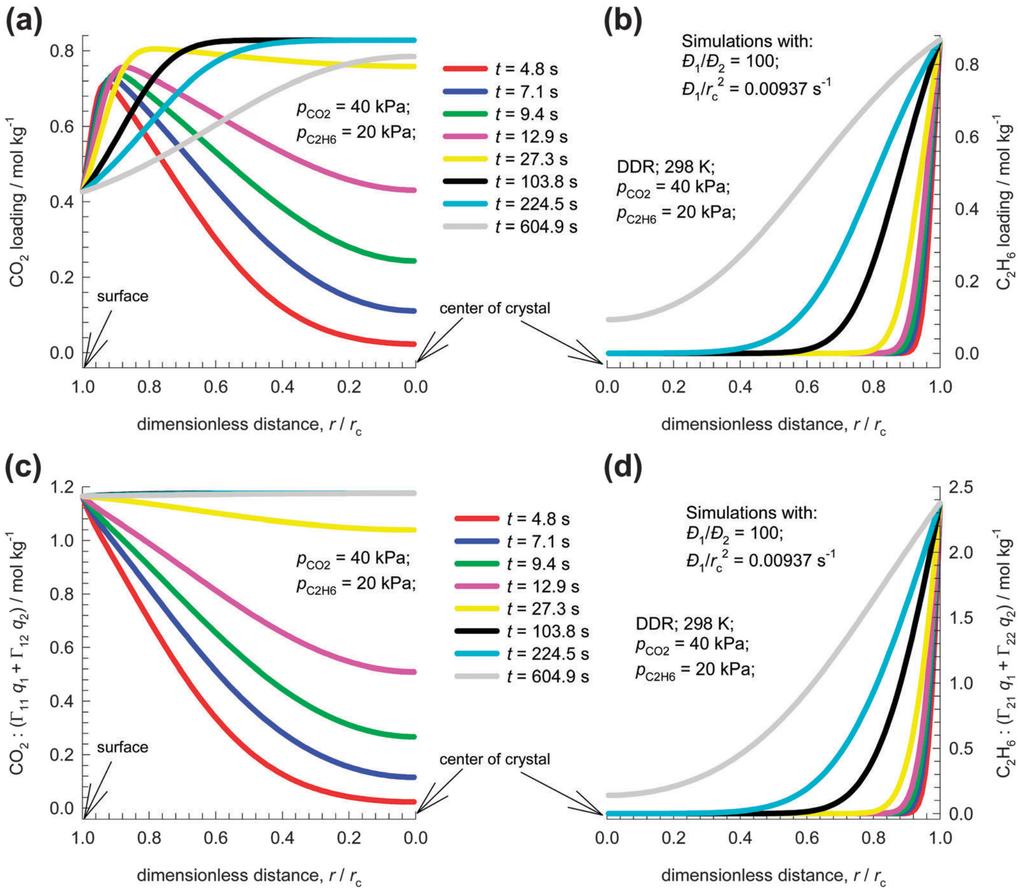

Fig. 7 Simulation results for transient development of (a and b) molar loadings, and (c and d) "corrected" molar loadings of CO_2(1), and C_2H_6(2) along the radius of DDR crystals (center, $r = 0$; surface of crystal, $r = r_c$) monitored at different times from the start of the uptake. In the bulk gas phase 298 K, p_1 = 40 kPa, p_2 = 20 kPa.

its origins, we need to examine the adsorption thermodynamics of the mixture in further detail. From the data on the $q_1(r,t)$, and $q_2(r,t)$ we determined the quantities $\Gamma_{11}q_1(r,t) + \Gamma_{12}q_2(r,t)$, and $\Gamma_{21}q_1(r,t) + \Gamma_{22}q_2(r,t)$ that are thermodynamically corrected measures of component loadings of components 1 and 2. Fig. 7c and d show the transient development of corrected loadings along the radius of DDR crystals. In terms of corrected loadings, there is no spatial overshoot of CO_2; this implies that CO_2 is not transported uphill of the gradient of its chemical potential.

It now remains to demonstrate that the use of corrected loadings serves to rationalize the experimentally observed spatio-temporal overshoots in the CO_2 loadings in the Binder, and Lauerer experiments.[19,20] From the experimental data on the $q_1(r,t)$, and $q_2(r,t)$ in Fig. 2, we determined the quantities $\Gamma_{11}q_1(r,t) + \Gamma_{12}q_2(r,t)$, and $\Gamma_{21}q_1(r,t) + \Gamma_{22}q_2(r,t)$ that are thermodynamically corrected measures of component loadings of components 1 and 2; the results are presented in Fig. 8a and b. In terms of corrected loadings, there are no spatio-temporal overshoots for CO_2. Indeed, the equilibration of both CO_2 and C_2H_6 proceeds in the same conventional manner. Both simulations (Fig. 7), and experiments (Fig. 8) confirm that the transport of CO_2 is downhill of the chemical potential gradient.

Though not mentioned in the papers by Binder, and Lauerer,[19,20] the results in Fig. 3 suggest that CO_2 removal from C_2H_6-rich streams can be achieved in fixed beds packed with DDR particles; in this case the separations rely on differences in both intra-crystalline diffusivities and thermodynamic coupling effects. Fig. 9 shows the simulations of transient breakthrough of 10/90 CO_2/C_2H_6 mixtures through a fixed bed adsorber packed with DDR crystals operating at 298 K, and total pressure $p_t = 100$ kPa. We note that C_2H_6 breaks through earlier and can be recovered in purified form during the early stages of the transient operations. The separation relies on the significantly higher intra-crystalline diffusivity of CO_2. If there is no intra-crystalline diffusional limitation, CO_2 breaks through earlier and the purification strategy will be ineffectual.

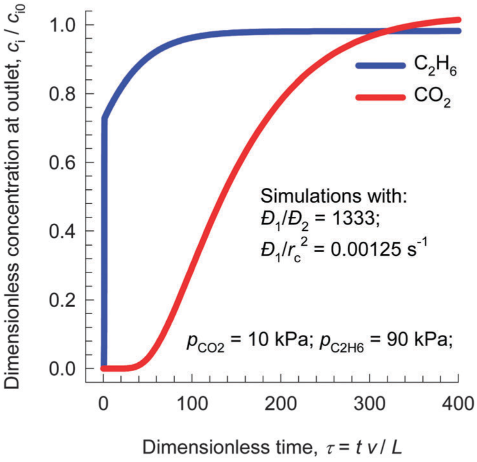

Fig. 9 Transient breakthrough of 10/90 CO_2/C_2H_6 mixtures through fixed bed adsorber packed with DDR crystals operating at 298 K, and total pressure $p_t = 100$ kPa. The parameter values are: $L = 0.3$ m; voidage of bed, $\varepsilon = 0.4$; interstitial gas velocity, $v = 0.1\ m\ s^{-1}$; radius of crystallite, $r_c = 40\ \mu m$; $_1/r_c^2 = 0.00125\ s^{-1}$; $Đ_1/Đ_2 = 1333$. The y-axis is the gas phase concentration at the adsorber outlet, normalized with respect to the feed concentrations at the inlet. The x-axis is the dimensionless time, $\tau = tv/L$, obtained by dividing the actual time, t, by the characteristic time, L/v. Further simulation details are provided in the ESI.†

4. Transient mixture uptake in other guest/host combinations

Precisely analogous conclusions can be drawn by comparison of M–S model simulations with the experimental data for O_2/N_2 uptake in CMS,[13] N_2/CH_4 uptake in LTA-4A,[14] and n-hexane (nC6)/2-methylpentane (2MP) uptake in MFI zeolites;[17] see Fig. 1, panels a, b, and c. The experimentally observed overshoots in the three experimental sets are adequately captured by the M–S eqn (11) that includes thermodynamic coupling; these are indicated by the continuous solid lines in Fig. 1. Video animations of the transient development of loadings along the crystal radius show spatio-temporal overshoots of the more

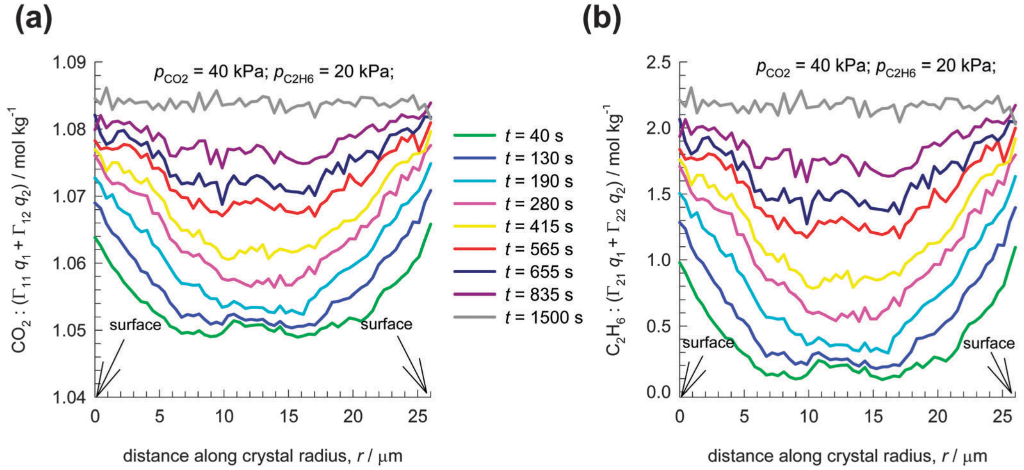

Fig. 8 Experimental data of Binder and Lauerer[19,20] for the transient development of "corrected" molar loadings of (a) $CO_2(1)$, and (b) $C_2H_6(2)$ along the radius of DDR crystals monitored at different times from the start of the uptake. In the bulk gas phase 298 K, $p_1 = 40$ kPa, $p_2 = 20$ kPa.

mobile N_2, O_2, and *n*C6 in the three respective experiments. If thermodynamic coupling effects are neglected, the more mobile species displays a monotonous approach to equilibrium, as indicated by the dashed lines in Fig. 1.

Overshoots in the transient uptake of the more mobile partner species have also been reported for benzene/*p*-xylene in ZSM-5,[50,51] benzene/ethylbenzene in ZSM-5,[50,51] *n*-heptane/benzene in NaX,[52] ethane/*n*-butane, ethane/*n*-pentane, and *n*-butane/*n*-pentane mixtures in extrudates of activated carbon (AC);[53] these data are amenable to interpretation in the same manner as in the foregoing examples.[7,21] Simulation results for these systems confirm that the experimentally observed overshoots are ascribable to thermodynamic coupling influences; see Fig. S46–S50 (ESI†).

Transient overshoots of the mobile species may also occur for adsorption–diffusion reaction within MFI catalysts; see Fig. S86–S94 (ESI†).

5. Influence of the ratio of M–S diffusivities, $Đ_1/Đ_2$, on overshoots

From a practical standpoint, it is of interest to know under what set of conditions transient overshoots may be expected to occur. To get some insights into this question, we investigated the binary $C_3H_6(1)/C_3H_8(2)$ mixture uptake in ZIF-8. In ZIF-8, the adsorption strength of the saturated propane is slightly higher than that of propene; at 303 K, the ratio of Langmuir constants, $b_2/b_1 = 1.07$. The windows of ZIF-8 have a dimension of about 3.3 Å. Due to subtle differences in bond lengths and bond angles of propene and propane (see Fig. 10), the diffusivity of C_3H_6 is higher than that of C_3H_8.[54] In the experimental study of Li *et al.*,[55] a value of the ratio $Đ_1/Đ_2 = 125$ has been obtained based on the data on pure component uptakes. The membrane permeation experiments of Pan *et al.*[56] and Liu *et al.*[57] indicate permeation selectivities in the range 30 – 35, which are consistent with the choice $Đ_1/Đ_2 \approx 40$. We undertook a parametric study of the influence of the ratio of $Đ_1/Đ_2$; three values for the ratio were chosen: 2, 10, and 125. In these three scenarios the diffusivity of the saturated alkane was held constant at the value $Đ_2/r_c^2 = 1.2 \times 10^{-4}\ s^{-1}$. The simulation results are shown in Fig. 10. The overshoot in the uptake of the unsaturated propene persists for the ratios $Đ_1/Đ_2 = 10$ and $Đ_1/Đ_2 = 125$; see video animations of the transient development of loadings. However, for the choice $Đ_1/Đ_2 = 2$, the overshoot in the C_3H_6 uptake is practically non-existent. We conclude that for sizable overshoots to occur, the diffusivity of the more mobile species must be significantly higher than that of the tardier partner species. Interestingly, C_3H_6 exhibits undershoot phenomena during desorption; see Fig. S55 (ESI†).

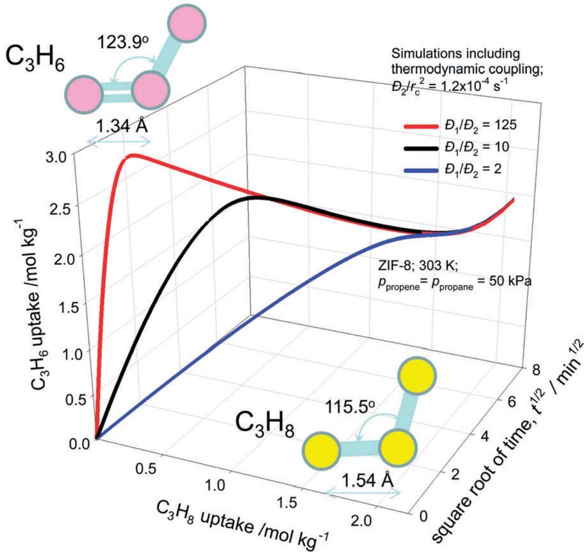

Fig. 10 Simulations of the transient uptake of $C_3H_6(1)/C_3H_8(2)$ within the crystals of ZIF-8 at 303 K. In the simulations $Đ_2/r_c^2 = 1.2 \times 10^{-4}\ s^{-1}$. The ratios $Đ_1/Đ_2$ have three different values: 2, 10, and 125. The three sets of simulations are based on the flux eqn (11). Further simulation details are provided in the ESI.†

6. Separating mono- and di-branched alkanes by exploiting uphill diffusion in the MFI zeolite

The isomerization of alkanes, for the purposes of octane improvement, is a process of importance in the petroleum industry.[2,7,58] The product from the isomerization reactor consists of an equilibrium distribution of linear alkanes, mono-branched alkanes, and di-branched alkanes with carbon numbers in the 5–7 range. The values of the Research Octane Number (RON) increases with the degree of branching; for hexane isomers: the RON values are: *n*C6 (*n*-hexane) = 30, 2MP (2-methylpentane) = 74.5, 3MP (3-methylpentane) = 75.5, 22DMB (2,2-dimethylbutane) = 94, 23DMB (2,3-dimethylbutane) = 105. Therefore, the di-branched isomers 22DMB and 23DMB are preferred products for incorporation into the high-octane gasoline pool. The separation of di-branched 22DMB and 23DMB from linear *n*C6 can be achieved by molecular sieving using, say, the LTA-5A zeolite. The separation of di-branched isomers from mono-branched isomers is much more challenging. An important strategy that is effective for this separation is the exploitation of configurational entropy effects,[7,44,59] combined with uphill diffusion of the more mobile guest species in the MFI zeolite. As an illustration, consider the separation of a ternary gaseous 2-methylbutane (2MB)/2MP/22DMB mixture. The adsorption and diffusivity data for MFI extrudates are reported by Jolimaître *et al.*[60,61] The adsorption hierarchy that is dictated by configurational entropy considerations[7,44,59] is 2MP > 22DMB > 2MB. The diffusivity hierarchy is also dictated by subtle differences in molecular configurations: $Đ_{2MB}/r_c^2 = 7.5 \times 10^{-3}\ s^{-1} > Đ_{2MP}/r_c^2 = 5 \times 10^{-3}\ s^{-1} \gg Đ_{22DMB}/r_c^2 = 6.25 \times 10^{-5}\ s^{-1}$.

Transient uptake inside MFI extrudates exposed to a ternary 2MB/2MP/22DMB gas phase mixture shows overshoots for the two mono-branched isomers 2MB and 2MP; see Fig. 11a. If thermodynamic coupling effects are ignored, the component loadings of all three components exhibit monotonous approaches

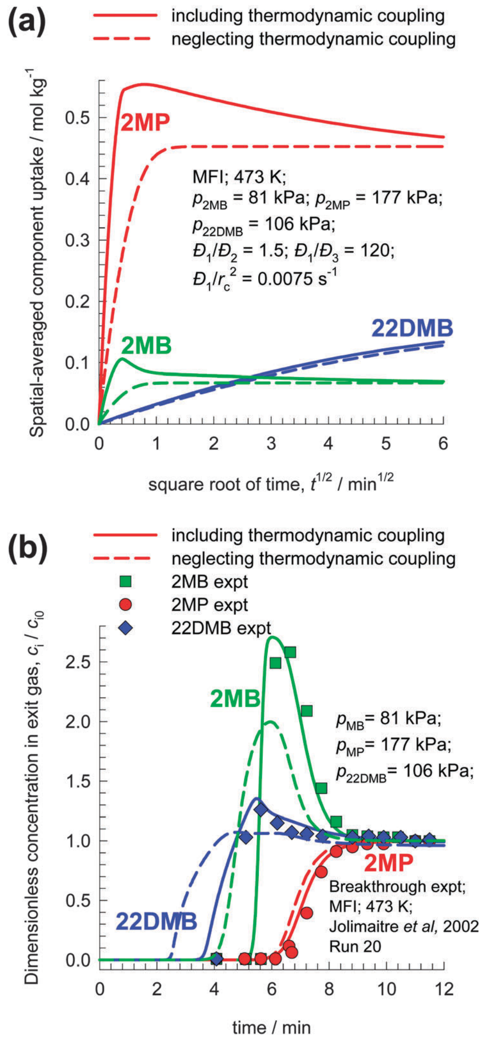

Fig. 11 (a) Transient uptake inside MFI crystals exposed to a gas phase 2MB/2MP/22DMB mixture at 473 K. (b) Comparison of transient breakthrough experimental data of Jolimaître *et al.*[61] with transient breakthrough simulations. The partial pressures of the components in the bulk gas phase at the inlet are p_1 = 81 kPa; p_2 = 177 kPa; p_2 = 106 kPa. These conditions correspond to Run 20 of Jolimaître *et al.*[61] Diffusional effects are quantified with $Đ_{2MB}/r_c^2$ = 0.0075 s^{-1} $Đ_{2MP}/r_c^2$ = 0.005 s^{-1}; $Đ_{2MP}/Đ_{22DMB}$ = 80. The continuous solid lines represent uptake simulations including thermodynamic coupling using the flux relations eqn (11). The dashed lines represent uptake simulations ignoring thermodynamic coupling and using uncoupled flux eqn (16). See video animations of the transient uptake within crystal and transient breakthrough in bed.

to equilibrium. Both mono-branched alkanes 2MB and 2MP experience uphill diffusion that allows the attainment of supra-equilibrium loadings. As a consequence of uphill diffusion, the transient breakthrough experimental data (indicated by symbols in Fig. 11b) show the elution sequence 22DMB, 2MB, followed by 2MP. This sequence is the desirable one, because the high-octane di-branched 22DMB can be recovered from the gas mixture exiting the adsorber for incorporation into the gasoline pool, during the initial transience.

The experimental breakthrough data are in good agreement with breakthrough simulations that take proper account of thermodynamic coupling, using the flux relations eqn (11); see continuous solid lines in Fig. 11b. If thermodynamic coupling effects are ignored (*i.e.* no uphill diffusion), the separation is less effective and is indicated by the dashed lines in Fig. 11b.

7. Separating linear alcohols by exploiting uphill diffusion in the CHA zeolite

The quantitative modelling of the transient uptake of ethanol/1-propanol mixtures in SAPO-34, shown in Fig. 1d, is not possible because the required unary isotherm data are not available. For this reason, we carried out uptake simulations in the CHA zeolite that has the same topology as SAPO-34; the unary isotherms for adsorption of 1-alcohols in CHA, determined

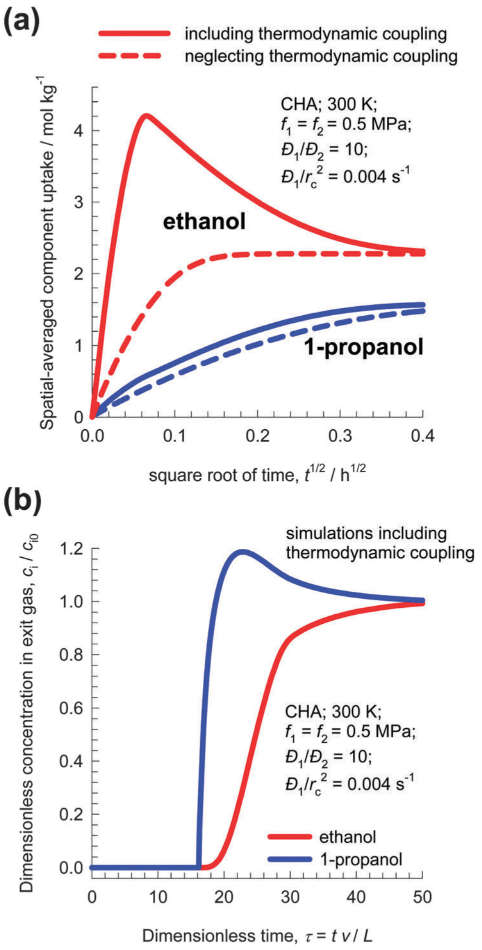

Fig. 12 (a) Simulations of transient uptake of ethanol(1)/1-propanol(2) mixtures within CHA crystals, exposed to binary gas mixtures with partial fugacities f_{ethanol} = $f_{\text{1-propanol}}$ = 0.5 MPa. (b) Breakthrough simulations for ethanol/1-propanol mixtures in a fixed bed adsorber packed with CHA. The Maxwell–Stefan diffusivities: $Đ_{\text{ethanol}}/r_c^2$ = 4 × 10^{-3} s^{-1}; $Đ_{\text{1-propanol}}/r_c^2$ = 4 × 10^{-5} s^{-1}. The continuous solid lines are the calculations with flux relations eqn (11). The dashed lines are the calculations neglecting thermodynamic coupling and using uncoupled flux eqn (16).

from Configurational-Bias Monte Carlo (CBMC) simulations, have been reported in the literature.[7,44,62] Transient uptake simulation results taking the mobility of ethanol to be 10 times that of 1-propanol are presented in Fig. 12a. The continuous solid lines are transient uptake simulations use eqn (11); in this scenario, substantial overshoots of ethanol are found. The dashed lines are the calculations using uncoupled flux eqn (16); in this scenario, no ethanol overshoot is detected.

The uphill transport of ethanol can be exploited for ethanol/1-propanol separations in fixed beds carried out under pore saturation conditions. Under pore saturation conditions, the adsorption equilibrium of the ethanol/1-propanol mixture favors the shorter alcohol because of the higher packing efficiency of the shorter alcohol within the cages of CHA.[7,44,62] Uphill transport of ethanol enhances the efficacy of this separation, and the component that elutes first in fixed-bed adsorbers is the longer chain alcohol; see Fig. 12b. The breakthrough experimental data of Remy *et al.*[63] for separation of ethanol/1-propanol mixtures in a fixed bed adsorber provide confirmation of the simulated elution sequence.

8. Overshoots in mixture permeation across microporous membrane layers

Geus *et al.*[22] provided experimental data on the permeation of a transient 50/50 CH_4/nC_4H_{10} mixture across an MFI membrane; the flux of the more mobile CH_4 exhibits a pronounced overshoot during the approach to steady state. Simulations were undertaken to rationalize the Geus experiments. Molecular dynamics (MD) simulation data[33,34] indicate that correlation effects for CH_4/nC_4H_{10} mixture diffusion within the intersecting channels of MFI are particularly strong; using the MD data as guidelines we choose $Đ_1/Đ_2 = 10$; and $Đ_1/Đ_{12} = 2$ for quantitative modelling. The adsorption equilibrium of the mixture is determined using the IAST. The transient permeation fluxes N_i, defined in terms of the cross-sectional area of the membrane, need to take account of both correlations and thermodynamic coupling; eqn (10) is the appropriate flux expression to use. The N_i are determined by solving the set of partial differential equations

$$\frac{\partial q_i(z,t)}{\partial t} = -\frac{1}{\rho}\frac{\partial}{\partial z}(N_i) \tag{17}$$

where z is the distance coordinate along the direction of membrane thickness.

The boundary conditions are the partial pressures and component molar loadings at the upstream ($z = 0$) and downstream ($z = \delta$) faces of the membrane

$$\begin{aligned} z &= 0; \quad p_i = p_{i0}; \quad q_i = q_{i0} \\ z &= \delta; \quad p_i = p_{i\delta}; \quad q_i = q_{i\delta} \end{aligned} \tag{18}$$

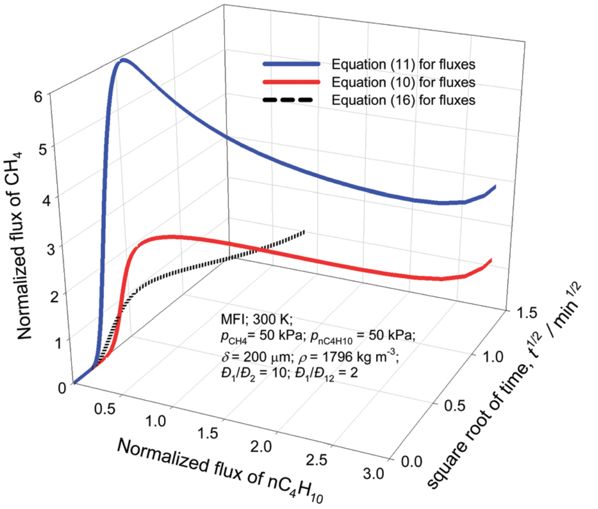

Fig. 13 Simulations of transient 50/50 $CH_4(1)/nC_4H_{10}(2)$ membrane permeation. The diffusivity data used are: $\rho Đ_2/\delta = 7.18 \times 10^{-3}$ kg m^{-2} s^{-1}, $\rho/Đ_2\delta = 7.18 \times 10^{-4}$ kg m^{-2} s^{-1}; $Đ_1/Đ_2 = 10$; $Đ_1/Đ_{12} = 2$; membrane thickness δ = 200 μm; partial pressures in the upstream membrane compartment, $p_{10} = p_{20}$ = 50 kPa. The downstream compartment is placed under vacuum, *i.e.* $p_{1\delta} = p_{2\delta} \approx 0$. The loadings at the upstream face are: q_{10} = 0.0063 mol kg^{-1}, q_{20} = 1.638 mol kg^{-1}. Three different flux expressions are used in the calculations: eqn (10), (11), and (16).

The continuous solid lines in Fig. 13 are the numerical simulations to eqn (17), in conjunction with the fluxes determined using eqn (10), eqn (11), or (16). The plot shows the normalized fluxes $N_1/(\rho q_{10}Đ_1/\delta)$, and $N_2/(\rho q_{20}Đ_2/\delta)$ as steady-state is approached. The inclusion of correlations in the flux calculations serves to reduce the magnitude of the overshoot in CH_4; this is because of the slowing-down of the more mobile species within the intersecting channels of the MFI zeolite. We conclude that correlation effects cannot cause overshoots; indeed, their inclusion only serves to smear them out. If both correlations and thermodynamic coupling effects are neglected, the overshoot in CH_4 disappears altogether; thermodynamic coupling is the sole cause of transient permeation overshoots.

Fig. 14a shows the transient development of CH_4 loadings, q_1, along the MFI membrane thickness, monitored at different times from the start of the permeation. The CH_4 loadings display spatio-temporal overshoots during the transient approach to steady-state, indicative of uphill transport; this is clearly evidenced in the video animations included in the ESI.† In terms of corrected loadings, $\Gamma_{11}q_1 + \Gamma_{12}q_2$, the loading profiles of CH_4 display monotonous characteristics; see Fig. 14b. These results prove that CH_4 permeation is downhill of the chemical potential gradient.

The experimental data of Bakker[23] for the transient permeation of the H_2/nC_4H_{10} mixture across an MFI membrane show a maximum in the flux of the more mobile H_2; the rationalization of these experiments proceeds along identical lines as in the foregoing analysis; the detailed simulation results are summarized in Fig. S72–S74 (ESI†).

For the permeation of *n*C6/2MP mixtures across an MFI membrane, Matsufuji *et al.*[25] provided experimental data showing overshoots in the *n*C6 flux during the transient approach to steady-state. The overshoot in the *n*C6 flux is precisely analogous to the *n*C6 loading overshoot observed in the Titze experiments (see Fig. 1c). Indeed, the *n*C6 flux overshoot manifests in

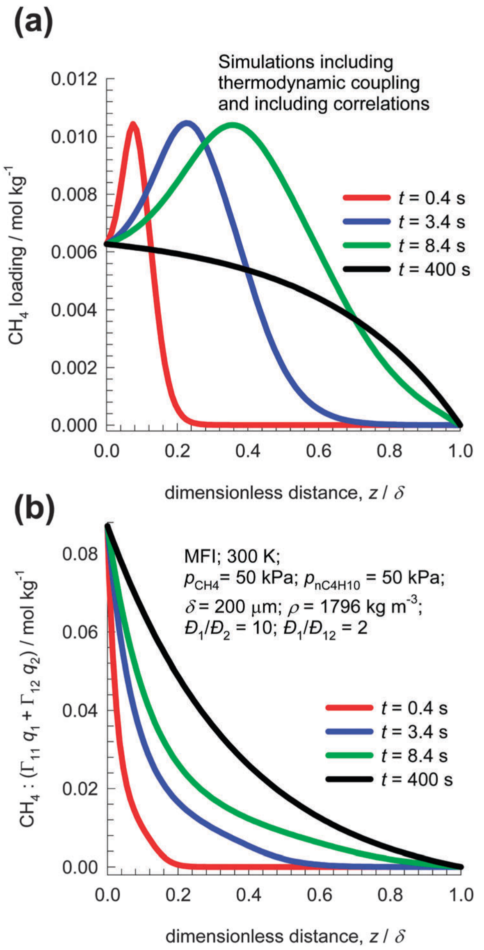

Fig. 14 Simulations of transient 50/50 CH_4(1)/nC_4H_{10}(2) MFI membrane permeation: transient development of (a) CH_4 loadings, q_1, and (b) corrected loadings, $\Gamma_{11}q_1 + \Gamma_{12}q_2$, along the MFI membrane thickness (upstream face, $z = 0$; downstream face, $z = \delta$) monitored at different times from the start of the permeation. In these simulations, correlation effects and thermodynamic coupling effects are accounted for by using eqn (10).

membrane permeation simulations using the same diffusivity data used to model the Titze mixture uptake; see Fig. S75–S78 (ESI†).

The experimental data of Matsufuji *et al.*[27] for the transient permeation of (a) 50/50 *m*-xylene/*p*-xylene and (b) 24/50/25 *p*-xylene/*m*-xylene/*o*-xylene mixtures across the MFI membrane show a maximum in the flux of *p*-xylene which is the most mobile species among the three xylene isomers; see Fig. S79 (ESI†). The origin of the flux overshoot of *p*-xylene can be traced to thermodynamic coupling effects; see Fig. S80 (ESI†).

For the permeation of the nC_4H_{10}/iso-C_4H_{10} mixture across a MFI membrane, curious overshoots and undershoots in the transient retentate and permeate concentrations have been reported in the experiments of Courthial *et al.*[24] As evidenced in the simulation results in Fig. S81 (ESI†), the origins of the *n*C4 overshoots can be traced to the influence of thermodynamic coupling.

Pervaporation of water/alcohol mixtures is an important process in the processing industry, and a wide variety of membrane materials has been used, including polymers, zeolites (*e.g.* CHA, LTA, MFI, FAU, DDR), ZIF-8, and mixed matrix membranes.[64–68] Due to the high mobility of water molecules, uphill transport of water is evidenced in simulations of transient water/ethanol permeation across DDR and LTA-4A membranes (see Fig. S82–S85, ESI†), but there is no experimental confirmation of the overshoot phenomena observed in these simulations.

9. Conclusions

The Maxwell–Stefan diffusion equations with chemical potential gradients as driving forces are able to quantitatively reproduce the temporal and spatial overshoots in the loading of the more mobile guest molecules for transient uptake in different guest/host combinations: CO_2/C_2H_6/DDR, N_2/CH_4/LTA-4A, O_2/N_2/CMS, *n*C6/2MP/MFI, and ethanol/1-propanol/CHA. The origins of the overshoots in the loadings of the more mobile guests can be traced to thermodynamic coupling effects that emanate from sizable off-diagonal contributions of the matrix of thermodynamic correction factors, $[\Gamma]$. During the transient approach to equilibrium, supra-equilibrium loadings within the particles are observed, signaling the phenomenon of uphill transport. The use of the corrected loadings $\Gamma_{11}q_1(r,t) + \Gamma_{12}q_2(r,t)$, and $\Gamma_{21}q_1(r,t) + \Gamma_{22}q_2(r,t)$ results in monotonous equilibration, without overshoots; see Fig. 7 and 8. While the transport of the more mobile species is uphill of the gradient in molar loading, the transport is downhill the gradient of chemical potential. If thermodynamic coupling effects are neglected, no overshoots are realized.

Our analysis also suggests the possibility of exploitation of uphill transport to achieve difficult separations. For example, the results in Fig. 9 suggest that CO_2 can be selectively adsorbed from C_2H_6 in fixed beds.

Analogous conclusions hold for the permeation of the transient CH_4/nC_4H_{10}, H_2/nC_4H_{10}, *n*C6/2MP, and nC_4H_{10}/iso-C_4H_{10} mixture across MFI membranes. In these three cases, overshoots disappear when both thermodynamic coupling and correlation effects are neglected. Transient overshoots in membrane permeation can be exploited to recover more mobile species during the early stages of the transient approach to steady-state.

The discussions and results presented in this article are of importance for the appropriate modelling of diffusion-selective separations carried out in fixed-bed adsorbers, catalytic reactors, and membrane permeation devices.

Notation

A	Surface area per kg of framework, $m^2\ kg^{-1}$
b_i	Langmuir adsorption constant for species i, Pa^{-1}
c_i	Molar concentration, mol m^{-3}
$Đ_i$	M–S diffusivity for molecule-wall interaction, $m^2\ s^{-1}$
$Đ_{12}$	M–S exchange coefficient, $m^2\ s^{-1}$
f_i	Partial fugacity of species i, Pa
k_1	Forward reaction rate constant, s^{-1}
k_2	Backward reaction rate constant, s^{-1}

L	Length of packed bed adsorber, m
N_i	Molar flux of species i with respect to framework, mol m^{-2} s^{-1}
p_i	Partial pressure of species i in mixture, Pa
p_t	Total system pressure, Pa
q_i	Component molar loading of species i, mol kg^{-1}
$q_{i,\text{sat}}$	Molar loading of species i at saturation, mol kg^{-1}
q_t	Total molar loading in mixture, mol kg^{-1}
$\bar{q}_i(t)$	Spatial-averaged component uptake of species i, mol kg^{-1}
r	Radial direction coordinate, m
r_c	Radius of crystallite, m
R	Gas constant, 8.314 J mol^{-1} K^{-1}
t	Time, s
u_i	Velocity of motion of adsorbate species i with respect to the framework material, m s^{-1}
v	Interstitial gas velocity in packed bed, m s^{-1}
V_p	Pore volume, m^3 kg^{-1}
T	Absolute temperature, K
z	Distance coordinate, m

Greek letters

δ	Thickness of microporous membrane, m
δ_{ij}	Kronecker delta, dimensionless
ε	Voidage of packed bed, dimensionless
Γ_{ij}	Thermodynamic factors, dimensionless
$[\Gamma]$	Matrix of thermodynamic factors, dimensionless
μ_i	Molar chemical potential of component i, J mol^{-1}
μ_i^0	Molar chemical potential of component i in the standard state, J mol^{-1}
π	Spreading pressure, N m^{-1}
θ_i	Fractional occupancy of component i, dimensionless
ρ	Framework density, kg m^{-3}
τ	Time, dimensionless

Subscripts

i	Referring to component i
t	Referring to the total mixture

References

1 R. Krishna and J. M. van Baten, *Phys. Chem. Chem. Phys.*, 2011, **13**, 10593–10616.
2 R. Krishna, *RSC Adv.*, 2015, **5**, 52269–52295.
3 J. Kärger, D. M. Ruthven and D. N. Theodorou, *Diffusion in Nanoporous Materials*, Wiley - VCH, Weinheim, 2012.
4 D. M. Ruthven, S. Farooq and K. S. Knaebel, *Pressure swing adsorption*, VCH Publishers, New York, 1994.
5 R. Krishna and R. Baur, *Sep. Purif. Technol.*, 2003, **33**, 213–254.
6 Y. He, R. Krishna and B. Chen, *Energy Environ. Sci.*, 2012, **5**, 9107–9120.
7 R. Krishna, *Microporous Mesoporous Mater.*, 2014, **185**, 30–50.
8 R. T. Yang, *Gas separation by adsorption processes*, Butterworth, Boston, 1987.
9 R. T. Yang, *Adsorbents: Fundamentals and Applications*, John Wiley & Sons, Inc., Hoboken, New Jersey, 2003.
10 S. Sircar and A. L. Myers, in *Handbook of Zeolite Science and Technology*, ed. S. M. Auerbach, K. A. Carrado and P. K. Dutta, Marcel Dekker, New York, 2003, pp. 1063–1104.
11 S. Farooq, M. N. Rathor and K. Hidajat, *Chem. Eng. Sci.*, 1993, **48**, 4129–4141.
12 S. Farooq, *Gas Sep. Purif.*, 1995, **9**, 205–212.
13 Y. D. Chen, R. T. Yang and P. Uawithya, *AIChE J.*, 1994, **40**, 577–585.
14 H. W. Habgood, *Can. J. Chem.*, 1958, **36**, 1384–1397.
15 S. J. Bhadra and S. Farooq, *Ind. Eng. Chem. Res.*, 2011, **50**, 14030–14045.
16 B. Majumdar, S. J. Bhadra, R. P. Marathe and S. Farooq, *Ind. Eng. Chem. Res.*, 2011, **50**, 3021–3034.
17 T. Titze, C. Chmelik, J. Kärger, J. M. van Baten and R. Krishna, *J. Phys. Chem. C*, 2014, **118**, 2660–2665.
18 J. C. Saint-Remi, G. V. Baron and J. F. M. Denayer, *J. Phys. Chem. C*, 2013, **117**, 9758–9765.
19 T. Binder, A. Lauerer, C. Chmelik, J. Haase, J. Kärger and D. M. Ruthven, *Ind. Eng. Chem. Res.*, 2015, **54**, 8997–9004.
20 A. Lauerer, T. Binder, C. Chmelik, E. Miersemann, J. Haase, D. M. Ruthven and J. Kärger, *Nat. Commun.*, 2015, **6**, 7697, DOI: http://dx.doi.org/doi:10.1038/ncomms8697.
21 R. Krishna, *Chem. Soc. Rev.*, 2015, **44**, 2812–2836.
22 E. R. Geus, H. van Bekkum, W. J. W. Bakker and J. A. Moulijn, *Microporous Mater.*, 1993, **1**, 131–147.
23 W. J. W. Bakker, PhD thesis, PhD Dissertation, Delft University of Technology, 1999.
24 L. Courthial, A. Bandot, M. Tayakout-Fayolle and C. Jallut, *AIChE J.*, 2013, **59**, 959–970.
25 T. Matsufuji, K. Watanabe, N. Nishiyama, Y. Egashira, M. Matsukata and K. Ueyama, *Ind. Eng. Chem. Res.*, 2000, **39**, 2434–2438.
26 R. Kolvenbach, N. Al-Yassir, S. S. Al-Khattaf, O. C. Gobin, J. H. Ahn, A. Jentys and J. A. Lercher, *Catal. Today*, 2011, **168**, 147–157.
27 T. Matsufuji, N. Nishiyama, M. Matsukata and K. Ueyama, *J. Membr. Sci.*, 2000, **178**, 25–34.
28 D. M. Ruthven, *Principles of Adsorption and Adsorption Processes*, John Wiley, New York, 1984.
29 A. L. Myers and J. M. Prausnitz, *AIChE J.*, 1965, **11**, 121–130.
30 J. D. Babbitt, *Can. J. Res.*, 1950, **28A**, 449–474.
31 J. D. Babbitt, *Can. J. Phys.*, 1951, **29**, 427–436.
32 R. Krishna, *Chem. Soc. Rev.*, 2012, **41**, 3099–3118.
33 R. Krishna, *J. Phys. Chem. C*, 2009, **113**, 19756–19781.
34 R. Krishna and J. M. van Baten, *J. Membr. Sci.*, 2013, **430**, 113–128.
35 R. Krishna and J. M. van Baten, *J. Phys. Chem. C*, 2010, **114**, 11557–11563.
36 R. Krishna and J. M. van Baten, *Chem. Eng. Sci.*, 2008, **63**, 3120–3140.

37 R. Krishna and J. M. van Baten, *Chem. Eng. Sci.*, 2009, **64**, 3159–3178.

38 R. Krishna and J. M. van Baten, *J. Membr. Sci.*, 2011, **383**, 289–300.

39 B. E. Poling, J. M. Prausnitz and J. P. O'Connell, *The Properties of Gases and Liquids*, McGraw-Hill, New York, 5th edn, 2001.

40 F. Kapteijn, J. A. Moulijn and R. Krishna, *Chem. Eng. Sci.*, 2000, **55**, 2923–2930.

41 A. I. Skoulidas, D. S. Sholl and R. Krishna, *Langmuir*, 2003, **19**, 7977–7988.

42 R. Krishna and J. M. van Baten, *Microporous Mesoporous Mater.*, 2008, **109**, 91–108.

43 R. Krishna and J. R. Long, *J. Phys. Chem. C*, 2011, **115**, 12941–12950.

44 R. Krishna, *Phys. Chem. Chem. Phys.*, 2015, **17**, 39–59.

45 R. Krishna and J. M. van Baten, *Microporous Mesoporous Mater.*, 2011, **137**, 83–91.

46 G. F. Round, H. W. Habgood and R. Newton, *Sep. Sci.*, 1966, **1**, 219–244.

47 S. Brandani, M. Jama and D. M. Ruthven, *Ind. Eng. Chem. Res.*, 2000, **39**, 821–828.

48 R. Krishna and J. M. van Baten, *Sep. Purif. Technol.*, 2008, **61**, 414–423.

49 R. Krishna and J. M. van Baten, *J. Membr. Sci.*, 2010, **360**, 323–333.

50 W. Niessen and H. G. Karge, *Microporous Mater.*, 1993, **1**, 1–8.

51 H. G. Karge, *C. R. Chim.*, 2005, **8**, 303–319.

52 J. Kärger and M. Bülow, *Chem. Eng. Sci.*, 1975, **30**, 893–896.

53 X. Hu and D. D. Do, *Chem. Eng. Sci.*, 1992, **47**, 1715–1725.

54 R. Krishna and J. M. van Baten, *J. Phys. Chem. C*, 2012, **116**, 23556–23568.

55 K. Li, D. H. Olson, J. Seidel, T. J. Emge, H. Gong, H. Zeng and J. Li, *J. Am. Chem. Soc.*, 2009, **131**, 10368–10369.

56 Y. Pan, T. Li, G. Lestari and Z. Lai, *J. Membr. Sci.*, 2012, **390–391**, 93–98.

57 D. Liu, X. Ma, H. Xi and Y. S. Lin, *J. Membr. Sci.*, 2014, **451**, 85–93.

58 Z. R. Herm, B. M. Wiers, J. M. Van Baten, M. R. Hudson, P. Zajdel, C. M. Brown, N. Maschiocchi, R. Krishna and J. R. Long, *Science*, 2013, **340**, 960–964.

59 T. J. H. Vlugt, R. Krishna and B. Smit, *J. Phys. Chem. B*, 1999, **103**, 1102–1118.

60 E. Jolimaître, M. Tayakout-Fayolle, C. Jallut and K. Ragil, *Ind. Eng. Chem. Res.*, 2001, **40**, 914–926.

61 E. Jolimaître, K. Ragil, M. Tayakout-Fayolle and C. Jallut, *AIChE J.*, 2002, **48**, 1927–1937.

62 R. Krishna and J. M. van Baten, *Sep. Purif. Technol.*, 2011, **76**, 325–330.

63 T. Remy, J. C. Saint-Remi, R. Singh, P. A. Webley, G. V. Baron and J. F. M. Denayer, *J. Phys. Chem. C*, 2011, **115**, 8117–8125.

64 P. Peng, B. Shi and Y. Lan, *Sep. Sci. Technol.*, 2011, **46**, 234–246.

65 K. Sato, K. Aoki, K. Sugimoto, K. Izumi, S. Inoue, J. Saito, S. Ikeda and T. Nakane, *Microporous Mesoporous Mater.*, 2008, **115**, 184–188.

66 K. Sato, K. Sugimoto, N. Shimosuma, T. Kikuchi, T. Kyotani and T. Kurata, *J. Membr. Sci.*, 2012, **409–410**, 82–95.

67 J. Kuhn, J. M. Castillo-Sanchez, J. Gascon, S. Calero, D. Dubbeldam, T. J. H. Vlugt, F. Kapteijn and J. Gross, *J. Phys. Chem. C*, 2009, **113**, 14290–14301.

68 M. Pera-Titus, C. Fité, V. Sebastián, E. Lorente, J. Llorens and F. Cunill, *Ind. Eng. Chem. Res.*, 2008, **47**, 3213–3224.

Electronic Supporting Information to accompany:

Tracing the Origins of Transient Overshoots for Binary Mixture Diffusion in Microporous Crystalline Materials

Rajamani Krishna

Van 't Hoff Institute for Molecular Sciences, University of Amsterdam, Science Park 904,

1098 XH Amsterdam, The Netherlands

Email: r.krishna@contact.uva.nl

Table of Contents

1. Preamble

This Electronic Supporting Information (ESI) accompanying the article *Tracing the Origins of Transient Overshoots for Binary Mixture Diffusion in Microporous Crystalline Materials* provides details of (a) pure component isotherm fits, (b) modelling of mixture adsorption equilibrium, (c) calculation of thermodynamic correction factors, (d) Maxwell-Stefan diffusion equations for describing transient uptake of mixtures, and (e) methodology for simulation of transient uptake, membrane permeation, and transient breakthroughs in fixed beds.

For ease of reading, this ESI is written as a stand-alone document; as a consequence, there is some overlap of material with the main manuscript.

Video animations

The following set of video animations have been uploaded as ESI.

(1) Transient development of loadings of CO_2/C_2H_6 in DDR crystal at 298 K, conditions corresponding to Experiment 1 of Binder and Lauerer. CO_2 exhibits spatio-temporal overshoots.

(2) Transient development of loadings of CO_2/C_2H_6 in DDR crystal at 298 K, conditions corresponding to Experiment 2 of Binder and Lauerer. CO_2 exhibits spatio-temporal overshoots.

(3) Transient development of loadings of CO_2/C_2H_6 in DDR crystal at 298 K, conditions corresponding to Experiment 3 of Binder and Lauerer. CO_2 exhibits spatio-temporal overshoots.

(4) Transient development of loadings of N_2/CH_4 uptake in LTA-4A at 194 K: simulation of Habgood experiment. N_2 exhibits spatio-temporal overshoots.

(5) Transient development of loadings of O_2/N_2 in CMS at 300 K, simulation of Chen experiment. O_2 exhibits spatio-temporal overshoots.

(6) Transient development of loadings of nC6/2MP in MFI at 298 K, simulation of Run 1 of Titze. nC6 exhibits spatio-temporal overshoots.

(7) Transient development of loadings of ethane/n-pentane mixture in extrudates of activated carbon at 303 K. Ethane exhibits spatio-temporal overshoots.

(8) Transient development of loadings of C_3H_6/C_3H_8 in ZIF-8 at 298 K taking $Đ_1/Đ_2$ = 125. C_3H_6 exhibits spatio-temporal overshoots.

(9) Transient development of loadings of 2MB/2MP/22DMB in MFI extrudate. Note that both 2MB and 2MP exhibit spatio-temporal overshoots

(10) Transient breakthrough of 2MB/2MP/22DMB mixture in fixed bed of MFI extrudates; these are the simulations of Run 20 of Jolimaître et al.

(11) Transient development of ethanol/1-propanol loadings in CHA zeolite. Ethanol exhibits spatio-temporal overshoots.

(12) Transient development of CH_4/nC_4H_{10} loadings in MFI membrane. CH_4 exhibits spatio-temporal overshoots.

(13) Transient development of H_2/nC_4H_{10} loadings in MFI membrane. H_2 exhibits spatio-temporal overshoots.

(14) Transient development of nC6/2MP loadings in MFI membrane. nC6 exhibits spatio-temporal overshoots.

(15) Transient development of water/ethanol loadings in DDR pervaporation membrane. Water exhibits spatio-temporal overshoots.

(16) Transient development of water/ethanol loadings in LTA-4A pervaporation membrane. Water exhibits spatio-temporal overshoots.

(17) Transient development of loadings of 2MP/22DMB in MFI catalyst carrying out the isomerization reaction $\mathrm{2MP(1)} \rightleftarrows \mathrm{22DMB(2)}$. 2MP exhibits spatio-temporal overshoots.

(18) Transient development of loadings of nC6/3MP/22DMB in MFI catalyst carrying out the isomerization reaction $\mathrm{nC6(1)} \rightleftarrows \mathrm{3MP(2)} \rightleftarrows \mathrm{22DMB(3)}$. nC6 exhibits spatio-temporal overshoots.

(19) Transient development of loadings of m-xylene/p-xylene in MFI catalyst carrying out the isomerization reaction $\mathrm{m-xylene(1)} \rightleftarrows \mathrm{p-xylene(2)}$. p-xylene exhibits spatio-temporal overshoots.

(20) Transient development of loadings of ethene/benzene/ethylbenzene in MFI catalyst carrying out the reaction $\mathrm{ethene(1)} + \mathrm{benzene(2)} \rightleftarrows \mathrm{ethylbenzene(3)}$. Ethene exhibits spatio-temporal overshoots.

These animations provide some "feel" of spatio-temporal overshoots of during transient uptake, membrane permeation, and transient breakthroughs in fixed-bed adsorbers.

2. The Babbitt equation for unary diffusion in micropores

Within microporous crystalline materials, the guest molecules exist in the adsorbed phase. The Gibbs adsorption equation[1] in differential form is

$$A d\pi = \sum q_i d\mu_i \tag{1}$$

The quantity A on the left side of Equation (1) is the surface area per kg of framework, with units of m^2 per kg of the framework of the crystalline material; q_i is the molar loading of component i in the adsorbed phase with units moles per kg of framework; μ_i is the molar chemical potential of component i. The spreading pressure π has the same units as surface tension, i.e. N m^{-1}; indeed the spreading pressure is the negative of the surface tension.[2]

For describing the *unary* transport of bound moisture in wood, Babbitt[3, 4] suggested the use of the gradient of the spreading pressure $\partial\pi/\partial r$ as the thermodynamically correct driving force. The units of $\partial\pi/\partial r$ are N m^{-2}, and this represents the force acting per m^2 of material surface. The number of moles of adsorbate per m^2 of surface is $\frac{q_i}{A}$. Therefore the force per mole of adsorbate is

$-\left(\frac{\partial \pi}{\partial r}\right) \Big/ \left(\frac{q_i}{A}\right) = -\frac{\partial \mu_i}{\partial r}$. This force is balanced by friction between the mobile adsorbates and the surface of the material.

$$-\left(\frac{\partial \pi}{\partial r}\right) \Big/ \left(\frac{q_i}{A}\right) = \frac{RT}{Đ_i} u_i; \quad -\frac{\partial \mu_i}{\partial r} = \frac{RT}{Đ_i} u_i \tag{2}$$

where u_i is the velocity of motion of the adsorbate with respect to the framework material. The quantity $\frac{RT}{Đ_i}$ in the right member of equation (2) is interpreted as the "drag coefficient". The unary diffusivity $Đ_i$, with the units m^2 s^{-1}, is to be interpreted as an inverse drag coefficient between the adsorbate and the surface. If we define N_i as the number of moles of species *i* transported per m^2 of crystalline material per second

$$N_i \equiv \rho q_i u_i \tag{3}$$

where ρ is the framework density with units of kg m^{-3}, we obtain the flux relation

$$-\rho \frac{A}{RT} \frac{\partial \pi}{\partial r} = \frac{N_i}{Đ_i} \tag{4}$$

Combining Equation (1) and (4) we obtain

$$-\rho \frac{q_i}{RT} \frac{\partial \mu_i}{\partial r} = \frac{N_i}{Đ_i} \tag{5}$$

Equation (5) is the familiar form of the Maxwell-Stefan (M-S) formulation[5-7] for unary diffusion.

The chemical potential gradient can be related to the gradient of the molar loading by defining a thermodynamic correction factor Γ_i

$$\frac{q_i}{RT} \frac{\partial \mu_i}{\partial r} = \Gamma_i \frac{\partial q_i}{\partial r}; \quad \Gamma_i \equiv \frac{q_i}{p_i} \frac{\partial p_i}{\partial q_i} \tag{6}$$

Combining Equations (5) and (6) we may write

$$N_i = -\rho Đ_i \frac{q_i}{RT}\frac{\partial \mu_i}{\partial r} = -\rho Đ_i \Gamma_i \frac{\partial q_i}{\partial r} \tag{7}$$

The product of the M-S diffusivity and the thermodynamic correction factor is the Fick diffusivity

$$D_i = Đ_i \Gamma_i \tag{8}$$

The magnitude of the M-S diffusivity varies with the spreading pressure. The spreading pressure can be determined from knowledge of the unary adsorption isotherm, $q(p)$, fitted with say the dual-Langmuir-Freundlich isotherm

$$q(p) = q_{A,sat}\frac{b_A p^{\nu_A}}{1+b_A p^{\nu_A}} + q_{B,sat}\frac{b_B p^{\nu_B}}{1+b_B p^{\nu_B}} \tag{9}$$

The spreading pressure is given by

$$\frac{\pi A}{RT} = \int_0^P \frac{q(p)}{p} dp \tag{10}$$

The units of $\frac{\pi A}{RT}$, also called the adsorption potential,[8] are mol kg^{-1}.

For the 2-site Langmuir-Freundlich isotherm, the integration yields

$$\frac{\pi A}{RT} = \int_{P=0}^{P} \frac{q(p)}{p} dp = \frac{q_{A,sat}}{\nu_A}\ln\left(1+b_A P^{\nu_A}\right) + \frac{q_{B,sat}}{\nu_B}\ln\left(1+b_B P^{\nu_B}\right) \tag{11}$$

Figures 1a, b, c presents MD data on the M-S diffusivities of various guest molecules in (a) all-silica FAU zeolite, (b) MFI zeolite, and (c) IRMOF-1. The MD data are at 300 K. The *x*-axis is the $\frac{\pi A}{RT}$ calculated on the basis of the molar loadings used in the MD simulations, in conjunction with CBMC simulation data for the unary isotherms of the guest molecules. The dependence of the M-S diffusivities on $\frac{\pi A}{RT}$ varies with different host materials. This aspect is best illustrated by the Figure 1d that compares the M-S diffusivity of CH_4 in various host materials.

Preferential location of molecules within the structural framework can cause strong isotherm inflections. For example, branched alkanes, benzene, alkyl benzenes, and cyclohexane prefer to locate at the channel intersections of MFI zeolite due to extra "leg-room" and other configurational considerations.[9] There are only 4 intersection sites available per unit cell of MFI. This implies that to obtain loadings higher than $\Theta_i = 4$ molecules per unit cell, an extra "push" will be required to locate the molecules elsewhere within the channels; this leads to isotherm inflection. Due to strong isotherm inflections, the $1/\Gamma_i$ exhibits a cusp-like inflection at a loading of $\Theta_i = 4$, when all the preferred adsorption sites are occupied; is demonstrated in the data on $1/\Gamma_i$ for iso-butane/MFI in Figures 2. In the range $0 < \Theta_i < 4$, $1/\Gamma_i$ decreases nearly linearly with Θ_i signifying the fact that the vacancy *decreases* almost linearly with loading. For $\Theta_i > 4$, $1/\Gamma_i$ increases with Θ_i because additional sites *within* the MFI channels are created to accommodate more than 4 molecules per unit cell, i.e. the number of available sites *increases* within this loading range. These additional sites must be accommodated within the channels, requiring the additional "push" that caused the inflection.

When molecular clustering occurs $1/\Gamma_i$ can exceed unity; such clustering may occur when the operating temperature is below the critical temperature of the guest molecule.[10] Figure 3 presents the experimental data of Chmelik et al.[11], for the loading dependence of n-butane (nC4, $T_c = 425$ K), iso-butane (iC4, $T_c = 408$ K), neopentane (neo-P, $T_c = 434$ K), and 2-methylbutane (2MB, $T_c = 460$ K) at $T = 298$ K, significantly lower than the critical temperatures of each of the four guest species. For all four guest molecules the dependence of M-S diffusivities on the spreading pressure goes hand-in-hand with the corresponding dependence of $1/\Gamma_i$.

3. The Maxwell-Stefan relations for *n*-component diffusion in micropores

The best starting point for developing the Maxwell-Stefan formulation for mixture diffusion is Equation (2), that needs extension. The force acting per mole of adsorbate species *i* is balanced by (1) friction between *i* and the pore walls (this is the same term as for unary transport), and (2) friction between species *i* and species *j*. We may write

$$-\frac{1}{RT}\frac{\partial \mu_i}{\partial r}=\sum_{\substack{j=1\\ j\neq i}}^{n}\frac{x_j}{Đ_{ij}}\left(u_i-u_j\right)+\frac{1}{Đ_i}\left(u_i\right);\quad i=1,2..n \tag{12}$$

The x_i in equations (12) represent the component mole fractions in the adsorbed phase within the pores

$$x_i=q_i/q_t;\quad q_t=\sum_{i=1}^{n}q_i;\quad i=1,2,..n \tag{13}$$

The $Đ_i$ have the same significance as for unary diffusion; they are inverse drag coefficients between the species *i* and the material surface. Indeed, an important persuasive advantage of the M-S equations is that the $Đ_i$ for mixture diffusion often retains the same magnitude and loading dependence as for unary diffusion.[5, 12, 13]

The $Đ_{ij}$ may be interpreted as the inverse drag coefficient between species *i* and species *j*. At the molecular level, the $Đ_{ij}$ reflect how the facility for transport of species *i correlates* with that of species *j*; they are also termed *exchange coefficients*. The multiplication factor x_j has been introduced in the numerator of the first right member of equation (12) because the friction experience by species *i* with the each of the other species in the adsorbed phase ($j =$ 2, 3, ..*n*) should be proportional to the relative amounts of species *j* (= 2, 3, ..*n*) in the adsorbed phase. Expressing the velocities u_j in terms of the intra-crystalline diffusion fluxes $u_i=N_i/\rho q_i$

$$-\frac{\rho}{RT}\frac{\partial \mu_i}{\partial r}=\sum_{\substack{j=1\\ j\neq i}}^{n}\frac{x_j}{Đ_{ij}}\left(\frac{N_i}{q_i}-\frac{N_j}{q_j}\right)+\frac{1}{Đ_i}\left(\frac{N_i}{q_i}\right);\quad i=1,2...n \tag{14}$$

Multiplying both sides of equation (14) by x_i we get

$$-\rho\frac{x_i}{RT}\frac{\partial \mu_i}{\partial r}=\sum_{\substack{j=1\\ j\neq i}}^{n}\frac{x_ix_j}{Đ_{ij}}\left(\frac{N_i}{q_i}-\frac{N_j}{q_j}\right)+\frac{1}{Đ_i}\left(\frac{x_iN_i}{q_i}\right);\quad i=1,2...n \tag{15}$$

In view of the equation (13), we may simplify equation (15) to write

$$-\rho \frac{q_i}{RT}\frac{\partial \mu_i}{\partial r} = \sum_{\substack{j=1 \\ j\neq i}}^{n}\left(\frac{x_j N_i - x_i N_j}{Đ_{ij}}\right) + \frac{N_i}{Đ_i}; \quad i = 1,2...n \tag{16}$$

The Onsager reciprocal relations demand the symmetry constraint

$$Đ_{ij} = Đ_{ji}; \quad i,j = 1,2,...n \tag{17}$$

As discussed in the following section, the exchange coefficients $Đ_{ij}$ bear a relation with the M-S diffusivity in the fluid mixture, $Đ_{ij,fl}$; this is an important advantage of the M-S formulation.

An entirely analogous manner of writing equation (16) is in terms of molar concentrations c_i, in the adsorbed phase, based on the accessible pore volume, V_p (= m^3 pore volume per kg framework)

$$c_i = \frac{q_i}{V_p}; \quad c_t = \sum_{i=1}^{n} c_i = \frac{q_t}{V_p} \tag{18}$$

This alternative formulation:

$$-\rho V_p \frac{c_i}{RT}\frac{\partial \mu_i}{\partial r} = \sum_{\substack{j=1 \\ j\neq i}}^{n}\left(\frac{x_j N_i - x_i N_j}{Đ_{ij}}\right) + \frac{N_i}{Đ_i}; \quad i = 1,2...n \tag{19}$$

The quantity ρV_p is the fractional pore volume

$$\rho V_p = \left(\frac{\text{kg framework}}{\text{m}^3 \text{ framework}}\right)\left(\frac{\text{m}^3 \text{ pore volume}}{\text{kg framework}}\right) = \left(\frac{\text{m}^3 \text{ pore volume}}{\text{m}^3 \text{ framework}}\right) = \varepsilon \tag{20}$$

So, we re-write equation (19) in the form

$$-\varepsilon \frac{c_i}{RT}\frac{\partial \mu_i}{\partial r} = \sum_{\substack{j=1 \\ j\neq i}}^{n}\left(\frac{x_j N_i - x_i N_j}{Đ_{ij}}\right) + \frac{N_i}{Đ_i}; \quad i = 1,2...n \tag{21}$$

The formulation (21) has been employed to develop a unified theory of mixture diffusion in both micropores and mesopores.[12, 14-16] The fluxes N_i in equation (21), and in this entire article are defined in terms of the moles transported per m^2 of the *total surface of crystal material*. Alternatively, if we just focus on fluxes inside a single pore, it is convenient to define the fluxes N_i in terms of the moles transported per m^2 surface of the pore, then the factor ρV_p has to be omitted in the left member of equation (21).

Early publications[17-20] on n-component mixture diffusion in micropores have been developed the M-S formulation in a different manner, using the fractional occupancies, θ_i, of species i in relation to the saturation capacities, $q_{i,sat}$, for adsorption of each species

$$\theta_i = \frac{q_i}{q_{i,sat}}; \quad i = 1,2,..n \tag{22}$$

as multiplication factor on the right member of equation (12). In this case we write

$$-\frac{1}{RT}\frac{\partial \mu_i}{\partial r} = \sum_{\substack{j=1 \\ j\neq i}}^{n} \frac{\theta_j}{Đ_{ij}^{\theta}}\left(u_i - u_j\right) + \frac{1}{Đ_i}\left(u_i\right); \quad i = 1,2..n \tag{23}$$

The superscript θ on the exchange coefficients $Đ_{ij}^{\theta}$ serves as a reminder that these coefficients are distinct from those defined in equation (12).

Expressing the velocities u_j in terms of the intra-crystalline diffusion fluxes $u_i = N_i / \rho q_i$ we get

$$-\frac{1}{RT}\frac{\partial \mu_i}{\partial r} = \sum_{\substack{j=1 \\ j\neq i}}^{n} \frac{\theta_j}{Đ_{ij}^{\theta}}\left(\frac{N_i}{\rho q_i} - \frac{N_j}{\rho q_j}\right) + \frac{1}{Đ_i}\left(\frac{N_i}{\rho q_i}\right); \quad i = 1,2..n \tag{24}$$

Multiplying both sides of equation (24) by θ_i and re-arranging we get

$$-\rho\frac{\theta_i}{RT}\frac{\partial \mu_i}{\partial r} = \sum_{\substack{j=1 \\ j\neq i}}^{n} \frac{\theta_i\theta_j}{Đ_{ij}^{\theta}}\left(\frac{N_i}{q_i} - \frac{N_j}{q_j}\right) + \frac{\theta_i}{Đ_i}\left(\frac{N_i}{q_i}\right); \quad i = 1,2..n \tag{25}$$

In view of equation (22), equation (25) can be re-arranged to

$$-\rho\frac{\theta_i}{RT}\frac{\partial \mu_i}{\partial r} = \sum_{\substack{j=1 \\ j\neq i}}^{n} \left(\frac{q_j N_i - q_i N_j}{q_{i,sat} q_{j,sat} Đ_{ij}^{\theta}}\right) + \frac{N_i}{q_{i,sat} Đ_i}; \quad i = 1,2..n \tag{26}$$

The Onsager reciprocal relations demand the symmetry

$$q_{j,sat} Đ_{ij}^{\theta} = q_{i,sat} Đ_{ji}^{\theta}; \quad i = 1,2..n \tag{27}$$

The two sets of exchange coefficients defined in equations (12) and (23) are inter-related

$$q_{j,sat} Đ_{ij}^{\theta} \big/ q_t = Đ_{ij} = Đ_{ji} = c_{i,sat} Đ_{ji}^{\theta} \big/ q_t \tag{28}$$

The exchange coefficients $Đ_{ij}^{\theta}$ cannot be simply related to the fluid phase M-S diffusivity, $Đ_{12,\mathrm{fl}}$. It is for this reason that we prefer the formulation in equation (16).

If the saturation capacities of all of the individual species are (nearly) equal to one another, equation (26) can be simplified to yield

$$-\rho \frac{1_i}{RT} \frac{\partial \mu_i}{\partial r} = \sum_{\substack{j=1 \\ j \neq i}}^{n} \left(\frac{\theta_j N_i - \theta_i N_j}{Đ_{ij}^{\theta}} \right) + \frac{N_i}{Đ_i}; \quad i = 1,2..n \tag{29}$$

The important advantage of the use of equation (29) is that by combining with the mixed-gas Langmuir model for mixture adsorption (discussed below), analytical solutions can be derived for the membrane permeation fluxes, and effectiveness factors.[21-24]

In this article, we use the M-S formulation given by equations (16).

4. The Maxwell-Stefan relations for binary mixture diffusion in micropores

For binary mixture diffusion inside porous crystalline materials the Maxwell-Stefan equations (16) are written as

$$\begin{aligned} -\rho \frac{q_1}{RT} \frac{\partial \mu_1}{\partial r} &= \frac{x_2 N_1 - x_1 N_2}{Đ_{12}} + \frac{N_1}{Đ_1} \\ -\rho \frac{q_2}{RT} \frac{\partial \mu_2}{\partial r} &= \frac{x_1 N_2 - x_2 N_1}{Đ_{12}} + \frac{N_2}{Đ_2} \end{aligned} \tag{30}$$

The first members on the right hand side of Equation (30) are required to quantify slowing-down effects that characterize binary mixture diffusion.[5, 12, 25] There is no experimental technique for direct determination of the exchange coefficients $Đ_{12}$, that quantify molecule-molecule interactions. Molecular dynamics (MD) simulation data from the literature[5, 12, 13, 20, 26, 27] provide the further insights into the characteristics of the exchange coefficients $Đ_{12}$. Figure 4 presents MD data for $Đ_{12}$ for six equimolar binary mixtures equimolar ($q_1 = q_2$) binary mixtures (a) H_2/CH_4, (b) CH_4/Ar, (c) CH_4/C_2H_6, (d) CO_2/CH_4, (e) CO_2/H_2, and (f) CO_2/N_2 at 300 K, in a variety of micro-porous host materials with varying pore size, pore topology and pore connectivity. Also included are MD data for mesoporous BTP-COF with hexagonal channels of 3.4 nm size. The data are compared at the total mixture pore concentration, $c_t = (q_1 + q_2)/V_p$.

For mesoporous materials with pores in the 20 Å to 100 Å size range the values of the exchange coefficient $Đ_{12}$ are the nearly the same as the binary *fluid phase* M-S diffusivity, $Đ_{12,\mathrm{fl}}$, over the entire range of pore concentrations.[5, 12, 15, 27] For micro-porous materials, the exchange coefficient $Đ_{12}$ cannot be directly identified with the corresponding fluid phase diffusivity $Đ_{12,\mathrm{fl}}$ because the molecule-molecule interactions are also significantly influenced by molecule-wall interactions. For microporous materials, the exchange coefficients $Đ_{12}$ are lower than the corresponding values of $Đ_{12,\mathrm{fl}}$ by a factor that depends on the pore size, connectivity and topology.[5, 12, 15, 27] Procedures for estimation of the $Đ_{12,\mathrm{fl}}$ are available in Poling et al.,[28] and therefore this provides a convenient starting point for the estimation of the $Đ_{12}$.

For purposes of calculations of the uptake within crystals and permeation fluxes across membranes, we need to calculate the chemical potential gradients, $\frac{\partial \mu_i}{\partial r}$, where r is the radius of a spherical crystal or distance along the membrane thickness. For an ideal gas mixture, the chemical potential gradients can be related to the partial pressure gradients in the bulk gas phase mixture

$$\frac{\partial \mu_i}{\partial r} = RT \frac{\partial \ln p_i}{\partial r} = RT \frac{1}{p_i} \frac{\partial p_i}{\partial r} \tag{31}$$

The gradients in the chemical potential can be related to the gradients of the molar loadings by defining thermodynamic correction factors Γ_{ij}

$$\frac{q_i}{RT} \frac{\partial \mu_i}{\partial r} = \sum_{j=1}^{2} \Gamma_{ij} \frac{\partial q_j}{\partial r}; \quad \Gamma_{ij} = \frac{q_i}{p_i} \frac{\partial p_i}{\partial q_j}; \quad i,j = 1,2 \tag{32}$$

In 2-dimensional matrix notation, equation (32) takes the form

$$-\begin{pmatrix} \frac{q_1}{RT}\frac{\partial \mu_1}{\partial r} \\ \frac{q_2}{RT}\frac{\partial \mu_2}{\partial r} \end{pmatrix} = [\Gamma] \begin{pmatrix} \frac{\partial q_1}{\partial r} \\ \frac{\partial q_2}{\partial r} \end{pmatrix} \tag{33}$$

The thermodynamic correction factors Γ_{ij} can be calculated by differentiation of the model describing mixture adsorption equilibrium. Generally speaking, the Ideal Adsorbed Solution Theory (IAST) of Myers and Prausnitz[2] is the preferred method for estimation of mixture adsorption equilibrium. In some special case, the mixed-gas Langmuir model

$$\frac{q_1}{q_{1,sat}} = \theta_1 = \frac{b_1 p_1}{1 + b_1 p_1 + b_2 p_2}; \quad \frac{q_2}{q_{2,sat}} = \theta_2 = \frac{b_2 p_2}{1 + b_1 p_1 + b_2 p_2} \tag{34}$$

may be of adequate accuracy.

For the mixed-gas Langmuir model, equation (34), we can derive simple analytic expressions for the four elements of the matrix of thermodynamic factors:[17]

$$\begin{bmatrix} \Gamma_{11} & \Gamma_{12} \\ \Gamma_{21} & \Gamma_{22} \end{bmatrix} = \frac{1}{1 - \theta_1 - \theta_2} \begin{bmatrix} 1 - \theta_2 & \frac{q_{1,sat}}{q_{2,sat}}\theta_1 \\ \frac{q_{2,sat}}{q_{1,sat}}\theta_2 & 1 - \theta_1 \end{bmatrix} \tag{35}$$

where the fractional occupancies, θ_i, are defined by Equation (22).

The elements of the matrix of thermodynamic factors Γ_{ij} can be calculated explicitly from information on the component loadings q_i in the adsorbed phase; this is the persuasive advantage of the use of the mixed-gas Langmuir model. By contrast, the IAST does not allow the calculation of Γ_{ij} explicitly from knowledge on the component loadings q_i in the adsorbed phase; an iterative procedure is required.

Let us define the square matrix $[B]$

$$[B] = \begin{bmatrix} \frac{1}{Đ_1} + \frac{x_2}{Đ_{12}} & -\frac{x_1}{Đ_{12}} \\ -\frac{x_2}{Đ_{12}} & \frac{1}{Đ_2} + \frac{x_1}{Đ_{12}} \end{bmatrix} \tag{36}$$

Equation (30) can be re-cast into 2-dimensional matrix notation

$$-\rho\begin{pmatrix}\frac{q_1}{RT}\frac{\partial\mu_1}{\partial r}\\ \frac{q_2}{RT}\frac{\partial\mu_2}{\partial r}\end{pmatrix}=[B]\begin{pmatrix}N_1\\ N_2\end{pmatrix};\quad \begin{pmatrix}N_1\\ N_2\end{pmatrix}=-\rho[B]^{-1}\begin{pmatrix}\frac{q_1}{RT}\frac{\partial\mu_1}{\partial r}\\ \frac{q_2}{RT}\frac{\partial\mu_2}{\partial r}\end{pmatrix} \tag{37}$$

The inverse of the square matrix $[B]$ can be obtained explicitly

$$[B]^{-1}=\frac{1}{1+\frac{x_1Đ_2}{Đ_{12}}+\frac{x_2Đ_1}{Đ_{12}}}\begin{bmatrix}Đ_1\left(1+\frac{x_1Đ_2}{Đ_{12}}\right) & \frac{x_1Đ_1Đ_2}{Đ_{12}}\\ \frac{x_2Đ_1Đ_2}{Đ_{12}} & Đ_2\left(1+\frac{x_2Đ_1}{Đ_{12}}\right)\end{bmatrix} \tag{38}$$

Combining equations (33), (37), and (38) we obtain

$$\begin{pmatrix}N_1\\ N_2\end{pmatrix}=-\frac{\rho}{1+\frac{x_1Đ_2}{Đ_{12}}+\frac{x_2Đ_1}{Đ_{12}}}\begin{bmatrix}Đ_1\left(1+\frac{x_1Đ_2}{Đ_{12}}\right) & \frac{x_1Đ_1Đ_2}{Đ_{12}}\\ \frac{x_2Đ_1Đ_2}{Đ_{12}} & Đ_2\left(1+\frac{x_2Đ_1}{Đ_{12}}\right)\end{bmatrix}\begin{bmatrix}\Gamma_{11} & \Gamma_{12}\\ \Gamma_{21} & \Gamma_{22}\end{bmatrix}\begin{pmatrix}\frac{\partial q_1}{\partial r}\\ \frac{\partial q_2}{\partial r}\end{pmatrix} \tag{39}$$

The ratio ($Đ_1/Đ_{12}$) is a reflection of the *degree of correlations*. We consider correlation effects to be strong when $Đ_1/Đ_{12}>1$. Figure 5 shows MD data on $Đ_1/Đ_{12}$ for diffusion of six different mixtures (a) H_2/CO_2, (b) CO_2/CH_4, (c) H_2/CH_4, (d) CH_4/nC_4H_{10}, (e) CH_4/C_2H_6, and (f) CH_4/C_3H_8 in a variety of host materials, expressed as a function of the total concentration, c_t, of the adsorbed mixture within the pores. The use of pore concentrations c_t rather than the molar loadings affords a fairer comparison of different host materials as explained in previous works.[15] For any guest/host combination, $Đ_1/Đ_{12}$ is seen to increase as the pore concentration increases; this implies that correlation effects are expected to be stronger for separations operating at higher pressures.

Consider Figure 5c that compares the data on $Đ_1/Đ_{12}$ for $H_2(1)/CH_4(2)$ mixtures in several hosts. For $H_2(1)/CH_4(2)$ mixtures, correlations are strongest in mesoporous BTP-COF, one-dimensional (1D) channel structures (e.g. MgMOF-74), intersecting channels (e.g. MFI), and "open" structures (e.g. NaX zeolite, CuBTC, IRMOF-1) consisting of large cages separated by wide windows. Strong correlation effects cause slowing-down of more-mobile-less-strongly-adsorbed molecules by tardier-more-strongly-adsorbed-partner species. For example, the mobility of less-strongly-adsorbed H_2 in the intersecting channels of MFI zeolite, is significantly retarded by the presence of its more-strongly-adsorbed-partner CH_4.

Extensive Molecular Dynamics (MD) simulations have shown that correlation effects are of negligible importance for mixture diffusion across materials such as LTA, ZIF-8, CHA, DDR, ERI that consist of cages separated by windows in the 3.4 Å – 4.2 Å size range.[5, 12, 25, 29] Molecules jump one-at-a-time across the narrow windows, and the assumption of negligible correlations is justified. As verification, we note from Figure 5c, that $Đ_1/Đ_{12} < 1$ for $H_2(1)/CH_4(2)$ mixture diffusion in LTA zeolite.

In cases in which correlations are negligible, Equation (39) simplifies to yield

$$\begin{pmatrix} N_1 \\ N_2 \end{pmatrix} = -\rho \begin{bmatrix} Đ_1 & 0 \\ 0 & Đ_2 \end{bmatrix} \begin{bmatrix} \Gamma_{11} & \Gamma_{12} \\ \Gamma_{21} & \Gamma_{22} \end{bmatrix} \begin{pmatrix} \dfrac{\partial q_1}{\partial r} \\ \dfrac{\partial q_2}{\partial r} \end{pmatrix} = -\rho \begin{bmatrix} Đ_1 & 0 \\ 0 & Đ_2 \end{bmatrix} \begin{pmatrix} \dfrac{\partial(\Gamma_{11}q_1 + \Gamma_{12}q_2)}{\partial r} \\ \dfrac{\partial(\Gamma_{21}q_1 + \Gamma_{22}q_2)}{\partial r} \end{pmatrix} \tag{40}$$

From Equation (40) we note that the intra-crystalline fluxes N_1, and N_2 are, respectively, proportional to the gradients of the corrected loadings $q_1(\mu_1 - \mu_1^0)/RT = \Gamma_{11}q_1 + \Gamma_{12}q_2$, and $q_2(\mu_2 - \mu_2^0)/RT = \Gamma_{21}q_1 + \Gamma_{22}q_2$. Here, μ_i^0 is the chemical potential of species *i* at the standard state.

5. Simulation methodology for transient uptake in microporous particle

For most crystal geometries, representation as an equivalent sphere is an acceptable approximation.[1] Indeed, most researchers report their uptake diffusivities in terms of a model that assumes uptake within a single spherical crystalline particle. The values thus obtained for the diffusivities within a spherical crystal can be translated to other crystal geometries by comparing values at the same characteristic dimension, defined as the ratio of the crystal volume to its external suface area. For a spherical shaped crystal of radius r_c, the ratio of the volume to the external surface area is $\dfrac{\left(\dfrac{4}{3}\pi r_c^3\right)}{4\pi r_c^2} = \dfrac{r_c}{3}$.

The radial distribution of molar loadings, q_i, within a spherical crystallite, of radius r_c, is obtained from a solution of a set of differential equations describing the uptake

$$\rho \frac{\partial q_i(r,t)}{\partial t} = -\frac{1}{r^2}\frac{\partial}{\partial r}\left(r^2 N_i\right) \tag{41}$$

The fluxes N_i, in turn, are related to the radial gradients in the molar loadings by Equation (39), or the simplified Equation (40). At time $t = 0$, i.e. the initial conditions, the molar loadings $q_i(r,0)$ at all locations r within the crystal are uniform (zero loadings). For all times $t \geq 0$, the exterior of the crystal is brought into contact with a bulk gas mixture at partial pressures $p_i(r_c,t)$ that is maintained constant till the crystal reaches thermodynamic equilibrium with the surrounding gas mixture.

$$t \geq 0; \quad q_i(r_c,t) \text{ in equilibrium with the initial values } p_i(r_c,t) \tag{42}$$

At any time t, during the transient approach to thermodynamic equilibrium, the spatial-averaged component loading within the crystallites of radius r_c is calculated using

$$\overline{q}_i(t) = \frac{3}{r_c^3}\int_0^{r_c} q_i(r,t) r^2 dr \tag{43}$$

The spatial-averaged $\overline{q}_i(t)$ can be compared directly with experimental transient uptake data.

In the concentration measures of adsorbed phase is terms of the molar concentrations $c_i = \frac{q_i}{V_p}$, the equation (41) is equivalent to

$$\rho V_p \frac{\partial c_i(r,t)}{\partial t} = \varepsilon \frac{\partial c_i(r,t)}{\partial t} = -\frac{1}{r^2}\frac{\partial}{\partial r}\left(r^2 N_i\right) \tag{44}$$

There is no generally applicable analytical solution to describe transient diffusion of binary mixtures and the set of Equations (39), (41), (42), and (43) need to be solved numerically using robust computational techniques. Equations (41) are first subjected to finite volume discretization. One of two strategies can be adopted: (a) equi-volume discretization, or (b) equi-distant discretization; see Figure 6. The choice of the discretization scheme used is crucially important in obtaining accurate, converged results. The choice of equi-volume slices is needed when the gradients of the loadings are particularly steep nearer to $r = r_c$. For either strategy, about 100 – 400 slices are employed, depending on the guest/host combination. Combination of the discretized partial differential equations (41) along with algebraic equations describing mixture adsorption equilibrium, results in a set of differential-algebraic equations (DAEs), which are solved using BESIRK.[30] BESIRK is a sparse matrix solver, based on the semi-implicit Runge-Kutta method originally developed by Michelsen,[31] and extended with the Bulirsch-Stoer extrapolation method.[32] Use of BESIRK improves the numerical solution efficiency in solving the set of DAEs. The evaluation of the sparse Jacobian required in the numerical algorithm is largely based on analytic expressions.[17] Further details of the numerical procedures used in this work, are provided by Krishna and co-workers;[17, 26, 33, 34] interested readers are referred to our website that contains the numerical details.[33]

6. Simulation methodology for transient membrane permeation

Thin microporous layers of zeolites, MOFs, and ZIFs have potential applications in membrane separations. The transient permeation fluxes N_i, defined in terms of the cross-sectional area of the membrane, are obtained by solving the set of partial differential equations

$$\frac{\partial q_i(z,t)}{\partial t} = -\frac{1}{\rho}\frac{\partial}{\partial z}\left(N_i\right) \tag{45}$$

where z is the distance coordinate along the direction of membrane thickness. In the general case when correlations are of importance, we need to use the M-S Equation (39) to describe the permeation fluxes.

For host materials such as DDR, CHA, ZIF-8, LTA-4A, correlations are of negligible importance because the guest molecules jump one-at-a-time across the narrow windows; in these circumstances, the simplified Equation (40) are used to describe permeation fluxes.

The boundary conditions are the partial pressures and component molar loadings at the upstream (z = 0) and downstream ($z = \delta$) faces of the membrane; see schematic in Figure **7**.

$$\begin{aligned} z = 0; &\quad p_i = p_{i0}; \quad q_i = q_{i0} \\ z = \delta; &\quad p_i = p_{i\delta}; \quad q_i = q_{i\delta} \end{aligned} \tag{46}$$

The membrane permeation selectivity, S_{perm}, is usually defined by

$$S_{perm} == \frac{N_1/(p_{10}-p_{1\delta})}{N_2/(p_{20}-p_{2\delta})} \tag{47}$$

The solution of Equation (39), and (45) requires discretization of the membrane layer into slices, about 100-200 in number, and solving the resulting set of differential-algebraic equations (DAE) using the same numerical procedures as for transient uptake within crystals.

A major proportion of the membrane permeation data available in the literature pertains to MFI zeolite membranes. Figure 8 presents a summary of the MD simulation data for the degree of correlations, $Đ_1/Đ_{12}$, for diffusion of equimolar binary H_2(1)/CH_4(2), CH_4(1)/nC_4H_{10}(2), CH_4(1)/CO_2(2), and H_2(1)/CO_2(2) mixtures in MFI zeolite at 300 K, as a function of the total mixture loading, q_t. Typically, the mixture molar loadings in the membrane layer will be in the range of 1 – 4 mol kg^{-1}. From the data in Figure 8 we must conclude that correlation effects will have an important bearing on the mixture permeation characteristics.

To provide a feel for the magnitude of slowing-down effects in membrane permeation we investigated the influence of $Đ_1/Đ_{12}$ on the steady-state permeation selectivity, S_{perm} (defined in Equation (47)), of binary 95/5 CH_4(1)/nC_4H_{10}(2) mixture permeation across MFI membrane at 300 K. The values of S_{perm} are calculated from steady-state permeation simulations for the fluxes, taking $p_{1\delta} = p_{2\delta} \approx 0$ and p_{10}/p_{20} = 95/5; see Figure 9a. We note that the highest selectivities in favor of *n*-butane is attained with $Đ_1/Đ_{12}$ = 4, indicating large slowing-down effects.

Figures 9b, and 9c are plots of the normalized fluxes $N_1/(\rho q_{10}Đ_1/\delta)$, and $N_2/(\rho q_{20}Đ_2/\delta)$ as a function of the total upstream pressure. We note that the normalized flux of n-butane is practically unaffected by the influence of correlations. On the other hand, the normalized flux of methane is reduced significantly with increasing values of $Đ_1/Đ_{12}$; this illustrates the importance of correlation effects.

Slowing-down effects retard the mobility of H_2 in $H_2(1)/CO_2(2)$ mixture permeation across MFI membranes, enhancing the separations in favor of $CO_2(2)$. In order to validate the M-S model equations to adequately describe mixture permeation across MFI membranes, Figure 10a,b compares the experimental data of Sjöberg et al.[35] for steady-state permeation of 50/50 equimolar $H_2(1)/CO_2(2)$ mixtures across MFI (silicalite-1) zeolite membrane at 273 K with (steady-state) solutions to Equation (39), and (45) taking $Đ_1/Đ_{12}$ = 20 based on the MD data in Figure 8. There is excellent agreement between the Sjöberg data and the M-S model. The $H_2(1)$ flux is particularly sensitive to the choice of the parameter $Đ_1/Đ_{12}$. If correlations are completely neglected, and Equation (40) is used the $H_2(1)$ flux is severely over-predicted; see Figure 10b. In the other extreme, if we assume that correlations are dominant, i.e. $Đ_1/Đ_{12} >>> 1$, the following expression can be derived

$$\begin{pmatrix} N_1 \\ N_2 \end{pmatrix} = \frac{\rho}{\frac{x_1}{Đ_1}+\frac{x_2}{Đ_2}} \begin{bmatrix} x_1 & x_1 \\ x_2 & x_2 \end{bmatrix} \begin{bmatrix} \Gamma_{11} & \Gamma_{12} \\ \Gamma_{21} & \Gamma_{22} \end{bmatrix} \begin{pmatrix} \frac{\partial q_1}{\partial r} \\ \frac{\partial q_2}{\partial r} \end{pmatrix}; \quad \text{correlations dominant} \tag{48}$$

The predictions of $H_2(1)$ flux using Equation (48) provides the “lower limit” for the flux values. The simulation data in Figure 10a,b underscore the importance of proper modelling of correlation effects for MFI membrane permeation.

7. Simulation methodology for transient breakthrough in fixed bed adsorbers

Assuming plug flow of an *n*-component gas mixture through a fixed bed (see schematic in Figure 11) maintained under isothermal conditions, the partial pressures in the gas phase at any position and instant of time are obtained by solving the following set of partial differential equations for each of the species *i* in the gas mixture.[6, 36]

$$\frac{1}{RT}\frac{\partial p_i(t,z)}{\partial t} = -\frac{1}{RT}\frac{\partial \left(v(t,z)p_i(t,z)\right)}{\partial z} - \frac{(1-\varepsilon)}{\varepsilon}\rho\frac{\partial \overline{q}_i(t,z)}{\partial t}; \quad i = 1,2,...n \tag{49}$$

In equation (49), t is the time, z is the distance along the adsorber, ρ is the framework density, ε is the bed voidage, v is the interstitial gas velocity, and $\overline{q}_i(t,z)$ is the *spatially averaged* molar loading within the crystallites of radius r_c, monitored at position z, and at time t. The $\overline{q}_i(t,z)$ is determined from Equations (30), (41), and (43).

In industrial practice, the most common operation is to use a step-wise input of mixtures to be separated into an adsorber bed that is initially free of adsorbates, i.e. we have the initial condition

$$t = 0; \quad q_i(0,z) = 0 \tag{50}$$

At time, $t = 0$, the inlet to the adsorber, $z = 0$, is subjected to a step input of the n-component gas mixture and this step input is maintained till the end of the adsorption cycle when steady-state conditions are reached.

$$t \geq 0; \quad p_i(0,t) = p_{i0} \tag{51}$$

For presenting the breakthrough simulation results, we use the dimensionless time, $\tau = \frac{tv}{L}$, obtained by dividing the actual time, t, by the characteristic time, $\frac{L}{v}$.

8. Transient CO_2/C_2H_6 mixture uptake in DDR zeolite

DDR zeolite consists of cages, of 278 Å^3 size, separated by narrow windows.[5, 37] Figures 12, and 13 provide details of the pore landscape of DDR zeolite. Of crucial importance for diffusion are the dimensions of the windows connecting the cages; this information is summarized in Figure 14. The window dimensions are 3.65 Å × 4.37 Å. The framework density of DDR zeolite ρ = 1760 kg m^{-3}. Molecular Dynamics (MD) simulations[25, 29, 38] have established that CO_2 molecules jump lengthwise across the windows. The cross-section of a CO_2 molecule has a dimension of 3.03 Å, significantly lower than that of C_2H_6 that has a cross section of 3.76 Å; see Figure 15. Using MD simulations[25, 29, 38] as guidelines, we anticipate the diffusivity of CO_2 to be about 1-3 orders of magnitude higher than that of C_2H_6.

Binder et al.[39] and Lauerer et al.[40] report a set of three mixture uptake experiments with 1:1, 2:1, and 3:1 partial pressure ratios for CO_2 and C_2H_6 in the gas phase. For modelling of the transient uptake of CO_2 (= component 1) and C_2H_6 (= component 2) within the DDR zeolite crystal, the first step in the simulations is to model mixture adsorption equilibrium.

The data on the unary isotherms of CO_2 and C_2H_6 at 298 K are provided in Figure 36, Chapter 4 of the PhD dissertation of Binder.[41] The unary isotherms for both CO_2, and C_2H_6 can be described adequately by a single-site Langmuir isotherm

$$q_i = \frac{q_{i,sat} b_i p_i}{1 + b_i p_i} \tag{52}$$

The single-site Langmuir parameters are provided in Table 2; these fit parameters are on the basis of the scanned data from the PhD dissertation.

Figure 16 provides a comparison of unary isotherm data with single-site Langmuir fits using the parameters reported in Table 2. The fits are of good accuracy.

Figure 3 of Binder et al.[39] presents IAST calculations for binary mixture adsorption with constant CO_2 partial pressures of p_1 = 20, 40, and 60 kPa for experiments (1), (2), and (3), respectively. The partial pressures of C_2H_6 ethane in the gas phase is varied. The IAST calculations of Binder et al.[39] are shown as symbols in Figure 17.

For the conditions of the Binder/Lauerer experiments,[39, 40] a good prediction of the mixture adsorption equilibrium is also provided by the mixed-gas Langmuir model. To demonstrate this, the calculations using the mixed-gas Langmuir model, equation (34) are presented as the continuous solid lines in Figure 17. For the range of experiments, the mixed-gas Langmuir model is in very good agreement with IAST calculations.

Since we have established the accuracy of the mixed-gas Langmuir model to describe CO_2/C_2H_6 mixture adsorption equilibrium in DDR, the calculations using Equation (35) are justified, and accurate. Figure 18 presents calculations of elements of the matrix of thermodynamic correction factors Γ_{ij}, using Equation (35), expressed as a function of total mixture loading, q_t, for (a) 1:1, (b) 2:1, and (c) 3:1 ratios of partial pressures in the gas phase. In these calculations the total gas pressure, p_t, was varied from 1 to 100 kPa. The off-diagonal elements Γ_{12}, and Γ_{21} become increasingly important with increasing loadings. In particular, it is to be noted that the ratio Γ_{12}/Γ_{11} gets progressively closer to unity as the mixture loading increases. This implies that thermodynamic coupling effects are of particular importance for the uptake of CO_2 (1) from $CO_2(1)/C_2H_6(2)$ gas mixtures.

Figure 19 presents calculations of (Γ_{12} q_2/Γ_{11} q_1), and (Γ_{21} q_1/Γ_{22} q_2) for binary $CO_2(1)/C_2H_6(2)$ mixture adsorption in DDR for 3:1 ratios of partial pressures in the gas phase. We note that (Γ_{12} q_2/Γ_{11} q_1) is significantly larger in magnitude than (Γ_{21} q_1/Γ_{22} q_2). This implies that thermodynamic coupling effects influence CO_2 to a greater extent that C_2H_6.

A further point to emphasize about the data presented in Figure 18 and Figure 19 is that during transient desorption, the influence of the thermodynamic coupling effects should be expected to get less significant with time progression. We will see later, that this causes the adsorption/desorption trajectories to follow different trajectories in composition space.

If μ_i^0 is the chemical potential of species i at the standard state, then the quantities $q_1(\mu_1 - \mu_1^0)/RT = \Gamma_{11}q_1 + \Gamma_{12}q_2$, and $q_2(\mu_2 - \mu_2^0)/RT = \Gamma_{21}q_1 + \Gamma_{22}q_2$ may be regarded as the "thermodynamically corrected" measures of component loadings of components 1 and 2. We will return to this point later in the discussions. At finite loadings, thermodynamic coupling effects cannot be ignored.

From Equation (40) we note that the intra-crystalline fluxes N_1, and N_2 are, respectively, proportional to the gradients of the corrected loadings $q_1(\mu_1 - \mu_1^0)/RT = \Gamma_{11}q_1 + \Gamma_{12}q_2$, and $q_2(\mu_2 - \mu_2^0)/RT = \Gamma_{21}q_1 + \Gamma_{22}q_2$. In view of the calculations presented in Figure 19, we should expect the flux of CO_2 (= component 1) to be significantly influenced by the driving force of C_2H_6 (= component 2).

In the Henry regime of adsorption, when the fractional occupancies are vanishingly small, we have the special case that the matrix of thermodynamic factors reduces to the identity matrix

$$\begin{bmatrix} \Gamma_{11} & \Gamma_{12} \\ \Gamma_{21} & \Gamma_{22} \end{bmatrix} \rightarrow \begin{bmatrix} 1 & 0 \\ 0 & 1 \end{bmatrix}; \quad \theta_1, \theta_2 \rightarrow 0 \tag{53}$$

If the thermodynamic coupling effects are neglected, and the elements of the matrix of thermodynamic factors Γij equals Kronecker delta, $\Gamma_{ij} = \delta_{ij}$ and we obtain the uncoupled form of the flux equations

$$\begin{pmatrix} N_1 \\ N_2 \end{pmatrix} = -\rho \begin{bmatrix} Đ_1 & 0 \\ 0 & Đ_2 \end{bmatrix} \begin{pmatrix} \frac{\partial q_1}{\partial r} \\ \frac{\partial q_2}{\partial r} \end{pmatrix}; \quad \text{neglecting thermodynamic coupling} \tag{54}$$

In the following discussions we shall compare the simulation using the flux relations (40), including thermodynamic coupling, with simulations using equation (54) that neglects thermodynamic coupling.

We simulated the three set of experiments reported by Binder/Lauerer,[39, 40]

Experiment 1: 1:1 $CO_2(1)/C_2H_6(2)$ bulk gas mixture at 298 K, p_1 = 20 kPa, p_2 = 20 kPa.

Experiment 2: 2:1 $CO_2(1)/C_2H_6(2)$ bulk gas mixture at 298 K, p_1 = 40 kPa, p_2 = 20 kPa.

Experiment 3: 3:1 $CO_2(1)/C_2H_6(2)$ bulk gas mixture at 298 K, p_1 = 60 kPa, p_2 = 20 kPa.

The hexagonal crystals of DDR zeolite (see Figure 20), used in the Binder/Lauerer experiments[39, 40] are modelled as spherical crystals of effective radius r_c.

The primary aim of our simulations is to trace the origins of the spatial and temporal overshoots in the uptake of CO_2. The approach taken was to obtain a reasonably good match between the observed overshoot in the spatial-averaged uptake $\overline{q}_i(t)$ vs time, t, data of Binder/Lauerer,[39, 40]

There are only two adjustable parameters in the simulations: $Đ_1/r_c^2$, and $Đ_2/r_c^2$. The parameter values that allowed good agreement between the experiments and simulations are listed below:

Experiment 1: $Đ_1/r_c^2 = 0.125$ s^{-1}; $Đ_1/Đ_2$ = 1333. See Figure 22.

Experiment 2: $Đ_1/r_c^2 = 9.375\times10^{-3}$ s^{-1}; $Đ_1/Đ_2$ = 100. See Figure 23.

Experiment 3: $Đ_1/r_c^2 = 6.25\times10^{-3}$ s^{-1}; $Đ_1/Đ_2$ = 50. See Figure 24.

Figure 21 presents plots of $Đ_1/r_c^2$, and $Đ_2/r_c^2$, for CO_2(1), and C_2H_6(2) in DDR on the corresponding component loadings, q_1, and q_2, in the adsorbed phase at final equilibration. The component diffusivities appear to correlate with their loadings in the mixture, an expected trend.

The transient overshoot in the spatial-averaged uptake of CO_2 is properly captured by the simulations of the Maxwell-Stefan model equation (**40**), including the influence of thermodynamic coupling; these set of simulations are shown by the continuous solid lines in Figure 22, Figure 23, are Figure 24. Also shown in Figure 22, Figure 23, are Figure 24 are comparisons of the simulations of the adsorption and desorption cycles, plotted in composition space. It is noteworthy that the composition adsorption/desorption trajectories follow completely different paths during equilibration. During desorption, the influence of the thermodynamic coupling effects become progressively less significant with time progression. Consequently, no undershoots are experienced during desorption.

If thermodynamic coupling effects are neglected and the uncoupled flux relation (**54**) is employed, then the overshoots time-averaged uptake of CO_2 disappear, and both components approach equilibrium in a monotonous manner; see the dashed lines in Figure 22, Figure 23, are Figure 24.

We conclude that thermodynamic coupling effects are the root cause of the temporal overshoots of CO_2. The attainment of supra-equilibrium loadings within the DDR crystals signals the phenomenon of uphill transport. In order to investigate the genesis of uphill transport of CO_2 we examine the spatial distribution of loadings within the crystal of DDR.

Figures 25, 26, and 27 present the simulation results, respectively for Experiments 1, 2, and 3, for the transient development of component loadings along the radius of DDR crystal (center, $r = 0$; surface of crystal, $r = r_c$) monitored at different times from start of the uptake. During the transient equilibration, the loading of CO_2 exhibits spatial overshoots in all three Experiments 1, 2 and 3.

The spatial overshoot of CO_2 is a clear indication of uphill transport. What causes this uphill transport? In order to answer this question, we need to examine the mixture adsorption thermodynamics. Consider the simulations corresponding to Experiments 2, and 3. From the data on the $q_1(r,t)$, and $q_2(r,t)$ we determined the quantities $\Gamma_{11}q_1(r,t)+\Gamma_{12}q_2(r,t)$, and $\Gamma_{21}q_1(r,t)+\Gamma_{22}q_2(r,t)$ that are thermodynamically corrected measures of component loadings of components 1 and 2. The radial profiles of these "corrected" loadings, are calculated using

$$\frac{\begin{pmatrix} q_1\left(\mu_1 - \mu_1^0\right) \\ q_2\left(\mu_2 - \mu_2^0\right) \end{pmatrix}}{RT} = \begin{bmatrix} \Gamma_{11} & \Gamma_{12} \\ \Gamma_{21} & \Gamma_{22} \end{bmatrix} \begin{pmatrix} q_1 \\ q_2 \end{pmatrix} = \frac{1}{1-\theta_1-\theta_2} \begin{bmatrix} 1-\theta_2 & \dfrac{q_{1,sat}}{q_{2,sat}}\theta_1 \\ \dfrac{q_{2,sat}}{q_{1,sat}}\theta_2 & 1-\theta_1 \end{bmatrix} \begin{pmatrix} q_1 \\ q_2 \end{pmatrix} \tag{55}$$

Figure 28 shows the transient development of corrected loadings $\Gamma_{11}q_1(r,t)+\Gamma_{12}q_2(r,t)$, and $\Gamma_{21}q_1(r,t)+\Gamma_{22}q_2(r,t)$ along the radius of DDR crystal for simulations of Experiment 2. In terms of corrected loadings, there is no spatial overshoot of CO_2; this implies that CO_2 is not transported uphill of the gradient of its (partial) spreading pressure $(A/RT)(\partial\pi_1/\partial r)=\Gamma_{11}(\partial q_1/\partial r)+\Gamma_{12}(\partial q_2/\partial r)$.

Figure 29 shows the transient development of corrected loadings $\Gamma_{11}q_1(r,t)+\Gamma_{12}q_2(r,t)$, and $\Gamma_{21}q_1(r,t)+\Gamma_{22}q_2(r,t)$ along the radius of DDR crystal for simulations of Experiment 3. In terms of corrected loadings, there is no spatial overshoot of CO_2; this implies that CO_2 is not transported uphill of the gradient of its (partial) spreading pressure $(A/RT)(\partial\pi_1/\partial r)=\Gamma_{11}(\partial q_1/\partial r)+\Gamma_{12}(\partial q_2/\partial r)$.

This conclusion is further strengthened in the results presented in Figure 30 wherein the radial profiles of $\left(\mu_1-\mu_1^0\right)/RT$, and $\left(\mu_2-\mu_2^0\right)/RT$ are plotted. The transient development of chemical potentials of the adsorbed components within the DDR crystal is monotonous. Diffusion of CO_2 is not uphill of its chemical potential gradient.

It now remains to demonstrate that the use of corrected loadings serves to rationalize the experimentally observed spatio-temporal overshoots in the CO_2 loadings in the Binder/Lauerer[39, 40] experiments. For this purpose, consider the IFM data on the radial profiles for uptake from 2:1 CO_2/C_2H_6 gas mixtures within the hexagonal crystals of DDR zeolite; the radial profiles for CO_2, and C_2H_6 loadings are reproduced in Figure 31. The overshoots in the CO_2 loadings during the transient approach to equilibration are analogous to those observed in the simulation results presented Figure 26. From the experimental data on the $q_1(r,t)$, and $q_2(r,t)$ in Figure 31, we determined the quantities

$\Gamma_{11}q_1(r,t)+\Gamma_{12}q_2(r,t)$, and $\Gamma_{21}q_1(r,t)+\Gamma_{22}q_2(r,t)$ that are thermodynamically corrected measures of component loadings of components 1 and 2; the results are presented in Figure 32. In terms of corrected loadings, there are no spatio-temporal overshoots for CO_2. Indeed, the equilibration of both CO_2, and C_2H_6 proceeds in the same, conventional, manner. Both simulations (Figure 28), and experiments (Figure 32) confirm that the transport of CO_2 is downhill of the chemical potential gradient.

9. CO_2/C_2H_6 separations in fixed bed DDR adsorber

The Binder/Lauerer uptake experiments suggest the possibility of diffusion-selective purification of ethane by selective removal of CO_2 present as impurities. To demonstrate this possibility, we carried out transient breakthrough simulations in a fixed bed adsorber packed with crystallites of DDR.

Figure 33 shows the transient breakthrough of 10/90 CO_2/C_2H_6 mixtures through fixed bed adsorber packed with DDR crystals operating at 298 K, and total pressure p_t = 100 kPa. The parameter values are: L = 0.3 m; voidage of bed, ε = 0.4; interstitial gas velocity, v = 0.1 m/s; radius of crystallite, r_c = 40 μm; $Đ_1/r_c^2$ = 0.00125 s^{-1}; $Đ_1/Đ_2$ = 1333. The y-axis is the gas phase concentration at the adsorber outlet, normalized with respect to the feed concentrations at the inlet. The x-axis is the dimensionless time, $\tau = tv/L$, obtained by dividing the actual time, t, by the characteristic time, L/v.

We note that C_2H_6 breaks through earlier and can be recovered in purified form during the early stages of the transient operations. The separation relies on the significantly higher intra-crystalline diffusivity of CO_2. If there is no intra-crystalline diffusional limitation, CO_2 breaks through earlier and the purification strategy will not work. The separation relies on the significantly higher diffusivity of CO_2. If there is no intra-crystalline diffusional limitation, CO_2 breaks through earlier, and the purification strategy will be ineffectual.

10. Transient uptake of N_2/CH_4 mixture in LTA-4A zeolite

The structural details for LTA-4A zeolite are shown in Figure 34.[29]

The Habgood[42] experimental data on transient mixture uptake, measured at 194 K with partial pressures p_1 =50.9 kPa and p_2 =49.1 kPa, are shown in Figure 35. The $N_2(1)/CH_4(2)$ mixture constitutes a combination of more-mobile-less-strongly-adsorbed-N_2 and tardier-more-strongly-adsorbed-CH_4. Nitrogen is a “pencil-like” molecule (4.4 Å × 3.3 Å) that can hop length-wise across the narrow windows; the “spherical” CH_4 (3.7 Å) is much more severely constrained and has a diffusivity that is 22 times lower than that of N_2.

Table 3 provides the 1-site Langmuir parameters for N_2 and CH_4 in LTA-4A zeolite at 194 K. N_2 has an adsorption strength that is a factor 2.2 lower than that of CH_4. The mixture adsorption equilibrium is described perfectly by the mixed-gas Langmuir equation (34).

During the initial stages of the transient uptake, the pores of LTA-4A are predominantly richer in the more mobile N_2, but this is displaced by the more strongly-adsorbed-but-tardier CH_4 molecules at longer times. This results in an overshoot in the N_2 uptake in the experimental data. Note that the maximum loading of N_2 is about a factor 2.5 times that of the final equilibrated uptake. Put another way, supra-equilibrium loadings are attained for N_2 during a short time interval in the early stages of the transient uptake.

Let us now model the transient uptake process. The windows separating adjacent cages of LTA-4A zeolite are about 4 Å in size; each of the constituent species hops across the windows one-at-a-time. Put another way, the jumps are not correlated, and equations (40) can be used to describe intra-crystalline diffusion within crystals. The continuous solid lines in Figure 35 are the calculations using Equation (40). The simulations including thermodynamic coupling are able to quantitatively capture the overshoot in the spatial-averaged loading of N_2. The parameter values used in the simulations are: $Đ_1/r_c^2 = 1.56\times10^{-5}$ s^{-1}; $Đ_2/r_c^2 = 7.2\times10^{-9}$ s^{-1}.

The dashed lines in Figure 35 are the calculations using uncoupled flux equation (54). No overshoot is observed in this case. We concluded that thermodynamic coupling effects are the root cause of the overshoot in the spatial-averaged loading of N_2.

Also shown in Figure 35 are comparisons of the simulations of the adsorption and desorption cycles, plotted in composition space. The adsorption and desorption cycles follow completely different paths in composition space; the rationalization is to be found in the influence of the thermodynamic factors. Also, no undershoots are experienced during desorption.

Figure 36 shows the transient development of $N_2(1)$, and $CH_4(2)$ loadings along the radius of LTA-4A crystal (center, $r = 0$; surface of crystal, $r = r_c$) monitored at different times from start of the uptake. During the transient equilibration, the loading of N_2 exhibits spatial overshoots. The spatial overshoot of N_2 is a clear indication of uphill transport. From the data on the $q_1(r,t)$, and $q_2(r,t)$ we determined the quantities $\Gamma_{11}q_1(r,t)+\Gamma_{12}q_2(r,t)$, and $\Gamma_{21}q_1(r,t)+\Gamma_{22}q_2(r,t)$ that are thermodynamically corrected measures of component loadings of components 1 and 2. The radial profiles of these corrected loadings are shown in Figure 37. In terms of "corrected" loadings there is no spatial overshoot of N_2; this implies that N_2 is not transported uphill of its thermodynamically "corrected" driving force $\Gamma_{11}\left(\partial q_1/\partial r\right)+\Gamma_{12}\left(\partial q_2/\partial r\right)$. In other words, the transport of N_2 is down its chemical potential gradient.

11. Transient uptake of O_2/N_2 mixture in CMS

For O_2/N_2 mixture separations, diffusion selectivity in favor of O_2 is achievable by use of Carbon Molecular Sieve (CMS).[43] The mixed-gas Langmuir equation (34) is of good accuracy for description of mixture adsorption equilibrium; the unary isotherm data are provided in Table 4. The adsorption is in favor of N_2, whereas the diffusion favors O_2.

The experimental data of Chen et al.[44] for transient uptake of O_2/N_2 mixture in CMS shows an overshoot for the more mobile O_2; see Figure 38. The experimentally observed O_2 overshoot is properly captured using the flux equations (40) with the ratio of diffusivities $Đ_{O2}/Đ_{N2}$ =36.8, based on the data provided by Chen et al.[44] If thermodynamic coupling is neglected, the O_2 overshoot disappears.

Figure 39 shows the transient development of $O_2(1)$, and $N_2(2)$ loadings along the radius of CMS particle (center, $r = 0$; surface of particles, $r = r_c$) monitored at different times from start of the uptake. The more mobile O_2 shows pronounced spatio-temporal overshoots during the transient approach to equilibrium.

12. Transient uptake of nC6/2MP mixture in MFI zeolite

Figures 40, and 41 provide the pore landscape and structural details of MFI zeolite.

The transient uptake of *n*-hexane(nC6)/2-methylpentane(2MP) mixtures in microporous crystals of MFI zeolite, exposed to an equimolar gas phase mixture at constant total pressure (= 2.6 Pa) have been reported by Titze et al.;[45] see Figure 42. The transient equilibration of nC6 displays a pronounced overshoot, achieving supra-equilibrium loadings during transient equilibration.

Titze et al.[45] have established the validity of the uncoupled M-S equations (40) to model intra-crystalline fluxes by detailed consideration of correlation effects. The mixture adsorption equilibrium is determined using the IAST; the unary isotherm data are provided in Table 5. The essential features of the transient uptake on nC6/2MP uptake in MFI zeolite can be adequately captured by the flux equation (40) taking $Đ_{nC6}/Đ_{2MP}$ = 100.[45] The lower diffusivity of the mono-branched isomer 2MP is due to the severe configurational constraints within 5.5 Å sized channels of MFI. The nC6 overshoot is caused by the off-diagonal elements of $[\Gamma]$. If we take $\Gamma_{ij} = \delta_{ij}$, the nC6 overshoot disappears.[45] The overshoot of nC6 signifies uphill diffusion within the crystals during transient equilibration; this phenomenon is advantageous in the PSA process for separation of hexane isomers, deployed in a process for octane enhancement of gasoline.[6]

There is one additional feature of nC6/2MP mixture uptake that distinguishes it from the CO_2/C_2H_6/DDR, N_2/CH_4/LTA-4A and O_2/N_2/CMS uptakes. For nC6/2MP/MFI both diffusion and adsorption favor the linear isomer; the two phenomena act in concert to enhance separations.[6]

Figure 43 shows the transient development of component loadings along the radius of MFI crystal (center, $r = 0$; surface of crystal, $r = r_c$) monitored at different times from start of the uptake. The more mobile nC6 shows pronounced spatio-temporal overshoots during transient equilibration process. From the data on the $q_1(r,t)$, and $q_2(r,t)$ we determined the quantities $\Gamma_{11}q_1(r,t)+\Gamma_{12}q_2(r,t)$, and $\Gamma_{21}q_1(r,t)+\Gamma_{22}q_2(r,t)$ that are thermodynamically corrected measures of component loadings of components 1 and 2. The radial profiles of these corrected loadings are shown in Figure 44. In terms of corrected loadings there is no spatial overshoot of nC6; this implies that nC6 is not transported uphill of its thermodynamically corrected driving force $\Gamma_{11}(\partial q_1/\partial r)+\Gamma_{12}(\partial q_2/\partial r)$. In other words, the transport of nC6 is down its chemical potential gradient.

13. Transient uptake of n-C_4H_{10}/iso-C_4H_{10} in MFI zeolite

Figure 45 presents simulations of the transient uptake of n-butane(nC4)/iso-butane(iC4) mixtures in MFI. The linear *n*-butane has a mobility that is about 1-2 orders of magnitude higher than that of the branched isomer because of subtle configurational differences; this has been established PFG NMR experiments of Fernandez et al.[46] Configurational-entropy effects also serve to prefer the adsorption of the linear isomer.[45] There is synergy between adsorption and diffusion, analogous to that for nC6/2MP uptake. The continuous solid lines in Figure 45 are simulation results that include the influence of thermodynamic coupling. We note that the more mobile nC4 exhibits an overshoot. If the thermodynamic coupling effects are ignored, this overshoot disappears.

14. Transient uptake of benzene/ethylbenzene, and benzene/p-xylene in H-ZSM-5

The experimental data of Niessen and Karge[47, 48] for transient uptake of benzene(1)/ethylbenzene(2), and benzene(1)/*p*-xylene(2) mixtures in MFI zeolite (H-ZSM-5) show overshoots in the benzene uptake; see Figure **46** and Figure 47. The experimentally observed overshoots for benzene results from thermodynamic coupling effects; is demonstrated in the transient uptake simulations for the spatial-averaged component uptakes, that are also shown in Figure **46** and Figure 47.

15. Transient uptake of n-heptane/benzene in NaX zeolite

The experimental data of Kärger and Bülow[49] for transient uptake of n-heptane(1)/benzene(2) mixture in NaX zeolite at 359 K shows an overshoot in the uptake of the more mobile n-heptane; see Figure **48**. Benzene is much more strongly adsorbed due to electrostatic interactions with the Na^+ cations. The stronger binding energy of benzene makes the mobility of benzene significantly lower than that of the non-polar n-heptane.[50] The windows separating the adjacent cages of NaX are about 7.4 Å, and correlations effects meed to be taken into consideration for quantitative modelling, and the appropriate flux expressions Equation (39), including correlations are required.[6, 25, 51] However, correlation effects are not responsible for overshoots, as these tend to "iron out" differences between the species mobilities and mitigate against overshoots. The overshoot of the n-heptane uptake is solely ascribable to the off-diagonal elements of $\begin{bmatrix} \Gamma_{11} & \Gamma_{12} \\ \Gamma_{21} & \Gamma_{21} \end{bmatrix}$; this is confirmed by the simulation results presented in Figure **48** that compares the calculations using Equation (40) with those obtained from uncoupled flux equation (54). We conclude that thermodynamic coupling cause overshoots of n-heptane.

16. Transient uptake of N_2/CH_4 in BaETS-4

By tuning the size of the microporous channels and using ETS-4 as adsorbent, both adsorption and diffusion characteristics favor the selective uptake of N_2 from $N_2(1)/CH_4(2)$ mixtures.[52-54] The transient uptake data of Majumdar et al.[53] for Ba-ETS-4 are shown in Figures 49a, and 49b for (a) 10/90, and (b) 50/50 mixtures show overshoots in the uptake of the more mobile N_2. The pores of BaETS-4 virtually exclude methane molecules, and it is not entirely clear that the IAST calculations can be used to calculate mixture adsorption equilibrium; for this reason no simulation results are presented here to trace the origins of the nitrogen overshoots.

17. Transient uptake of hydrocarbon mixtures in Activated Carbon

Hu and Do[55] report experimental data for transient uptake of (a) ethane/n-butane, (b) ethane/n-pentane, and (c) n-butane/n-pentane mixtures in extrudates of activated carbon (AC) at 303 K; see Figures 8, 9, and 10 of their paper. In all three experiments, the more mobile species in the mixture exhibits an overshoot during equilibration. Figures 50a, b, c present our simulation results using the isotherm input data provided in Table 1 of Hu and Do.[55] The mixture adsorption equilibrium is determined using the IAST. The continuous solid lines using Equation (40) that include thermodynamic coupling effects. The dashed lines are simulations using uncoupled flux equation (54). In all three cases, overshoots are observed only when thermodynamic coupling effects are included. If thermodynamic coupling effects are ignored, i.e. $\Gamma_{ij} = \delta_{ij}$, no overshoots are observed.

Video animations for uptake of ethane/n-pentane mixture uptake, uploaded as ESI, demonstrate that the more mobile ethane exhibits spatio-temporal overshoots along the radius of the AC extrudate during its approach to equilibrium. Interestingly, Figure 11 of the paper by Hu and Do[55] also show similar overshoots, but these authors do not offer any explanation in terms of thermodynamic coupling effects.

The experimental data of Qiao and Hu[56] for transient uptake of ethane/propane mixtures in Ajax AC and Norrit AC show ethane overshoots in all of the reported experiments. The overshoot phenomena can be properly captured by using Equation (40) for the fluxes.

18. Influence of the ratio of M-S diffusivities, $Đ_1/Đ_2$, on overshoots

From a practical standpoint, it is of interest to know under what set of conditions transient overshoots can be expect to occur. To get some insights into this question, we investigated binary C_3H_6(1)/C_3H_8(2) mixture uptake in ZIF-8. The pore landscape and structural details for ZIF-8 are provided in Figure 51, and Figure 52. In ZIF-8, the adsorption strength of the saturated propane is higher than that of propene. From the experimental isotherm data of Li et al.,[57] the ratio of single-site Langmuir parameter b_2/b_1 = 1.07 at 303 K. The windows of ZIF-8 have a dimension of about 3.3 Å. Due to subtle differences in bond lengths and bond angles (see Figures 53), the diffusivity of C_3H_6 is higher than that of C_3H_8; Li et al.[57] report the value of the ratio $Đ_1/Đ_2$ =125 based on the data on pure component uptakes.

Figure 53 presents simulations of transient uptake of C_3H_6(1)/C_3H_8(2) mixture within crystals of ZIF-8, taking $Đ_1/Đ_2$ =125. The more mobile propene exhibits a sharp overshoot in the uptake for simulations in which thermodynamic coupling is properly accounted for. If thermodynamic coupling effects are ignored, both C_3H_6, and C_3H_8 display monotonous equilibration characteristics.

We undertook a parametric study to study the influence of the ratio of $Đ_1/Đ_2$. Three values for the ratio were chosen: 2, 10, and 125. In these three scenarios the diffusivity of the saturated alkane was held constant at the value $Đ_2/r_c^2$ = 1.2×10^{-4} s^{-1}. The results are presented in Figure 54. The overshoot in the uptake of the unsaturated propene persists for the ratios $Đ_1/Đ_2$ = 10 and $Đ_1/Đ_2$ = 125. However, for the choice $Đ_1/Đ_2$ = 2, the overshoot in the C_3H_6 uptake is practically non-existent. We conclude that for overshoots to occur, the diffusivity of the more mobile partner species must be significantly higher than that of the partner species.

19. Demonstrating the possibility of transient undershoots

For separations in fixed beds, the adsorption cycle is followed by a desorption cycle. During desorption, there exists the possibility of undershoots in the loadings of the more mobile species. To demonstrate this possibility, Figure 55 presents simulations of transient desorption of $C_3H_6(1)/C_3H_8(2)$ from crystals of ZIF-8 at 303 K. Initially, the crystals are equilibrated by exposing the crystals to bulk gas mixture with p_1 = 50 kPa; p_2 = 50 kPa. This equilibrated crystal is then brought into contact with a bulk gas phase with p_1 = 10 kPa; p_2 = 10 kPa. The continuous solid lines are transient uptake simulations use Equation (40). We note that the more mobile C_3H_6 experiences an undershoot during transient desorption. The dashed lines are the calculations using uncoupled flux equation (54); in this scenario, no undershoot is detected.

20. Separating mono- and di-branched alkanes by exploiting uphill diffusion in MFI zeolite

The isomerization of alkanes, for the purposes of octane improvement, is a process of importance in the petroleum industry.[6, 36, 58] The product from the isomerization reactor, that commonly uses MOR or MFI zeolite as catalyst, consists of an equilibrium distribution of linear alkanes, mono-branched alkanes, and di-branched alkanes with carbon numbers in the 5-7 range. The values of the Research Octane Number (RON) increases with the degree of branching; for hexane isomers (n-hexane (nC6), 2-methylpentane (2MP), 3-methylpentane (3MP), 2,2-dimethylbutane (22DMB), 2,3-dimethylbutane (23DMB)) the RON values are as follows:. nC6 = 30, 2MP = 74.5, 3MP = 75.5, 22DMB = 94, 23DMB = 105. Therefore, di-branched isomers are preferred products for incorporation into the high-octane gasoline pool. The separation of di-branched 22DMB and 23DMB from linear nC6 can be achieved by molecular sieving using, say, LTA-5A zeolite. The separation of di-branched isomers from mono-branched isomers is much more challenging. An important strategy that is effective for this separation is the exploitation of uphill diffusion by using MFI zeolite.

As illustration of uphill diffusion we consider the separations of two different mixtures: (a) binary 2MP/22DMB gaseous mixture, and ternary 2-methylbutane (2MB)/2MP/22DMB gaseous mixtures. The chosen conditions for the separation correspond to the experimental data for, respectively, Run 17, and Run 20 of Jolimaître et al. that were conducted in a packed bed adsorber using MFI extrudates.[59] For each of these mixtures we perform transient uptake simulations within an MFI extrudate, along with transient breakthrough simulations for the packed bed adsorber. The adsorption and diffusivity data for MFI extrudates, reported by Jolimaître et al.,[59, 60] are summarized in Table 6. The adsorption hierarchy is 2MP > 22DMB > 2MB, whereas the diffusivity hierarchy is 2MB > 2MP > > 22DMB: $Đ_{2MB}/r_c^2$ = 7.5×10^{-3} s^{-1}; $Đ_{2MP}/r_c^2 = 5\times10^{-3}$ s^{-1}; $Đ_{22DMB}/r_c^2 = 6.25\times10^{-5}$ s^{-1}.

Consider first the transient uptake within MFI extrudates exposed to a gas phase 2MP/22DMB mixture at 473 K with the partial pressures of the components in the bulk gas phase are p_1 = 22.7 kPa; p_2 = 26.6 kPa. The continuous solid lines in Figure 56 represent the transient simulations that include thermodynamic coupling using the flux relations Equation (40); there is a pronounced overshoot in the uptake of 2MP. The dashed lines represent uptake simulations ignoring thermodynamic coupling and use uncoupled flux equation (54); no overshoot in 2MP uptake is observed. This leads us to conclude that thermodynamic coupling is the origin of the transient overshoot in the 2MP uptake.

Figure 57 shows the transient development of 2MP and 22DMB loadings along the radius of MFI extrudate (center, $r = 0$; surface of crystal, $r = r_c$) monitored at different times from start of the uptake. The 2MP loading experiences spatio-temporal overshoots along the radius of the MFI extrudate. The 2MP loading peak traverses towards the centre of the extrudate as time progresses. Eventually the loadings are uniform over the entire radius of the extrudate.

Figure 58 shows the corresponding transient development of "corrected" loadings $q_1(\mu_1 - \mu_1^0)/RT = \Gamma_{11}q_1 + \Gamma_{12}q_2$, and $q_2(\mu_2 - \mu_2^0)/RT = \Gamma_{21}q_1 + \Gamma_{22}q_2$ of 2MP, and 22DMB along the radius of MFI extrudate (center, $r = 0$; surface of crystal, $r = r_c$) monitored at different times from start of the uptake. In terms of the corrected loadings, the transient equilibration of both 2MP and 22DMB occurs in a monotonous manner. This leads us to conclude that the transport of 2MP is down the gradient of its chemical potential.

Figure 59 presents a comparison of transient breakthrough experimental data (for Run 17) of Jolimaître et al.[59] with transient breakthrough simulations. There is good agreement between the transient breakthrough simulations, including thermodynamic coupling, with the experimental data.

Consider next the separation of a ternary gaseous 2-methylbutane (2MB)/2MP/22DMB mixture. Transient uptake inside MFI crystal exposed to a gas phase 2MB/2MP/22DMB mixture shows overshoots for the two mono-branched isomers 2MB, and 2MP; see Figure 60. If thermodynamic coupling effects are ignored, the component loadings of all three components exhibit monotonous approaches to equilibrium. Both mono-branched alkanes 2MB, and 2MP experience uphill diffusion that allows the attainment of supra-equilibrium loadings within MFI. As a consequence of uphill diffusion, the transient breakthrough experimental data (indicated by symbols in Figure 61) show the elution sequence 22DMB, 2MB, 2MP. This sequence is desirable, because the high-octane di-branched 22DMB can be recovered from the gas mixture exiting the adsorber in the initial transience, for incorporation into the gasoline pool.

The experimental breakthrough data are in good agreement with breakthrough simulations that takes take proper account of thermodynamic coupling, using the flux relations Equation (40); see continuous solid lines in Figure 61. If thermodynamic coupling effects are ignored (i.e. no uphill diffusion), the separation is less effective and is indicated by the dashed lines in Figure 61.

21. Separating linear alcohols by exploiting uphill diffusion in CHA zeolite

The experimental data of Saint-Remi et al.[61] for transient uptake of ethanol/1-propanol mixtures within SAPO-34, that is the structural analog of CHA zeolite, are shown in Figure 62. The more mobile ethanol is found to exhibit a pronounced maximum in the uptake transience. The mixture adsorption equilibrium favors the shorter alcohol because of the higher packing efficiency of the shorter alcohol within the cages of SAPO-34.[6, 62, 63] The uphill diffusion of ethanol further assists in the preferential adsorption of the shorter alcohol. Indeed, as in the case of nC6/2MP uptake in MFI, both adsorption and diffusion phenomena favor the shorter chain alcohol. This adsorption-diffusion synergy can be exploited in fixed bed separations. The breakthrough experimental data of Remy et al.[64] for separation of ethanol/1-propanol mixtures in a fixed bed adsorber packed with SAPO-34, (Figure 63) shows that the component that is eluted first from the adsorber is the alcohol with the longer chain length. The efficacy of this separation relies on a combination of packing effects, and uphill diffusion.

Transient uptake simulation were performed for ethanol/1-propanol mixtures within CHA crystals, for which the data on pure component isotherms are available from Configurational-Bias Monte Carlo (CBMC) simulations; see Figure 64a. The Maxwell-Stefan diffusivities were chosen in the simulations are $Đ_{ethanol}/r_c^2 = 4\times10^{-3}$ s^{-1}; $Đ_{1-propanol}/r_c^2 = 4\times10^{-5}$ s^{-1}. The continuous solid lines are transient uptake simulations use Equation (40). The dashed lines are the calculations using uncoupled flux equation (54); in this scenario, no ethanol overshoot is detected. The simulated uptake characteristics are in qualitative agreement with the experimental uptake data of Saint-Remi et al.[61] The more mobile ethanol exhibits spatio-temporal overshoots in the loadings, confirming that diffusion of ethanol occurs uphill its molar gradient; see Figure 64.

Transient breakthrough simulations (Figure 65) confirm that the component to be eluted first from the adsorber is the longer chain alcohol.

22. Transient C_3H_6/C_3H_8 permeation across ZIF-8 membrane

For steady-state C_3H_6/C_3H_8 permeation across ZIF-8 membrane, Pan et al.[65] and Liu et al.[66] report permeation selectivities in the range 30 – 35, strongly favoring the unsaturated alkene. Let us examine the transient membrane permeation characteristics. Figure 66 shows the results for simulation of transient permeation of $C_3H_6(1)/C_3H_8(2)$ mixture across ZIF-8 membrane of thickness δ = 10 μm. The partial pressures in upstream membrane compartment, $p_{10} = p_{20} = 50$ kPa. The downstream compartment is placed under vacuum, i.e. $p_{1\delta} = p_{2\delta} \approx 0$. As in the transient uptake simulations we take $Đ_1/Đ_2$ = 125. The simulation results are presented in terms of the normalized fluxes $N_1/(\rho q_{10} Đ_1/\delta)$, and $N_2/(\rho q_{20} Đ_2/\delta)$ in which the loadings at the upstream face are: q_{10} = 1.937 mol kg^{-1}, q_{20} = 2.067 mol kg^{-1}. The continuous solid lines are the calculations using Equation (40). We note an overshoot in the flux of the alkene during early stages of the transience. If thermodynamic coupling effects are neglected, the C_3H_6 flux overshoot disappears; see the dashed lines using uncoupled flux equation (54). These conclusions are precisely analogous to those reached on the basis of the transient uptake simulations presented in Figure 53.

The value of the permeation selectivity at steady-state, S_{perm} = 117 for both scenarios, either including thermodynamic coupling or neglecting thermodynamic coupling. The membrane permeation experiments of Pan et al.[65] and Liu et al.[66] are consistent with the choice $Đ_1/Đ_2$ ≈ 40.

Figure 67 shows the transient development of C_3H_6(1), and C_3H_8(2) loadings along the membrane thickness (upstream face, z = 0; downstream face, $z = \delta$) monitored at different times from start of the permeation. The loading of C_3H_6 shows an overshoot in the transient approach to steady-state; this signifies uphill diffusion across the membrane. In terms of corrected loadings $q_1(\mu_1 - \mu_1^0)/RT = \Gamma_{11} q_1 + \Gamma_{12} q_2$, and $q_2(\mu_2 - \mu_2^0)/RT = \Gamma_{21} q_1 + \Gamma_{22} q_2$ the loading profiles of both C_3H_6(1), and C_3H_8(2) display monotonous characteristics; see Figure 68. This indicates that membrane permeation is downhill of the chemical potential gradient.

23. Transient CH_4/nC_4H_{10} permeation across MFI membrane

Geus et al.[67] report experimental data on transient permeation 50/50 CH_4/nC_4H_{10} mixture across an MFI membrane. The flux of the more mobile CH_4 exhibits a pronounced overshoot during transient approach to steady state; see Figure 69a. We performed transient simulations to capture the experimentally observed overshoots. Unlike all of the simulations discussed in the foregoing sections, the proper modelling of mixture diffusion of light hydrocarbons in MFI zeolite requires us to take proper account of correlation effects.[25] We need to take account of both correlations and thermodynamic coupling using Equation (39). On the basis of the MD simulation data in Figure 8, and the permeation selectivity calculations in Figure 9, we take $Đ_1/Đ_{12} = 2$ as a good estimate of the degree of correlations based on the mixture loadings at the upstream face of the membrane.

Figure 69b shows the shows the normalized fluxes $N_1/(\rho q_{10} Đ_1/\delta)$, and $N_2/(\rho q_{20} Đ_2/\delta)$ as a function of the square root of time. The continuous solid lines in Figure 69b are the calculations using Equation (39), including both correlations and thermodynamic coupling. Also shown are simulations using Equation (40) that include thermodynamic coupling but neglect correlations. Including correlation effects tends to smear out the magnitude of the overshoots. In other words, correlation effects cannot cause overshoots. The dashed lines in Figure 69b are the calculations using uncoupled flux equation (54). The overshoot in the methane flux is essentially captured by both the M-S Equation (39) and Equation (40). If both correlations, and thermodynamic coupling effects are neglected, the overshoot in CH_4 flux disappears.

Figure 70 shows the transient development of CH_4(1), and nC_4H_{10}(2) loadings along the MFI membrane thickness (upstream face, $z = 0$; downstream face, $z = \delta$) monitored at different times from start of the permeation. The loading of the more mobile CH_4 shows spatio-temporal overshoots during the approach to steady-state.

In terms of corrected loadings $q_1(\mu_1 - \mu_1^0)/RT = \Gamma_{11} q_1 + \Gamma_{12} q_2$, and $q_2(\mu_2 - \mu_2^0)/RT = \Gamma_{21} q_1 + \Gamma_{22} q_2$ the loading profiles of CH_4(1), and nC_4H_{10}(2) display monotonous characteristics; see Figure 71. This indicates that CH_4 membrane permeation is downhill of the chemical potential gradient.

24. Transient H_2/nC_4H_{10} permeation across MFI membrane

The experimental data of Bakker[68] for transient permeation H_2/nC_4H_{10} mixture across an MFI membrane shows a maximum in the flux of the more mobile H_2; see Figure 72a. Since the mobility of H_2 is about two orders of magnitude higher than that of nC_4H_{10}, the overshoot in the H_2 flux is very prominent.

From the data in Figure 9, we use $Đ_1/Đ_{12} = 5$ as a good estimate of the degree of correlations. The continuous solid lines in Figure 72b are the calculations using Equation (39), including both correlations and thermodynamic coupling. The plot shows the normalized fluxes $N_1/(\rho q_{10}Đ_1/\delta)$, and $N_2/(\rho q_{20}Đ_2/\delta)$ as a function of the square root of time. The dashed lines are the calculations using uncoupled flux equation (54). The overshoot in the hydrogen flux is adequately captured by the M-S Equation (39). If both correlations, and thermodynamic coupling effects are neglected, the overshoot in H_2 flux disappears.

Figure 73 shows the transient development of $H_2(1)$, and $nC_4H_{10}(2)$ loadings along the MFI membrane thickness (upstream face, $z = 0$; downstream face, $z = \delta$) monitored at different times from start of the permeation. The loading of the more mobile H_2 shows spatio-temporal overshoots during the transient approach to steady-state.

In terms of corrected loadings $q_1(\mu_1 - \mu_1^0)/RT = \Gamma_{11}q_1 + \Gamma_{12}q_2$, and $q_2(\mu_2 - \mu_2^0)/RT = \Gamma_{21}q_1 + \Gamma_{22}q_2$ the loading profiles of $H_2(1)$, and $nC_4H_{10}(2)$ display monotonous characteristics; see Figure 74. This indicates that H_2 membrane permeation is downhill of the chemical potential gradient.

25. Transient nC6/2MP permeation across MFI membrane

For permeation of nC6/2MP, and nC6/2,3dimethylbutane (23DMB) mixture across an MFI membrane, Matsufuji et al.[69] have reported experimental data showing overshoots in the nC6 flux during transient approach to steady-state; see Figures 75a, and 75b. For a rationalization and understanding of the nC6 overshoots, we carried out performed a set of simulations. Figure 76 shows the simulation results for transient permeation of nC6(1)/2MP(2) mixture across MFI membrane of thickness δ = 50 μm at 300 K. The partial pressures in upstream membrane compartment, $p_{10} = p_{20}$ = 1.3 Pa, corresponding to the Titze uptake experiment. The plots in Figure 76 show the normalized fluxes $N_1/(\rho q_{10}Đ_1/\delta)$, and $N_2/(\rho q_{20}Đ_2/\delta)$ as a function of the square root of time. The linear alkane displays an overshoot during transient approach to steady-state. If thermodynamic coupling effects are neglected, the nC6 flux overshoot disappears; see the dashed lines using uncoupled flux equation (54).

These conclusions are precisely analogous to those reached on the basis of the transient uptake simulations presented in Figure 42.

Figure 77 shows the transient development of nC6(1), and 2MP(2) loadings loadings along the membrane thickness (upstream face, $z = 0$; downstream face, $z = \delta$) monitored at different times from start of the permeation. The loading of nC6 shows an overshoot in the transient approach to steady-state; this signifies uphill diffusion of nC6 across the membrane. In terms of corrected loadings $q_1\left(\mu_1 - \mu_1^0\right)/RT = \Gamma_{11}q_1 + \Gamma_{12}q_2$, and $q_2\left(\mu_2 - \mu_2^0\right)/RT = \Gamma_{21}q_1 + \Gamma_{22}q_2$ the loading profiles of nC6(1), and 2MP(2) display monotonous characteristics; see Figure 78. This indicates that nC6 membrane permeation is downhill of the chemical potential gradient.

26. Transient xylenes permeation across MFI membrane

The experimental data of Matsufuji et al.[70] for transient permeation of (a) 50/50 m-xylene/p-xylene, and (b) 24/51/25 p-xylene/m-xylene/o-xylene mixtures across MFI membrane show a maximum in the flux of p-xylene which is the most mobile of the three xylene isomers; see Figures 79a, and 79b. The most likely cause of this maximum is the influence of thermodynamic coupling. To verify this conclusion we carried out simulations of transient membrane for 50/50 m-xylene/p-xylene mixtures across an MFI membrane. O-xylene and m-xylene locate preferentially at the intersections of MFI, whereas the linear p-xylene molecules align the channels; see snapshots in Figure 79. The pure component isotherms, obtained from CBMC simulations,[71] show that, up to a loading of 4 molecules per unit cell the guest molecules are located at the channel intersections. At these locations, the adsorption strength of m-xylene is higher than that of p-xylene; this is due to more optimal interactions with the framework atoms. Para-xylene has the higher mobility because it has a more slender configuration allowing higher mobility along the intersecting channel topology of MFI zeolite. Transient uptake simulation results for two different scenarios are presented in Figure 80. Inclusion of thermodynamic coupling effects (continuous solid lines), and use of the flux equations (40) produces a maximum in the flux of the more mobile p-xylene during the early stages of the transience. Use the using uncoupled flux equation (54), ignoring thermodynamic coupling (dashed lines), with $\Gamma_{ij} = \delta_{ij}$, results in a monotonous approach to steady-state for both components. It must be remarked that Matsufuji et al.[70] offer the explanation that the maximum in the flux of p-xylene is caused due to "blocking" of the transport of p-xylene in the later stages of the transience due to increasing occupation of the channels by the more strongly adsorbed m-xylene and o-xylene. Our belief, based on the presented simulations evidence, is that the maximum is ascribable to the influence of thermodynamic coupling.

27. Transient nC4/iC4 permeation across MFI membrane

For nC4/iC4 mixture permeation across a MFI membrane, curious overshoots, and undershoots, in the transient retentate and permeate concentrations have been reported in the experiments of Courthial et al.[72] Figure 81 present simulation of transient permeation of 5/95 nC4(1)/iC4(2) mixtures across a MFI membrane at 300 K. When thermodynamic coupling effects are included, the flux of nC4 exhibits a pronounced overshoot. This overshoot disappears if thermodynamic coupling effects are neglected. We conclude that the overshoots observed in the experiments of Courthial et al.[72] are ascribable to thermodynamic coupling.

28. Transient water/ethanol permeation across DDR, and LTA-4A membrane

Pervaporation of water/alcohol mixtures is an important process in the processing industry, and a wide variety of membrane materials has been used, including polymers, zeolites (e.g. CHA, LTA, MFI, FAU, DDR), ZIF-8, and mixed matrix membranes.[73-76] Due to the high mobility of water molecules, uphill transport of water is to be expected during the transient approach to steady-state.

In order to demonstrate the possibility of uphill diffusion, we carried out a set of membrane permeation simulations for 5/95 water/ethanol mixtures across a DDR membrane; see Figure 82. The water diffusivity is taken to be 10 times that of ethanol diffusivity in the mixture. Simulations including thermodynamic coupling show pronounced overshoot in the water flux. If thermodynamic coupling is neglected, the transient approach to steady-state occurs in a monotonous manner.

Figure 83 shows the water(1), and ethanol(2) loading across the DDR membrane thickness (upstream face, z = 0; downstream face, $z = \delta$) monitored at different times from start of the permeation. The spatio-temporal overshoot in the water loading is a clear indication of uphill transport.

Figure 84, and Figure 85 show the corresponding results for 5/95 water/ethanol pervaporation across LTA-4A membrane; these calculations are based on the isotherm data of Pera-Titus et al.[77] The conclusions that emerge are analogous to those reached for DDR membrane pervaporation.

29. Transient overshoots for alkane isomerization using MFI catalyst

In all of the examples considered in the foregoing, no formation or destruction of components were assumed to occur as a result of chemical reactions. We now demonstrate the possibility of transient overshoots with microporous catalysts. The phenomena involve an interplay between mixture adsorption, microporous diffusion and chemical reaction. For illustration, we restrict our analysis to a reversible isomerization reaction $\mathrm{A}_1 \leftrightarrow \mathrm{A}_2$; such isomerization reactions are of great significance to the petroleum industry.[21-23, 78-81] Let us consider the specific example of isomerization of 2-methylpentane (2MP) to its dibranched isomer 2,2 dimethylbutane (22DMB) in a packed bed reactor using extrudates of MFI zeolite as catalyst. The process conditions correspond to those used in Run 17 by Jolimaître et al.,[59, 60] that are summarized in Table 6. The rate of chemical reaction, $\mathrm{2MP(1)} \rightleftarrows \mathrm{22DMB(2)}$, expressed as moles per kg of catalyst per second, is written as

$$Rate = k_1 q_1 - k_2 q_2 \tag{56}$$

The mixed-gas Langmuir model for mixture adsorption equilibrium, equation (34), relates the molar loadings of components 1 (= 2MP) and 2 (= 22DMB) to the partial pressures p_1 and p_2 in the bulk gas phase surrounding the MFI catalyst. The reaction rate constants, taken from Baur and Krishna,[21] are k_1 = 0.0011 s^{-1}, k_2 = 0.00055 s^{-1}.

The radial distribution of molar loadings, q_i, within a spherical MFI extrudate catalyst, of radius r_c, is obtained from a solution of a set of differential equations describing the uptake

$$\frac{\partial q_i(r,t)}{\partial t} = -\frac{1}{\rho}\frac{1}{r^2}\frac{\partial}{\partial r}\left(r^2 N_i\right) + \rho \nu_i Rate \tag{57}$$

where ν_i is the reaction stoichiometric coefficient; $\nu_1 = -1$ for reactant 2MP; $\nu_2 = 1$ for product 22DMB.

The fluxes N_i, in turn, are related to the radial gradients in the molar loadings by Equation (40). At time $t = 0$, i.e. the initial conditions, the molar loadings $q_i(r,0)$ at all locations r within the catalyst are uniform (zero loadings). For all times $t \geq 0$, the exterior of the crystal is brought into contact with a bulk gas mixture at partial pressures $p_i(r_c,t)$ that is maintained constant till the crystal reaches thermodynamic equilibrium with the surrounding gas mixture. At any time t, during the transient approach to thermodynamic equilibrium, the spatial-averaged component loading within the crystallites of radius r_c is calculated using $\overline{q}_i(t) = \frac{3}{r_c^3}\int_0^{r_c} q_i(r,t) r^2 dr$.

The numerical details are provided on our website.[33]

Before proceeding to transient uptake simulations, let us analyze the influence of intra-crystalline diffusion on the isomerization reaction under steady-state conditions for which we have

$$\frac{1}{\rho}\frac{1}{r^2}\frac{\partial}{\partial r}\left(r^2 N_i\right) = -\rho \nu_i Rate; \quad \text{steady-state} \tag{58}$$

After insertion of the appropriate rate expressions for the chemical reaction rate, *Rate*, and the flux equations for N_i, the equation (58) can be solved to obtain the steady-state distribution of the loadings of the components along the crystal radius, r.

$$\eta = \frac{\int_0^1 Rate \left(r/r_c\right)^2 d\left(r/r_c\right)}{\int_0^1 Rate\big|_{r=r_c} \left(r/r_c\right)^2 d\left(r/r_c\right)} \tag{59}$$

The chemical reaction rate, *Rate* defined in equation (56), varies with loading and *r*-dependent. The effectiveness factor, η, quantifies the influence of intra-crystalline diffusion on the effective rate of chemical reaction. In the absence of any diffusional limitations, $\eta = 1$, and the chemical reaction rate can be calculated using the loadings at the external surface, $Rate\big|_{r=r_c}$.

Baur and Krishna.[21] have presented analytic solutions to equation (58) for a variety of scenarios.

(1) Classical scenario: the diffusivities are independent of loading (called the weak confinement scenario), and thermodynamic coupling effects are ignored, $\Gamma_{ij} = \delta_{ij}$. Also ignored are the correlation effects, i.e. $Đ_1/Đ_{12} \to 0; \quad Đ_2/Đ_{12} \to 0$.

(2) Weak confinement scenario for the diffusivities. Also ignored are the correlation effects, i.e. $Đ_1/Đ_{12} \to 0; \quad Đ_2/Đ_{12} \to 0$. Thermodynamic coupling effects are accounted for using the mixed-gas Langmuir isotherm model

(3) Strong confinement scenario for the diffusivities in which the diffusivities are related to the zero-loading diffusivities by $Đ_i = Đ_i(0)\theta_V$. Also ignored are the correlation effects, i.e. $Đ_1/Đ_{12} \to 0; \quad Đ_2/Đ_{12} \to 0$. Thermodynamic coupling effects are accounted for using the mixed-gas Langmuir isotherm model

(4) Weak confinement scenario for the diffusivities. Thermodynamic coupling effects are accounted for using the mixed-gas Langmuir isotherm model. Correlation effects are accounted for with finite values of $Đ_1/Đ_{12}; \quad Đ_2/Đ_{12}$

(5) Strong confinement scenario for the diffusivities in which the diffusivities are related to the zero-loading diffusivities by $Đ_i = Đ_i(0)\theta_V$. Thermodynamic coupling effects are accounted for using the mixed-gas Langmuir isotherm model. Correlation effects are accounted for with finite values of $Đ_1/Đ_{12}; \quad Đ_2/Đ_{12}$

For the classical scenario (1), the effectiveness factor is given by

$$\eta = \frac{1}{\phi}\left(\frac{1}{\tanh(3\phi)} - \frac{1}{(3\phi)}\right); \quad \text{classical scenario (1)} \tag{60}$$

where the Thiele modulus is calculated from

$$\phi \equiv \frac{r_c}{3}\sqrt{\frac{k_1}{Đ_1(0)} + \frac{k_2}{Đ_2(0)}} \tag{61}$$

Analytical solutions are derived for the other four scenarios by Baur and Krishna[21] and the results for the effectiveness factor are expressed as

$$\eta = \frac{1}{\Phi}\left(\frac{1}{\tanh(3\Phi)} - \frac{1}{(3\Phi)}\right); \quad \text{General scenario} \tag{62}$$

where the generalized Thiele modulus Φ is obtained by multiplying the classical Thiele modulus ϕ by various "correction factors" as listed in Table 13.[21]

As illustration, Figure 86 presents calculations of the (steady-state) effectiveness factor, η, for uptake inside MFI catalyst exposed to a gas phase 2MP(1)/22DMB(2) mixture at 473 K, carrying out the isomerization reaction $\text{2MP(1)} \rightleftarrows \text{22DMB(2)}$. The partial pressures of the components in the bulk gas phase are p_1 = 22.7 kPa; p_2 = 26.6 kPa. The ratio of rate constants k_1/k_2 = 2. The values of the rate constant k_1 are varied. The zero-loading diffusivities $Đ_1(0)$ = 2×10^{-14} m^2 s^{-1}; $Đ_1(0)$ = 2.5×10^{-16} m^2 s^{-1}. The radius of the crystal r_c = 2 μm. The *x*-axis in Figure 86 is the classical Thiele modulus calculated using equation (61). The calculations using the five different scenarios are based on the analytical solutions provided by Baur and Krishna;[21] for scenarios (4) and (5) the correlation effects are quantified taking $Đ_1/Đ_{12} = 1; \quad Đ_2/Đ_{12} = 0.0125$. The highest effectiveness factors are obtained with the classical scenario in which thermodynamic coupling effects are ignored, by taking $\Gamma_{ij} = \delta_{ij}$. As is to be expected, diffusion effects are strongest for the scenarios in which the M-S diffusivities are linearly related to the vacancies, $Đ_i = Đ_i(0)\theta_V$. For the choice $Đ_1/Đ_{12} = 1; \quad Đ_2/Đ_{12} = 0.0125$, the influence of correlation effects is negligible.

In all the transient simulations for uptake in MFI catalyst considered below, we compare the results obtained from the classical scenario 1 (neglecting thermodynamic coupling) with that of scenario 2 (including thermodynamic coupling). The equilibrated loadings inside the catalyst will be different in these two scenarios; we return to this point later.

Consider first the transient uptake with chemical reaction within MFI extrudates exposed to a gas phase 2MP/22DMB mixture at 473 K with the partial pressures of the components in the bulk gas phase are p_1 = 22.7 kPa; p_2 = 26.6 kPa. The continuous solid lines in Figure 87 represent the transient simulations that include thermodynamic coupling using the flux relations Equation (40); there is a pronounced overshoot in the uptake of 2MP. The dashed lines represent uptake simulations ignoring thermodynamic coupling and use uncoupled flux equation (54); no overshoot in 2MP uptake is observed. This leads us to conclude that thermodynamic coupling is the origin of the transient overshoot in the 2MP uptake.

Figure 88 shows the transient development of 2MP and 22DMB loadings along the radius of MFI catalyst (center, r = 0; surface of crystal, $r = r_c$) monitored at different times from start of the uptake. The 2MP loading experiences spatio-temporal overshoots along the radius of the MFI extrudate. The 2MP loading peak traverses towards the centre of the extrudate as time progresses. Eventually the loadings are uniform over the entire radius of the extrudate.

Figure 89 shows the corresponding transient development of “corrected” loadings $q_1(\mu_1 - \mu_1^0)/RT = \Gamma_{11}q_1 + \Gamma_{12}q_2$, and $q_2(\mu_2 - \mu_2^0)/RT = \Gamma_{21}q_1 + \Gamma_{22}q_2$ of 2MP, and 22DMB along the radius of MFI catalyst (center, r = 0; surface of crystal, $r = r_c$) monitored at different times from start of the uptake. In terms of the corrected loadings, the transient equilibration of both 2MP and 22DMB occurs in a monotonous manner. This leads us to conclude that the transport of 2MP is down the gradient of its chemical potential.

Figure 90 presents the transient breakthrough simulations for fixed bed 2MP/22DMB isomerization reactor with MFI extrudates. The continuous solid lines represent breakthrough simulations include thermodynamic coupling using the flux relations Equation (40). The dashed lines represent breakthrough simulations ignoring thermodynamic coupling and using uncoupled flux equation (54).

Consider uptake within MFI catalyst carrying out the isomerization of nC6 to produce a product containing mono-branched 3-methylpentane (3MP) and di-branched 22DMB. We restrict our analysis to the simplified reaction scheme

$$\mathrm{nC6}(1) \rightleftarrows \mathrm{3MP}(2) \rightleftarrows \mathrm{22DMB}(3) \tag{63}$$

where the Langmuir-Hinshelwood (LH) reaction rate expressions for the two constituent reversible reactions, expressed as moles per m^3 catalyst per second are

$$Rate_1 = \left(k_{f1}p_1 - k_{b1}p_2\right)\theta_V; \quad Rate_2 = \left(k_{f2}p_2 - k_{b2}p_3\right)\theta_V; \quad \theta_V = 1 - \theta_1 - \theta_2 \tag{64}$$

where the subscripts f and b refer to the forward and reverse reactions, and the subscripts 1 and 2 refer to the first and second isomerization reaction steps in Eq. (63). From available information for the free energies of formation[28] we can estimate the values of the equilibrium constants k_{f1}/k_{b1} and k_{f2}/k_{b2}. On the basis of this information, along with data on reaction kinetics[82] we take $k_{f1} = k_{f2} = 0.009$ mol m^{-3} Pa^{-1} s^{-1} and $k_{b1} = k_{b2} = 0.007$ mol m^{-3} Pa^{-1} s^{-1}. Further details of the kinetics are provided by Krishna and Baur.[81] The catalyst radius is taken to be $r_c = 100$ μm.

Figure 91 presents simulations of transient uptake inside MFI catalyst exposed to a gas phase nC6(1)/3MP(2)/22DMB(3) mixture at 362 K. $\mathrm{nC6}(1) \rightleftarrows \mathrm{3MP}(2) \rightleftarrows \mathrm{22DMB}(3)$. The partial pressures of the components in the bulk gas phase are $p_1 = 2$ kPa; $p_2 = 40$ kPa, $p_3 = 60$ kPa. Diffusional effects are quantified with $Đ_{nC6}/r_c^2 = 2\times10^{-2}$ s^{-1} , $Đ_{3MP}/r_c^2 = 2\times10^{-3}$ s^{-1}; $Đ_{22DMB}/r_c^2 = 1\times10^{-3}$ s^{-1}. All three M-S diffusivities are assumed to follow the loading dependence $Đ_i(\theta) = Đ_i(0)\theta_V$. The continuous solid lines represent uptake simulations include thermodynamic coupling using the flux relations (40). We note that the most mobile nC6 displays an overshoot during transient uptake. The dashed lines represent uptake simulations ignoring thermodynamic coupling and use uncoupled flux equation (54); in this scenario, nC6 approaches equilibrium in a monotonous manner.

30. Transient overshoots for xylene isomerization using MFI catalyst

Para-xylene is an important feedstock in the petrochemical industry.[63] The largest use of p-xylene is in its oxidation to make terephthalic acid, that is used in turn to make polymers such as polyethylene terephthalate (PET) and polybutylene terephthalate (PBT). PET is one of the largest volume polymers in the world, and is used to produce fibers, resins, films, and blown beverage bottles. Isomerization of xylenes with MFI catalyst is of importance.

For illustration, we consider the isomerization of m-xylene to p-xylene: $\mathrm{m-xylene(1)} \rightleftarrows \mathrm{p-xylene(2)}$. The rate of chemical reaction, expressed as moles per kg of catalyst per second is written as $Rate = k_1 q_1 - k_2 q_2$. The rate constants are taken as: k_1 = 0.001 s^{-1}, k_2 = 0.0005 s^{-1}. Unlike the example of the $\mathrm{2MP(1)} \rightleftarrows \mathrm{22DMB(2)}$ reaction considered in a foregoing section, p-xylene has a higher diffusivity than m-xylene due to configurational considerations. We assume that the diffusivity of p-xylene is five times that of m-xylene.

Figure 92 shows the transient uptake inside MFI catalyst exposed to a gas phase m-xylene(1)/p-xylene(2) mixture at 303 K. The partial pressures of the components in the bulk gas phase are p_1 = 10 Pa; p_2 = 10 Pa. The continuous solid lines represent uptake simulations include thermodynamic coupling using the flux relations Equation (40). In this scenario, we note that p-xylene shows a pronounced overshoot in the uptake. The dashed lines represent uptake simulations ignoring thermodynamic coupling and use uncoupled flux equation (54); in this scenario no m-xylene overshoot is observed.

31. Transient overshoots for ethylation of benzene using MFI catalyst

H-ZSM-5, which has the MFI topology, is used as a catalyst for carrying out the ethylation of benzene to produce ethylbenzene $\text{ethene}(1)+\text{benzene}(2)\rightleftarrows\text{ethylbenzene}(3)$; for background on process and reaction kinetics, see Hansen et al.[83, 84] For feed mixtures with ethene/benzene far in excess of the stoichiometric ratio of 1:1, we may assume that the rate of chemical reaction, expressed as moles per kg of catalyst per second, is written as

$$Rate = k_f q_2 - k_b q_3 \tag{65}$$

Using the data in the papers of Hansen et al.[83, 84] as guidelines for the kinetics, we take $k_f = 1\times10^{-2}\ \text{s}^{-1}$ and $k_b = 5\times10^{-3}\ \text{s}^{-1}$.

Figure 93 presents the simulation results for transient uptake inside MFI catalyst exposed to a gas phase ethene(1)/benzene(2)/ethylbenzene(3) mixture at 653 K; the partial pressures of the components in the bulk gas phase are $p_1 = 800$ kPa; $p_2 = 200$ kPa; $p_3 = 0$ kPa. Diffusional effects are quantified with $Đ_{ethene}/r_c^2 = 1\times10^{-3}\ \text{s}^{-1}$, $Đ_{benzene}/r_c^2 = 2\times10^{-5}\ \text{s}^{-1}$; $Đ_{ethylbenzene}/r_c^2 = 1\times10^{-5}\ \text{s}^{-1}$. The continuous solid lines represent uptake simulations include thermodynamic coupling using the flux relations (40). We note that the most mobile species ethene displays an overshoot during equilibration. The dashed lines represent uptake simulations ignoring thermodynamic coupling and use uncoupled flux equation (54); in this scenario, no ethene overshoot is observed.

32. Transient overshoots for dehydrogenation of ethane using MFI catalyst

Hansen et al.[83, 84] describe the use of MFI catalyst for the dehydrogenation of ethane to produce ethene $\text{ethane}(1)\rightleftarrows\text{ethene}(2)+\text{hydrogen}(3)$. In view of the low adsorption strength of hydrogen, the reaction rate expressed as moles per kg catalyst per second may be written as

$$Rate = k_f q_1 - k_b q_2 \tag{66}$$

For our simulations we take $k_f = 1\ \text{s}^{-1}$ and $k_b = 1\ \text{s}^{-1}$.

Figure 94 presents the simulation results for transient uptake inside MFI catalyst exposed to a gas phase ethane(1)/ethene(2)/hydrogen(3) mixture at 653 K. The partial pressures of the components in the bulk gas phase are p_1 = 0.2 MPa; p_2 = 0.1 MPa, p_3 = 1 MPa. Diffusional effects are quantified with $Đ_{ethane}/r_c^2$ = 2.5×10^{-4} s^{-1}; $Đ_{ethene}/r_c^2$ = 5×10^{-4} s^{-1}; $Đ_{hydrogen}/r_c^2$ = 1.25×10^{-2} s^{-1}. The continuous solid lines represent uptake simulations include thermodynamic coupling using the flux relations (40). We note that more mobile species hydrogen displays a slight overshoot during equilibration. The dashed lines represent uptake simulations ignoring thermodynamic coupling and use uncoupled flux equation (54); in this scenario, no hydrogen overshoot is observed.

33. Notation

A	surface area per kg of framework, $\mathrm{m^2\ kg^{-1}}$
b_i	Langmuir constant for species i, Pa^{-1}
b_i	Langmuir-Freundlich constant, $\mathrm{Pa}^{-\nu}$
c_i	molar concentration, $\mathrm{mol\ m^{-3}}$
$\bar{c}_i(t)$	spatial-averaged concentration of species i inside particle, $\mathrm{mol\ m^{-3}}$
c_t	total pore concentration in mixture, $\mathrm{mol\ m^{-3}}$
d_p	pore diameter, m
$Đ_\mathrm{i}$	Maxwell-Stefan diffusivity for molecule-wall interaction, $\mathrm{m^2\ s^{-1}}$
$Đ_\mathrm{ij}$	M-S exchange coefficient for n-component mixture, $\mathrm{m^2\ s^{-1}}$
$Đ_{ij}^{\theta}$	M-S exchange coefficient for n-component mixture defined by equation (23), $\mathrm{m^2\ s^{-1}}$
$Đ_{12}$	M-S exchange coefficient for binary mixture, $\mathrm{m^2\ s^{-1}}$
$[D]$	matrix of diffusivities, $\mathrm{m^2\ s^{-1}}$
f_i	partial fugacity of species i, Pa
n	number of species in the mixture, dimensionless
k_1	forward reaction rate constant, $\mathrm{s^{-1}}$
k_2	backward reaction rate constant, $\mathrm{s^{-1}}$
L	length of packed bed adsorber, m
M_i	molar mass of species i, $\mathrm{kg\ mol^{-1}}$
M	excess amount injected in Taylor dispersion experiment, mol
N_i	molar flux of species i with respect to framework, $\mathrm{mol\ m^{-2}\ s^{-1}}$
p_i	partial pressure of species i in mixture, Pa
p_t	total system pressure, Pa
q_i	component molar loading of species i, $\mathrm{mol\ kg^{-1}}$
$q_\mathrm{i,sat}$	molar loading of species i at saturation, $\mathrm{mol\ kg^{-1}}$
q_t	total molar loading in mixture, $\mathrm{mol\ kg^{-1}}$
$\bar{q}_i(t)$	spatial-averaged component uptake of species i, $\mathrm{mol\ kg^{-1}}$

r	radial direction coordinate, m
r_c	radius of crystallite, m
R	gas constant, 8.314 J mol^{-1} K^{-1}
S_{perm}	membrane permeation selectivity, dimensionless
t	time, s
T	absolute temperature, K
u	cross-sectional averaged velocity in tube, m s^{-1}
u_i	velocity of motion of adsorbate species *i* with respect to the framework material, m s^{-1}
v	interstitial gas velocity in packed bed, m s^{-1}
V_p	pore volume, m^3 kg^{-1}
x_i	mole fraction of species *i* in adsorbed phase, dimensionless
z	distance coordinate, m

Greek letters

β	dimensionless parameter, $\beta \equiv \sqrt{\dfrac{\dfrac{Đ_2(0)}{Đ_1(0)}\left(\Lambda \dfrac{k_1}{k_2}+1\right)}{\Lambda\left(\dfrac{Đ_2(0)}{Đ_1(0)}\dfrac{k_1}{k_2}+1\right)}}$
γ	confinement parameter, $\gamma = 0$ for weak , $\gamma = 1$ for strong, dimensionless
δ	thickness of microporous membrane, m
δ_{ij}	Kronecker delta, dimensionless
ε	fractional pore volume of particle, dimensionless
ε	voidage of packed bed, dimensionless
ϕ	Thiele modulus, $\phi \equiv \dfrac{r_c}{3}\sqrt{\dfrac{k_1}{Đ_1(0)}+\dfrac{k_2}{Đ_2(0)}}$, dimensionless
Φ	modified Thiele modulus; see Table 1 of by Baur and Krishna[21], dimensionless
Γ_{ij}	thermodynamic factors, dimensionless
$[\Gamma]$	matrix of thermodynamic factors, dimensionless

η	effectiveness factor, dimensionless
Λ	dimensionless diffusivity ratio, $\Lambda \equiv \frac{Đ_2(0)}{Đ_1(0)} \frac{\left(1+(\theta_{1s}+\theta_{2s})\frac{Đ_1(0)}{Đ_{12}(0)}\right)}{\left(1+(\theta_{1s}+\theta_{2s})\frac{Đ_2(0)}{Đ_{12}(0)}\right)}$
μ_i	molar chemical potential of component *i*, J mol^{-1}
μ_i^0	molar chemical potential of component *i* at standard state, J mol^{-1}
ν_i	reaction stoichiometric coefficient, dimensionless
ν	Freundlich exponent, dimensionless
π	spreading pressure, N m^{-1}
θ_i	fractional occupancy of component *i*, dimensionless
θ_V	fractional vacancy, $\theta_V = 1-\theta_1-\theta_2$, dimensionless
θ_{is}	fractional occupancy at catalyst surface, dimensionless
θ_{i0}	fractional occupancy at centre of catalyst, dimensionless
Θ	dimensionless parameter, $\Theta \equiv \frac{\sqrt{2\left(1-1/\Psi^2-2\ln(\Psi)/\Psi^2\right)}}{\left|1-1/\Psi^2\right|}$
Ξ	$\Xi \equiv \sqrt{\frac{1}{\theta_{Vs}^{\gamma}}\left(1+(\theta_{1s}+\theta_{2s})\frac{Đ_1(0)}{Đ_{12}(0)}\right)}$
Ψ	dimensionless parameter, $\Psi \equiv \sqrt{\frac{\left(\Lambda+(1-\Lambda)\theta_{1s}\right)k_1+\left(1+(\Lambda-1)\theta_{2s}\right)k_2}{\left(\Lambda k_1+k_2\right)}}$
ρ	framework density, kg m^{-3}
τ	tortuosity, dimensionless
τ	time, dimensionless

Subscripts

i	referring to component *i*
t	referring to total mixture
0	referring to surface at centre of catalyst, $\xi = 0$.

1	referring to species 1
2	referring to species 2
s	referring to surface at position $\xi = 1$.
sat	referring to saturation conditions
V	vacancy
ξ	at position ξ within catalyst

Table 1. Dual-Langmuir parameter fits for CO_2 and H_2 in MFI (silicalite-1) zeolite. The CO_2 isotherm fits are based on CBMC simulation data at three different temperatures, 200 K, 253 K, and 300 K. The H_2 fits are based on CBMC simulation data at 300 K, combined with experimental data of Golden and Sircar [85] at 305.15 K, and 353.25 K.

$$\Theta = \Theta_{A,sat} \frac{b_A p}{1+b_A p} + \Theta_{B,sat} \frac{b_B p}{1+b_B p}; \; b_A = b_{A0} \exp\left(\frac{E_A}{RT}\right); \quad b_B = b_{B0} \exp\left(\frac{E_B}{RT}\right)$$

	Site A			Site B		
	$\Theta_{i,A,sat}$ molecules uc^{-1}	$b_{i,A}$ Pa^{-1}	E_A kJ mol^{-1}	$\Theta_{i,B,sat}$ molecules uc^{-1}	$b_{i,B}$ Pa^{-1}	E_B kJ mol^{-1}
CO_2	21	1.56×10^{-10}	26	12	1.9×10^{-14}	31
H_2	32	5.8×10^{-10}	10	41	2.18×10^{-11}	10

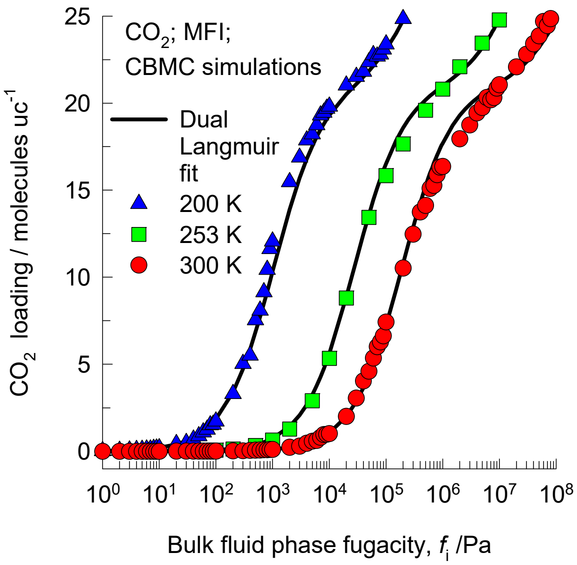

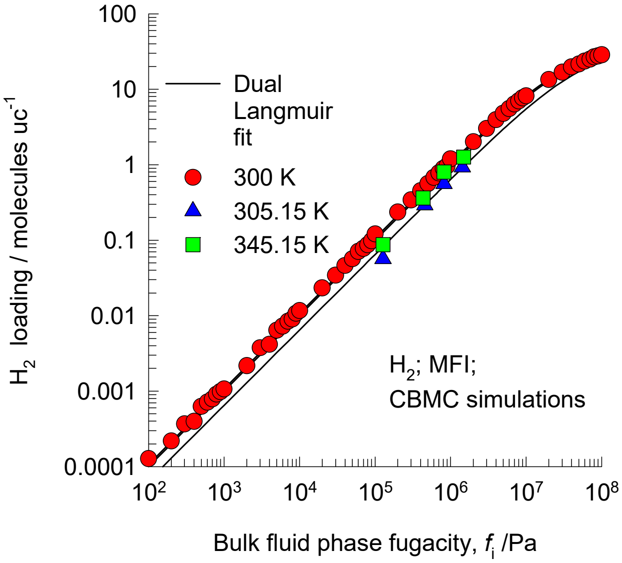

Table 2. 1-site Langmuir parameters for CO_2 and C_2H_6 in DDR zeolite at 298 K. These parameters have been fitted from the data scanned from Figure 36, Chapter 4 of the PhD dissertation of Binder.[41]

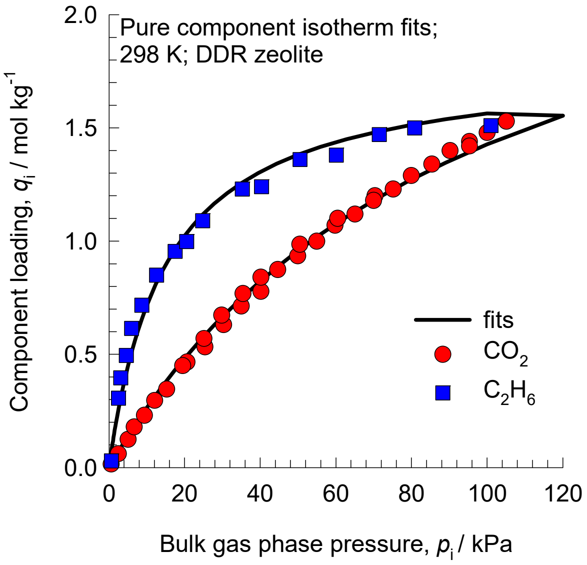

	q_{sat} mol kg^{-1}	b Pa^{-1}
CO_2	2.8	1.04×10^{-5}
C_2H_6	1.8	6.6×10^{-5}

Table 3. 1-site Langmuir parameters for N_2 and CH_4 in LTA-4A zeolite at 194 K. These parameters have been fitted from the isotherm data scanned from the paper by Habgood[42]

	q_{sat} mol kg^{-1}	b Pa^{-1}
N_2	3.6	9.4×10^{-5}
CH_4	3.6	2.08×10^{-4}

Table 4. 1-site Langmuir parameters for O_2 and N_2 Carbon Molecular Sieve (CMS).

	q_{sat} mol kg^{-1}	b Pa^{-1}
O_2	1.9	1.45×10^{-6}
N_2	1.4	1.5×10^{-6}

Table 5. Dual-site Langmuir-Freundlich parameters for pure component isotherms for hexane and butane isomers in MFI at 298 K. This data is from the Supporting Information of Titze et al.[45] The unary isotherm data are fitted with the dual-Langmuir-Freundlich model

$$\Theta_i = \Theta_{i,A,sat} \frac{b_{i,A} p_i^{\nu_A}}{1+b_{i,A_i}^{\nu_A}} + \Theta_{i,B,sat} \frac{b_{i,B} p_i^{\nu_B}}{1+b_{i,B} p_i^{\nu_B}}$$

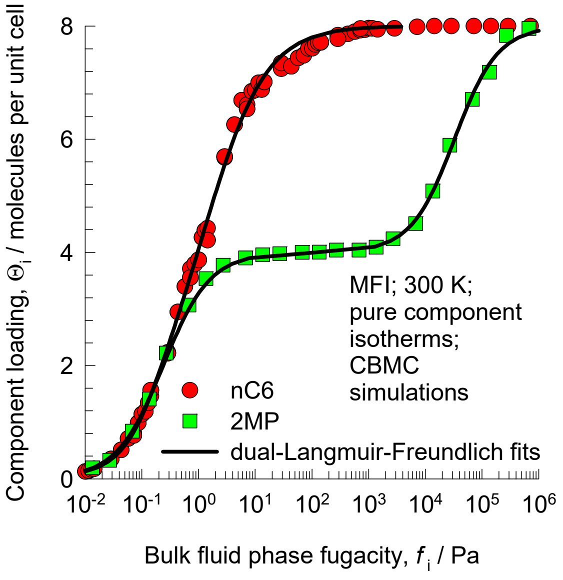

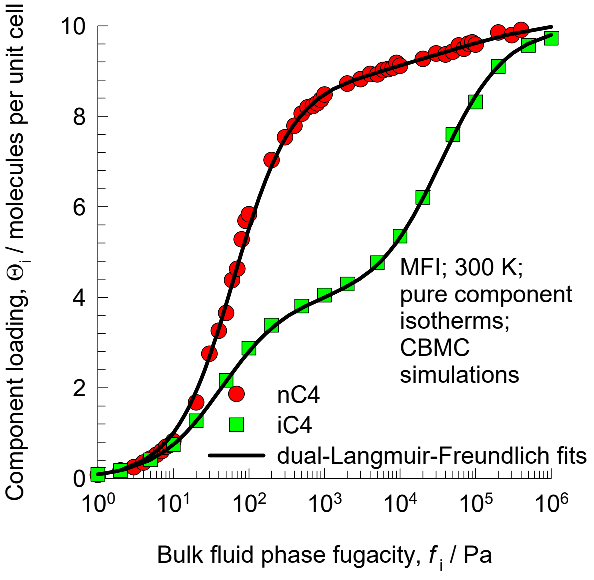

	Site A			Site B		
	$\Theta_{i,A,sat}$ molecules uc^{-1}	$b_{i,A}$ $Pa^{-\nu_i}$	$\nu_{i,A}$ dimensionless	$\Theta_{i,B,sat}$ molecules uc^{-1}	$b_{i,B}$ $Pa^{-\nu_i}$	$\nu_{i,B}$ dimensionless
nC6	6.6	0.708	0.83	1.4	16.6	1.5
2MP	4	4.51	1.05	4	7.92×10^{-6}	1.13
nC_4H_{10}	1.5	2.24×10^{-3}	0.57	8.7	9.75×10^{-3}	1.12
iC_4H_{10}	4	2.29×10^{-2}	1	6	2.87×10^{-5}	1

Table 6. Single-site Langmuir parameters, and M-S diffusivities $Đ_i / r_c^2$, for pure component 2MB, 2MP, and 22DMB at 473 K in MFI zeolite. The parameters are based on the experimental data of Jolimaître et al.[59, 60] All simulations of the breakthrough experiments of Jolimaître et al.[59] were performed for extrudate 2; bed voidage, $\varepsilon = 0.4$; density of extrudate 2, $\rho = 620.8$ kg m^{-3}; The interstitial velocity v varied with each run and were taken from Table 6 of Jolimaître et al.[59] The partial pressures of each of the components 2MB, 2MP, and 22DMB at the inlet to the adsorber are specified using the data provided in Table 6 of Jolimaître et al.[59]

$$\Theta_i^0(p) = \frac{\Theta_{i,sat} b_i p}{1 + b_{i,} p}$$

	$\Theta_{i,sat}$ molecules uc^{-1}	b_i Pa^{-1}	$Đ_i / r_c^2$ s^{-1}
2MB	4	4.12×10^{-5}	0.0075
2MP	4	1.27×10^{-4}	0.005
22DMB	4	7.12×10^{-5}	0.0000625

Table 7. 1-site Langmuir parameters for propene and propane in ZIF-8.[86] The *T*-dependent parameters are obtained by fitting the combined sets of pure component isotherm data of Li et al.[57] and Böhme et al.[87] determined for a variety of temperatures in the range 273 K to 408 K.

$$q = q_{sat} \frac{bp}{1+bp}; \; b_A = b_0 \exp\left(\frac{E}{RT}\right)$$

	q_{sat} mol kg^{-1}	b_0 Pa^{-1}	E kJ mol^{-1}
propene	5.2	4.57×10^{-11}	33.9
propane	5.2	1.39×10^{-10}	31.3

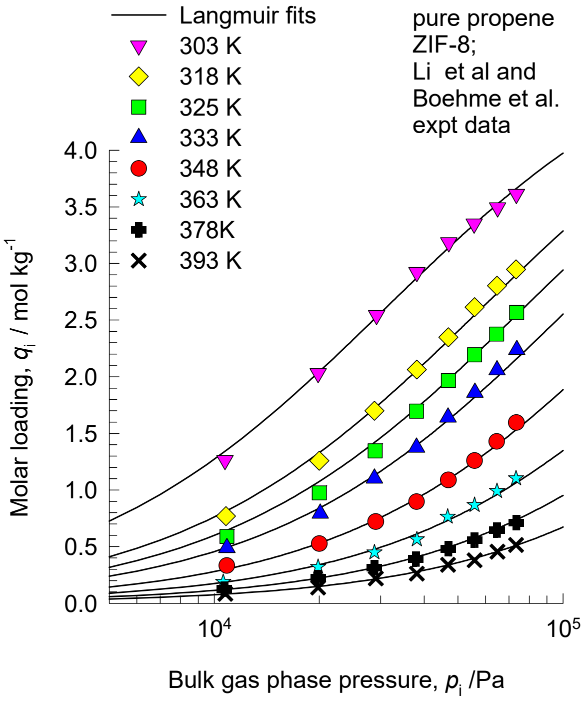

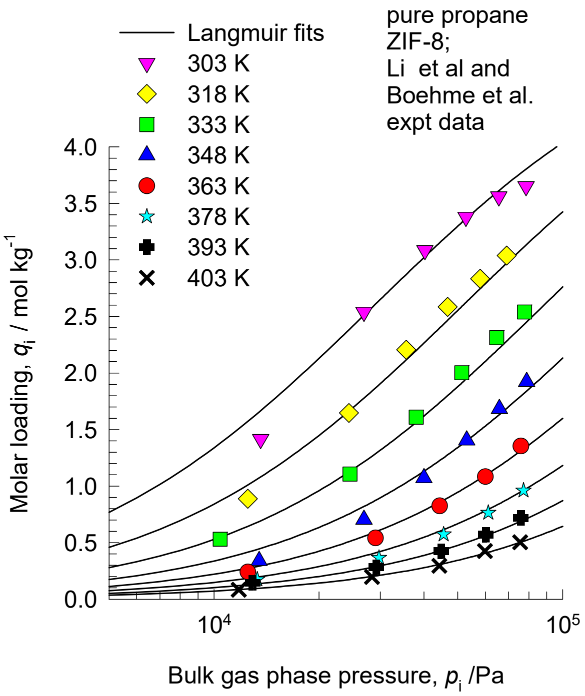

Table 8. Dual-site Langmuir-Freundlich parameters for pure component isotherms in MFI at 300 K. Note that the saturation capacities are specified in molecules per unit cell; multiply these by 0.1734 to obtain the loading values in mol per kg framework. The fits are based on CBMC simulation data from a variety of previous works.[5, 10, 12-16, 20, 25, 27, 50, 88-91] The unary isotherm data are fitted with the dual-Langmuir-Freundlich model $\Theta_i = \Theta_{i,A,sat}\frac{b_{i,A}p_i^{\nu_A}}{1+b_{i,A}{}_i^{\nu_A}} + \Theta_{i,B,sat}\frac{b_{i,B}p_i^{\nu_B}}{1+b_{i,B}p_i^{\nu_B}}$

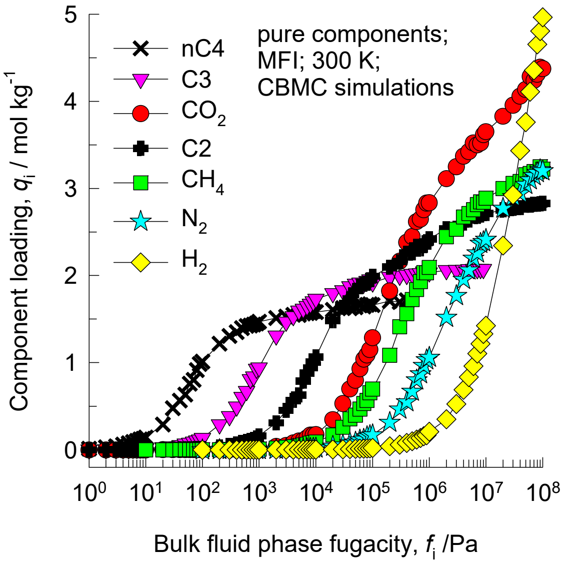

	Site A			Site B		
	$\Theta_{i,A,sat}$ molecules uc^{-1}	$b_{i,A}$ Pa$^{-\nu_i}$	$\nu_{i,A}$ dimensionless	$\Theta_{i,B,sat}$ molecules uc^{-1}	$b_{i,B}$ Pa$^{-\nu_i}$	$\nu_{i,B}$ dimensionless
CO_2	19	6.12×10^{-6}	1	11	1.73×10^{-8}	1
H_2	30	3.57×10^{-8}	1	42	1.39×10^{-9}	1
CH_4	16	3.1×10^{-6}	1	7	5×10^{-9}	1
nC_4H_{10}	1.5	2.24×10^{-3}	0.57	8.7	9.75×10^{-3}	1.12

Table 9. Dual-site Langmuir-Freundlich parameters for pure component 1-alcohols in CHA at 300 K. The fit parameters are based on the CBMC simulations of pure component isotherms presented in earlier work.[62] Note that the saturation capacities are specified in molecules per cage; multiply these by 1.387 to obtain the values in mol per kg framework.

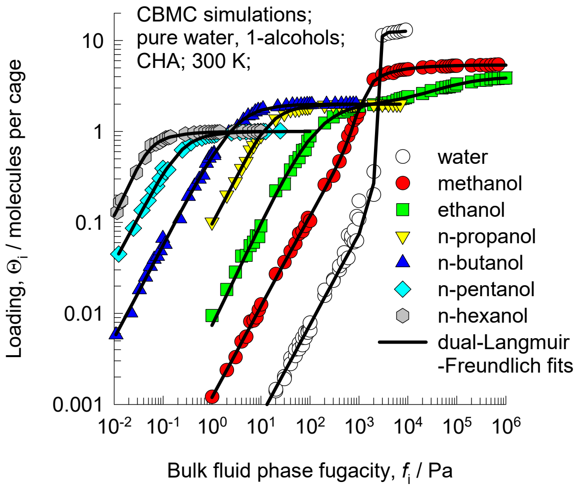

	Site A			Site B		
	$\Theta_{i,A,sat}$ Molecules cage^{-1}	$b_{i,A}$ $\mathrm{Pa}^{-\nu_i}$	$\nu_{i,A}$ dimensionless	$\Theta_{i,B,sat}$ molecules cage^{-1}	$b_{i,B}$ $\mathrm{Pa}^{-\nu_i}$	$\nu_{i,B}$ dimensionless
methanol	2.7	6.77×10^{-11}	3.3	2.7	4.45×10^{-4}	1
ethanol	2	7.93×10^{-5}	0.87	2	3.6×10^{-3}	1.14
1-propanol	1	1.28×10^{-2}	1.8	1	9.11×10^{-2}	1
1-butanol	1	0.231	1.46	1	0.5066	1
1-pentanol	0.5	19.26	1.72	0.5	6.91	1
1-hexanol	0.5	2561	2.4	0.5	24.8	1

Table 10. Single-site Langmuir fit parameters of the isotherms for m-xylene and p-xylene in MFI zeolite at 300 K. The pure component isotherms are obtained from the molecular simulation data (for the orthorhombic (often denoted as ORTHO) MFI framework) of Chempath et al.[71] The p-xylene data is considered to reach saturation at 4 molecules per unit cell.

$$\Theta_i^0(p) = \frac{\Theta_{i,sat} b_i p}{1 + b_{i,} p}$$

	$\Theta_{i,sat}$ molecules uc^{-1}	b_i Pa^{-1}
m-xylene	4	1.2
p-xylene	4	0.6

Table 11. Dual-site Langmuir-Freundlich parameters for pure component water, methanol, and ethanol at 300 K in all-silica DDR zeolite. The fit parameters are based on the CBMC simulations of pure component isotherms presented in earlier work.[92] Note that the saturation capacities are specified in molecules per cage; multiply these by 0.832157 to obtain the values in mol per kg framework.

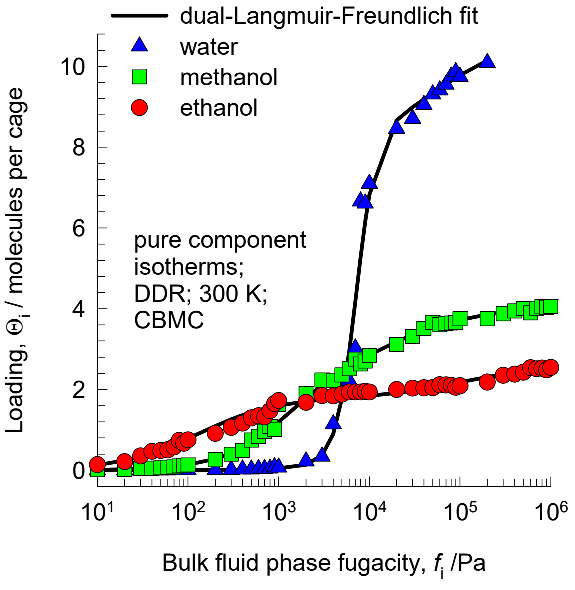

$$\Theta_i^0(p) \equiv \Theta_{i,A} + \Theta_{i,B} = \frac{\Theta_{i,sat,A} b_{i,A} p}{1+b_{i,A}p} + \frac{\Theta_{i,sat,B} b_{i,B} p}{1+b_{i,B}p}$$

	Site A			Site B		
	$\Theta_{i,A,sat}$ Molecules cage^{-1}	$b_{i,A}$ $\mathrm{Pa}^{-\nu_i}$	$\nu_{i,A}$ dimensionless	$\Theta_{i,B,sat}$ molecules cage^{-1}	$b_{i,B}$ $\mathrm{Pa}^{-\nu_i}$	$\nu_{i,B}$ dimensionless
water	8.083	3.85×10^{-16}	4	2.667	1.73×10^{-5}	1
methanol	2.1667	1.49×10^{-4}	1.25	1.9167	6×10^{-4}	0.77
ethanol	1.8167	7.66×10^{-3}	1	0.775	8.59×10^{-6}	1

Table 12. Dual-Langmuir-Freundlich fits of the isotherms of water, and ethanol in LTA-4A zeolite. The isotherm fits are based on the experimental data of Pera-Titus et al.[77]

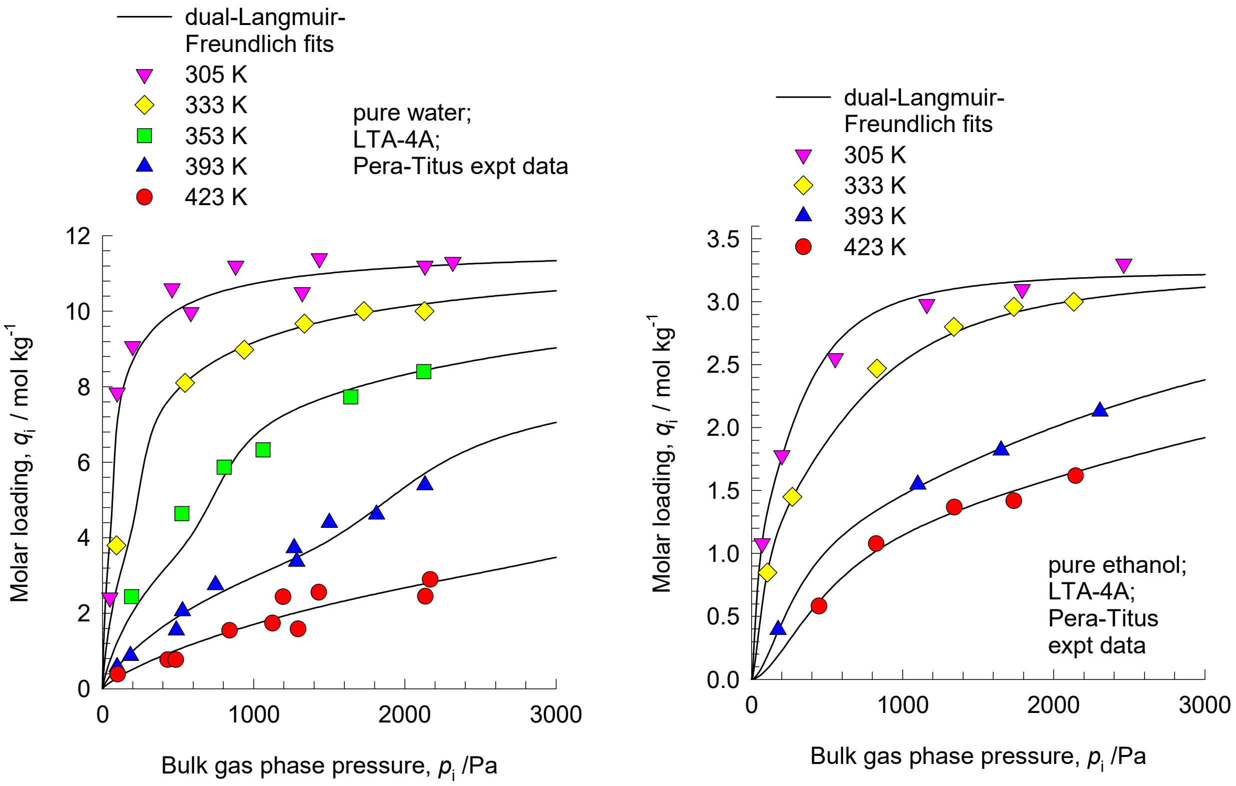

	Site A				Site B			
	$q_{A,sat}$ mol kg^{-1}	b_{A0} $\mathrm{Pa}^{-\nu_i}$	E_A kJ mol^{-1}	ν_A dimensionless	$q_{B,sat}$ mol kg^{-1}	b_{B0} $\mathrm{Pa}^{-\nu_i}$	E_B kJ mol^{-1}	ν_B dimensionless
water	2.1	2.1×10^{-60}	269	7.26	9.7	5.81×10^{-8}	33	0.83
ethanol	1.85	5.24×10^{-13}	43.3	1.9	1.4	2.65×10^{-10}	40	1.7

Table 13. Calculation of modified Thiele modulus for various scenarios. Adapted from Baur and Krishna.[21]

Scenario	Formula for modified Thiele Modulus	Remarks about analytic solution
Equal diffusivities: $Đ_1(0) = Đ_2(0)$	$\Phi = \phi\ \Xi$	Exact for facile exchange. For finite exchange, a very good approximation.
Strong confinement	$\Phi = \phi\ \beta\ \Xi\Psi$	Exact for facile exchange. For finite exchange, a very good approximation.
Weak confinement	$\Phi = \frac{\phi\ \beta\Xi\Psi}{\Theta}$	Exact for facile exchange in the limiting cases $\phi \to \infty$ and $\phi \to 0$. For all other cases, including that for finite exchange, a very good approximation.

(1) Classical scenario: $\Phi = \phi$.

(2) Weak confinement scenario for the diffusivities. Also ignored are the correlation effects, i.e. $Đ_1/Đ_{12} \to 0; \quad Đ_2/Đ_{12} \to 0$. Thermodynamic coupling effects are accounted for using the mixed-gas Langmuir isotherm model. $\Phi = \frac{\phi\ \beta\Xi\Psi}{\Theta}$

(3) Strong confinement scenario for the diffusivities in which the diffusivities are related to the zero-loading diffusivities by $Đ_i = Đ_i(0)\theta_V$. Also ignored are the correlation effects, i.e. $Đ_1/Đ_{12} \to 0; \quad Đ_2/Đ_{12} \to 0$. Thermodynamic coupling effects are accounted for using the mixed-gas Langmuir isotherm model. $\Phi = \phi\ \beta\ \Xi\Psi$

(4) Weak confinement scenario for the diffusivities. Thermodynamic coupling effects are accounted for using the mixed-gas Langmuir isotherm model. Correlation effects are accounted for with finite values of $Đ_1/Đ_{12}; \quad Đ_2/Đ_{12}$. $\Phi = \frac{\phi\ \beta\Xi\Psi}{\Theta}$

(5) Strong confinement scenario for the diffusivities in which the diffusivities are related to the zero-loading diffusivities by $Đ_i = Đ_i(0)\theta_V$. Thermodynamic coupling effects are accounted for using the mixed-gas Langmuir isotherm model. Correlation effects are accounted for with finite values of $Đ_1/Đ_{12}; \quad Đ_2/Đ_{12}$. $\Phi = \phi\ \beta\ \Xi\Psi$

Table 14. Dual-site Langmuir parameters for hexane isomers in MFI at 362 K. The fits correspond to CBMC simulations. [17, 93, 94]

$$\Theta_i^0(p) \equiv \Theta_{i,A} + \Theta_{i,B} = \frac{\Theta_{i,sat,A} b_{i,A} p}{1 + b_{i,A} p} + \frac{\Theta_{i,sat,B} b_{i,B} p}{1 + b_{i,B} p}$$

Component	Dual Langmuir Parameters			
	Site A		Site B	
	$b_{\mathrm{i,A}}$ /Pa^{-1}	$\Theta_{\mathrm{i,sat,A}}$ /molecules uc^{-1}	$b_{\mathrm{i,B}}$ /Pa^{-1}	$\Theta_{\mathrm{i,sat,B}}$ /molecules uc^{-1}
nC_6	6.32×10^{-2}	4.0	1.7×10^{-3}	4.0
3MP	4.75×10^{-2}	4.0	2.27×10^{-5}	2.3
2DMB	1.085×10^{-2}	4.0	2.27×10^{-5}	0.0

Table 15. Single-site Langmuir fit parameters of the isotherms for hydrogen, ethene, ethane, benzene, and ethylbenzene in MFI zeolite at 653 K. The pure component isotherms are obtained from the molecular simulation data of Hansen et al.[83, 84] for the range of pressure up to 1 MPa. Hansen provides the isotherm fit parameters for a 3-site Langmuir fit. For our purposes in this article the simpler single site $\Theta_i^0(p) = \frac{\Theta_{i,sat} b_i p}{1 + b_{i,} p}$ is of sufficient accuracy for total mixture loadings below 4 molecules per unit cell.

	$\Theta_{i,sat}$ molecules uc^{-1}	b_i Pa^{-1}
hydrogen	4	5×10^{-8}
ethene	4	2.75×10^{-7}
ethane	4	6×10^{-7}
benzene	4	1.93×10^{-6}
ethylbenzene	4	2.55×10^{-6}

34. References

(1) Ruthven, D. M. *Principles of Adsorption and Adsorption Processes*; John Wiley: New York, 1984.

(2) Myers, A. L.; Prausnitz, J. M. Thermodynamics of Mixed Gas Adsorption. *A.I.Ch.E.J.* **1965**, *11*, 121-130.

(3) Babbitt, J. D. On the Differential Equations of Diffusion. *Canad. J. Res.* **1950**, *28 A*, 449-474.

(4) Babbitt, J. D. A Unified Picture of Diffusion. *Canad. J. Phys.* **1951**, *29*, 427-436.

(5) Krishna, R. Diffusion in Porous Crystalline Materials. *Chem. Soc. Rev.* **2012**, *41*, 3099-3118.

(6) Krishna, R. The Maxwell-Stefan Description of Mixture Diffusion in Nanoporous Crystalline Materials. *Microporous Mesoporous Mater.* **2014**, *185*, 30-50.

(7) Krishna, R. Uphill Diffusion in Multicomponent Mixtures. *Chem. Soc. Rev.* **2015**, *44*, 2812-2836.

(8) Siperstein, F. R.; Myers, A. L. Mixed-Gas Adsorption. *A.I.Ch.E.J.* **2001**, *47*, 1141-1159.

(9) Gupta, A.; Clark, L. A.; Snurr, R. Q. Grand canonical Monte Carlo simulations of nonrigid molecules: Siting and segregation in silicalite zeolite. *Langmuir* **2000**, *16*, 3910-3919.

(10) Krishna, R.; van Baten, J. M. Influence of Adsorption Thermodynamics on Guest Diffusivities in Nanoporous Crystalline Materials. *Phys. Chem. Chem. Phys.* **2013**, *15*, 7994-8016.

(11) Chmelik, C.; Kärger, J.; Wiebcke, M.; Caro, J.; van Baten, J. M.; Krishna, R. Adsorption and Diffusion of Alkanes in CuBTC Crystals Investigated Using Infrared Microscopy and Molecular Simulations. *Microporous Mesoporous Mater.* **2009**, *117*, 22-32.

(12) Krishna, R. Describing the Diffusion of Guest Molecules inside Porous Structures. *J. Phys. Chem. C* **2009**, *113*, 19756-19781.

(13) Krishna, R.; van Baten, J. M. Onsager coefficients for binary mixture diffusion in nanopores. *Chem. Eng. Sci.* **2008**, *63*, 3120-3140.

(14) Krishna, R.; van Baten, J. M. An Investigation of the Characteristics of Maxwell-Stefan Diffusivities of Binary Mixtures in Silica Nanopores. *Chem. Eng. Sci.* **2009**, *64*, 870-882.

(15) Krishna, R.; van Baten, J. M. Unified Maxwell-Stefan Description of Binary Mixture Diffusion in Micro- and Meso- Porous Materials. *Chem. Eng. Sci.* **2009**, *64*, 3159-3178.

(16) Krishna, R.; van Baten, J. M. Describing Mixture Diffusion in Microporous Materials under Conditions of Pore Saturation. *J. Phys. Chem. C* **2010**, *114*, 11557-11563.

(17) Krishna, R.; Baur, R. Modelling Issues in Zeolite Based Separation Processes. *Sep. Purif. Technol.* **2003**, *33*, 213-254.

(18) Kapteijn, F.; Moulijn, J. A.; Krishna, R. The generalized Maxwell-Stefan model for diffusion in zeolites: sorbate molecules with different saturation loadings. *Chem. Eng. Sci.* **2000**, *55*, 2923-2930.

(19) Skoulidas, A. I.; Sholl, D. S.; Krishna, R. Correlation effects in diffusion of CH_4/CF_4 mixtures in MFI zeolite. A study linking MD simulations with the Maxwell-Stefan formulation. *Langmuir* **2003**, *19*, 7977-7988.

(20) Krishna, R.; van Baten, J. M. Insights into diffusion of gases in zeolites gained from molecular dynamics simulations. *Microporous Mesoporous Mater.* **2008**, *109*, 91-108.

(21) Baur, R.; Krishna, R. Effectiveness factor for zeolite catalysed isomerization reactions. *Chem. Eng. J.* **2004**, *99*, 105-116.

(22) Baur, R.; Krishna, R. The effectiveness factor for zeolite catalysed reactions. *Catal. Today* **2005**, *105*, 173-179.

(23) Baur, R.; Krishna, R. A moving bed reactor concept for alkane isomerization. *Chem. Eng. J.* **2005**, *109*, 107-113.

(24) Krishna, R.; Baur, R. Analytic solution of the Maxwell-Stefan equations for multicomponent permeation across a zeolite membrane. *Chem. Eng. J.* **2004**, *97*, 37-45.

(25) Krishna, R.; van Baten, J. M. Investigating the Influence of Diffusional Coupling on Mixture Permeation across Porous Membranes *J. Membr. Sci.* **2013**, *430*, 113-128.

(26) Krishna, R.; van Baten, J. M. Investigating the potential of MgMOF-74 membranes for CO_2 capture. *J. Membr. Sci.* **2011**, *377*, 249-260.

(27) Krishna, R.; van Baten, J. M. Maxwell-Stefan modeling of slowing-down effects in mixed gas permeation across porous membranes. *J. Membr. Sci.* **2011**, *383*, 289-300.

(28) Poling, B. E.; Prausnitz, J. M.; O'Connell, J. P. *The Properties of Gases and Liquids*; 5th Edition, McGraw-Hill: New York, 2001.

(29) Krishna, R.; van Baten, J. M. A molecular dynamics investigation of the diffusion characteristics of cavity-type zeolites with 8-ring windows. *Microporous Mesoporous Mater.* **2011**, *137*, 83-91.

(30) Kooijman, H. A.; Taylor, R. A dynamic nonequilibrium model of tray distillation columns. *A.I.Ch.E.J.* **1995**, *41*, 1852-1863.

(31) Michelsen, M. An efficient general purpose method of integration of stiff ordinary differential equations. *A.I.Ch.E.J.* **1976**, *22*, 594-597.

(32) Bulirsch, R.; Stoer, J. Numerical treatment of ordinary differential equations by extrapolation methods. *Numer. Math.* **1966**, *8*, 1-14.

(33) Krishna, R.; Baur, R. Diffusion, Adsorption and Reaction in Zeolites: Modelling and Numerical Issues. http://krishna.amsterchem.com/zeolite/, University of Amsterdam, Amsterdam, 1 January 2015.

(34) He, Y.; Krishna, R.; Chen, B. Metal-Organic Frameworks with Potential for Energy-Efficient Adsorptive Separation of Light Hydrocarbons. *Energy Environ. Sci.* **2012**, *5*, 9107-9120.

(35) Sjöberg, E.; Barnes, S.; Korelskiy, D.; Hedlund, J. MFI membranes for separation of carbon dioxide from synthesis gas at high pressures. *J. Membr. Sci.* **2015**, *486*, 132-137.

(36) Krishna, R. Methodologies for Evaluation of Metal-Organic Frameworks in Separation Applications. *RSC Adv.* **2015**, *5*, 52269-52295.

(37) Krishna, R.; van Baten, J. M. Comment on Comparative Molecular Simulation Study of CO_2/N_2 and CH_4/N_2 Separation in Zeolites and Metal-Organic Frameworks. *Langmuir* **2010**, *26*, 2975-2978.

(38) Krishna, R.; van Baten, J. M. Segregation effects in adsorption of CO_2 containing mixtures and their consequences for separation selectivities in cage-type zeolites. *Sep. Purif. Technol.* **2008**, *61*, 414-423.

(39) Binder, T.; Lauerer, A.; Chmelik, C.; Haase, J.; Kärger, J.; Ruthven, D. M. Micro-imaging of transient intracrystalline concentration profiles during two-component uptake of light hydrocarbon - carbon dioxide mixtures by DDR-type zeolites. *Ind. Eng. Chem. Res.* **2015**, *54*, 8997-9004.

(40) Lauerer, A.; Binder, T.; Chmelik, C.; Miersemann, E.; Haase, J.; Ruthven, D. M.; Kärger, J. Uphill Diffusion and Overshooting in the Adsorption of Binary Mixtures in Nanoporous Solids. *Nat. Commun.* **2015**, *6*, 7697. http://dx.doi.org/doi:10.1038/ncomms8697.

(41) Binder, T. *Mass Transport in Nanoporous Materials: New Insights from Micro-Imaging by Interference Microscopy*. Ph.D. Dissertation, Universität Leipzig, Leipzig, 2013.

(42) Habgood, H. W. The Kinetics of Molecular Sieve Action. Sorption of Nitrogen-Methane Mixtures by Linde Molecular Sieve 4A. *Canad. J. Chem.* **1958**, *36*, 1384-1397.

(43) Yang, R. T. *Adsorbents: Fundamentals and Applications*; John Wiley & Sons, Inc.: Hoboken, New Jersey, 2003.

(44) Chen, Y. D.; Yang, R. T.; Uawithya, P. Diffusion of oxygen, nitrogen and their mixtures in Carbon Molecular-Sieve. *A.I.Ch.E.J.* **1994**, *40*, 577-585.

(45) Titze, T.; Chmelik, C.; Kärger, J.; van Baten, J. M.; Krishna, R. Uncommon Synergy Between Adsorption and Diffusion of Hexane Isomer Mixtures in MFI Zeolite Induced by Configurational Entropy Effects *J. Phys. Chem. C* **2014**, *118*, 2660-2665.

(46) Fernandez, M.; Kärger, J.; Freude, D.; Pampel, A.; van Baten, J. M.; Krishna, R. Mixture Diffusion in Zeolites Studied by MAS PFG NMR and Molecular Simulation. *Microporous Mesoporous Mater.* **2007**, *105*, 124-131.

(47) Niessen, W.; Karge, H. G. Diffusion of *p*-xylene in Single and Binary Systems Investigated by FTIR Spectroscopy. *Microporous Mater.* **1993**, *1*, 1-8.

(48) Karge, H. G. Infrared Spectroscopic Investigation of Diffusion, Co-diffusion and Counter-diffusion of Hydrocarbon Molecules in Zeolites. *C.R. Chim.* **2005**, *8*, 303-319.

(49) Kärger, J.; Bülow, M. Theoretical Prediction of Uptake Behaviour in Adsorption Kinetics of Binary Gas Mixtures Using Irreversible Thermodynamics. *Chem. Eng. Sci.* **1975**, *30*, 893-896.

(50) Krishna, R.; van Baten, J. M. Investigating the Relative Influences of Molecular Dimensions and Binding Energies on Diffusivities of Guest Species Inside Nanoporous Crystalline Materials *J. Phys. Chem. C* **2012**, *116*, 23556-23568.

(51) Krishna, R. Multicomponent Surface Diffusion of Adsorbed Species - A Description Based on the Generalized Maxwell-Stefan Equations. *Chem. Eng. Sci.* **1990**, *45*, 1779-1791.

(52) Kuznicki, S. M.; Bell, V. A.; Nair, S.; Hillhouse, H. W.; Jacubinas, R. M.; Braunbarth, C. M.; Toby, B. H.; Tsapatsis, M. A titanosilicate molecular sieve with adjustable pores for size-selective adsorption of molecules. *Nature* **2001**, *412*, 720-724.

(53) Majumdar, B.; Bhadra, S. J.; Marathe, R. P.; Farooq, S. Adsorption and Diffusion of Methane and Nitrogen in Barium Exchanged ETS-4. *Ind. Eng. Chem. Res.* **2011**, *50*, 3021-3034.

(54) Bhadra, S. J.; Farooq, S. Separation of Methane▯ Nitrogen Mixture by Pressure Swing Adsorption for Natural Gas Upgrading. *Ind. Eng. Chem. Res.* **2011**, *50*, 14030-14045.

(55) Hu, X.; Do, D. D. Multicomponent Adsorption Kinetics of Hydrocarbons onto Activated Carbon: Effect of Adsorption Equilibrium Equations. *Chem. Eng. Sci.* **1992**, *47*, 1715-1725.

(56) Qiao, S.; Hu, X. Use IAST with MPSD to Predict Binary Adsorption Kinetics on Activated Carbon. *A.I.Ch.E.J.* **2000**, *46*, 1743-1752.

(57) Li, K.; Olson, D. H.; Seidel, J.; Emge, T. J.; Gong, H.; Zeng, H.; Li, J. Zeolitic Imidazolate Frameworks for Kinetic Separation of Propane and Propene. *J. Am. Chem. Soc.* **2009**, *131*, 10368-10369.

(58) Herm, Z. R.; Wiers, B. M.; Van Baten, J. M.; Hudson, M. R.; Zajdel, P.; Brown, C. M.; Maschiocchi, N.; Krishna, R.; Long, J. R. Separation of Hexane Isomers in a Metal-Organic Framework with Triangular Channels *Science* **2013**, *340*, 960-964.

(59) Jolimaître, E.; Ragil, K.; Tayakout-Fayolle, M.; Jallut, C. Separation of Mono- and Dibranched Hydrocarbons on Silicalite. *A.I.Ch.E.J.* **2002**, *48*, 1927-1937.

(60) Jolimaître, E.; Tayakout-Fayolle, M.; Jallut, C.; Ragil, K. Determination of mass transfer and thermodynamic properties of branched paraffins in silicalite by inverse chromatography technique. *Ind. Eng. Chem. Res.* **2001**, *40*, 914-926.

(61) Saint-Remi, J. C.; Baron, G. V.; Denayer, J. F. M. Non-Uniform Chain Length Dependent Diffusion of Short 1-Alcohols in SAPO-34 in Liquid Phase. *J. Phys. Chem. C* **2013**, *117*, 9758-9765.

(62) Krishna, R.; van Baten, J. M. Entropy-based Separation of Linear Chain Molecules by Exploiting Differences in the Saturation Capacities in Cage-type Zeolites. *Sep. Purif. Technol.* **2011**, *76*, 325-330.

(63) Krishna, R. Separating Mixtures by Exploiting Molecular Packing Effects in Microporous Materials. *Phys. Chem. Chem. Phys.* **2015**, *17*, 39-59.

(64) Remy, T.; Saint-Remi, J. C.; Singh, R.; Webley, P. A.; Baron, G. V.; Denayer, J. F. M. Adsorption and Separation of C1-C8 Alcohols on SAPO-34. *J. Phys. Chem. C* **2011**, *115*, 8117-8125.

(65) Pan, Y.; Li, T.; Lestari, G.; Lai, Z. Effective Separation of Propylene/Propane Binary Mixtures by ZIF-8 Membranes. *J. Membr. Sci.* **2012**, *390-391*, 93-98.

(66) Liu, D.; Ma, X.; Xi, H.; Lin, Y. S. Gas transport properties and propylene/propane separation characteristics of ZIF-8 membranes. *J. Membr. Sci.* **2014**, *451*, 85-93.

(67) Geus, E. R.; van Bekkum, H.; Bakker, W. J. W.; Moulijn, J. A. High-temperature Stainless Steel Supported Zeolite (MFI) Membranes: Preparation, Module Construction, and Permeation Experiments. *Microporous Mater.* **1993**, *1*, 131-147.

(68) Bakker, W. J. W. *Structured systems in gas separation*. Ph.D. Dissertation, Delft University of Technology, Delft, 1999.

(69) Matsufuji, T.; Watanabe, K.; Nishiyama, N.; Egashira, Y.; Matsukata, M.; Ueyama, K. Permeation of Hexane Isomers Through an MFI Membrane. *Ind. Eng. Chem. Res.* **2000**, *39*, 2434-2438.

(70) Matsufuji, T.; Nishiyama, N.; Matsukata, M.; Ueyama, K. Separation of Butane and Xylene Isomers with MFI-type Zeolitic Membrane Synthesized by a Vapor-Phase Transport Method. *J. Membr. Sci.* **2000**, *178*, 25-34.

(71) Chempath, S.; Snurr, R. Q.; Low, J. J. Molecular Modeling of Binary Liquid-phase Adsorption of Aromatics in Silicalite. *A.I.Ch.E.J.* **2004**, *50*, 463-469.

(72) Courthial, L.; Bandot, A.; Tayakout-Fayolle, M.; Jallut, C. Transient Method for Mass-Transfer Characterization Through Supported Zeolite Membranes: Extension to Two Components. *A.I.Ch.E.J.* **2013**, *59*, 959-970.

(73) Peng, P.; Shi, B.; Lan, Y. A Review of Membrane Materials for Ethanol Recovery by Pervaporation. *Separ. Sci. Technol.* **2011**, *46*, 234-246.

(74) Sato, K.; Aoki, K.; Sugimoto, K.; Izumi, K.; Inoue, S.; Saito, J.; Ikeda, S.; Nakane, T. Dehydrating performance of commercial LTA zeolite membranes and application to fuel grade bio-ethanol production by hybrid distillation/vapor permeation process. *Microporous Mesoporous Mater.* **2008**, *115*, 184-188.

(75) Sato, K.; Sugimoto, K.; Shimosuma, N.; Kikuchi, T.; Kyotani, T.; Kurata, T. Development of practically available up-scaled high-silica CHA-type zeolite membranes for industrial purpose in dehydration of N-methyl pyrrolidone solution. *J. Membr. Sci.* **2012**, *409-410*, 82-95.

(76) Kuhn, J.; Castillo-Sanchez, J. M.; Gascon, J.; Calero, S.; Dubbeldam, D.; Vlugt, T. J. H.; Kapteijn, F.; Gross, J. Adsorption and Diffusion of Water, Methanol, and Ethanol in All-Silica DD3R: Experiments and Simulation. *J. Phys. Chem. C* **2009**, *113*, 14290-14301.

(77) Pera-Titus, M.; Fité, C.; Sebastián, V.; Lorente, E.; Llorens, J.; Cunill, F. Modeling Pervaporation of Ethanol/Water Mixtures within 'Real' Zeolite NaA Membranes. *Ind. Eng. Chem. Res.* **2008**, *47*, 3213-3224.

(78) Corma, A. State of the art and future challenges of zeolites as catalysts. *J. Catal.* **2003**, *216*, 298-312.

(79) Degnan, T. F. The implications of the fundamentals of shape selectivity for the development of catalysts for the petroleum and petrochemical industries. *J. Catal.* **2003**, *216*, 32-46.

(80) Marcilly, C. Present status and future trends in catalysis for refining and petrochemicals. *J. Catal.* **2003**, *216*, 47-62.

(81) Krishna, R.; Baur, R. On the Langmuir-Hinshelwood formulation for zeolite catalysed reactions. *Chem. Eng. Sci.* **2005**, *60*, 1155 - 1166.

(82) van Donk, S.; Broersma, A.; Gijzeman, O. L. J.; van Bokhoven, J. A.; Bitter, J. H.; de Jong, K. P. Combined Diffusion, Adsorption, and Reaction Studies of n-Hexane Hydroisomerization over Pt/H-Mordenite in an Oscillating Microbalance. *J. Catal.* **2001**, *204*, 272-280.

(83) Hansen, N.; Krishna, R.; van Baten, J. M.; Bell, A. T.; Keil, F. J. Analysis of Diffusion Limitation in the Alkylation of Benzene over H-ZSM-5 by Combining Quantum Chemical Calculations, Molecular Simulations, and a Continuum Approach. *J. Phys. Chem. C* **2009**, *113*, 235-246.

(84) Hansen, N.; Krishna, R.; van Baten, J. M.; Bell, A. T.; Keil, F. J. Reactor simulation of benzene ethylation and ethane dehydrogenation catalyzed by ZSM-5: A multiscale approach. *Chem. Eng. Sci.* **2010**, *65*, 2472-2480.

(85) Golden, T. C.; Sircar, S. Gas Adsorption on Silicalite. *J. Colloid Interface Sci.* **1994**, *162*, 182-188.

(86) Krishna, R. Evaluation of Procedures for Estimation of the Isosteric Heat of Adsorption in Microporous Materials. *Chem. Eng. Sci.* **2015**, *123*, 191-196.

(87) Böhme, U.; Barth, B.; Paula, C.; Kuhnt, A.; Schwieger, W.; Mundstock, A.; Caro, J.; Hartmann, M. Ethene/Ethane and Propene/Propane Separation via the Olefin and Paraffin Selective Metal−Organic Framework Adsorbents CPO-27 and ZIF-8. *Langmuir* **2013**, *29*, 8592-8600.

(88) Krishna, R.; van Baten, J. M. Diffusion of alkane mixtures in zeolites. Validating the Maxwell-Stefan formulation using MD simulations. *J. Phys. Chem. B* **2005**, *109*, 6386-6396.

(89) Krishna, R.; van Baten, J. M. Diffusion of Hydrocarbon Mixtures in MFI Zeolite: Influence of Intersection Blocking. *Chem. Eng. J.* **2008**, *140*, 614-620.

(90) Krishna, R.; van Baten, J. M. Influence of Adsorption on the Diffusion Selectivity for Mixture Permeation across Mesoporous Membranes. *J. Membr. Sci.* **2011**, *369*, 545-549.

(91) Krishna, R.; van Baten, J. M. In silico screening of metal-organic frameworks in separation applications. *Phys. Chem. Chem. Phys.* **2011**, *13*, 10593-10616.

(92) Krishna, R.; van Baten, J. M. Hydrogen Bonding Effects in Adsorption of Water-alcohol Mixtures in Zeolites and the Consequences for the Characteristics of the Maxwell-Stefan Diffusivities. *Langmuir* **2010**, *26*, 10854-10867.

(93) Calero, S.; Smit, B.; Krishna, R. Configurational entropy effects during sorption of hexane isomers in silicalite. *J. Catal.* **2001**, *202*, 395-401.

(94) Schenk, M.; Vidal, S. L.; Vlugt, T. J. H.; Smit, B.; Krishna, R. Separation of alkane isomers by exploiting entropy effects during adsorption on silicalite-1: A configurational-bias Monte Carlo simulation study. *Langmuir* **2001**, *17*, 1558-1570.

(95) Chmelik, C.; Heinke, L.; Kärger, J.; Shah, D. B.; Schmidt, W.; van Baten, J. M.; Krishna, R. Inflection in the Loading Dependence of the Maxwell-Stefan Diffusivity of Iso-butane in MFI Zeolite. *Chem. Phys. Lett.* **2008**, *459*, 141-145.

(96) Krishna, R. Adsorptive separation of CO_2/CH_4/CO gas mixtures at high pressures. *Microporous Mesoporous Mater.* **2012**, *156*, 217-223.

(97) Krishna, R.; van Baten, J. M. Diffusion of alkane mixtures in MFI zeolite. *Microporous Mesoporous Mater.* **2008**, *107*, 296-298.

(98) Krishna, R.; van Baten, J. M. Investigating the Validity of the Knudsen Prescription for Diffusivities in a Mesoporous Covalent Organic Framework. *Ind. Eng. Chem. Res.* **2011**, *50*, 7083-7087.

(99) Krishna, R.; van Baten, J. M. Investigating the Validity of the Bosanquet Formula for Estimation of Diffusivities in Mesopores. *Chem. Eng. Sci.* **2012**, *69*, 684-688.

35. Caption for Figures

Figure 1. (a) MD data on the M-S diffusivities of various guest molecules in (a) all-silica FAU zeolite, (b) MFI zeolite, and (c) IRMOF-1. The MD data are at 300 K. The *x*-axis is the spreading pressure calculated on the basis of the molar loadings used in the MD simulations, in conjunction with CBMC simulation data for the unary isotherms of the guest molecules. (b) MD data on the M-S diffusivities of CH_4 in various host materials. The MD data are at 300 K. The *x*-axis is the spreading pressure calculated on the basis of the molar loadings used in the MD simulations, in conjunction with CBMC simulation data for the unary isotherms of the guest molecules.

Figure 2. Experimental data on the M-S diffusivity, $Đ_\mathrm{i}$, of is-butane in MFI as a function of the spreading pressure,[95] compared with the corresponding dependence of the inverse thermodynamic factor $1/\Gamma_i$.

Figure 3. Dependence of the Maxwell-Stefan diffusivity $Đ_\mathrm{i}$, and the inverse thermodynamic factor $1/\Gamma_i$ in CuBTC of (a) n-butane, (b) iso-butane, (c) 2,2-dimethylpropane, and (d) 2-methylbutane on the spreading pressure. These data are re-plotted using the information from the published literature.[11]

Figure 4. The M-S binary exchange coefficients $Đ_{12}$, for diffusion of equimolar ($c_1 = c_2$) binary mixtures (a) H_2/CH_4, (b) CH_4/Ar, (c) CH_4/C_2H_6, (d) $CO_2/$ CH_4, (e) CO_2/H_2, and (f) CO_2/N_2 at 300 K in a variety of host materials as a function of the total pore concentration, $c_t = (q_1 + q_2)/V_p$. The $Đ_{12,\mathrm{fl}}$ for binary

fluid phase mixture diffusion, obtained from independent MD simulations. The MD data are culled from the published literature.[5, 13, 15, 20, 26, 27, 50, 88, 96-99].

Figure 5. MD simulation data for the degree of correlations, $Đ_1/Đ_{12}$, for diffusion of equimolar binary mixtures ($c_1 = c_2$) (a) H_2/CO_2, (b) CO_2/CH_4, (c) H_2/CH_4, (d) CH_4/nC_4H_{10}, (e) CH_4/C_2H_6, and (f) CH_4/C_3H_8 at 300 K in a variety of host materials, as a function of the total pore concentration, $c_t = (q_1 + q_2)/V_p$.

Figure 6. Discretization schemes for a single spherical crystallite.

Figure 7. Schematic of membrane permeation device.

Figure 8. MD simulation data for the degree of correlations, $Đ_1/Đ_{12}$, for diffusion of equimolar binary $H_2(1)/CH_4(2)$, $CH_4(1)/nC_4H_{10}(2)$, $CH_4(1)/CO_2(2)$, and $H_2(1)/CO_2(2)$ mixtures in MFI zeolite at 300 K, as a function of the total mixture loading, q_t.

Figure 9. (a) Influence of $Đ_1/Đ_{12}$ on the permeation selectivity, S_{perm}, of binary 95/5 $CH_4(1)/nC_4H_{10}(2)$ mixture permeation across MFI membrane at 300 K. The values of S_{perm} are calculated from steady-state permeation simulations for the fluxes and calculations using Equation (47), taking $p_{1\delta} = p_{2\delta} \approx 0$ and $p_{10}/p_{20} = 95/5$. (b, c) The plots show the normalized fluxes $N_1/(\rho q_{10}Đ_1/\delta)$, and $N_2/(\rho q_{20}Đ_2/\delta)$ as a function of the total upstream pressure. In the simulations the M-S diffusivity is assumed to be independent of the loading. The mixture adsorption equilibrium is calculated using IAST; the pure component isotherms are specified in Table 8.

Figure 10. (a, b) Experimental data of Sjöberg et al.[35] for steady-state permeation of 50/50 equimolar H_2(1)/CO_2(2) mixtures across MFI (silicalite-1) zeolite membrane at 273 K. The continuous solid lines are the steady-state permeation flux calculations using the following diffusivity: $\rho Đ_1/\delta$ = 64 kg m^{-2} s^{-1}, $\rho Đ_2/\delta$ = 3.2 kg m^{-2} s^{-1}; and $Đ_1/Đ_{12} = 20$. The downstream compartment pressure = 1 bar, with partial pressures, $p_{1\delta}$ = 95 kPa; $p_{2\delta}$ = 5 kPa; these estimates are based on the data on separation factors determined experimentally. The mixture adsorption equilibrium is calculated using IAST; the unary isotherm data is provided in Table 1. The model used for the flux calculations correspond to Equations (3), and (4) of our earlier work;[25] these equations are based on the model in which the loading dependence of the M-S diffusivities are taken to be proportional to the vacancy: $Đ_i(\theta) = Đ_i(0)\theta_V$; for this assumption the $[\Gamma]$ "drops out" in the final expressions because they "cancel out" with the vacancy corrections, as explained in the Supporting Information to our work. (b) For H_2(1) flux, the experimental data of Sjöberg are also compared to the model neglecting correlations, Equation (40), and the dominant correlations model, Equation (48).

Figure 11. Schematic of fixed bed adsorber.

Figure 12. Pore landscape and structural details of DDR zeolite.[5, 37]

Figure 13. Pore landscape and structural details of DDR zeolite.[5, 37]

Figure 14. Window dimensions, and structural details of DDR zeolite.

Figure 15. Molecular dimensions of CO_2 and C_2H_6.

Figure 16. Comparison of unary isotherm data with single-site Langmuir fits using the parameters reported in Table 2.

Figure 17. The symbols are scanned from Figure 3 of Binder et al;[39] they represent IAST calculations for binary CO_2 (1)/C_2H_6(2) mixture adsorption in DDR crystals with constant CO_2 partial pressures of p_1 = 20, 40, and 60 kPa for experiments 1, 2, and 3, respectively. The partial pressures of C_2H_6 ethane in the gas phase is varied. The continuous solid lines are our calculations using mixed-gas Langmuir model using the single-site Langmuir parameters reported in in Table 2.

Figure 18. Elements of the matrix of thermodynamic correction factors Γ_{ij} as a function of total mixture loading, q_t, calculated using the mixed-gas Langmuir model for binary CO_2(1)/C_2H_6(2) mixture adsorption in DDR for (a) 1:1, (b) 2:1, and (c) 3:1 ratios of partial pressures in the gas phase. In these calculations the total gas pressure, p_t, was varied from 1 to 100 kPa.

Figure 19. Calculations of ($\Gamma_{12}\, q_2/\Gamma_{11}\, q_1$), and ($\Gamma_{21}\, q_1/\Gamma_{22}\, q_2$) as a function of total mixture loading, q_t, for binary CO_2(1)/C_2H_6(2) mixture adsorption in DDR for 3:1 ratios of partial pressures in the gas phase. In these calculations the total gas pressure, p_t, was varied from 1 to 100 kPa.

Figure 20. The hexagonal crystals of DDR zeolite are modelled as spherical crystals of radius r_c. The single spherical crystallite of DDR zeolite is divided into 100 equidistant segments in the numerical procedure for determining transient uptakes.

Figure 21. The dependence of the diffusivities $Đ_1/r_c^2$, and $Đ_2/r_c^2$ for CO_2(1), and C_2H_6(2) in DDR on the corresponding component loadings, q_1, and q_2, in the adsorbed phase at equilibrium.

Figure 22. Experimental data of Binder[39] for transient uptake of 1:1 CO_2(1)/C_2H_6(2) within crystals of DDR zeolite. In the bulk gas phase 298 K, p_1 = 20 kPa, p_2 = 20 kPa. The parameter values are $Đ_1/r_c^2$ = 0.125 s^{-1}; $Đ_1/Đ_2$ = 1333. The continuous solid lines are the calculations using Equation (**40**). The dashed lines are the calculations using uncoupled flux equation (**54**).

Figure 23. Experimental data of Binder[39] for transient uptake of 2:1 CO_2(1)/C_2H_6(2) within crystals of DDR zeolite. In the bulk gas phase 298 K, p_1 = 40 kPa, p_2 = 20 kPa. The parameter values are $Đ_1/r_c^2$ = 9.375×10^{-3} s^{-1}; $Đ_1/Đ_2$ = 100. The continuous solid lines are the calculations using Equation (**40**). The dashed lines are the calculations using uncoupled flux equation (**54**).

Figure 24. Experimental data of Binder[39] for transient uptake of 3:1 CO_2(1)/C_2H_6(2) within crystals of DDR zeolite. In the bulk gas phase 298 K, p_1 = 60 kPa, p_2 = 20 kPa. The parameter values are $Đ_1/r_c^2$ = 6.25×10^{-3} s^{-1}; $Đ_1/Đ_2$ = 50. The continuous solid lines are the calculations using Equation (**40**). The dashed lines are the calculations using uncoupled flux equation (**54**).

Figure 25. Transient development of CO_2(1), and C_2H_6(2) loadings along the radius of DDR crystal (center, $r = 0$; surface of crystal, $r = r_c$) monitored at different times from start of the uptake. In the bulk gas phase 298 K, p_1 = 20 kPa, p_2 = 20 kPa. The input data are the same as in Figure 22.

Figure 26. Transient development of CO_2(1), and C_2H_6(2) loadings along the radius of DDR crystal (center, $r = 0$; surface of crystal, $r = r_c$) monitored at different times from start of the uptake.

Figure 27. Transient development of CO_2(1), and C_2H_6(2) loadings along the radius of DDR crystal (center, $r = 0$; surface of crystal, $r = r_c$) monitored at different times from start of the uptake. In the bulk gas phase 298 K, $p_1 = 60$ kPa, $p_2 = 20$ kPa. The input data are the same as in Figure 24.

Figure 28. Transient development of "corrected" loadings $q_1\left(\mu_1 - \mu_1^0\right)/RT = \Gamma_{11}q_1 + \Gamma_{12}q_2$, and $q_2\left(\mu_2 - \mu_2^0\right)/RT = \Gamma_{21}q_1 + \Gamma_{22}q_2$ of CO_2(1), and C_2H_6(2) along the radius of DDR crystal (center, $r = 0$; surface of crystal, $r = r_c$) monitored at different times from start of the uptake. In the bulk gas phase 298 K, $p_1 = 40$ kPa, $p_2 = 20$ kPa. The input data are the same as in Figure 23.

Figure 29. Transient development of "corrected" loadings $q_1\left(\mu_1 - \mu_1^0\right)/RT = \Gamma_{11}q_1 + \Gamma_{12}q_2$, and $q_2\left(\mu_2 - \mu_2^0\right)/RT = \Gamma_{21}q_1 + \Gamma_{22}q_2$ of CO_2(1), and C_2H_6(2) along the radius of DDR crystal (center, $r = 0$; surface of crystal, $r = r_c$) monitored at different times from start of the uptake. In the bulk gas phase 298 K, $p_1 = 60$ kPa, $p_2 = 20$ kPa. The input data are the same as in Figure 24.

Figure 30. Transient development of the chemical potentials $\left(\mu_1 - \mu_1^0\right)/RT$, and $\left(\mu_2 - \mu_2^0\right)/RT$ along the radius of DDR crystal (center, $r = 0$; surface of crystal, $r = r_c$) of CO_2(1), and C_2H_6(2) monitored at different times from start of the uptake. In the bulk gas phase 298 K, $p_1 = 60$ kPa, $p_2 = 20$ kPa. The input data are the same as in Figure 24.

Figure 31. Experimental data of Binder[39] for transient development of molar loadings of CO_2(1), and C_2H_6(2) along the radius of DDR crystal monitored at different times from start of the uptake. In the bulk gas phase 298 K, p_1 = 40 kPa, p_2 = 20 kPa. The experimental data in (a) has been scanned from Figure S1 of the Supporting Information accompanying the paper by Binder.[39]

Figure 32. Experimental data of Binder[39] for transient development of "corrected" molar loadings $q_1\left(\mu_1 - \mu_1^0\right)/RT = \Gamma_{11}q_1 + \Gamma_{12}q_2$, and $q_2\left(\mu_2 - \mu_2^0\right)/RT = \Gamma_{21}q_1 + \Gamma_{22}q_2$ of CO_2(1), and C_2H_6(2) along the radius of DDR crystal monitored at different times from start of the uptake. In the bulk gas phase 298 K, p_1 = 40 kPa, p_2 = 20 kPa.

Figure 33. Transient breakthrough of 10/90 CO_2/C_2H_6 mixtures through fixed bed adsorber packed with DDR crystals operating at 298 K, and total pressure p_t = 100 kPa. The parameter values are: L = 0.3 m; voidage of bed, ε = 0.4; interstitial gas velocity, v = 0.1 m/s; radius of crystallite, r_c = 40 μm; $Đ_1/r_c^2$ = 0.00125 s^{-1}; $Đ_1/Đ_2$ = 1333.

Figure 34. Structural details for LTA-4A zeolite.[29]

Figure 35. Experimental data of Habgood[42] on transient uptake of N_2(1)/CH_4(2) mixture within LTA-4A crystals, exposed to binary gas mixtures at 194 K and partial pressures p_1 =50.9 kPa; p_2 = 49.1 kPa. Maxwell-Stefan diffusivities: $Đ_1/r_c^2$ = 1.56×10^{-5} s^{-1}; $Đ_2/r_c^2$ = 7.2×10^{-9} s^{-1}. The continuous solid lines

are the calculations using Equation (40). The dashed lines are the calculations using uncoupled flux equation (54). Table 3 provides the 1-site Langmuir parameters for N_2 and CH_4 in LTA-4A zeolite at 194 K.

Figure 36. Transient development of $N_2(1)$, and $CH_4(2)$ loadings along the radius of LTA-4A crystal (center, $r = 0$; surface of crystal, $r = r_c$) monitored at different times from start of the uptake. The input data are the same as in Figure 35.

Figure 37. Transient development of "corrected" loadings $q_1\left(\mu_1 - \mu_1^0\right)/RT = \Gamma_{11}q_1 + \Gamma_{12}q_2$, and $q_2\left(\mu_2 - \mu_2^0\right)/RT = \Gamma_{21}q_1 + \Gamma_{22}q_2$ of $N_2(1)$, and $CH_4(2)$ along the radius of LTA-4A crystal (center, $r = 0$; surface of crystal, $r = r_c$) monitored at different times from start of the uptake. The input data are the same as in Figure 35.

Figure 38. Experimental data of Chen et al.[44] for transient uptake of $O_2(1)/N_2(2)$ mixture in carbon molecular sieve (CMS) at 300 K exposed to binary gas mixtures at partial pressures p_1 =109.6 kPa; p_2 = 432.56 kPa. The continuous solid lines are transient uptake simulations use Equation (40) taking $Đ_{O2}/r_c^2 = 3.5\times10^{-4}$ s^{-1}; $Đ_{N2}/r_c^2 = 9.5\times10^{-6}$ s^{-1}; $Đ_{O2}/Đ_{N2} = 36.8$. The dashed lines are the calculations using uncoupled flux equation (54). The unary isotherm data are provided in Table 4.

Figure 39. Transient development of $O_2(1)$, and $N_2(2)$ loadings along the radius of CMS particle (center, $r = 0$; surface of particles, $r = r_c$) monitored at different times from start of the uptake. The input data are the same as in Figure 38.

Figure 40. Pore landscape for MFI zeolite.

Figure 41. Structural details for MFI zeolite.

Figure 42. Experimental data of Titze et al.[45] for Run 1 transient uptake of nC6/2MP mixtures in MFI zeolite. The continuous solid lines are Maxwell-Stefan model simulation results using Equation (40) that includes thermodynamic coupling. The dashed lines are the calculations using uncoupled flux equation (54). Input data simulation of Run 1: $Đ_1/r_c^2$ = 0.016 s^{-1}; $Đ_2/r_c^2$ = 1.6×10^{-4} s^{-1}; $t = 0$; $p_1(r_c,0) = p_2(r_c,0)$ = 0 Pa; $t \geq 0$; $p_1(r_c,t) = p_2(r_c,t)$ = 1.3 Pa. The isotherm data are provided in Table 5. The mixture adsorption equilibrium is determined using the IAST.

Figure 43. Transient development of nC6, and 2MP loadings along the radius of MFI crystal (center, r = 0; surface of crystal, $r = r_c$) monitored at different times from start of the uptake. The input data are the same as in Figure 42.

Figure 44. Transient development of "corrected" loadings $q_1(\mu_1 - \mu_1^0)/RT = \Gamma_{11}q_1 + \Gamma_{12}q_2$, and $q_2(\mu_2 - \mu_2^0)/RT = \Gamma_{21}q_1 + \Gamma_{22}q_2$ of nC6, and 2MP along the radius of MFI crystal (center, r = 0; surface of crystal, $r = r_c$) monitored at different times from start of the uptake. The input data are the same as in Figure 42.

Figure 45. Transient uptake of nC4/iC4 mixture in MFI at 298 K. The initial partial pressures $p_1 = p_2 = 0$ Pa; final partial pressures $p_1 = p_2 = 100$ Pa. Input data: $Đ_1/r_c^2$ = 0.08 s^{-1}; $Đ_2/r_c^2$ = 4×10^{-3} s^{-1}. The isotherm data are provided in Table 5. The mixture adsorption equilibrium is determined using the IAST. The continuous solid lines using Equation (40) that include thermodynamic coupling effects. The dashed lines are simulations using uncoupled flux equation (54).

Figure 46. Experimental data of Niessen and Karge[47, 48] for uptake of benzene(1)/ethylbenzene(2) mixture in MFI zeolite (H-ZSM-5). Also shown are transient uptake simulations taking the ratio of diffusivities $Đ_1/Đ_2$ = 100.

Figure 47. Experimental data of Niessen and Karge[47, 48] for uptake of benzene(1)/*p*-xylene(2) mixture in MFI zeolite (H-ZSM-5). Also shown are transient uptake simulations taking the ratio of diffusivities $Đ_1/Đ_2$ = 25.

Figure 48. Experimental data of Kärger and Bülow[49] for transient uptake of n-heptane(1)/benzene(2) mixture in NaX zeolite at 359 K. Input data: $Đ_1/r_c^2$ = 2×10^{-4} s^{-1}; $Đ_2/r_c^2$ = 2×10^{-6} s^{-1}. The continuous solid lines using Equation (40) that include thermodynamic coupling effects. The dashed lines are simulations using uncoupled flux equation (54).

Figure 49. (a, b) Experimental data of Majumdar et al.[53] for transient uptake of (a) 10/90, and (b) 50/50 mixtures of $N_2(1)/CH_4(2)$ mixtures in Ba-ETS-4 at 283 K and total pressure of 0.7 MPa. Note that the *y*-axes represent the fractional uptake of each component; this is obtained by dividing each of the component loadings by the final equilibrated loading within the crystal.

Figure 50. Transient uptake of (a) ethane/n-butane, (b) ethane/n-pentane, and (c) n-butane/n-pentane mixtures in extrudates of activated carbon (AC) at 303 K. Note that the *y*-axes correspond to the molar uptake normalized with respect to the final equilibrated molar loadings. The conditions are chosen to correspond to those in the experiments reported in Figures 8, 9, and 10 of Hu and Do.[55] The single-site Langmuir parameters are provided in Table 1 of Hu and Do.[55] The mixture adsorption equilibrium is determined using the IAST. The continuous solid lines using Equation (40) that include thermodynamic coupling effects. The dashed lines are simulations using uncoupled flux equation (54). Input data on diffusivities: $Đ_{C2}/r_c^2$ = 0.005 s^{-1}; $Đ_{nC4}/r_c^2$ = 9×10^{-4} s^{-1}; $Đ_{nC5}/r_c^2$ = 3×10^{-4} s^{-1}.

Figure 51. The structure and pore landscapes of ZIF-8.

Figure 52. Structural details of ZIF-8.

Figure 53. Simulations of transient uptake of $C_3H_6(1)/C_3H_8(2)$ within crystals of ZIF-8 at 303 K. The simulations use the isotherm parameters specified in Table **7**, along with $Đ_1/r_c^2$ = 1.5×10^{-2} s^{-1}; $Đ_2/r_c^2$ = 1.2×10^{-4} s^{-1}; $Đ_1/Đ_2$ = 125; ratio of single-site Langmuir parameter b_2/b_1 = 1.07. The continuous solid

lines are the calculations using Equation (40). The dashed lines are the calculations using uncoupled flux equation (54).

Figure 54. Simulations of transient uptake of $C_3H_6(1)/C_3H_8(2)$ within crystals of ZIF-8 at 303 K. The three sets of simulations include thermodynamic coupling. In the simulations $Đ_2/r_c^2$ = 1.2×10^{-4} s^{-1}. The ratios $Đ_1/Đ_2$ have three different values: 2, 10, and 125. The continuous solid lines are transient uptake simulations use Equation (40).

Figure 55. Simulations of transient desorption of $C_3H_6(1)/C_3H_8(2)$ from crystals of ZIF-8 at 303 K. Initially, the crystals are equilibrated by exposing the crystals to bulk gas mixture with p_1 = 50 kPa; p_2 = 50 kPa. This equilibrated crystal is then brought into contact with a bulk gas phase with p_1 = 10 kPa; p_2 = 10 kPa. In the simulations $Đ_2/r_c^2$ = 1.2×10^{-4} s^{-1}. The ratio $Đ_1/Đ_2$ = 125. The continuous solid lines are transient uptake simulations use Equation (40). The dashed lines are the calculations using uncoupled flux equation (54).

Figure 56. Transient uptake inside MFI extrudate exposed to a gas phase 2MP(1)/22DMB(2) mixture at 473 K. The partial pressures of the components in the bulk gas phase are p_1 = 22.7 kPa; p_2 = 26.6 kPa. These conditions correspond to Run 17 of Jolimaître et al.[59] Diffusional effects are quantified with $Đ_{2MP}/r_c^2$ = 5×10^{-3} s^{-1}; $Đ_{22DMB}/r_c^2$ = 6.25×10^{-5} s^{-1}. The continuous solid lines represent uptake simulations include thermodynamic coupling using the flux relations Equation (40). The dashed lines represent uptake simulations ignoring thermodynamic coupling and use uncoupled flux equation (54). The input data are provided in Table 6.

Figure 57. Transient development of 2MP and 22DMB loadings along the radius of MFI extrudate (center, $r = 0$; surface of crystal, $r = r_c$) monitored at different times from start of the uptake. The input data are the same as in Figure 56.

Figure 58. Transient development of "corrected" loadings $q_1(\mu_1 - \mu_1^0)/RT = \Gamma_{11}q_1 + \Gamma_{12}q_2$, and $q_2(\mu_2 - \mu_2^0)/RT = \Gamma_{21}q_1 + \Gamma_{22}q_2$ of 2MP(1), and 22DMB(2) along the radius of MFI extrudate (center, $r = 0$; surface of crystal, $r = r_c$) monitored at different times from start of the uptake. The input data are the same as in Figure 56.

Figure 59. Comparison of transient breakthrough experimental data for 2MP(1)/22DMB(2) mixtures (Run 17) of Jolimaître et al.[59] with transient breakthrough simulations. The partial pressures of the components in the bulk gas phase at the inlet are $p_1 = 22.7$ kPa; $p_2 = 26.6$ kPa. The parameter values are: $L = 0.795$ m; voidage of bed, $\varepsilon = 0.4$; interstitial gas velocity, $v = 0.019$ m/s. The continuous solid lines represent breakthrough simulations include thermodynamic coupling using the flux relations Equation (40). The dashed lines represent breakthrough simulations ignoring thermodynamic coupling and using uncoupled flux equation (54). The input data are provided in Table 6.

Figure 60. Transient uptake inside MFI extrudate exposed to a gas phase 2MB(1)/2MP(2)/22DMB(3) mixture at 473 K. The partial pressures of the components in the bulk gas phase are $p_1 = 81$ kPa; $p_2 = 177$ kPa; $p_2 = 106$ kPa. These conditions correspond to Run 20 of Jolimaître et al.[59] Diffusional effects are quantified with $Đ_{2MB}/r_c^2 = 7.5\times10^{-3}$ s^{-1}; $Đ_{2MP}/r_c^2 = 5\times10^{-3}$ s^{-1}; $Đ_{22DMB}/r_c^2 = 6.25\times10^{-5}$ s^{-1}. The continuous solid lines represent uptake simulations include thermodynamic coupling using the flux

relations Equation (40). The dashed lines represent uptake simulations ignoring thermodynamic coupling and use uncoupled flux equation (54). The input data are provided in Table 6.

Figure 61. Comparison of transient breakthrough experimental data for 2MB(1)/2MP(2)/22DMB(3) mixtures (for Run 20) of Jolimaître et al.[59] with transient breakthrough simulations. The parameter values are: L = 0.795 m; voidage of bed, ε = 0.4; interstitial gas velocity, v = 0.0198 m/s. The continuous solid lines represent breakthrough simulations include thermodynamic coupling using the flux relations Equation (40). The dashed lines represent breakthrough simulations ignoring thermodynamic coupling and using uncoupled flux equation (54). The input data are provided in Table 6.

Figure 62. Experimental data of Saint-Remi et al.[61] for transient uptake of ethanol/1-propanol mixtures within SAPO-34, that is the structural analog of CHA zeolite.

Figure 63. Breakthrough experimental data of Remy et al.[64] for separation of ethanol/1-propanol mixtures in a fixed bed adsorber packed with SAPO-34.

Figure 64. (a) Simulations of transient uptake of ethanol(1)/1-propanol(2) mixtures within CHA crystals, exposed to binary fluid mixtures with partial fugacities $f_{\mathrm{ethanol}} = f_{\mathrm{1\text{-}propanol}}$ = 0.5 MPa. The pure component isotherms were fitted to the experimental data using the dual-site Langmuir Freundlich parameters as specified in Table 9. The adsorption equilibrium is calculated using the IAST, using the pure component fit parameters in Table 9. The Maxwell-Stefan diffusivities: $Đ_{ethanol}/r_c^2$ = 4×10^{-3} s^{-1};

$Đ_{1-propanol}/r_c^2$ = 4×10^{-5} s^{-1}. The continuous solid lines are the calculations with flux relations Equation (40). The dashed lines are the calculations neglecting thermodynamic coupling and using uncoupled flux equation (54). (b) Transient development of loadings of ethanol(1), and 1-propanol(2) inside CHA crystal.

Figure 65. Breakthrough simulations for ethanol/1-propanol mixtures in a fixed bed adsorber packed with CHA. The continuous solid lines are the calculations with flux relations Equation (40). The adsorption equilibrium is calculated using the IAST, using the pure component fit parameters in Table 9.

Figure 66. Simulation of transient permeation of C_3H_6(1)/C_3H_8(2) mixture across ZIF-8 membrane at 303 K. The diffusivity data used are:[57] $\rho Đ_1/\delta$ = 1.39×10^{-4} kg m^{-2} s^{-1}, $\rho Đ_2/\delta$ = 1.11×10^{-6} kg m^{-2} s^{-1}; $Đ_1/Đ_2$ = 125; ratio of single-site Langmuir parameter b_2/b_1 = 1.07; membrane thickness δ = 10 μm; partial pressures in upstream membrane compartment, p_{10} = p_{20} = 50 kPa. The downstream compartment is placed under vacuum, i.e. $p_{1\delta} = p_{2\delta} \approx 0$. The loadings at the upstream face are: q_{10} = 1.937 mol kg^{-1}, q_{20} = 2.067 mol kg^{-1}. The loadings at the downstream face are: $q_{1\delta} = q_{2\delta} \approx 0$. The plots show the normalized fluxes $N_1/(\rho q_{10} Đ_1/\delta)$, and $N_2/(\rho q_{20} Đ_2/\delta)$ as a function of the square root of time. The continuous solid lines are the calculations using Equation (40). The dashed lines are the calculations using uncoupled flux equation (54).

Figure 67. Transient development of $C_3H_6(1)$, and $C_3H_8(2)$ loadings along the membrane thickness (upstream face, $z = 0$; downstream face, $z = \delta$) monitored at different times from start of the permeation. Input data are the same as in Figure 66.

Figure 68. Transient development of "corrected" loadings $q_1\left(\mu_1 - \mu_1^0\right)/RT = \Gamma_{11}q_1 + \Gamma_{12}q_2$, and $q_2\left(\mu_2 - \mu_2^0\right)/RT = \Gamma_{21}q_1 + \Gamma_{22}q_2$ of $C_3H_6(1)$, and $C_3H_8(2)$ along the membrane thickness (upstream face, $z = 0$; downstream face, $z = \delta$) monitored at different times from start of the permeation. Input data are the same as in Figure 66.

Figure 69. (a) Experimental data of Geus et al.[67] for transient permeation 50/50 CH_4/nC_4H_{10} mixture across an MFI membrane. (b) Transient simulations of $CH_4(1)/nC_4H_{10}(2)$ membrane permeation. The diffusivity data used are: $\rho Đ_1/\delta = 7.18\times10^{-3}$ kg m^{-2} s^{-1}, $\rho Đ_2/\delta = 7.18\times10^{-4}$ kg m^{-2} s^{-1}; $Đ_1/Đ_2 = 10$; $Đ_1/Đ_{12} = 2$; membrane thickness $\delta = 200$ μm; partial pressures in upstream membrane compartment, $p_{10} = p_{20} = 50$ kPa. The downstream compartment is placed under vacuum, i.e. $p_{1\delta} = p_{2\delta} \approx 0$. The loadings at the upstream face are: $q_{10} = 0.0063$ mol kg^{-1}, $q_{20} = 1.638$ mol kg^{-1}. The loadings at the downstream face are: $q_{1\delta} = q_{2\delta} \approx 0$. The plot shows the normalized fluxes $N_1/\left(\rho q_{10} Đ_1/\delta\right)$, and $N_2/\left(\rho q_{20} Đ_2/\delta\right)$ as a function of the square root of time. The continuous solid lines are the calculations using Equation (39), including both correlations and thermodynamic coupling. The dashed lines are the calculations using uncoupled flux equation (54). The mixture adsorption equilibrium is calculated using IAST; the pure component isotherms are specified in Table 8.

Figure 70. Transient development of CH_4(1), and nC_4H_{10}(2) loadings along the MFI membrane thickness (upstream face, $z = 0$; downstream face, $z = \delta$) monitored at different times from start of the permeation. Input data are the same as in Figure 69.

Figure 71. Transient development of "corrected" loadings $q_1(\mu_1 - \mu_1^0)/RT = \Gamma_{11}q_1 + \Gamma_{12}q_2$, and $q_2(\mu_2 - \mu_2^0)/RT = \Gamma_{21}q_1 + \Gamma_{22}q_2$ of CH_4(1), and nC_4H_{10}(2) along the MFI membrane thickness (upstream face, $z = 0$; downstream face, $z = \delta$) monitored at different times from start of the permeation. Input data are the same as in Figure 69.

Figure 72. (a) Experimental data of Bakker[68] for transient permeation 95/5 H_2/nC_4H_{10} mixture across an MFI membrane. (b) Transient simulations of membrane permeation. The diffusivity data used are: $\rho Đ_1/\delta =$ 0.359 kg m^{-2} s^{-1}, $\rho Đ_2/\delta =$ 7.18×10^{-4} kg m^{-2} s^{-1}; $Đ_1/Đ_2$ = 500; $Đ_1/Đ_{12} = 5$; membrane thickness δ = 200 μm; partial pressures in upstream membrane compartment, p_{10} = 95 kPa; p_{20} = 5 kPa. The downstream compartment is placed under vacuum, i.e. $p_{1\delta} = p_{2\delta} \approx 0$. The loadings at the upstream face are: q_{10} = 0.00235 mol kg^{-1}, q_{20} = 1.555 mol kg^{-1}. The loadings at the downstream face are: $q_{1\delta} = q_{2\delta} \approx 0$. The plot shows the normalized fluxes $N_1/(\rho q_{10}Đ_1/\delta)$, and $N_2/(\rho q_{20}Đ_2/\delta)$ as a function of the square root of time. The continuous solid lines are the calculations using either Equation (39), including both correlations and thermodynamic coupling, or Equation (40) that include thermodynamic coupling but neglect correlations. The dashed lines are the calculations using uncoupled flux equation (54). The mixture adsorption equilibrium is calculated using IAST; the pure component isotherms are specified in Table 8.

Figure 73. Transient development of H_2(1), and nC_4H_{10}(2) loadings along the MFI membrane thickness (upstream face, $z = 0$; downstream face, $z = \delta$) monitored at different times from start of the permeation. Input data are the same as in Figure 72.

Figure 74. Transient development of "corrected" loadings $q_1(\mu_1 - \mu_1^0)/RT = \Gamma_{11}q_1 + \Gamma_{12}q_2$, and $q_2(\mu_2 - \mu_2^0)/RT = \Gamma_{21}q_1 + \Gamma_{22}q_2$ of H_2(1), and nC_4H_{10}(2) along the MFI membrane thickness (upstream face, $z = 0$; downstream face, $z = \delta$) monitored at different times from start of the permeation. Input data are the same as in Figure 72.

Figure 75. (a, b) Experimental data of Matsufuji et al.[69] for transient permeation of (a) nC6/2MP, and (b) nC6/23DMB mixtures across an MFI membrane.

Figure 76. Simulation of transient permeation of nC6(1)/2MP(2) mixture across an MFI membrane at 300 K. The diffusivity data used are: $\rho Đ_1/\delta = 1.8\times10^{-4}$ kg m^{-2} s^{-1}, $\rho Đ_2/\delta = 1.8\times10^{-6}$ kg m^{-2} s^{-1}; $Đ_1/Đ_2 = 100$; membrane thickness $\delta = 50$ μm; partial pressures in upstream membrane compartment, $p_{10} = p_{20} = 1.3$ Pa. The downstream compartment is placed under vacuum, i.e. $p_{1\delta} = p_{2\delta} \approx 0$. The loadings at the upstream face are: $q_{10} = 0.458$ mol kg^{-1}, $q_{20} = 0.32$ mol kg^{-1}. The loadings at the downstream face are: $q_{1\delta} = q_{2\delta} \approx 0$. The plots show the normalized fluxes $N_1/(\rho q_{10}Đ_1/\delta)$, and $N_2/(\rho q_{20}Đ_2/\delta)$ as a function of the square root of time. The continuous solid lines are the calculations using Equation (40). The dashed lines are the calculations using uncoupled flux equation (54). The isotherm data are provided in Table 5. The mixture adsorption equilibrium is determined using the IAST.

Figure 77. Transient development of nC6(1), and 2MP(2) loadings along the MFI membrane thickness (upstream face, $z = 0$; downstream face, $z = \delta$) monitored at different times from start of the permeation. The partial pressures in upstream membrane compartment, $p_{10} = p_{20} = 1.3$ Pa. Input data are the same as in Figure 76.

Figure 78. Transient development of "corrected" loadings $q_1(\mu_1 - \mu_1^0)/RT = \Gamma_{11}q_1 + \Gamma_{12}q_2$, and $q_2(\mu_2 - \mu_2^0)/RT = \Gamma_{21}q_1 + \Gamma_{22}q_2$ of nC6(1), and 2MP(2) along the MFI membrane thickness (upstream face, $z = 0$; downstream face, $z = \delta$) monitored at different times from start of the permeation. The partial pressures in upstream membrane compartment, $p_{10} = p_{20} = 1.3$ Pa. Input data are the same as in Figure 76.

Figure 79. (a, b) Experimental data of Matsufuji et al.[70] for transient permeation of (a) 50/50 m-xylene/p-xylene, and (b) 24/51/25 *p*-xylene/*m*-xylene/*o*-xylene mixtures across MFI membrane at 303 K.

Figure 80. Simulation of transient permeation of 50/50 m-xylene(1)/p-xylene(2) mixture across an MFI membrane at 300 K. The diffusivity data used are: $\rho Đ_1/\delta = 3.59\times10^{-5}$ kg m^{-2} s^{-1}, $\rho Đ_2/\delta = 1.8\times10^{-4}$ kg m^{-2} s^{-1}; $Đ_1/Đ_2 = 0.1$; membrane thickness $\delta = 50$ μm; partial pressures in upstream membrane compartment, $p_{10} = 10$ Pa; $p_{20} = 10$ Pa. The downstream compartment is placed under vacuum, i.e. $p_{1\delta} = p_{2\delta} \approx 0$. The pure component isotherms are obtained from the molecular simulation data (for the

orthorhombic (often denoted as ORTHO) MFI framework) of Chempath et al;[71] see Table 10. The mixture adsorption equilibrium is determined using the mixed gas Langmuir model. The loadings at the upstream face are: q_{10} = 0.438 mol kg^{-1}, q_{20} = 0.219 mol kg^{-1}. The plots show the normalized fluxes $N_1/(\rho q_{10}Đ_1/\delta)$, and $N_2/(\rho q_{20}Đ_2/\delta)$ as a function of the square root of time. The continuous solid lines are the calculations using Equation (40). The dashed lines are the calculations using uncoupled flux equation (54).

Figure 81. Simulation of transient permeation of nC4(1)/iC4(2) mixture across an MFI membrane at 300 K. The diffusivity data used are: $\rho Đ_1/\delta$ = 1.45×10^{-4} kg m^{-2} s^{-1}, $\rho Đ_2/\delta$ = 6.92×10^{-5} kg m^{-2} s^{-1}; $Đ_1/Đ_2$ = 20; membrane thickness δ = 200 μm; partial pressures in upstream membrane compartment, p_{10} = 5 kPa; p_{20} = 95 kPa. The downstream compartment is placed under vacuum, i.e. $p_{1\delta} = p_{2\delta} \approx 0$. The loadings at the upstream face are: q_{10} = 0.8072 mol kg^{-1}, q_{20} = 0.7706 mol kg^{-1}. The loadings at the downstream face are: $q_{1\delta} = q_{2\delta} \approx 0$. The plots show the normalized fluxes $N_1/(\rho q_{10}Đ_1/\delta)$, and $N_2/(\rho q_{20}Đ_2/\delta)$ as a function of the square root of time. The continuous solid lines are the calculations using Equation (40). The dashed lines are the calculations using uncoupled flux equation (54). The isotherm data are provided in Table 5. The mixture adsorption equilibrium is determined using the IAST.

Figure 82. Simulation of transient permeation of water(1)/ethanol(2) mixture across a DDR membrane at 300 K. The diffusivity data used are: $\rho Đ_1/\delta$ = 6.8×10^{-4} kg m^{-2} s^{-1}, $\rho Đ_2/\delta$ = 6.8×10^{-5} kg m^{-2} s^{-1}; $Đ_1/Đ_2$ = 10; membrane thickness δ = 200 μm; partial pressures in upstream membrane compartment, p_{10} = 5 kPa; p_{20} = 95 kPa. The downstream compartment is placed under vacuum, i.e. $p_{1\delta} = p_{2\delta} \approx 0$. The loadings at the upstream face are: q_{10} = 0.344 mol kg^{-1}, q_{20} = 1.744 mol kg^{-1}. The loadings at the

downstream face are: $q_{1\delta} = q_{2\delta} \approx 0$. The plots show the normalized fluxes $N_1/(\rho q_{10}Đ_1/\delta)$, and $N_2/(\rho q_{20}Đ_2/\delta)$ as a function of the square root of time. The isotherm data are provided in Table 11. The mixture adsorption equilibrium is determined using the IAST. The continuous solid lines are the calculations using Equation (40). The dashed lines are the calculations using uncoupled flux equation (54).

Figure 83. Transient development of water(1)/ethanol(2) mixture across the DDR membrane thickness (upstream face, $z = 0$; downstream face, $z = \delta$) monitored at different times from start of the permeation. Input data are the same as in Figure 82.

Figure 84. Simulation of transient permeation of water(1)/ethanol(2) mixture across a LTA-4A membrane at 333 K. The diffusivity data used are: $\rho Đ_1/\delta = 7.65\times10^{-3}$ kg m^{-2} s^{-1}, $\rho Đ_2/\delta = 7.65\times10^{-4}$ kg m^{-2} s^{-1}; $Đ_1/Đ_2 = 10$; membrane thickness $\delta = 200$ μm; partial pressures in upstream membrane compartment, $p_{10} = 50$ Pa; $p_{20} = 950$ Pa. The downstream compartment is placed under vacuum, i.e. $p_{1\delta} = p_{2\delta} \approx 0$. The loadings at the upstream face are: $q_{10} = 0.9774$ mol kg^{-1}, $q_{20} = 2.025$ mol kg^{-1}. The loadings at the downstream face are: $q_{1\delta} = q_{2\delta} \approx 0$. The plots show the normalized fluxes $N_1/(\rho q_{10}Đ_1/\delta)$, and $N_2/(\rho q_{20}Đ_2/\delta)$ as a function of the square root of time. The isotherm data are provided in Table 12. The mixture adsorption equilibrium is determined using the IAST. The continuous solid lines are the calculations using flux Equation (40). The dashed lines are the calculations using uncoupled flux equation (54).

Figure 85. Transient development of water(1)/ethanol(2) mixture across the LTA-4A membrane thickness (upstream face, $z = 0$; downstream face, $z = \delta$) monitored at different times from start of the permeation. Input data are the same as in Figure 84.

Figure 86. Calculation of the (steady-state) effectiveness factor, η, for uptake inside MFI catalyst exposed to a gas phase 2MP(1)/22DMB(2) mixture at 473 K, carrying out the isomerization reaction $2\text{MP}(1) \rightleftarrows 22\text{DMB}(2)$. The partial pressures of the components in the bulk gas phase are $p_1 = 22.7$ kPa; $p_2 = 26.6$ kPa. The ratio of rate constants $k_1/k_2 = 2$. The values of the rate constant k_1 are varied. The zero-loading diffusivities $Đ_1(0) = 2\times10^{-14}$ m^2 s^{-1}; $Đ_1(0) = 2.5\times10^{-16}$ m^2 s^{-1}. The radius of the crystal $r_c = 2$ μm. The Thiele modulus is calculated from $\phi \equiv \frac{r_c}{3}\sqrt{\frac{k_1}{Đ_1(0)} + \frac{k_2}{Đ_2(0)}}$. The calculations using the five different scenarios are based on the analytical solutions provided by Baur and Krishna.[21]

Figure 87. Transient uptake inside MFI catalyst exposed to a gas phase 2MP(1)/22DMB(2) mixture at 473 K, carrying out the isomerization reaction $2\text{MP}(1) \rightleftarrows 22\text{DMB}(2)$. The partial pressures of the components in the bulk gas phase are $p_1 = 22.7$ kPa; $p_2 = 26.6$ kPa. These conditions correspond to Run 17 of Jolimaître et al.[59] Diffusional effects are quantified with $Đ_{2MP}/r_c^2 = 5\times10^{-3}$ s^{-1}; $Đ_{22DMB}/r_c^2 = 6.25\times10^{-5}$ s^{-1}. The reaction rate constants are $k_1 = 0.0011$ s^{-1}, $k_2 = 0.00055$ s^{-1}; these rate constants are taken from Baur and Krishna.[21] The continuous solid lines represent uptake simulations include thermodynamic coupling using the flux relations (40). The dashed lines represent uptake simulations

ignoring thermodynamic coupling and use uncoupled flux equation (54). The input data are provided in Table 6.

Figure 88. Transient development of 2MP(1) and 22DMB(2) loadings along the radius of MFI catalyst (center, $r = 0$; surface of crystal, $r = r_c$), carrying out the isomerization reaction $\mathrm{2MP(1)} \rightleftarrows \mathrm{22DMB(2)}$, monitored at different times from start of the uptake. The input data are the same as in Figure 87.

Figure 89. Transient development of "corrected" loadings $q_1\left(\mu_1 - \mu_1^0\right)/RT = \Gamma_{11}q_1 + \Gamma_{12}q_2$, and $q_2\left(\mu_2 - \mu_2^0\right)/RT = \Gamma_{21}q_1 + \Gamma_{22}q_2$ of 2MP(1), and 22DMB(2) along the radius of MFI catalyst (center, $r = 0$; surface of crystal, $r = r_c$) , carrying out the isomerization reaction $\mathrm{2MP(1)} \rightleftarrows \mathrm{22DMB(2)}$, monitored at different times from start of the uptake. The input data are the same as in Figure 87.

Figure 90. Transient breakthrough simulations for fixed bed 2MP(1)/22DMB(2) isomerization reactor with MFI extrudates, carrying out the isomerization reaction $\mathrm{2MP(1)} \rightleftarrows \mathrm{22DMB(2)}$. The parameter values are: $L = 0.795$ m; voidage of bed, $\varepsilon = 0.4$; interstitial gas velocity, $v = 0.019$ m/s. The continuous solid lines represent breakthrough simulations include thermodynamic coupling using the flux relations (40). The dashed lines represent breakthrough simulations ignoring thermodynamic coupling and using uncoupled flux equation (54). The input data are provided in Table 6.

Figure 91. Transient uptake inside MFI catalyst exposed to a gas phase nC6(1)/3MP(2)/22DMB(3) mixture at 362 K, carrying out the isomerization reaction $\mathrm{nC6(1)} \rightleftarrows \mathrm{3MP(2)} \rightleftarrows \mathrm{22DMB(3)}$. The partial pressures of the components in the bulk gas phase are p_1 = 2 kPa; p_2 = 40 kPa, p_3 = 60 kPa. Diffusional effects are quantified with $Đ_{nC6}/r_c^2$ = 2×10^{-2} s^{-1}; $Đ_{3MP}/r_c^2$ = 2×10^{-3} s^{-1}; $Đ_{22DMB}/r_c^2$ = 1×10^{-3} s^{-1}. All three M-S diffusivities are assumed to follow the loading dependence $Đ_i(\theta) = Đ_i(0)\theta_V$. The reaction rate constants are k_{f1} = 0.009 Pa^{-1} s^{-1}, k_{b1} = 0.007 Pa^{-1} s^{-1}; k_{f2} = 0.009 Pa^{-1} s^{-1}, k_{b2} = 0.007 Pa^{-1} s^{-1}. The continuous solid lines represent uptake simulations include thermodynamic coupling using the flux relations (40). The dashed lines represent uptake simulations ignoring thermodynamic coupling and use uncoupled flux equation (54). The isotherm input data are provided in Table 14.

Figure 92. Transient uptake inside MFI catalyst exposed to a gas phase m-xylene(1)/p-xylene(2) mixture at 303 K, carrying out the isomerization reaction $\mathrm{m-xylene(1)} \rightleftarrows \mathrm{p-xylene(2)}$. The partial pressures of the components in the bulk gas phase are p_1 = 10 Pa; p_2 = 10 Pa. Diffusional effects are quantified with $Đ_1/r_c^2$ = 2×10^{-5} s^{-1}; $Đ_2/r_c^2$ = 1×10^{-4} s^{-1}. The reaction rate constants are k_1 = 0.001 s^{-1}, k_2 = 0.0005 s^{-1}. The continuous solid lines represent uptake simulations include thermodynamic coupling using the flux relations (40). The dashed lines represent uptake simulations ignoring thermodynamic coupling and use uncoupled flux equation (54). The isotherm input data are provided in Table 10.

Figure 93. Transient uptake inside MFI catalyst exposed to a gas phase ethene(1)/benzene(2)/ethylbenzene(3) mixture at 653 K, carrying out the ethylation reaction

$\text{ethene}(1) + \text{benzene}(2) \rightleftarrows \text{ethylbenzene}(3)$. The partial pressures of the components in the bulk gas phase are p_1 = 800 kPa; p_2 = 200 kPa, p_3 = 0 kPa. Diffusional effects are quantified with $Đ_{ethene}/r_c^2$ = 1×10^{-3} s^{-1}; $Đ_{benzene}/r_c^2$ = 2×10^{-5} s^{-1}; $Đ_{ethylbenzene}/r_c^2$ = 1×10^{-5} s^{-1}. The continuous solid lines represent uptake simulations include thermodynamic coupling using the flux relations (40). The dashed lines represent uptake simulations ignoring thermodynamic coupling and use uncoupled flux equation (54). The isotherm input data are provided in Table 15.

Figure 94. Transient uptake inside MFI catalyst exposed to a gas phase ethane(1)/ethene(2)/hydrogen(3) mixture at 653 K, carrying out the dehydrogenation reaction $\text{ethane}(1) \rightleftarrows \text{ethene}(2) + \text{hydrogen}(3)$. The partial pressures of the components in the bulk gas phase are p_1 = 0.2 MPa; p_2 = 0.1 MPa, p_3 = 1 MPa. Diffusional effects are quantified with $Đ_{ethane}/r_c^2$ = 2.5×10^{-4} s^{-1}; $Đ_{ethene}/r_c^2$ = 5×10^{-4} s^{-1}; $Đ_{hydrogen}/r_c^2$ = 1.25×10^{-2} s^{-1}. The continuous solid lines represent uptake simulations include thermodynamic coupling using the flux relations (40). The dashed lines represent uptake simulations ignoring thermodynamic coupling and use uncoupled flux equation (54). The isotherm input data are provided in Table 15.

Figure S1

Unary diffusivities vs spreading pressure

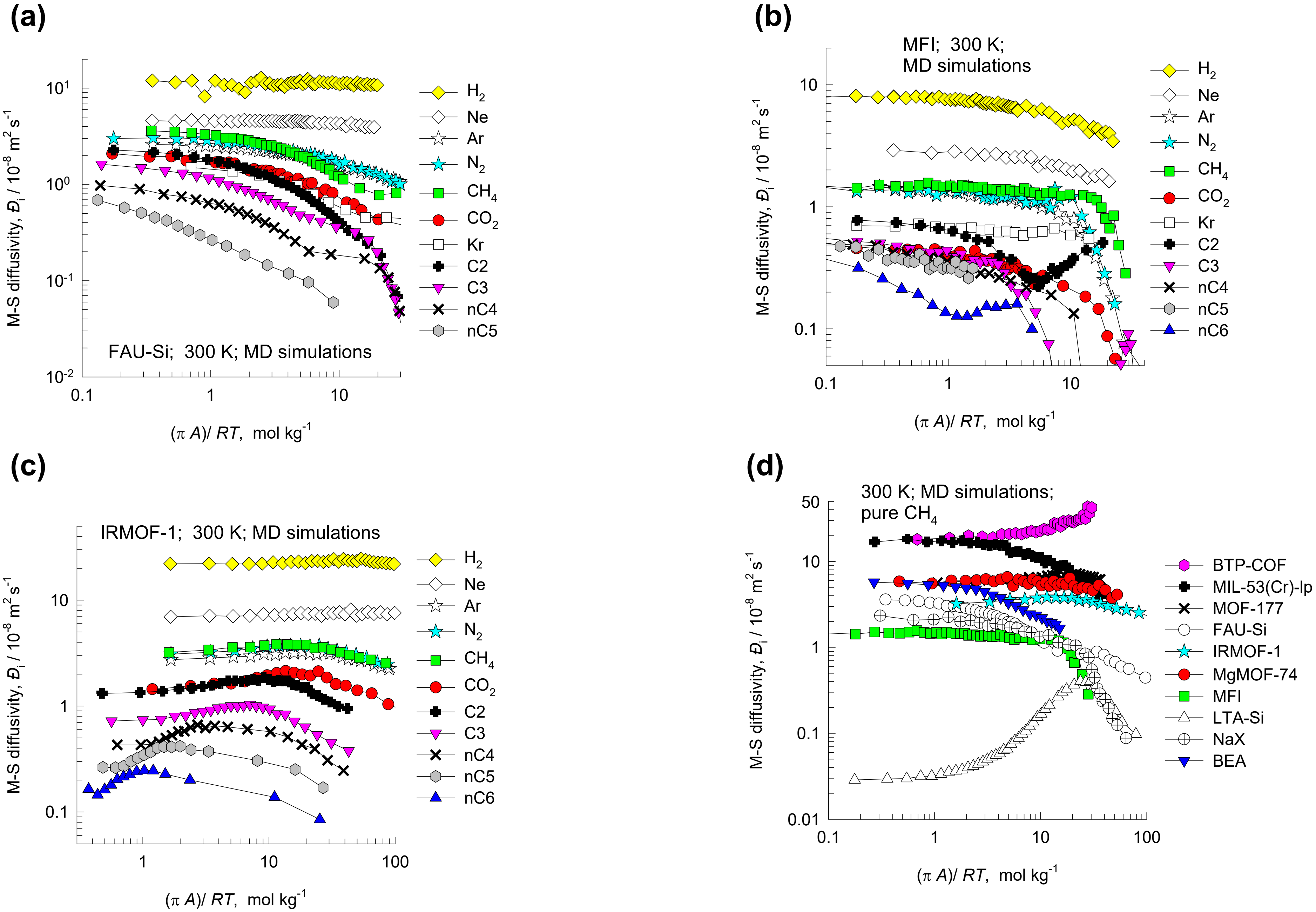

Figure S2

Unary diffusivities vs spreading pressure

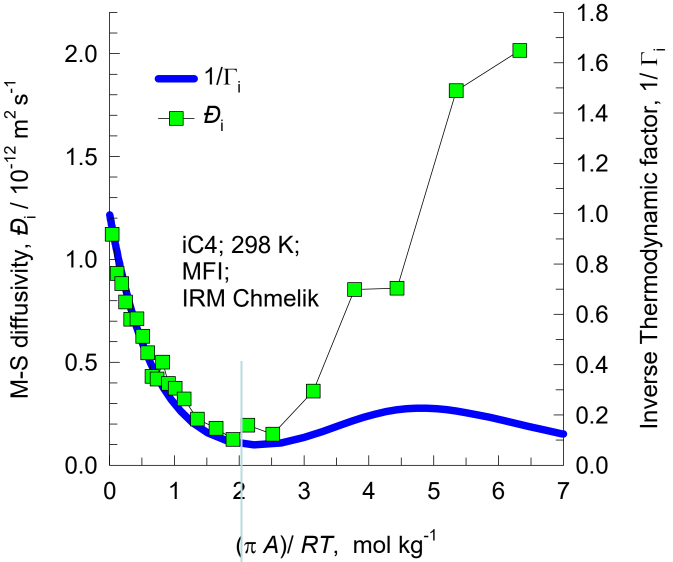

4 molecules
per uc

Figure S3

Unary diffusivities vs spreading pressure

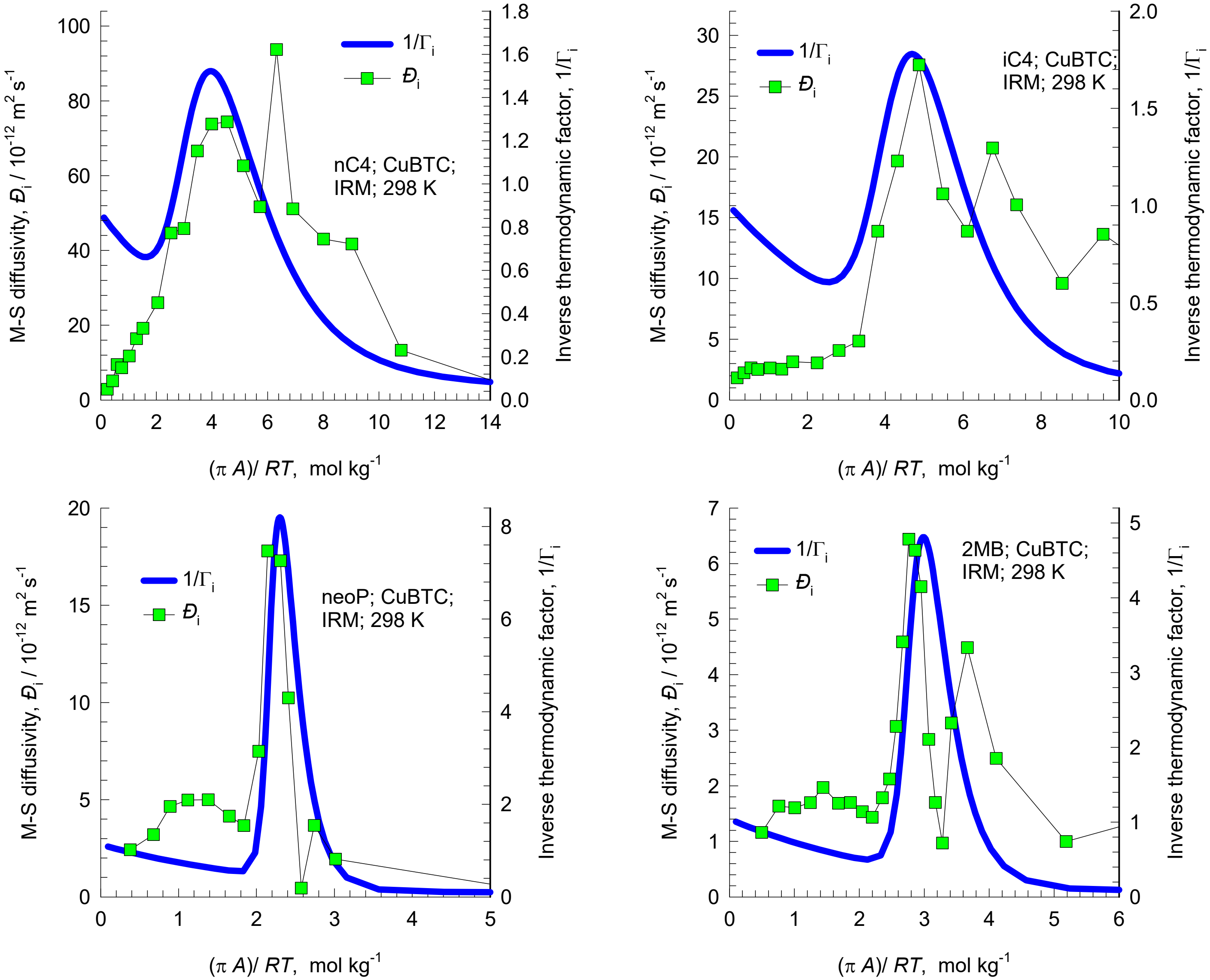

Figure S4

Exchange coefficients $Đ_{12}$

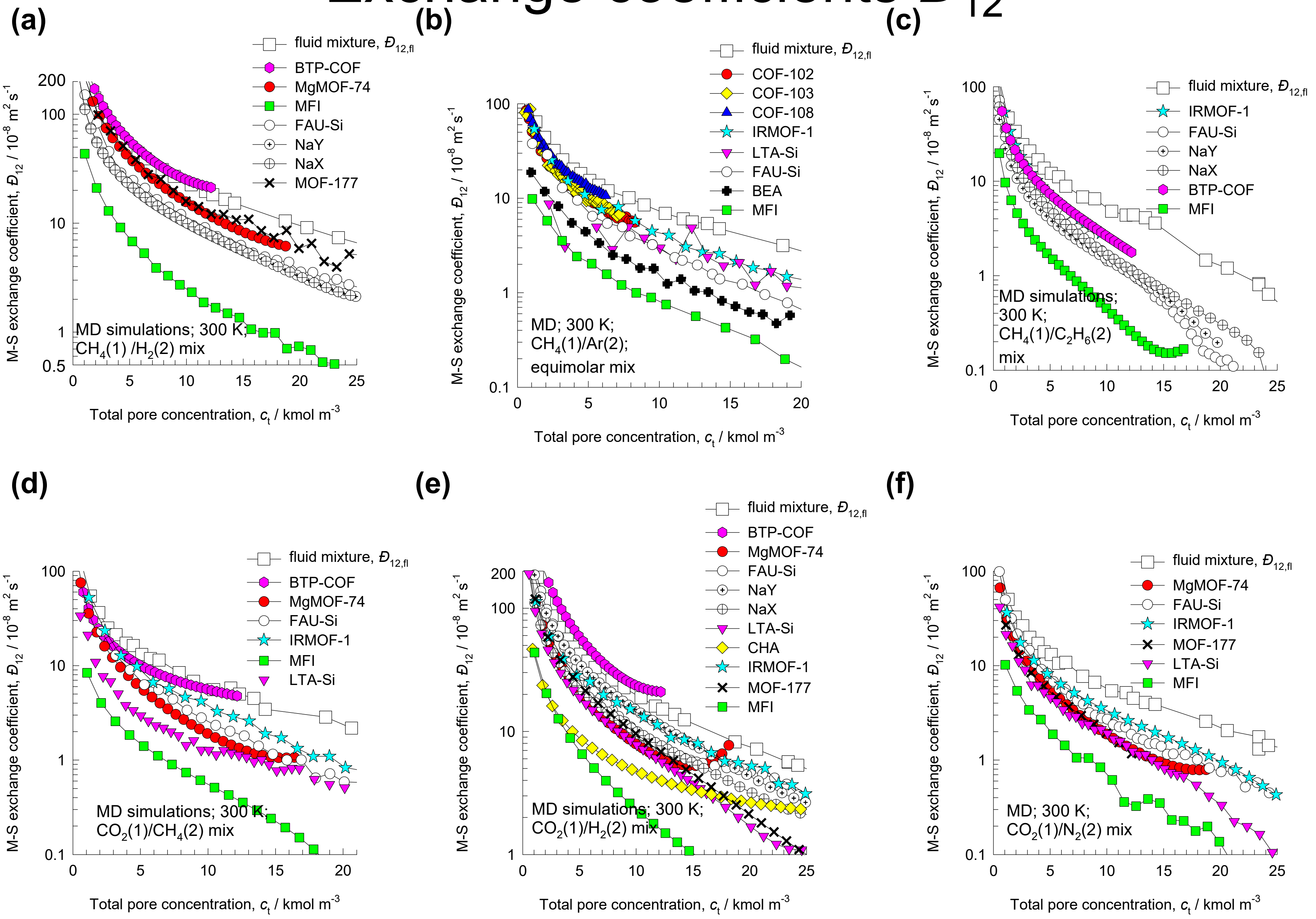

Degree of correlations

Figure S5

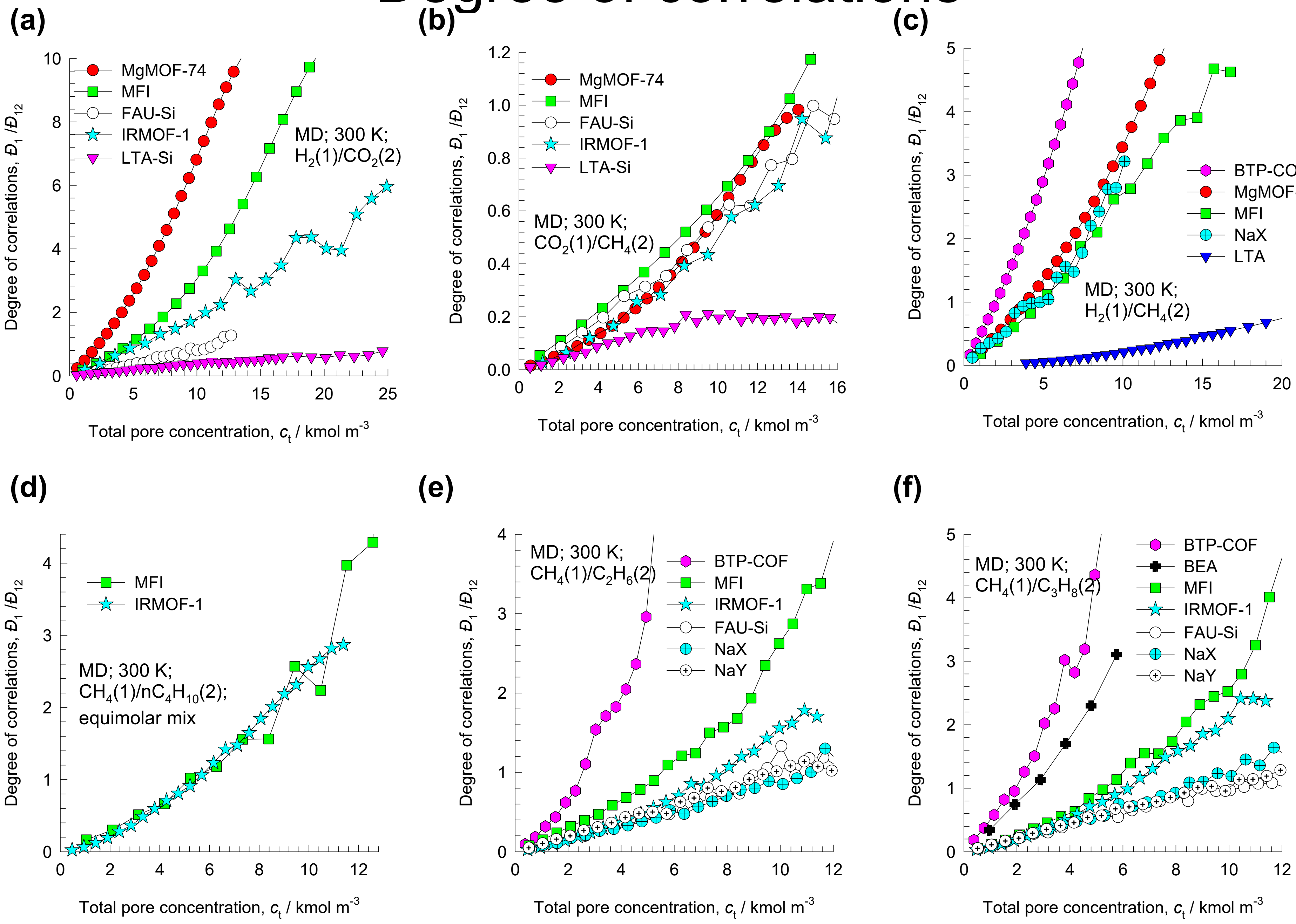

Figure S6

Discretization strategies

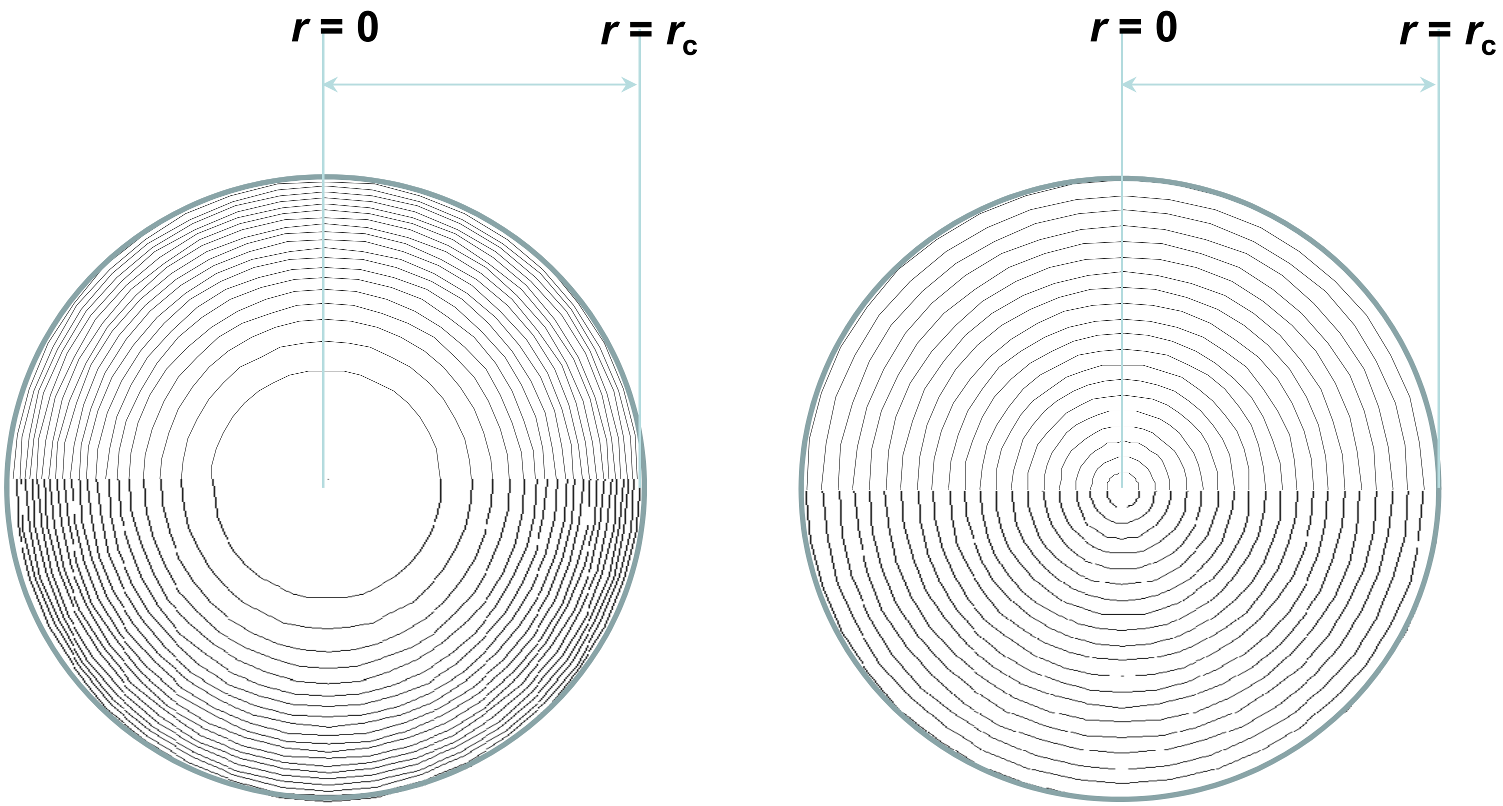

(a) Equi-volume slices

(b) Equi-distant slices

Figure S7

Model for membrane permeation

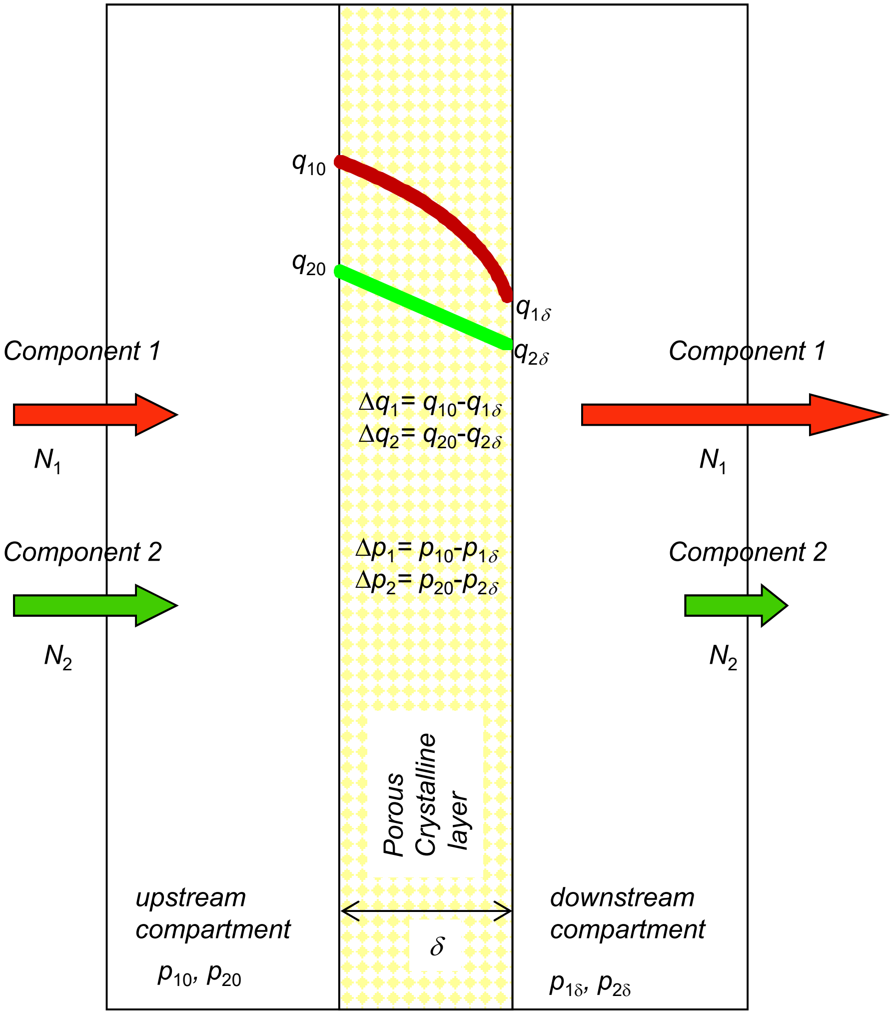

Figure S8

Degree of correlations in MFI membrane

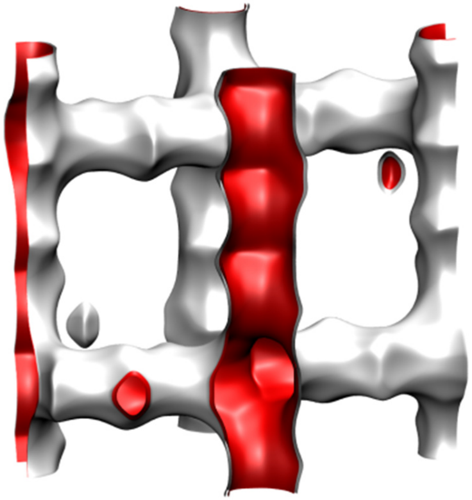

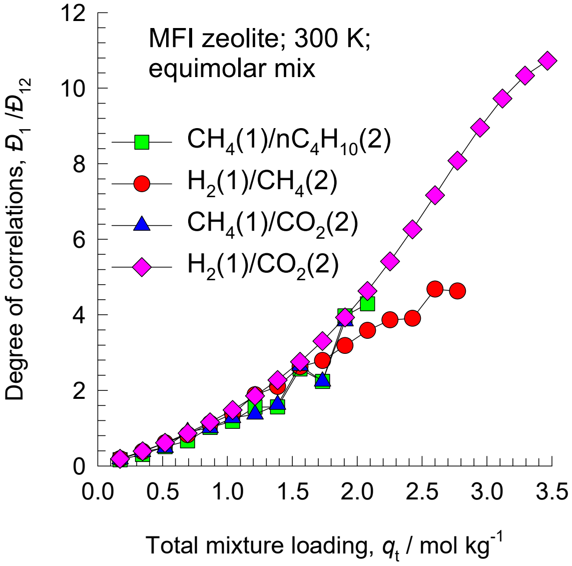

Figure S9

Degree of correlations in MFI zeolite

(a)

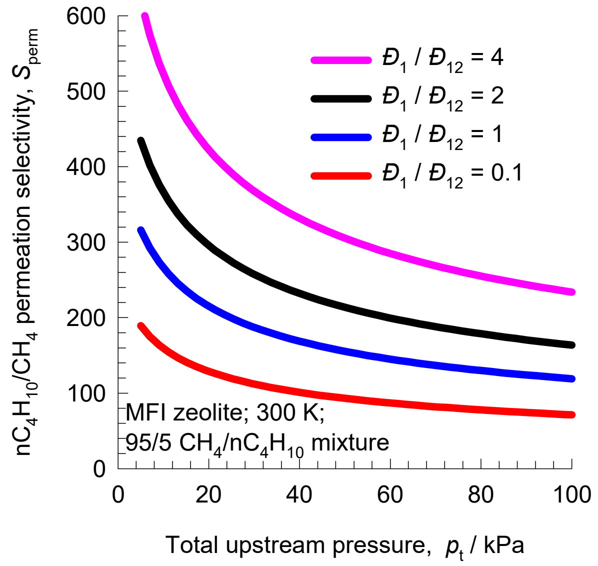

(b)

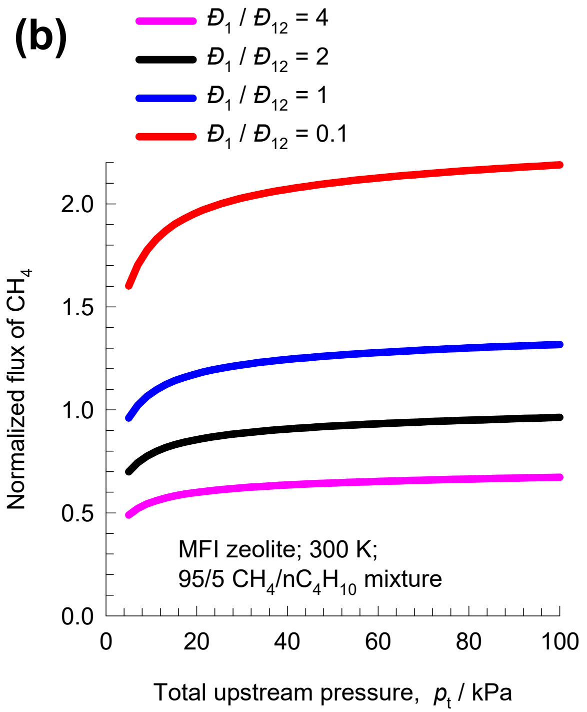

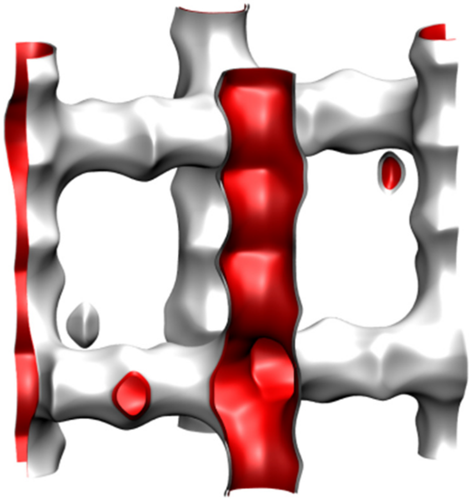

(c)

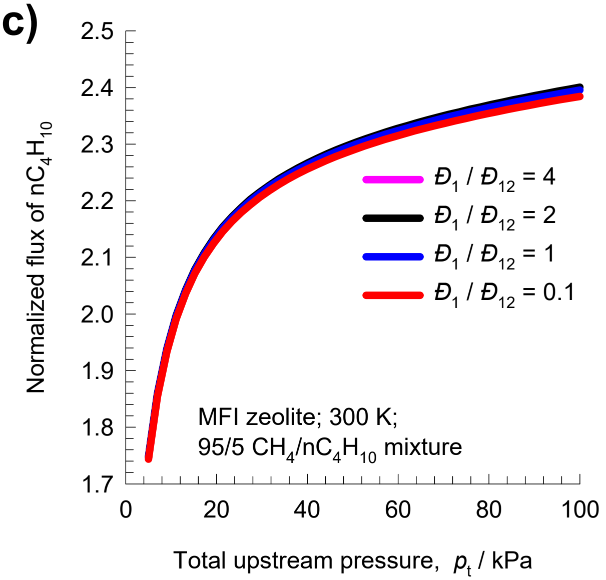

Figure S10

Degree of correlations in MFI zeolite

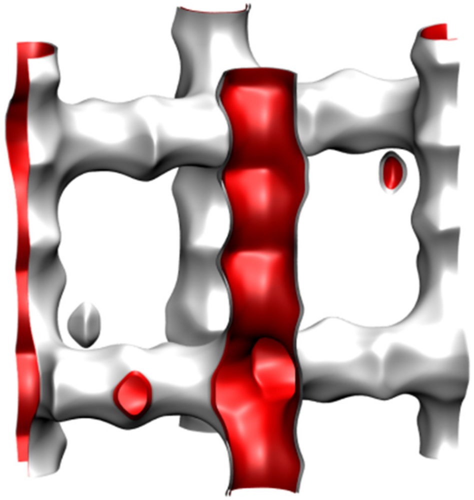

(a)

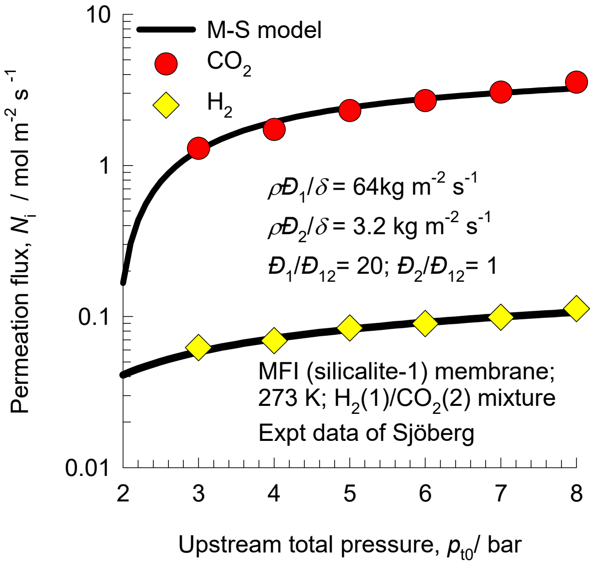

(b)

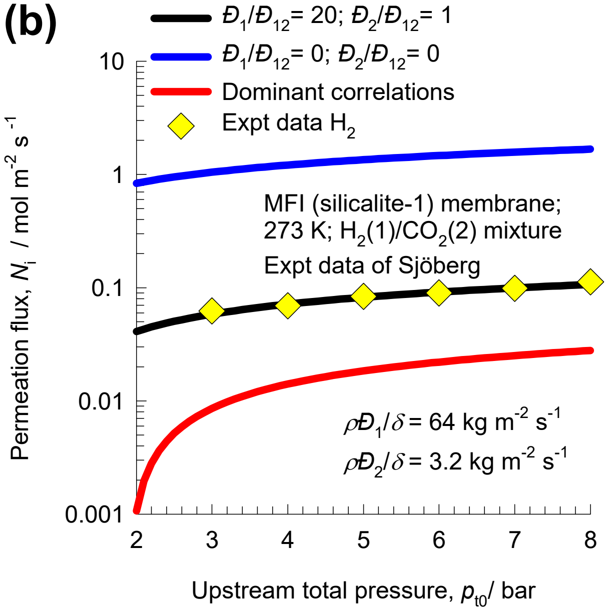

Fixed bed adsorber

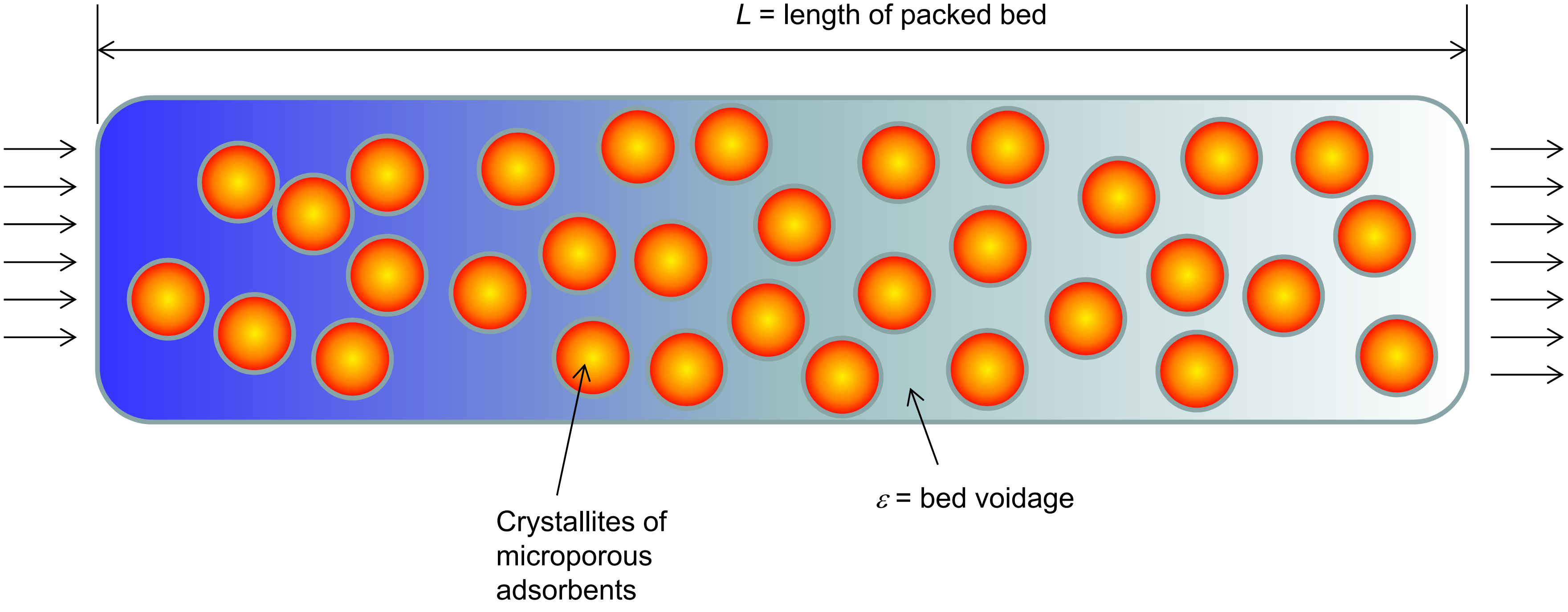

DDR landscape

Figure S12

There are 12 cages per unit cell. The volume of one DDR cage is 278 Å^3, significantly smaller than that of a single cage of FAU (786 Å^3), or ZIF-8 (1168 Å^3).

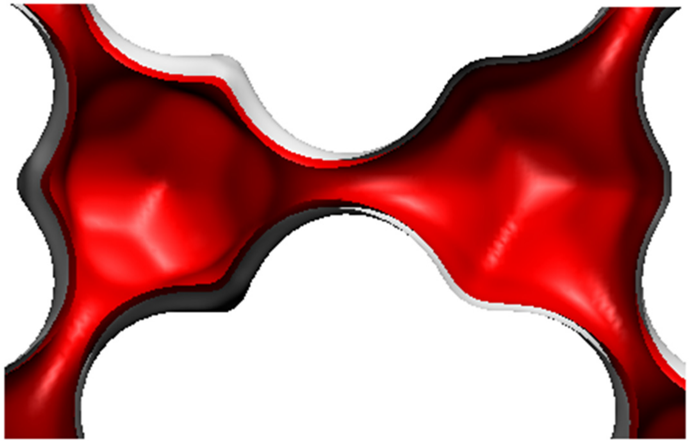

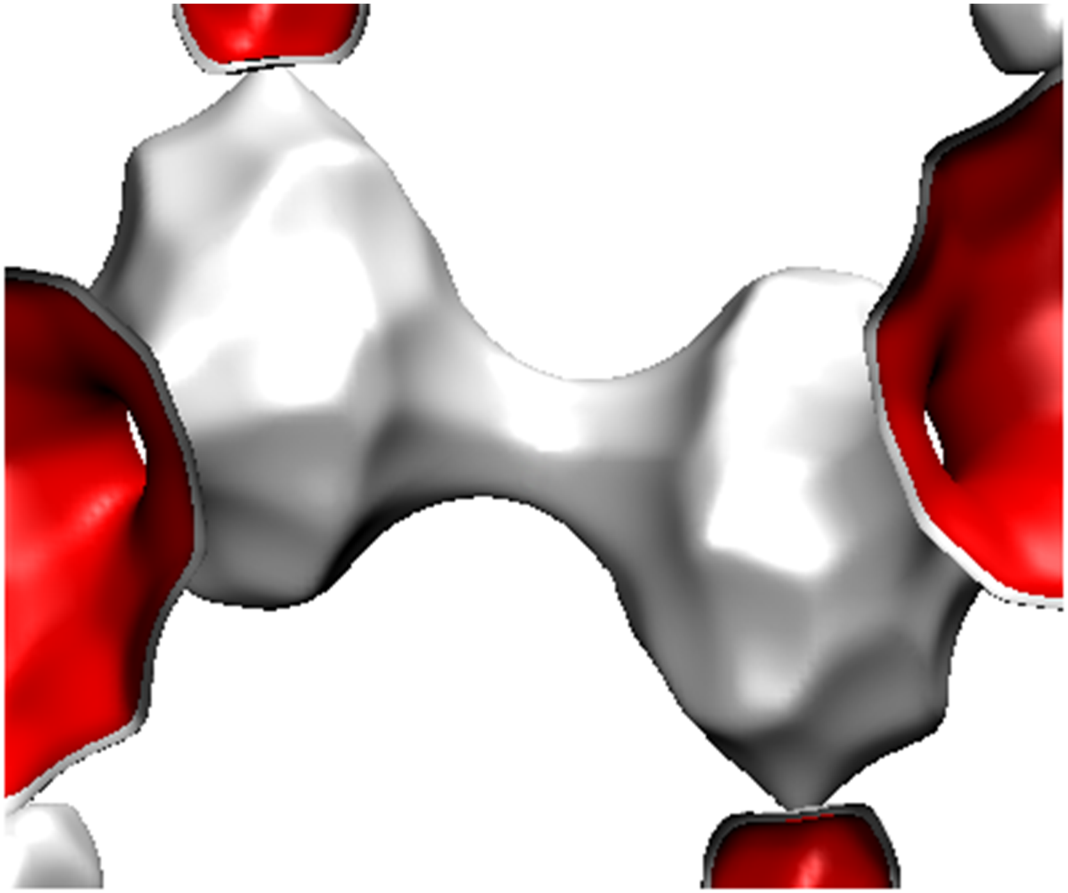

Structural information from: C. Baerlocher, L.B. McCusker, Database of Zeolite Structures, International Zeolite Association, http://www.iza-structure.org/databases/

Figure S13

DDR pore landscapes

To convert from molecules per unit cell to mol kg^{-1}, multiply by 0.06936.
The pore volume is 0.182 cm^3/g.

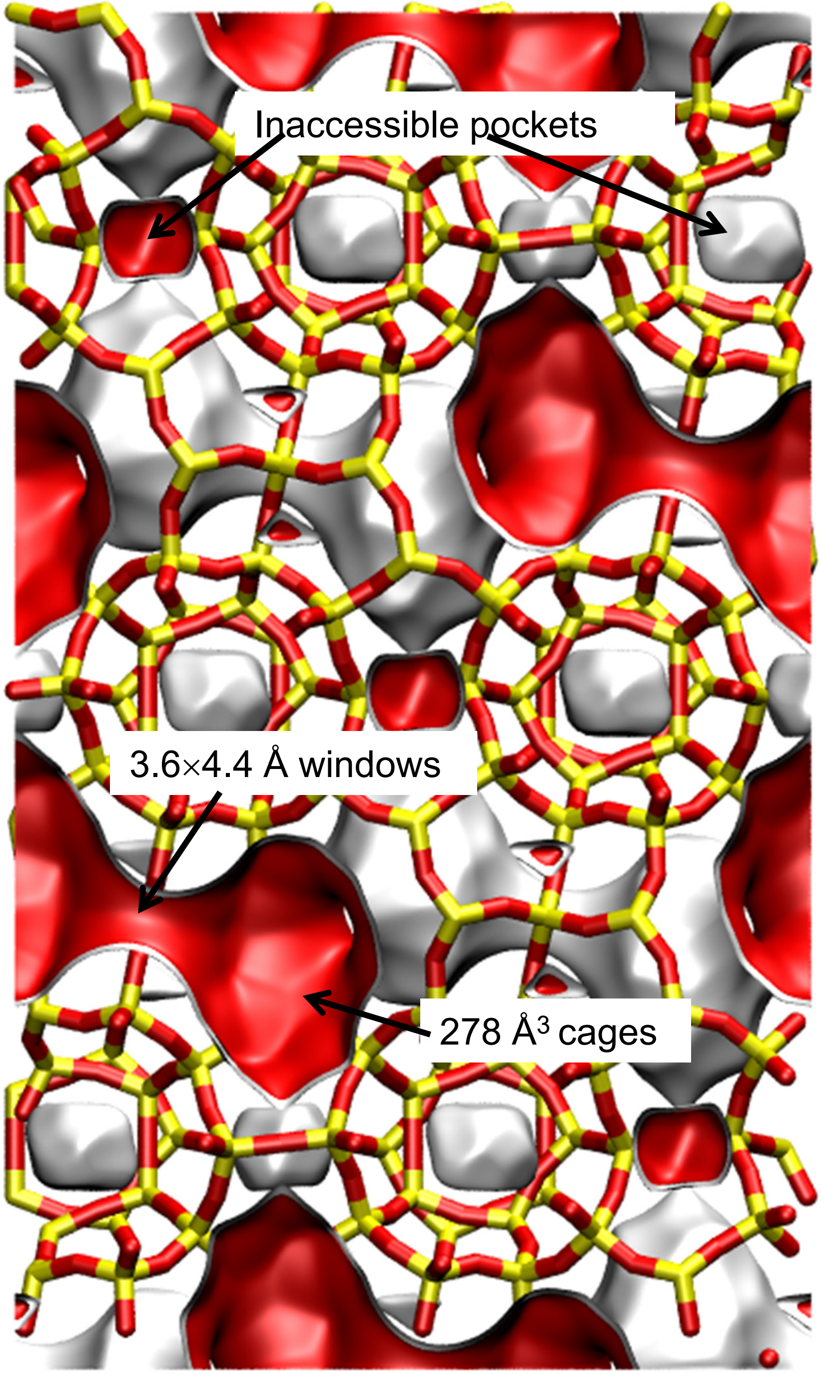

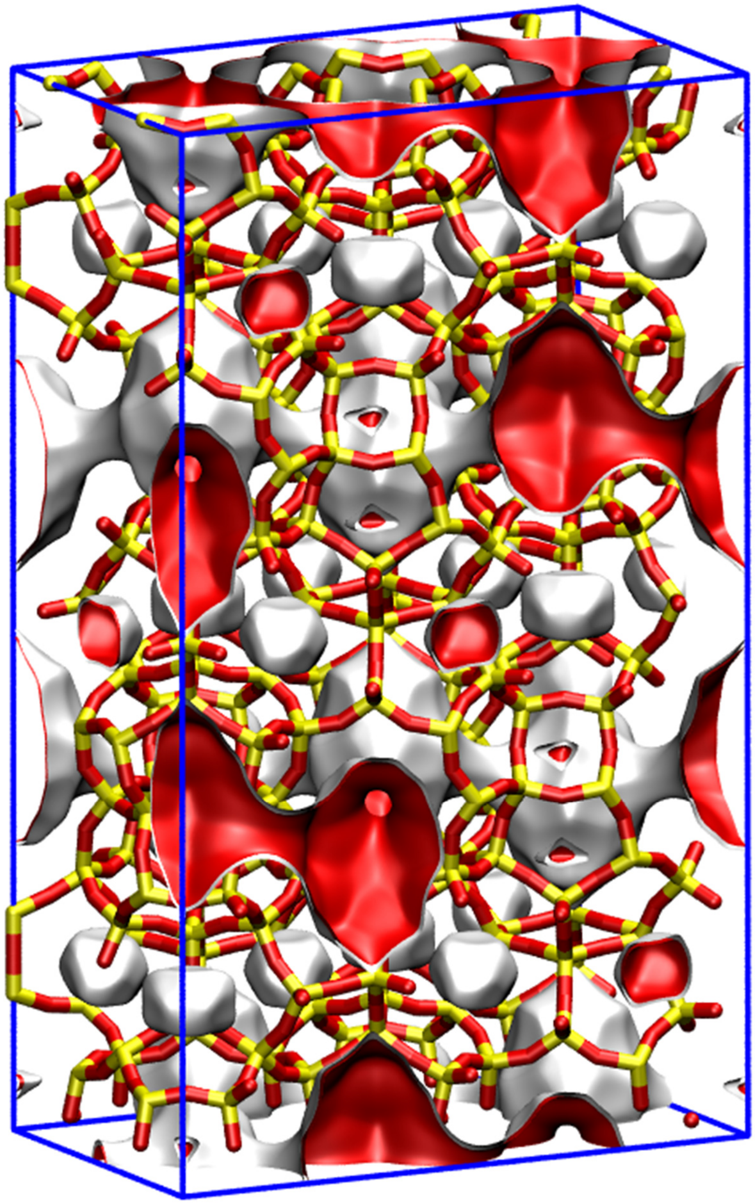

DDR window and pore dimensions

Figure S14

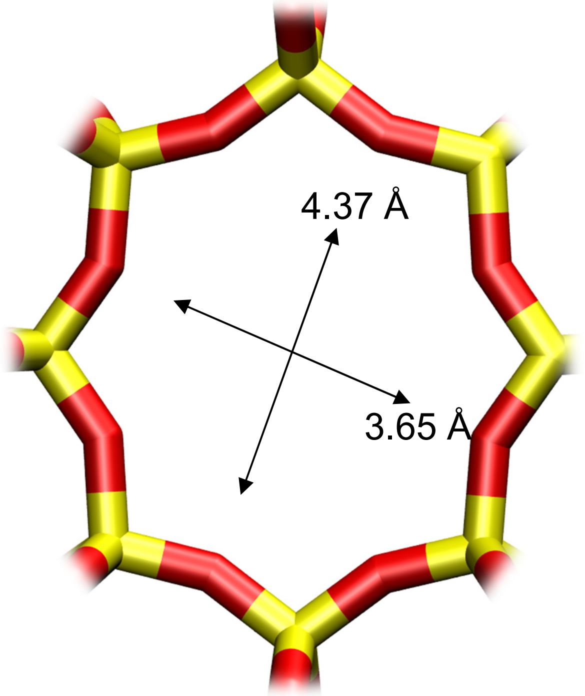

DDR

The window dimensions calculated using the van der Waals diameter of framework atoms = 2.7 Å are indicated above by the arrows.

	DDR
a /Å	24.006
b /Å	13.86
c /Å	40.892
Cell volume / Å^3	13605.72
conversion factor for [molec/uc] to [mol per kg Framework]	0.0693
conversion factor for [molec/uc] to [kmol/m^3]	0.4981
ρ [kg/m3]	1759.991
MW unit cell [g/mol(framework)]	14420.35
ϕ, fractional pore volume	0.245
open space / Å^3/uc	3333.5
Pore volume / cm^3/g	0.139
Surface area /m^2/g	350.0
DeLaunay diameter /Å	3.65

DDR molecular dimension

Figure S15

CO$_2$ is a pencil-like molecule. It hops lengthwise across the narrow windows.

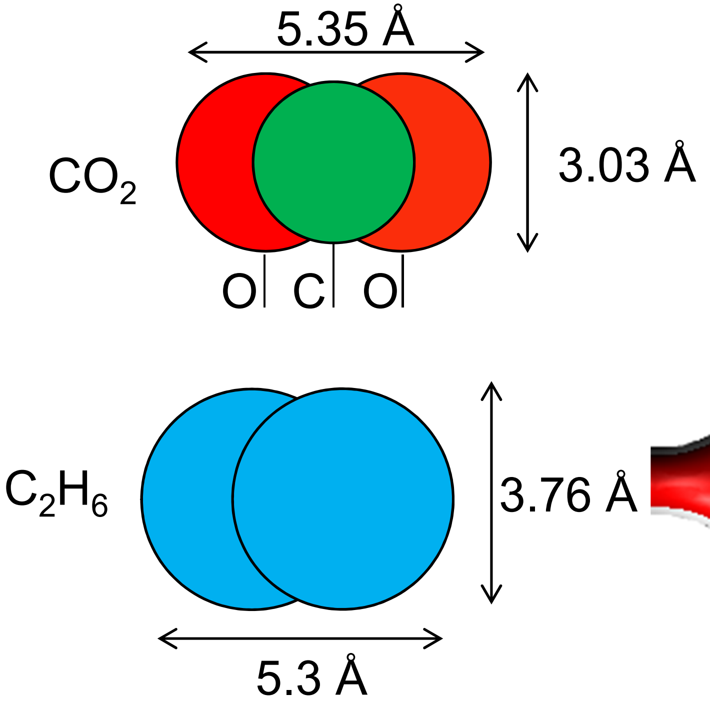

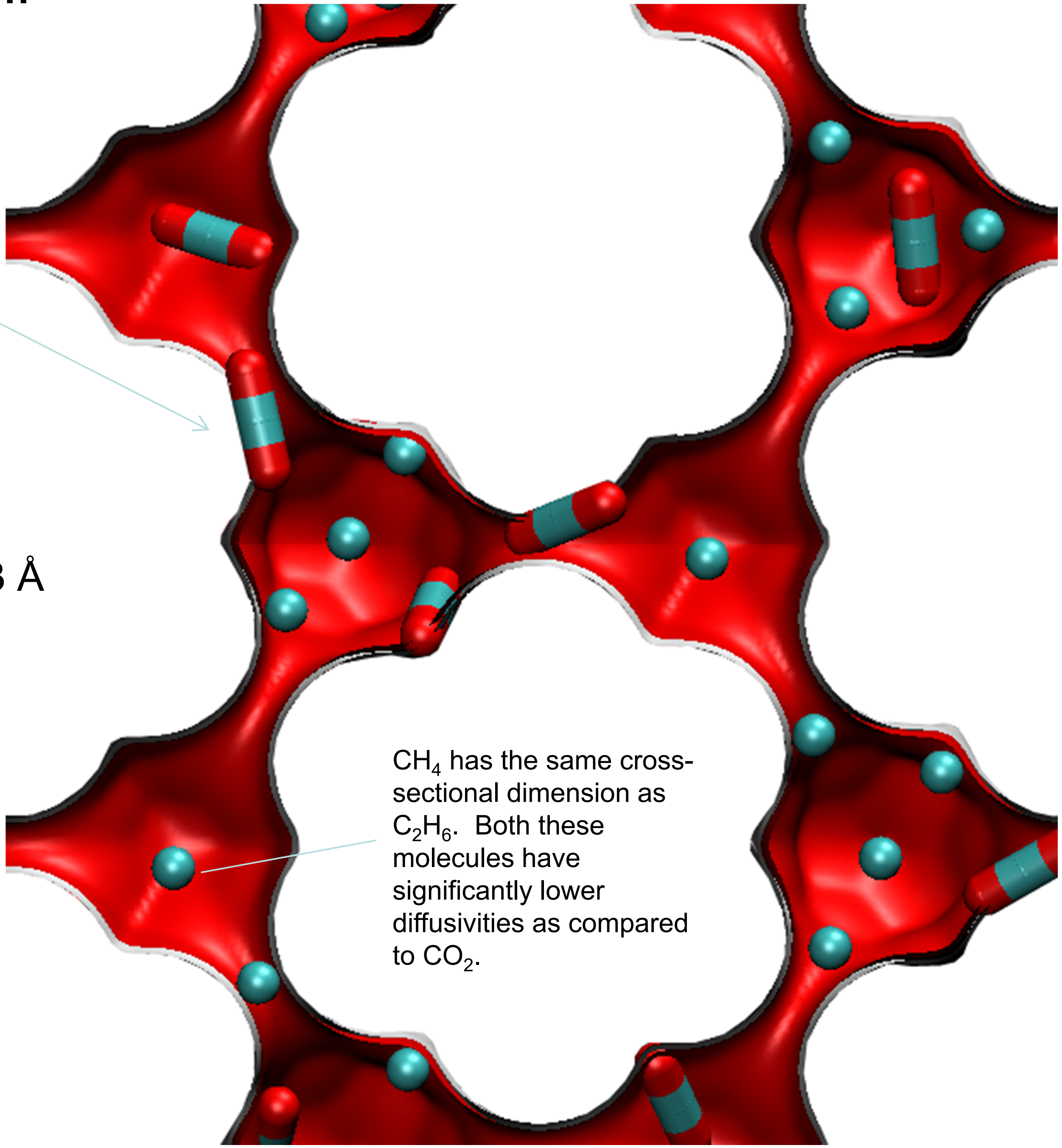

CH$_4$ has the same cross-sectional dimension as C$_2$H$_6$. Both these molecules have significantly lower diffusivities as compared to CO$_2$.

Figure S16

Unary isotherms

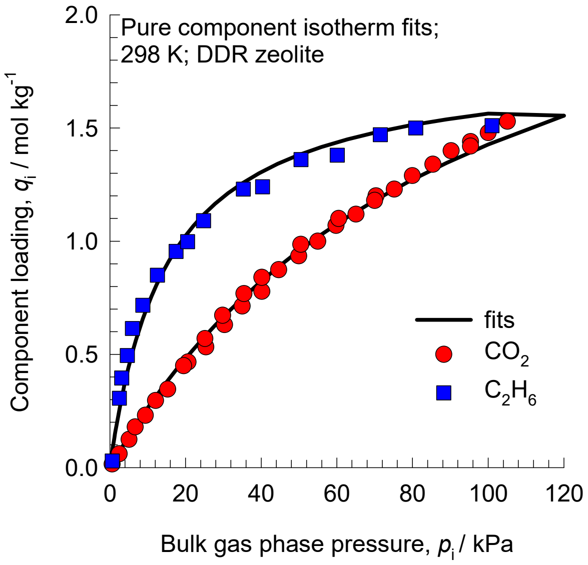

Figure S17

Mixture adsorption equilibrium

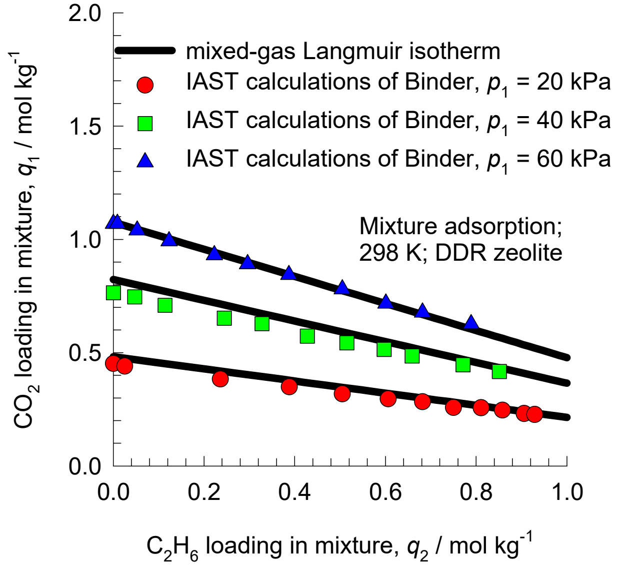

Figure S18

Matrix of thermodynamic factors

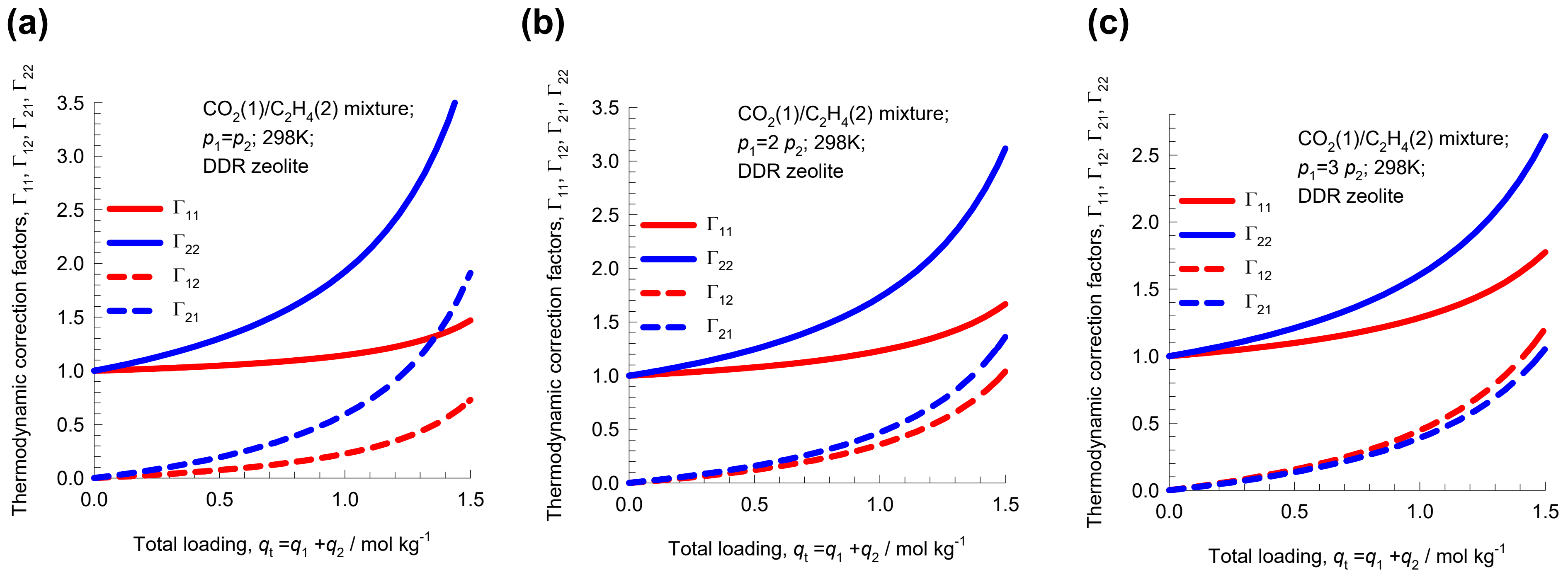

Figure S19

Significance of thermodynamic coupling

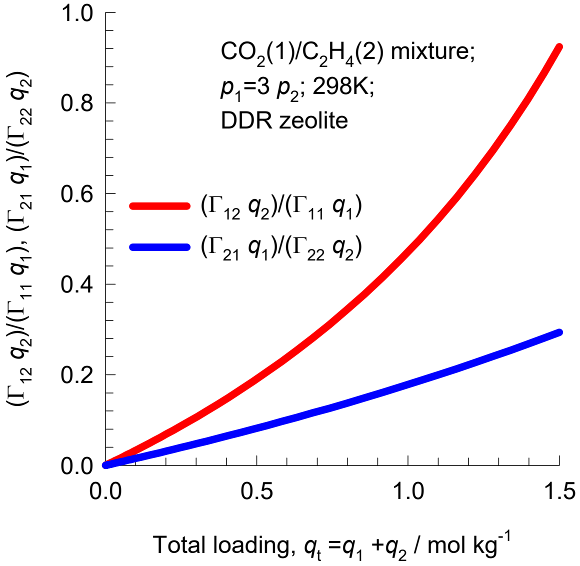

Figure S20

Crystal geometry

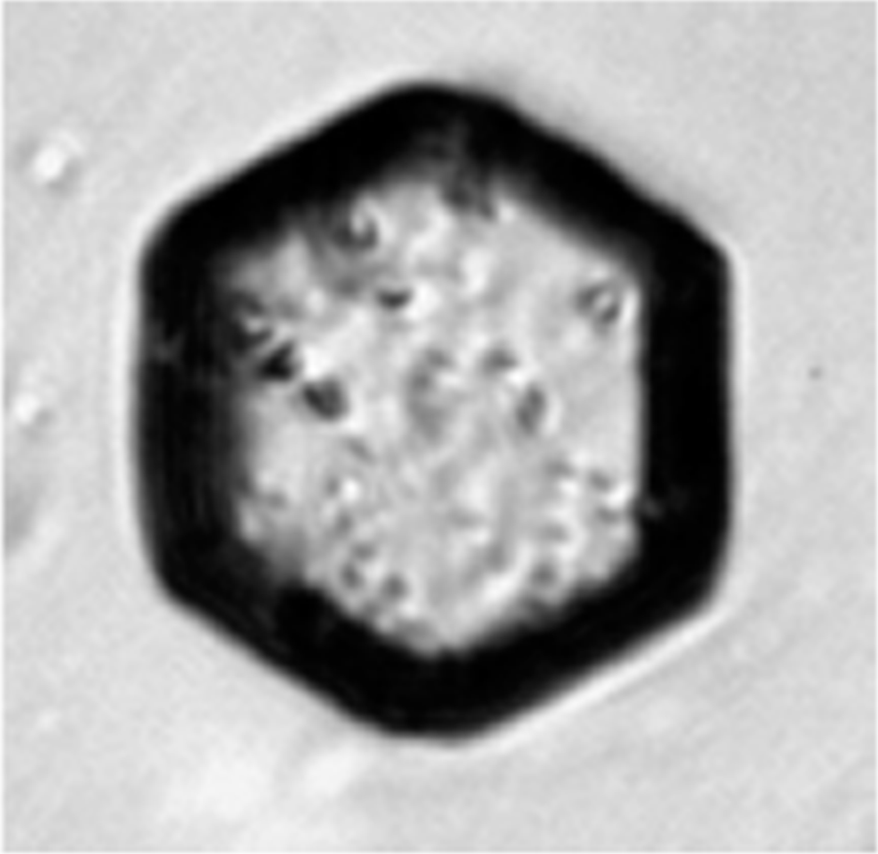

Hexagonal crystal used in experiments

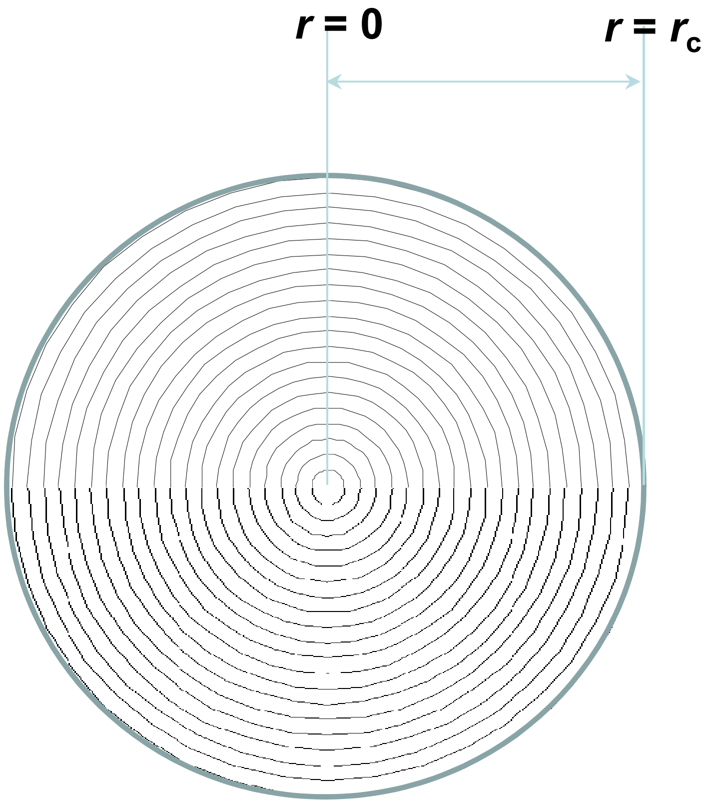

Spherical crystal model

Figure S21

Diffusivities

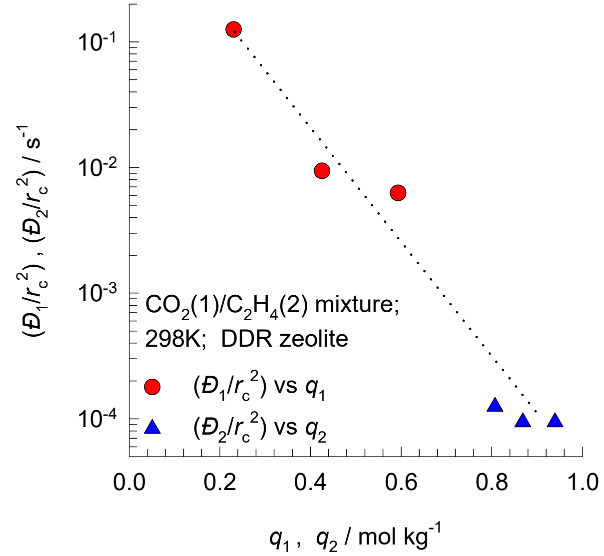

1:1 CO_2/C_2H_6 time-averaged uptake in DDR

Figure S22

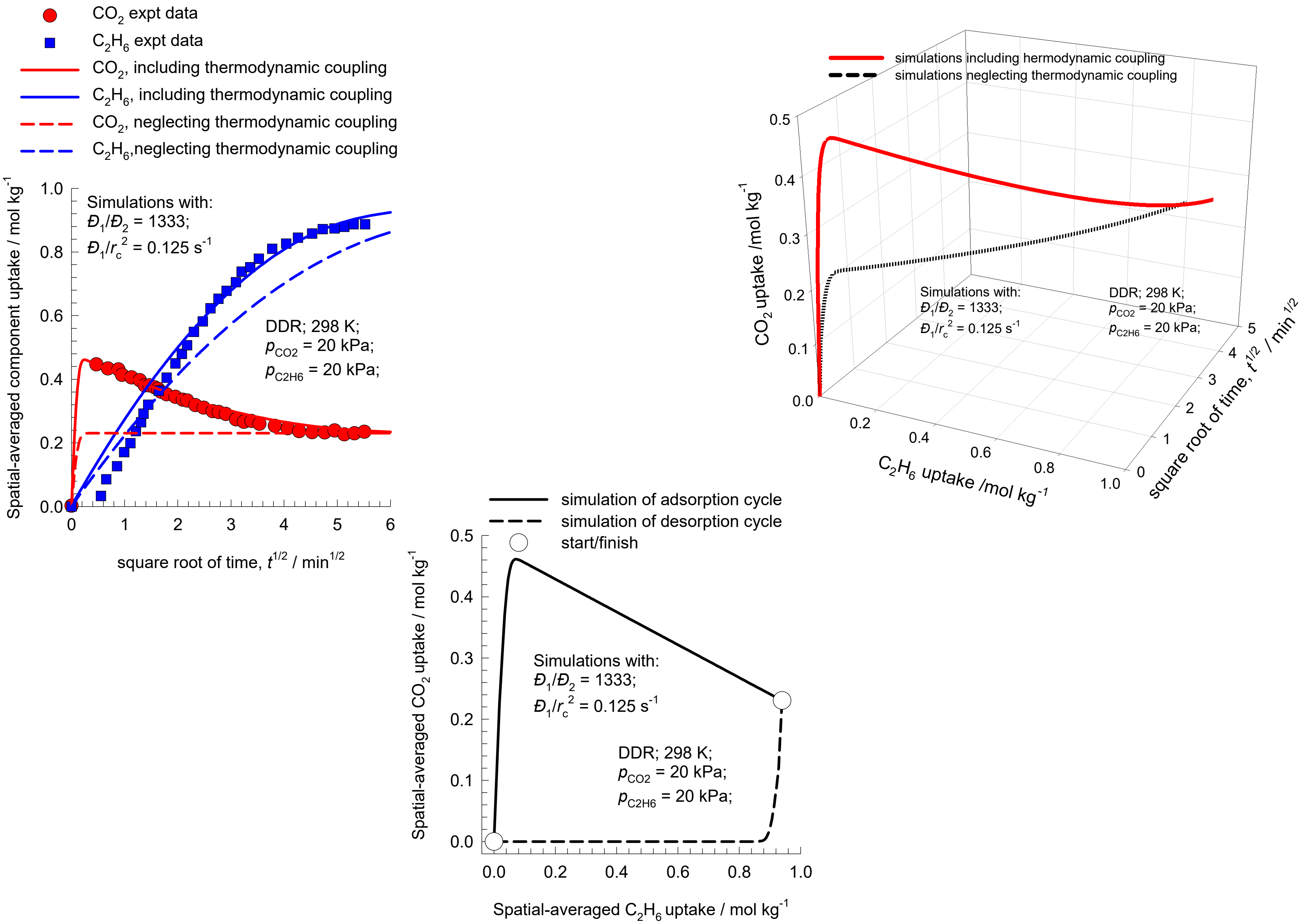

2:1 CO_2/C_2H_6 uptake in DDR

Figure S23

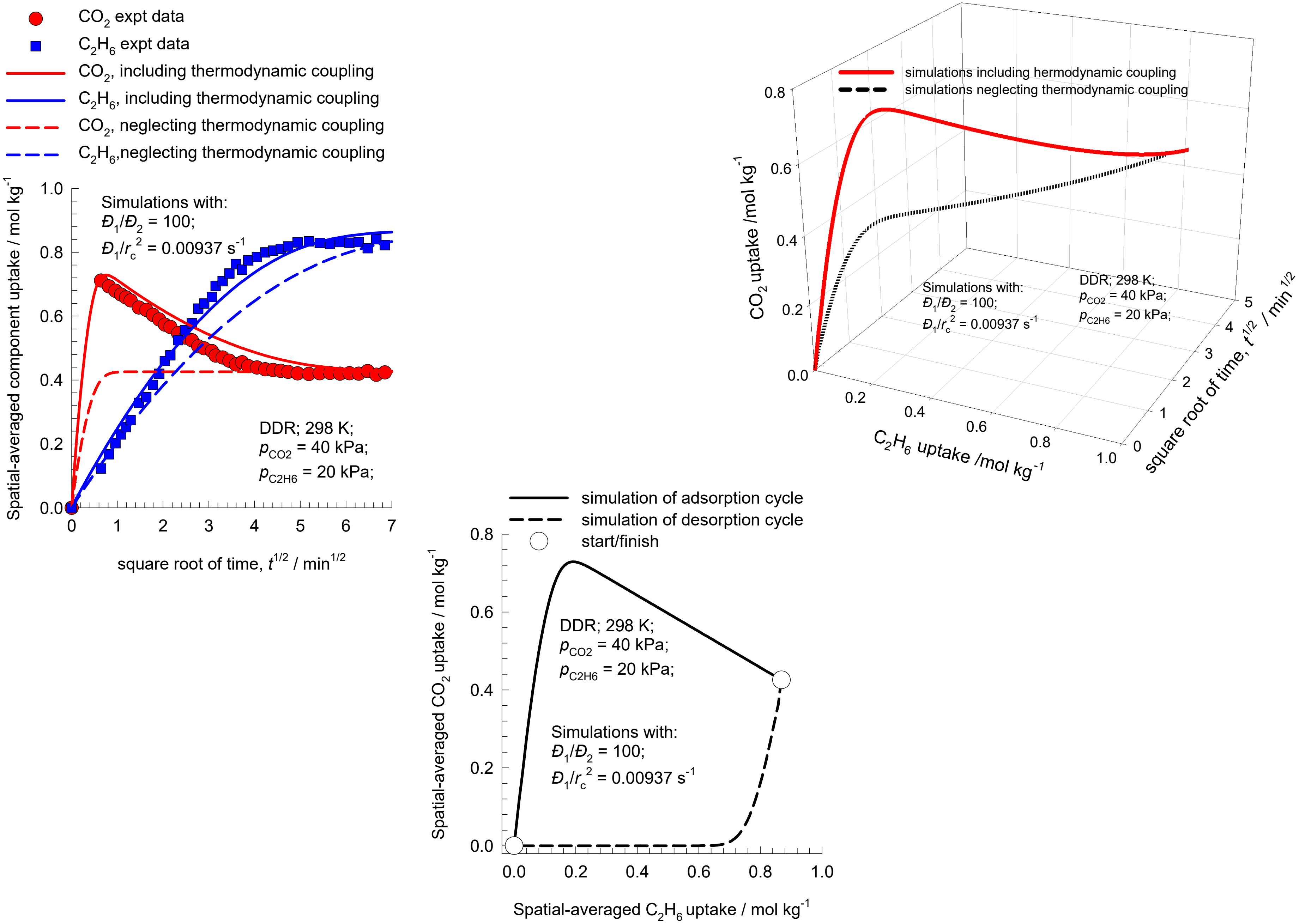

3:1 CO_2/C_2H_6 uptake in DDR

Figure S24

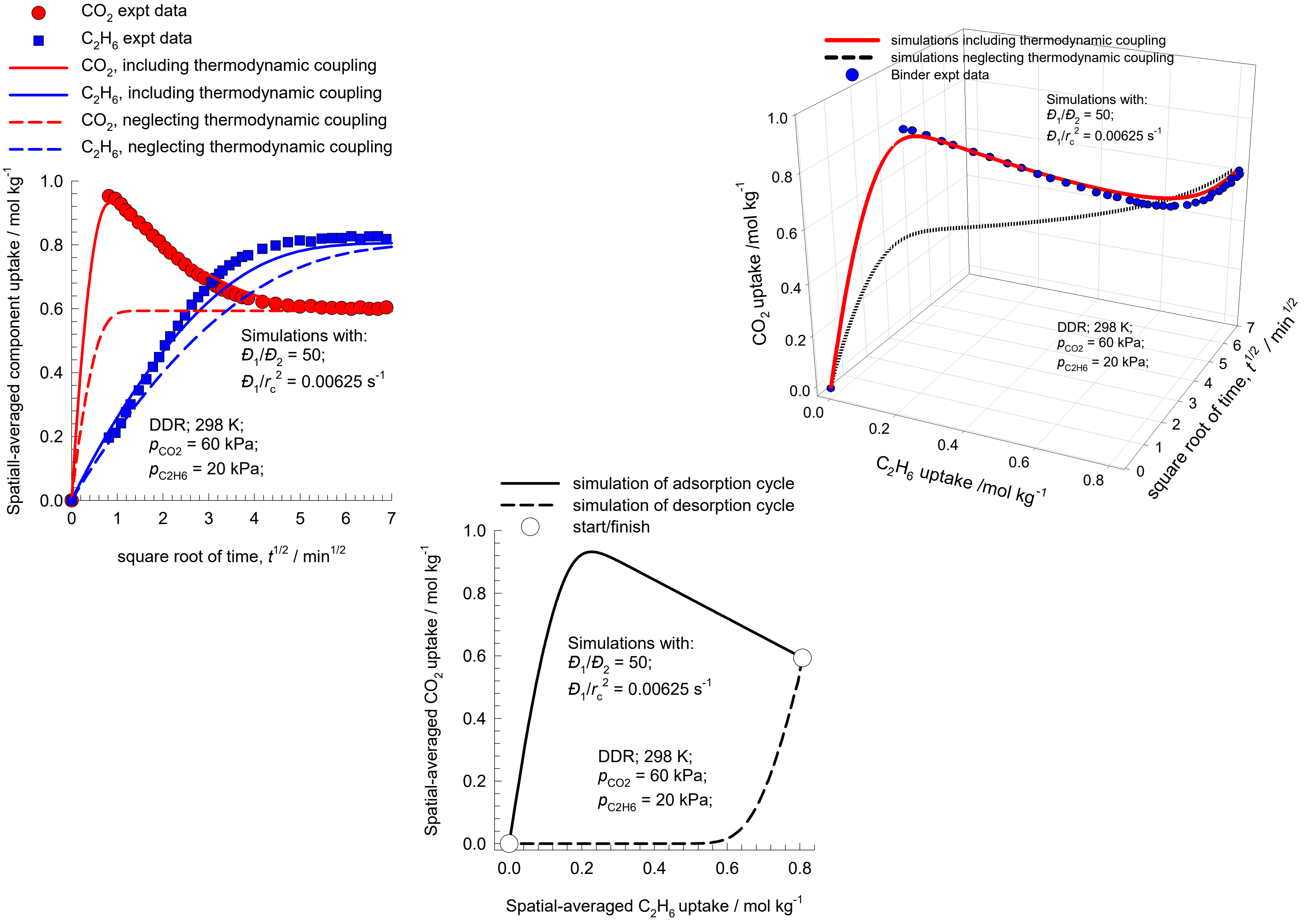

1:1 CO_2/C_2H_6 transient development of loadings in DDR crystal

Figure S25

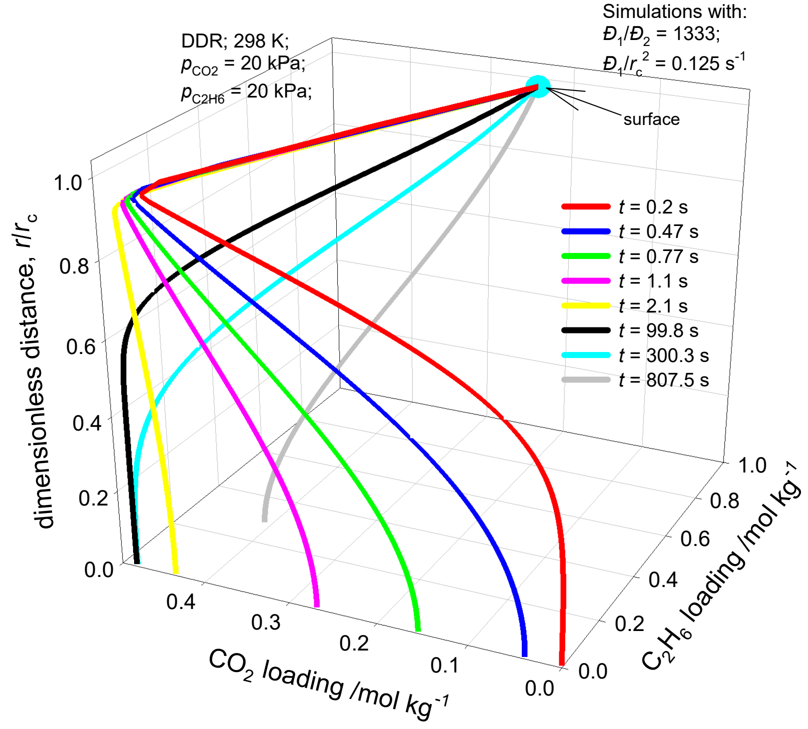

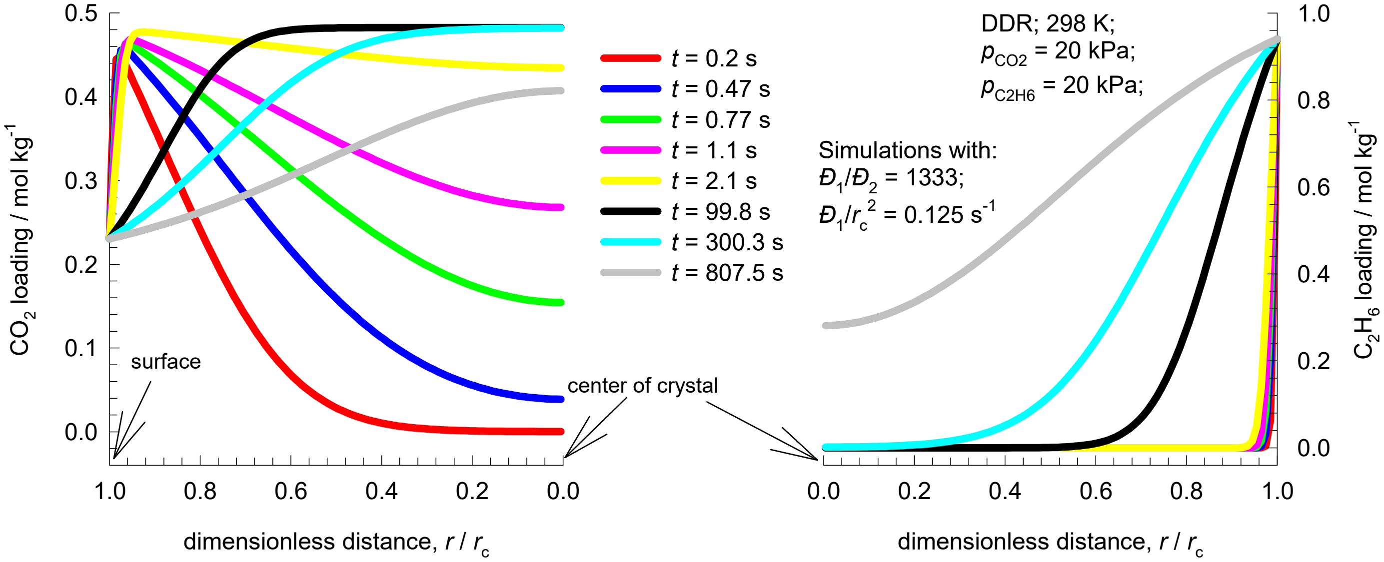

2:1 CO_2/C_2H_6 transient development of loadings in DDR crystal

Figure S26

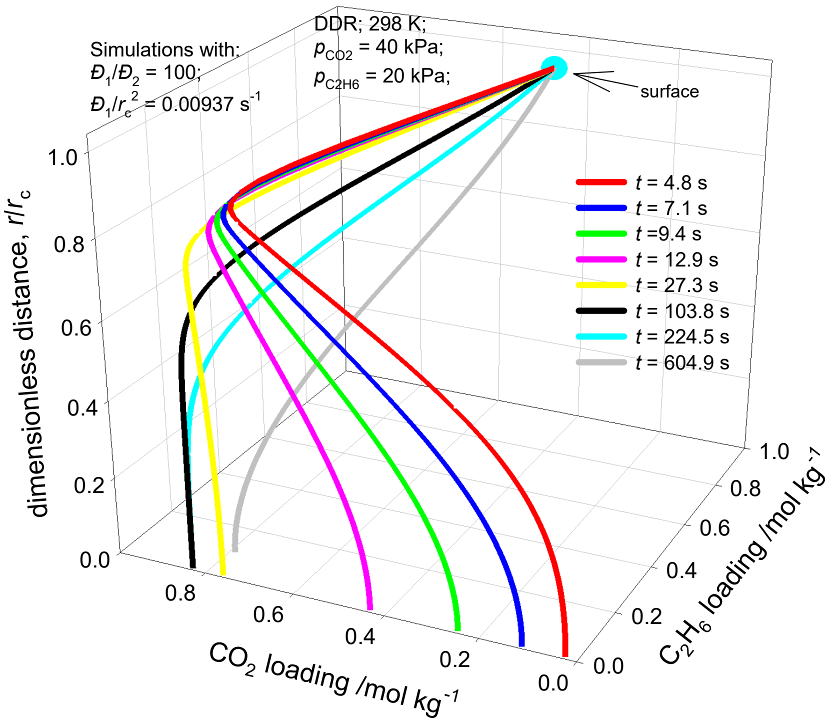

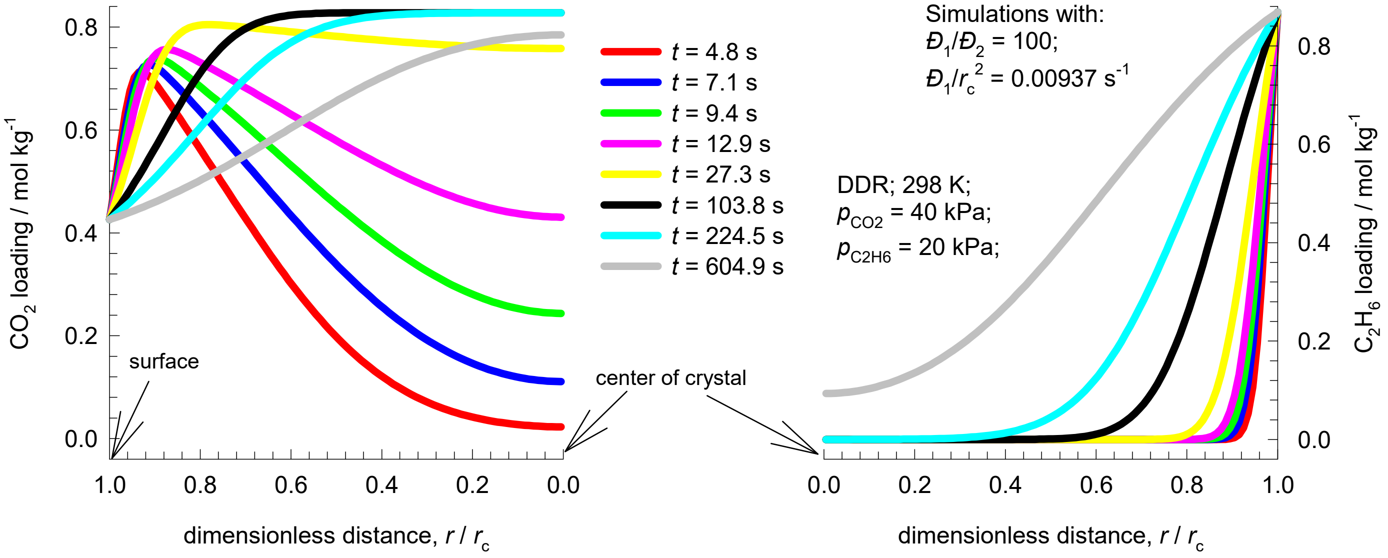

3:1 CO_2/C_2H_6 transient development of loadings in DDR crystal

Figure S27

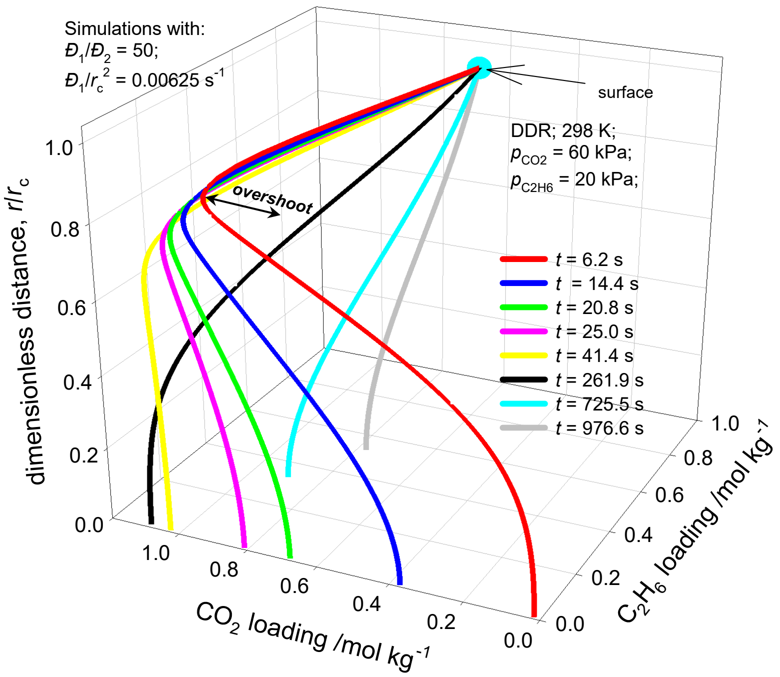

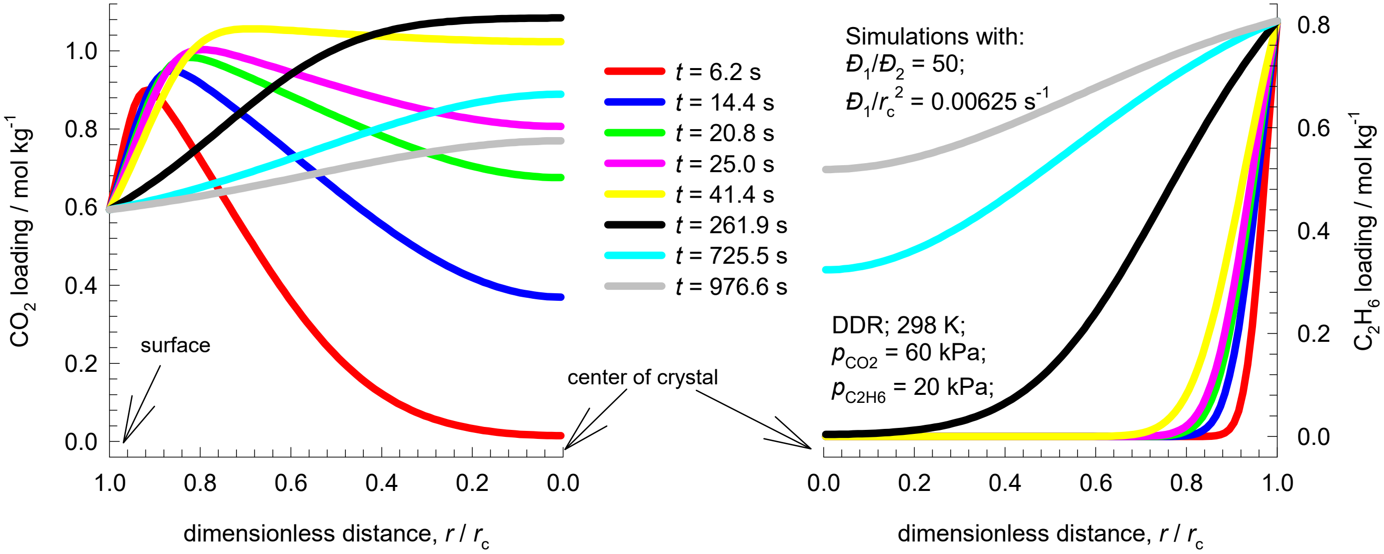

Figure S28

2:1 CO_2/C_2H_6 transient development of “corrected” loadings in DDR crystal

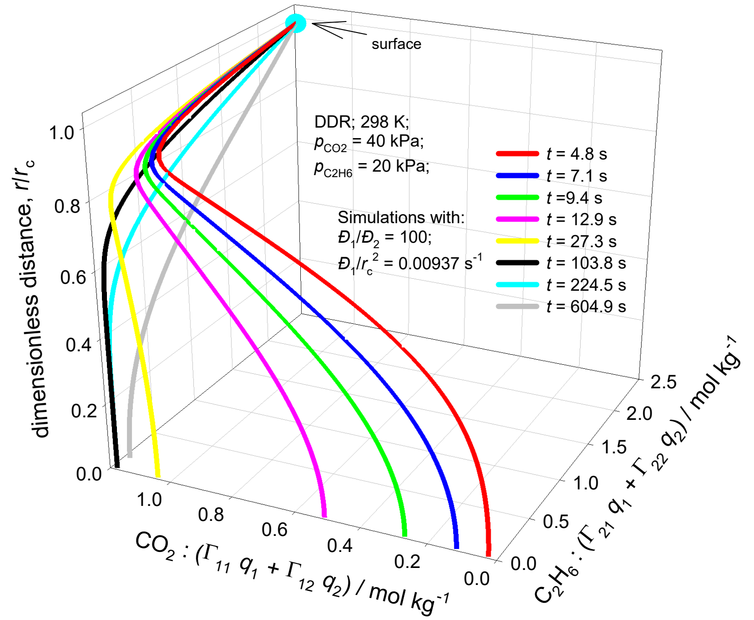

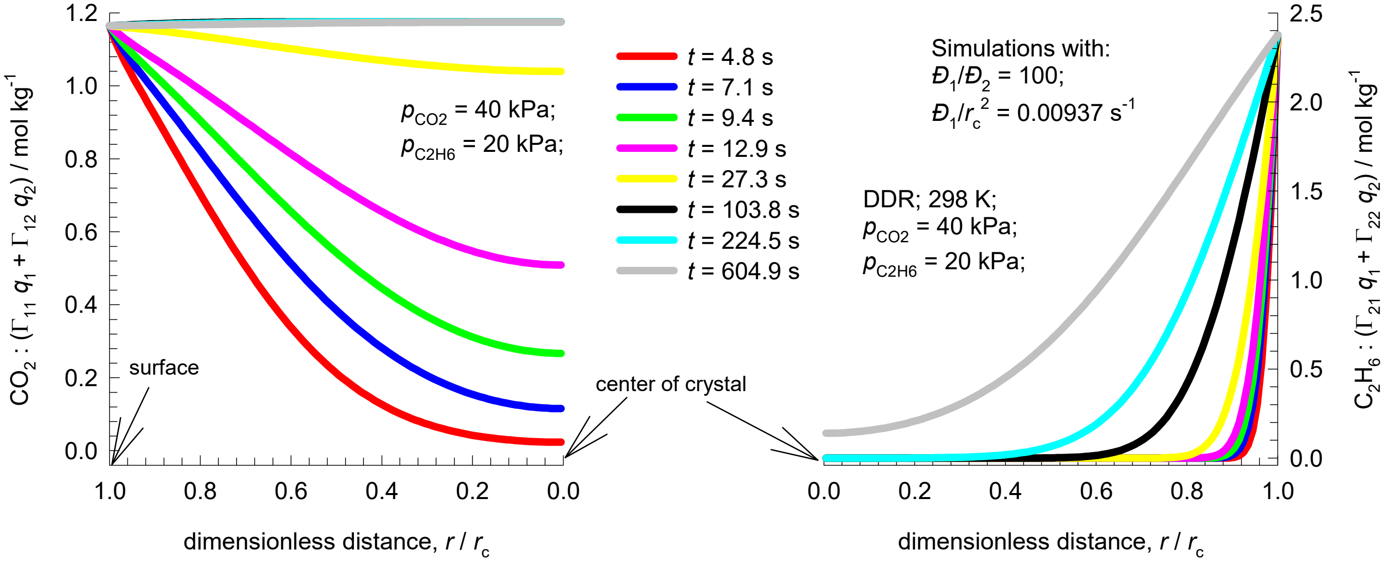

Figure S29

3:1 CO_2/C_2H_6 transient development of “corrected” loadings in DDR crystal

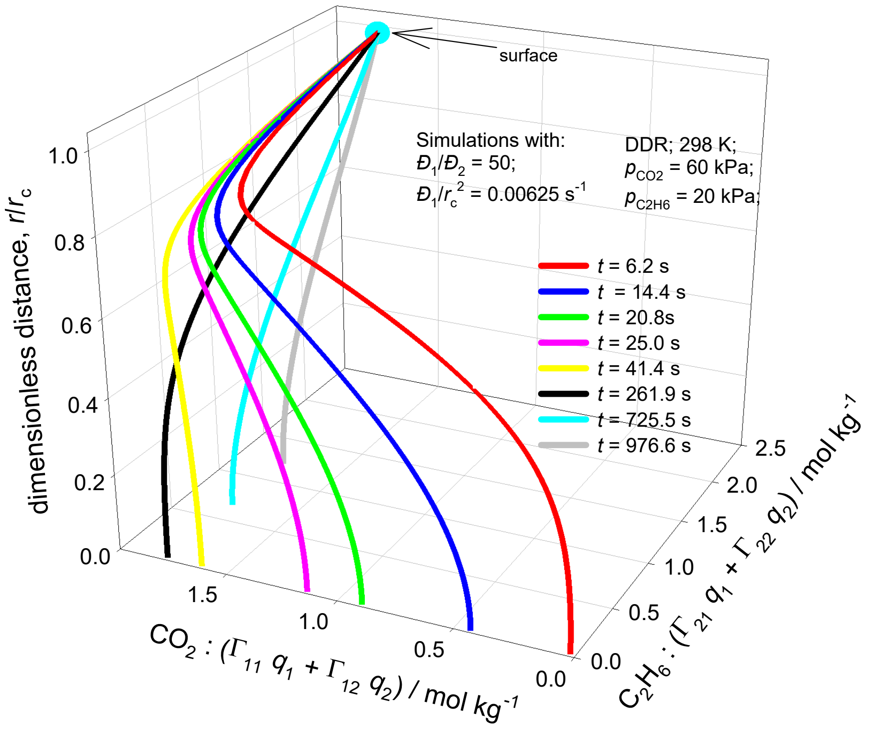

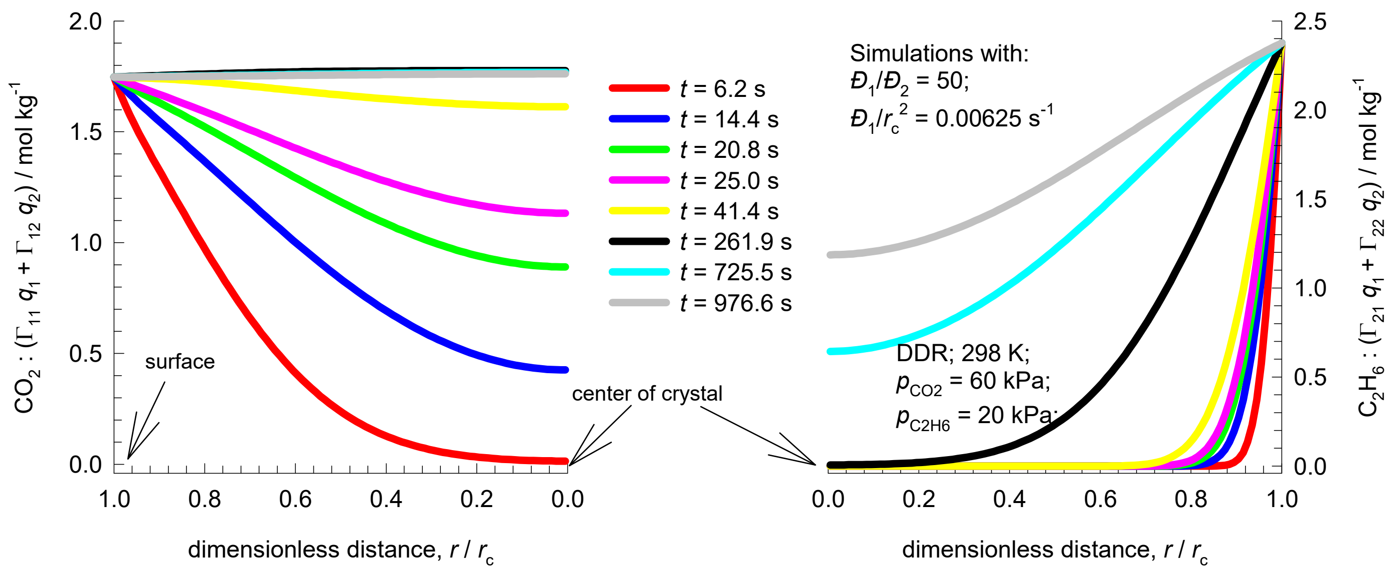

Figure S30

3:1 CO_2/C_2H_6 transient development of chemical potentials within DDR crystal

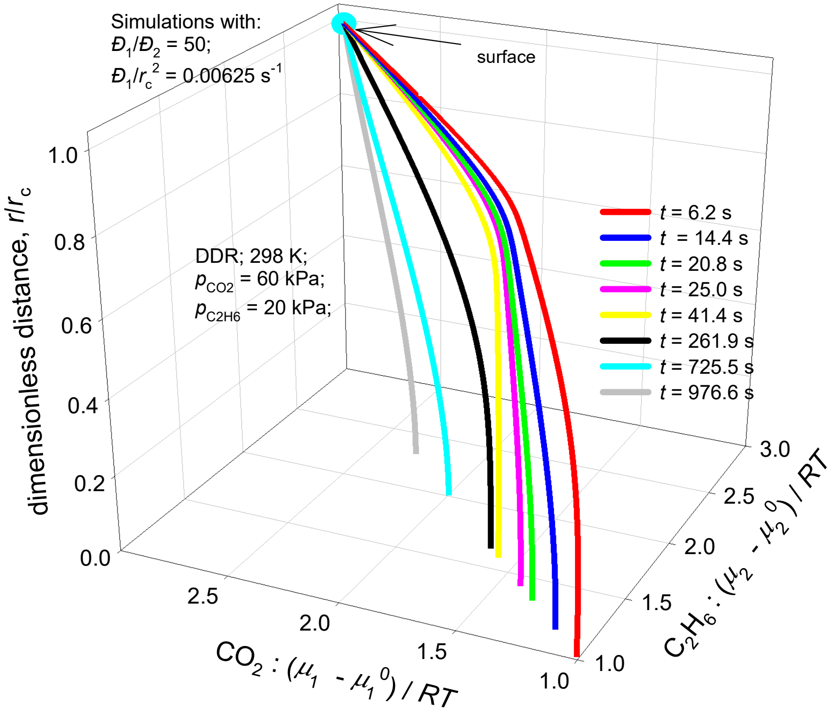

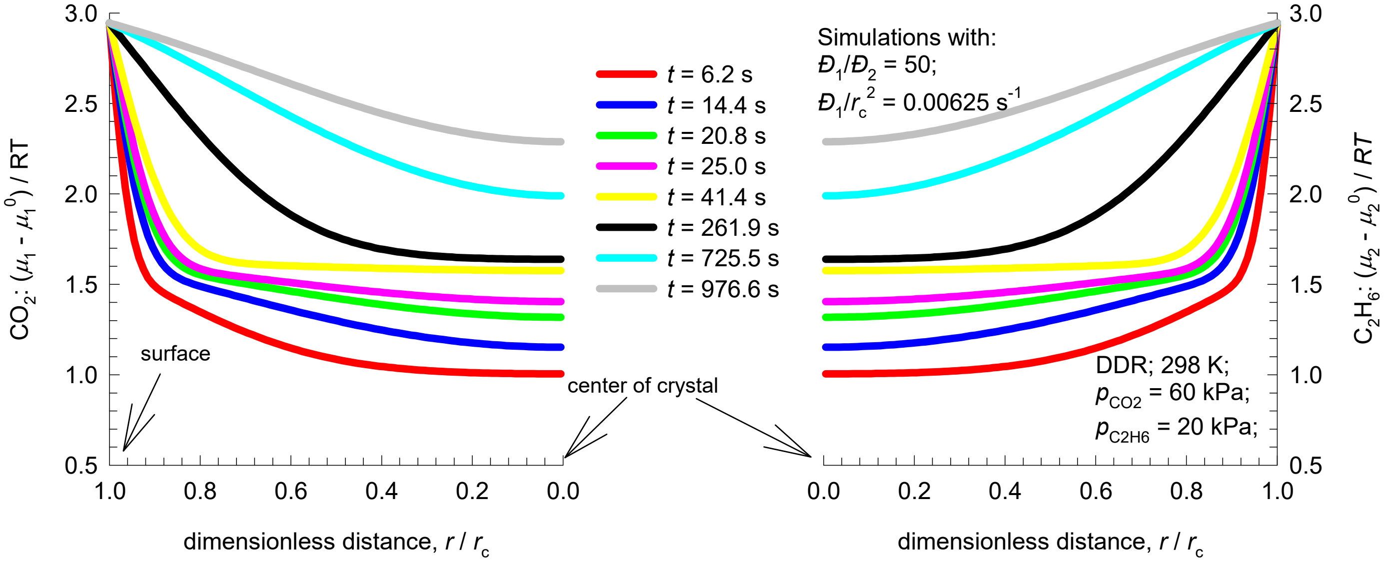

Figure S31

2:1 CO_2/C_2H_6 transient development of loadings in DDR crystal:

Experimental data

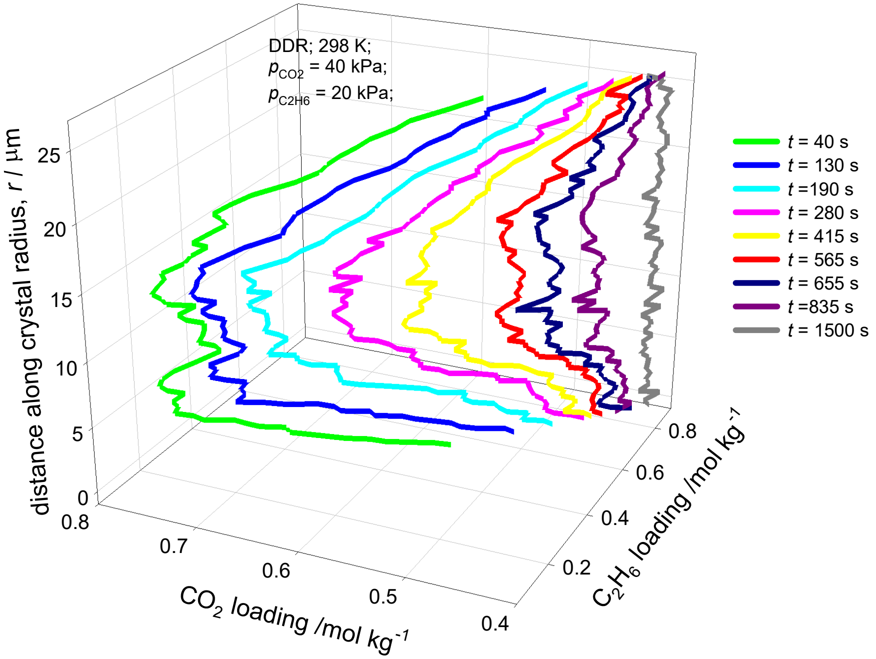

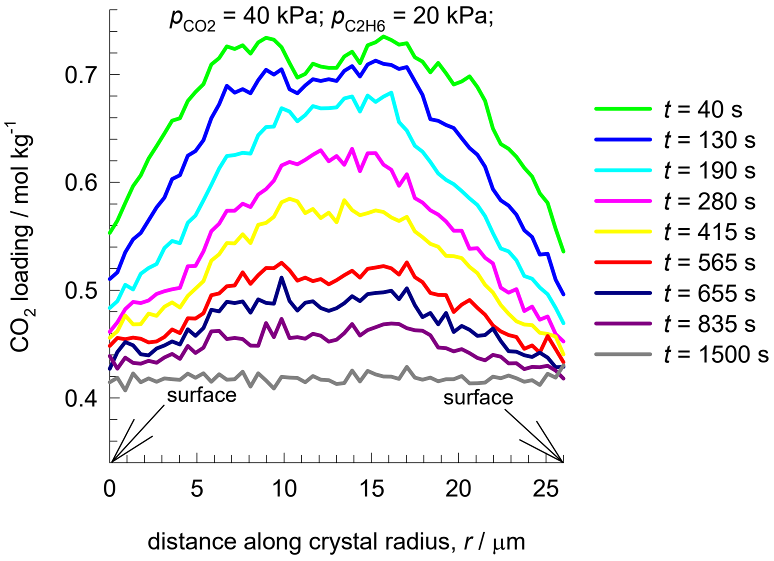

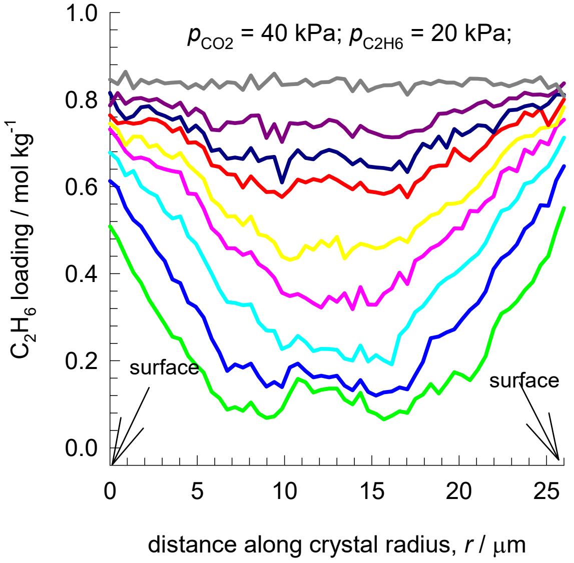

2:1 CO_2/C_2H_6 transient development of “corrected” loadings in DDR crystal:

Experimental data

Figure S32

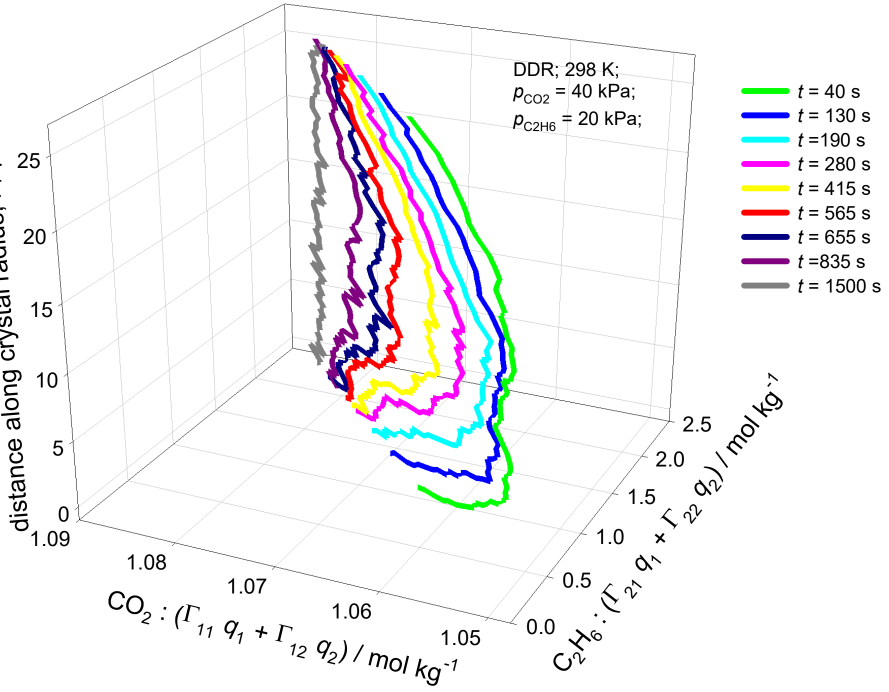

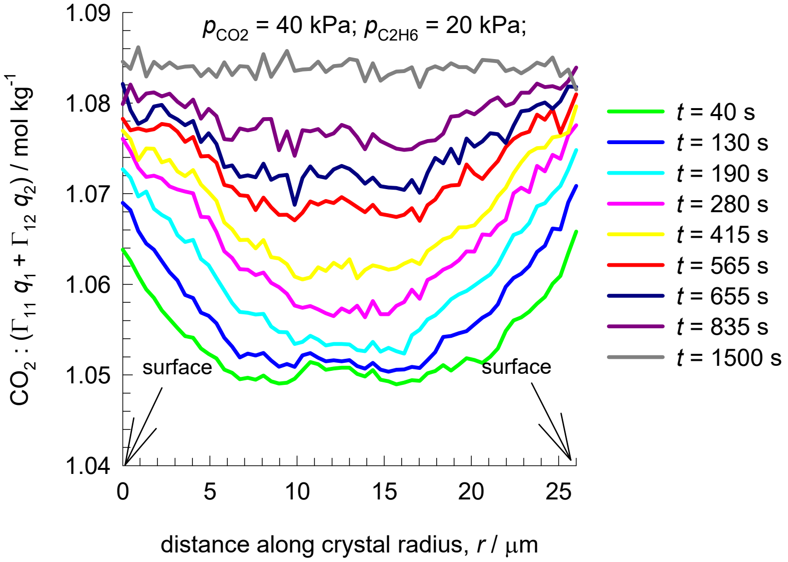

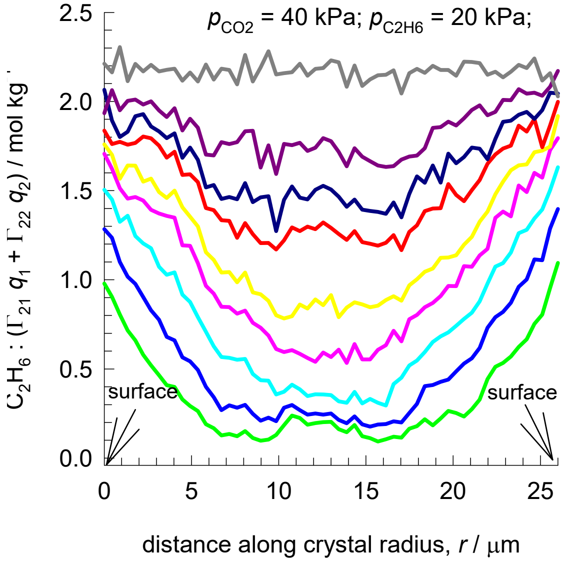

Figure S33

Transient breakthrough in DDR fixed bed

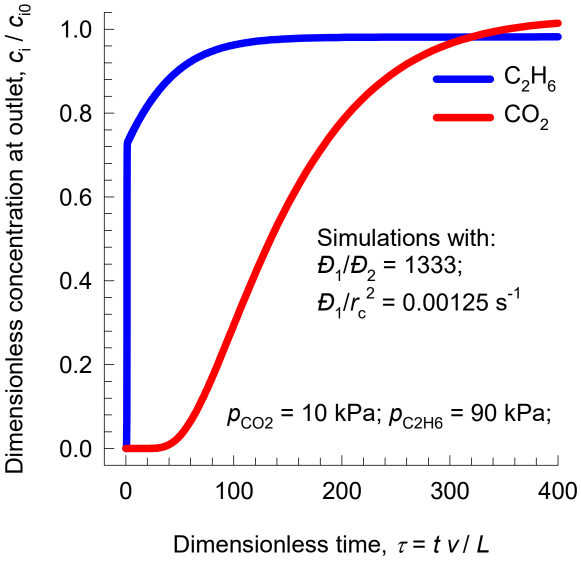

Simulations with:
$Đ_1/Đ_2 = 1333$;
$Đ_1/r_c^2 = 0.00125\ s^{-1}$

$p_{CO2} = 10$ kPa; $p_{C2H6} = 90$ kPa;

LTA-4A

To convert from molecules per unit cell to mol kg^{-1}, multiply by 0.0733.
The pore volume is 0.245 cm^3/g.

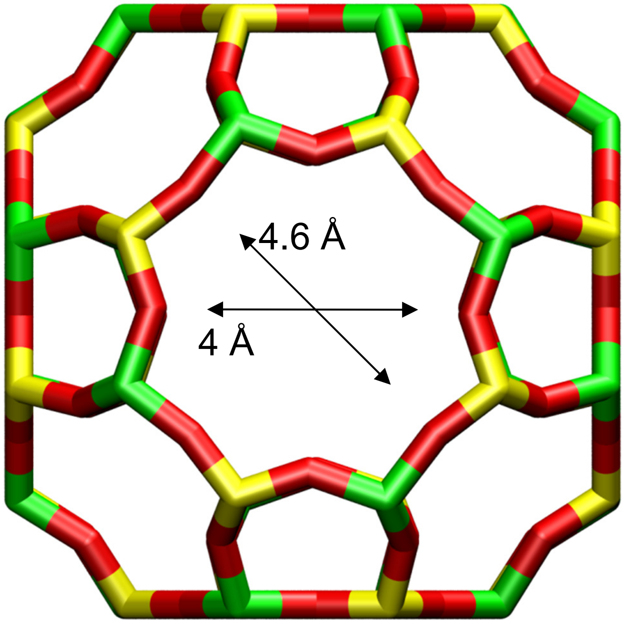

LTA-4A (96 Na+)

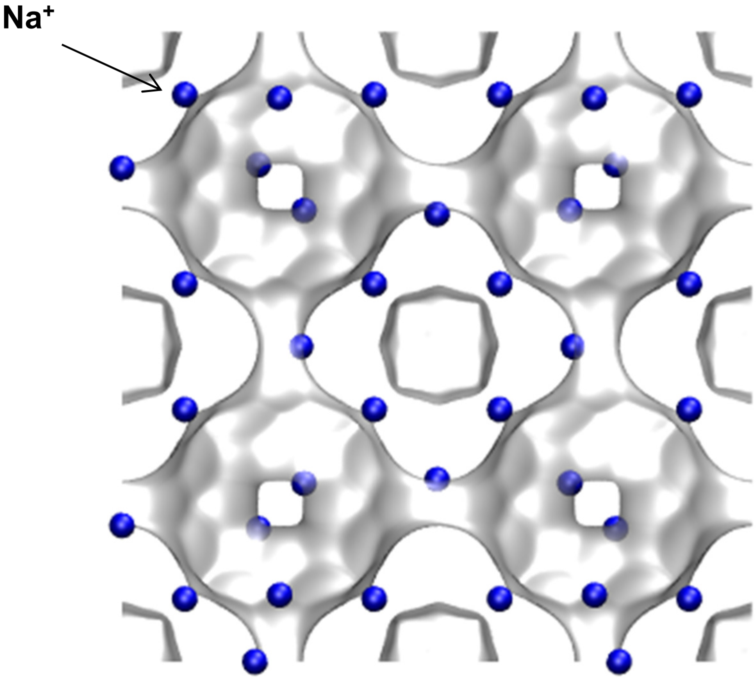

LTA-4A

The window dimension calculated using the van der Waals diameter of framework atoms = 2.7 Å is indicated above by the arrow. The pore landscape is also shown in the above picture.

Note that the Na$^+$ ions partially block the windows and therefore the diffusivities in LTA-4A are significantly lower than that for all-silica LTA.

N_2/CH_4 mixture uptake in LTA-4A

Figure S35

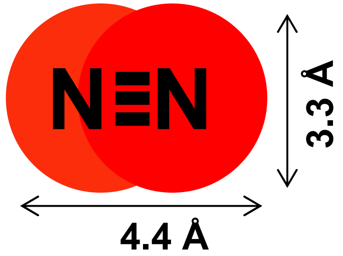

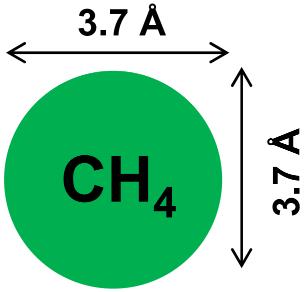

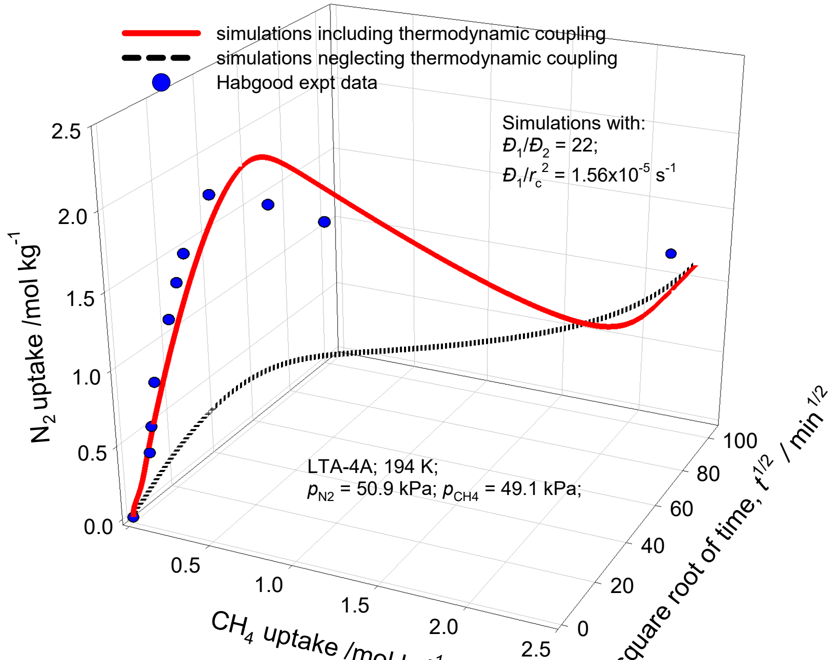

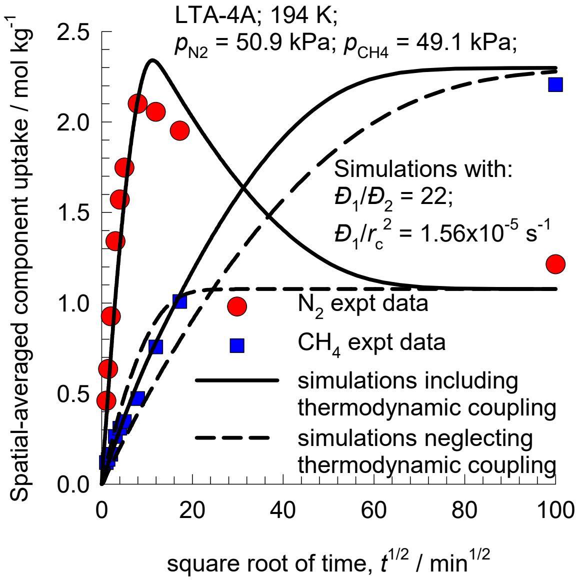

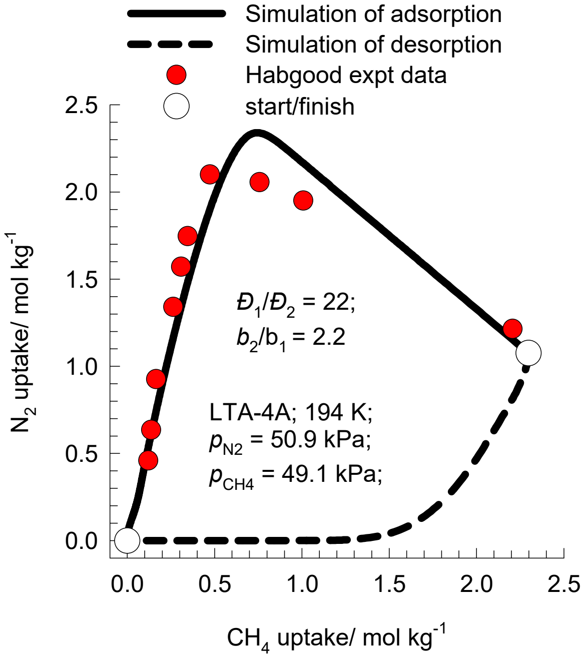

Transient development of loadings in LTA-4A crystal

Figure S36

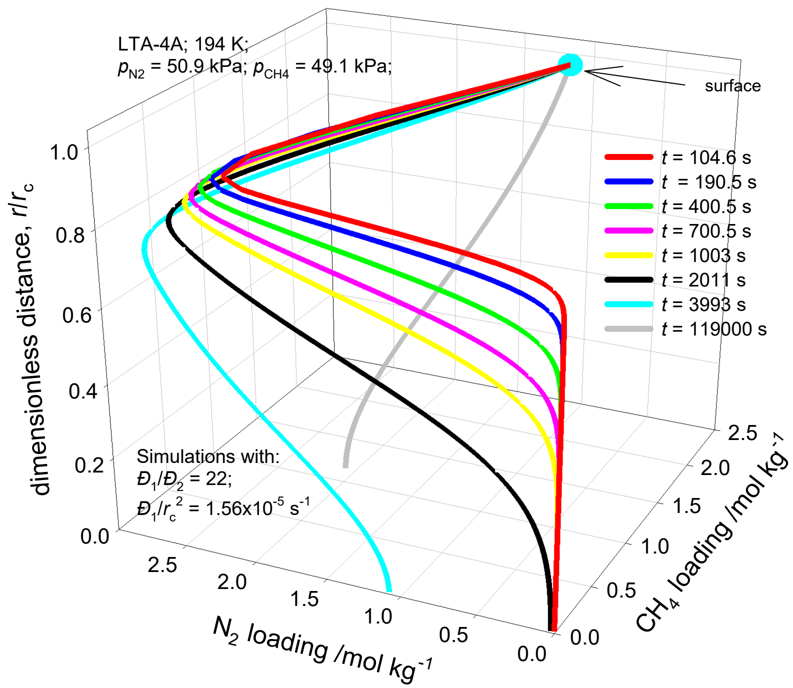

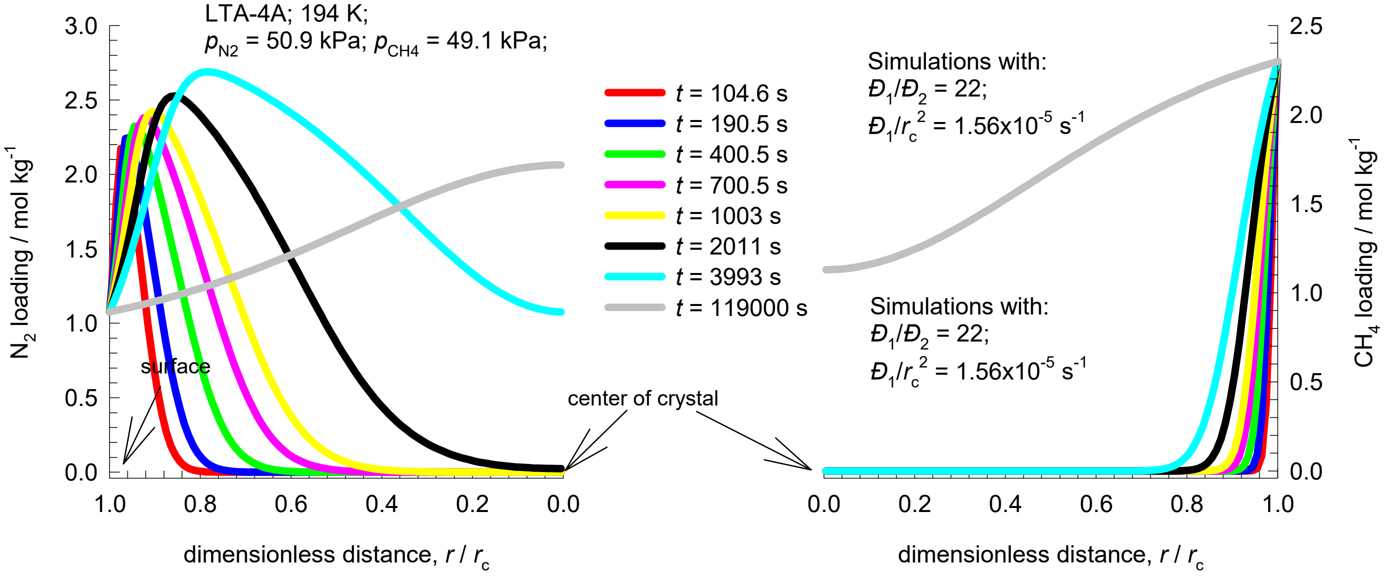

Transient development of “corrected” loadings in LTA-4A crystal

Figure S37

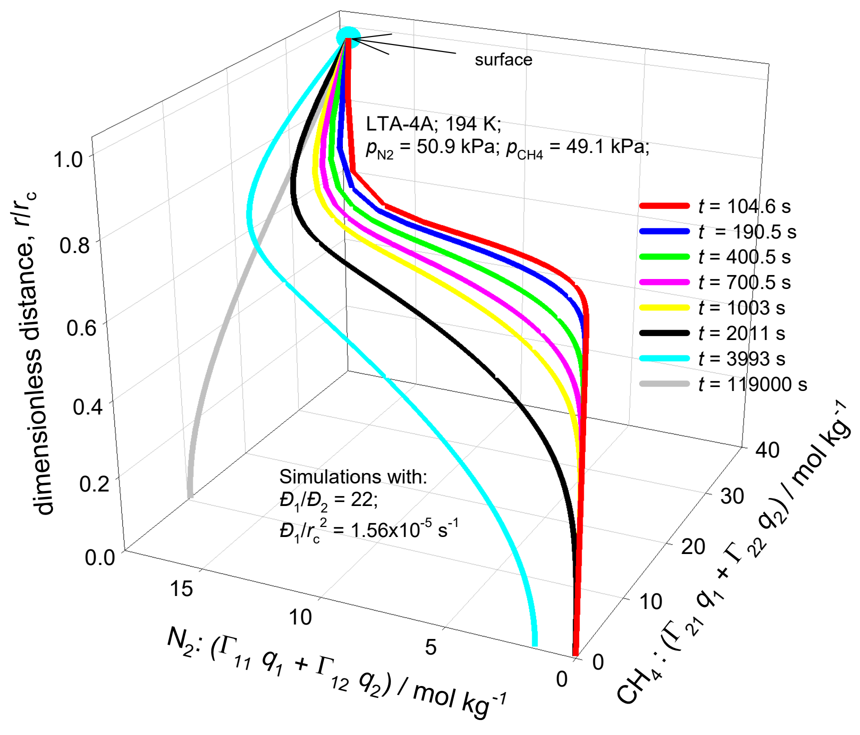

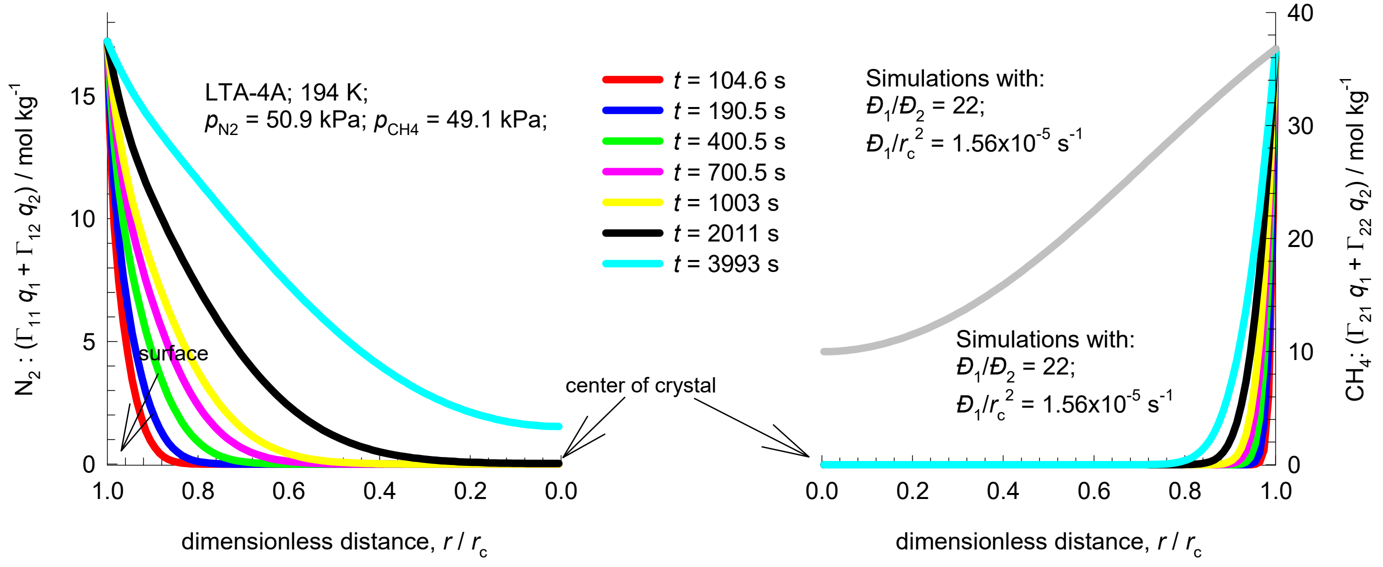

Transient uptake of O_2/N_2 in CMS

Figure S38

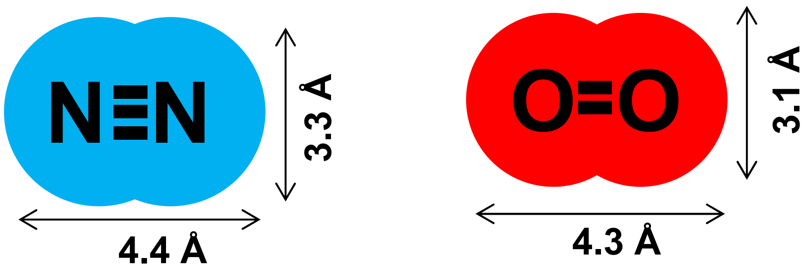

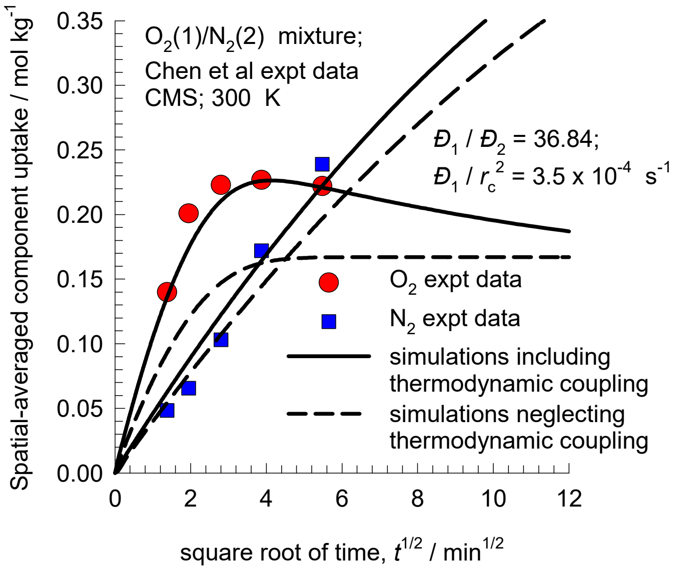

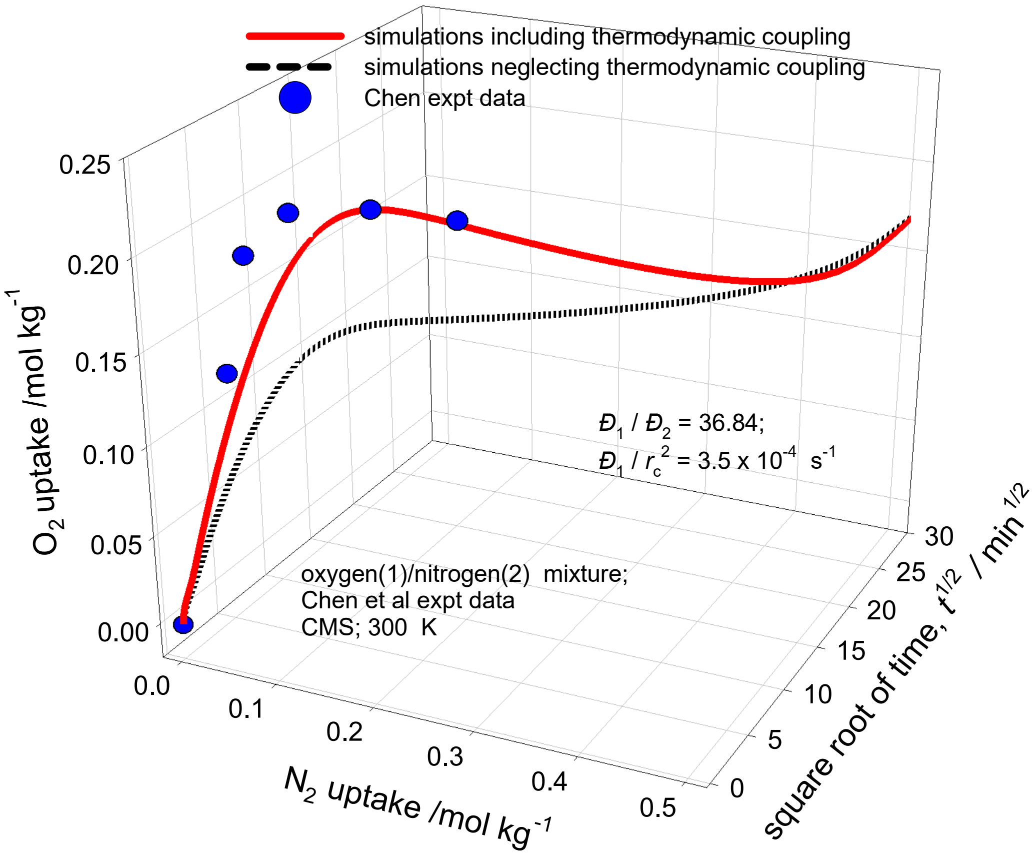

Transient development of loadings in CMS particle

Figure S39

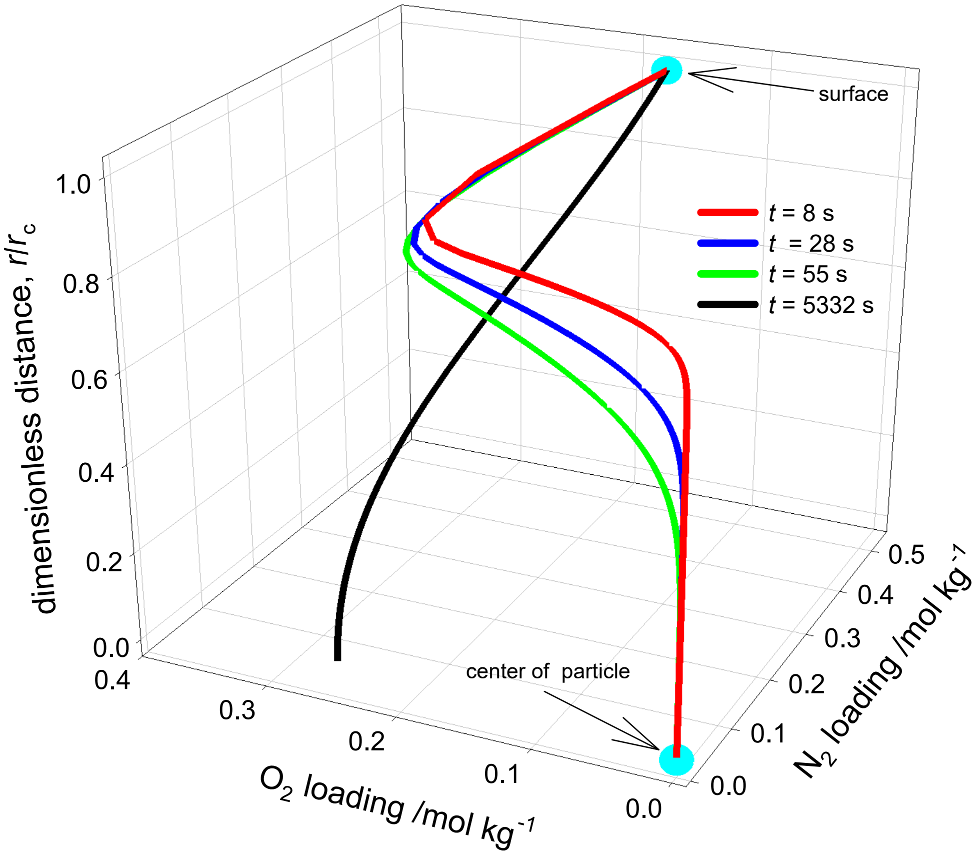

MFI pore landscape

Figure S40

	MFI
a /Å	20.022
b /Å	19.899
c /Å	13.383
Cell volume / Å^3	5332.025
conversion factor for [molec/uc] to [mol per kg Framework]	0.1734
conversion factor for [molec/uc] to [kmol/m^3]	1.0477
ρ [kg/m3]	1796.386
MW unit cell [g/mol(framework)]	5768.141
ϕ, fractional pore volume	0.297
open space / Å^3/uc	1584.9
Pore volume / cm^3/g	0.165
Surface area /m^2/g	487.0
DeLaunay diameter /Å	5.16

Structural information from: C. Baerlocher, L.B. McCusker,
Database of Zeolite Structures, International Zeolite Association,
http://www.iza-structure.org/databases/

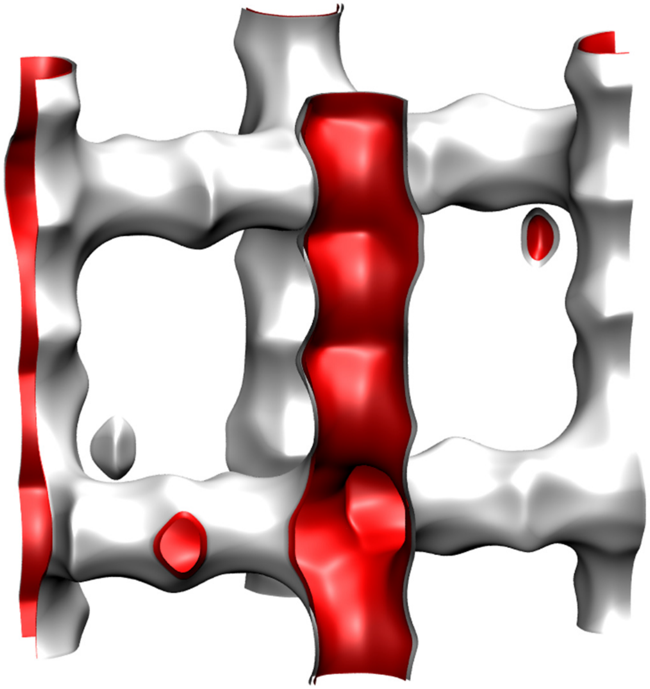

MFI pore dimensions

Figure S41

10 ring channel of MFI viewed along [100]

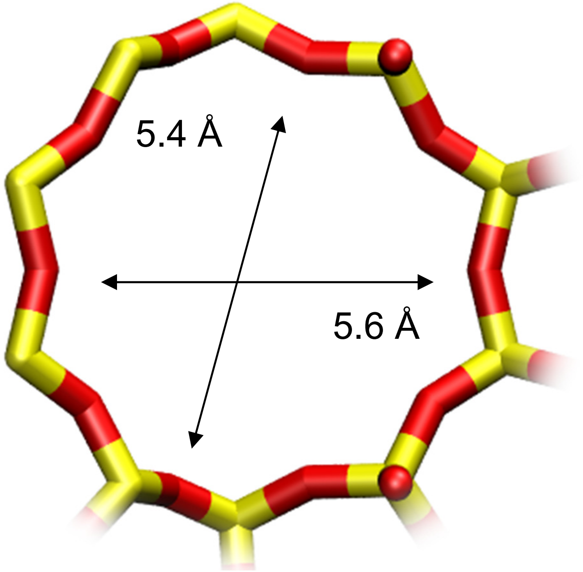

10 ring channel of MFI viewed along [010]

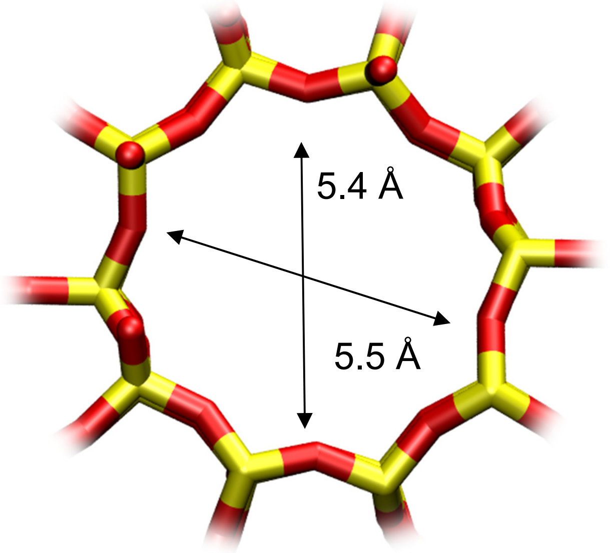

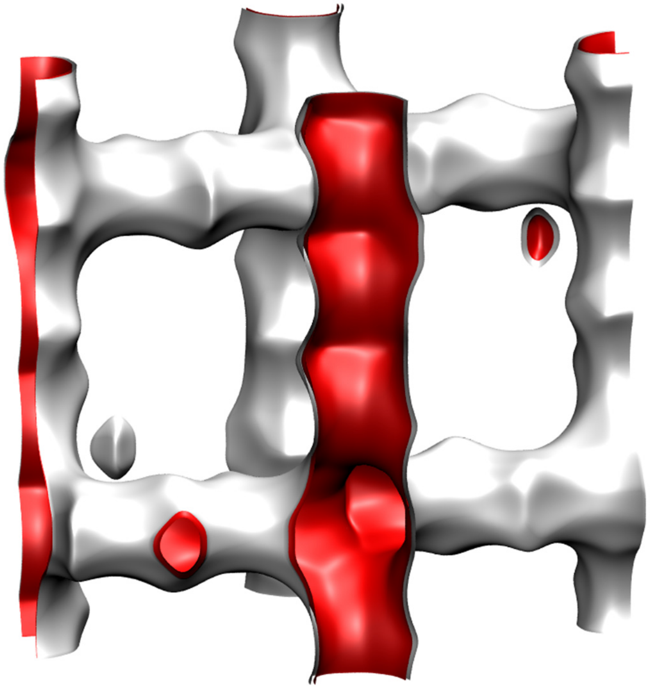

nC6/2MP mixture uptake in MFI

Figure S42

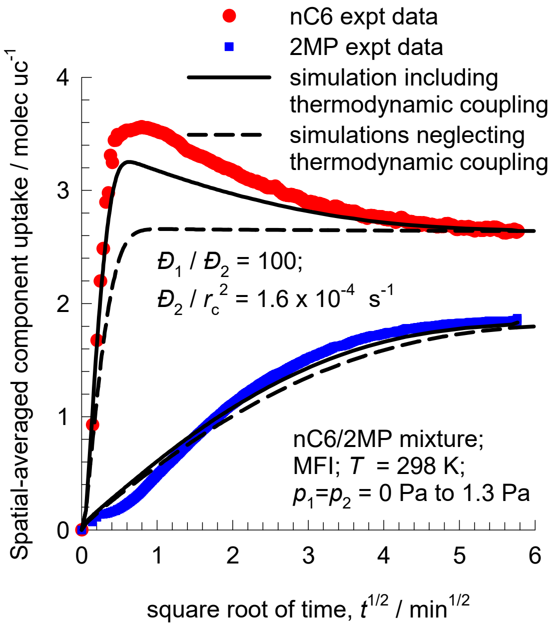

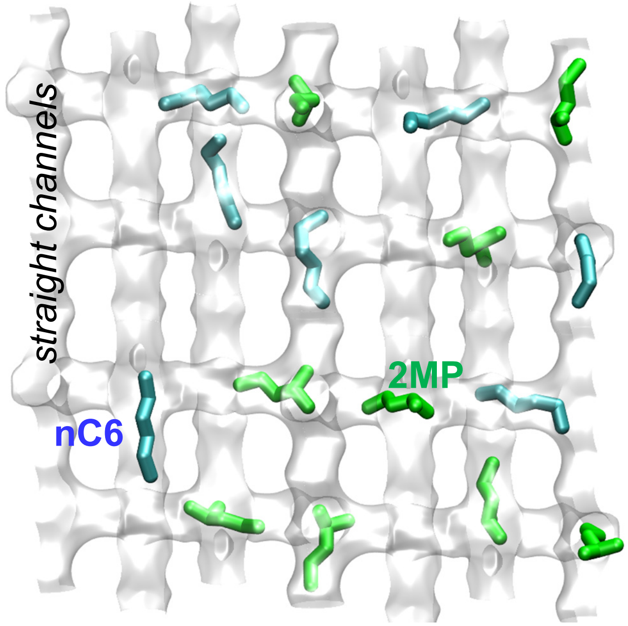

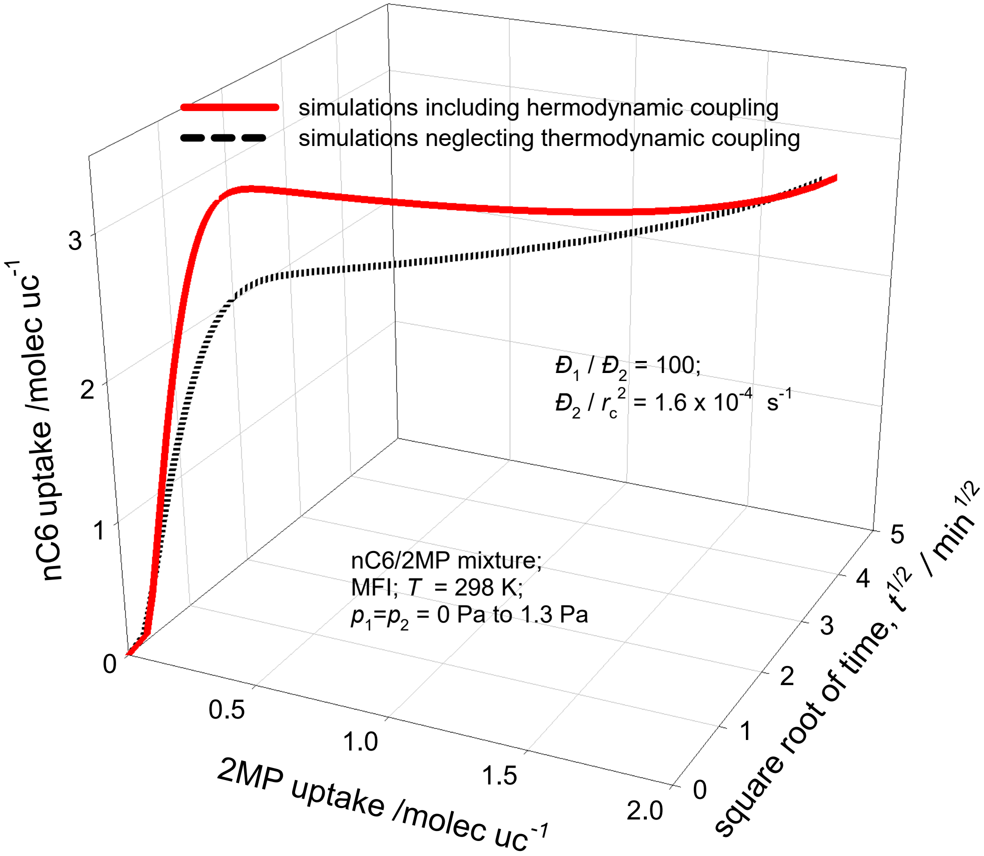

Transient development of loadings in MFI crystal

Figure S43

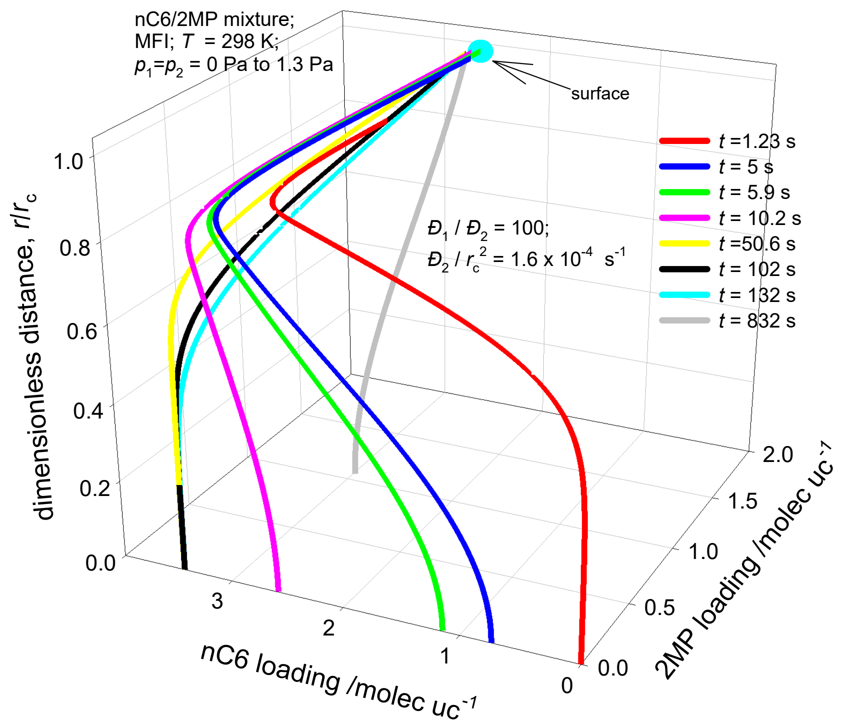

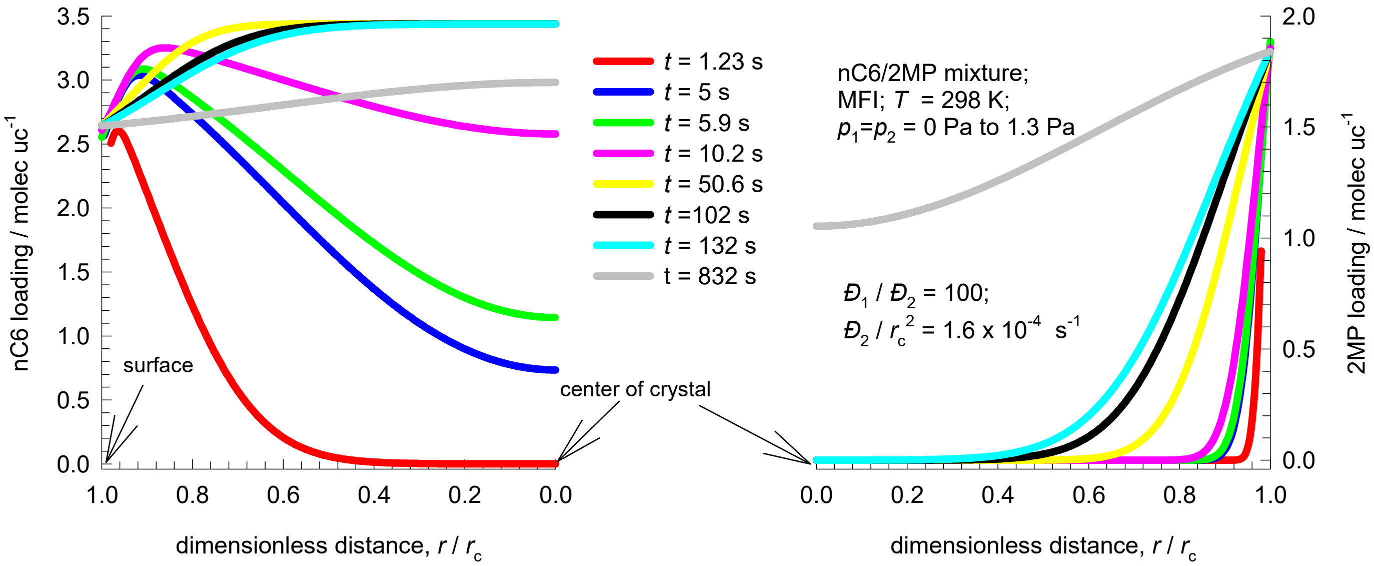

Transient development of “corrected” loadings in MFI

Figure S44

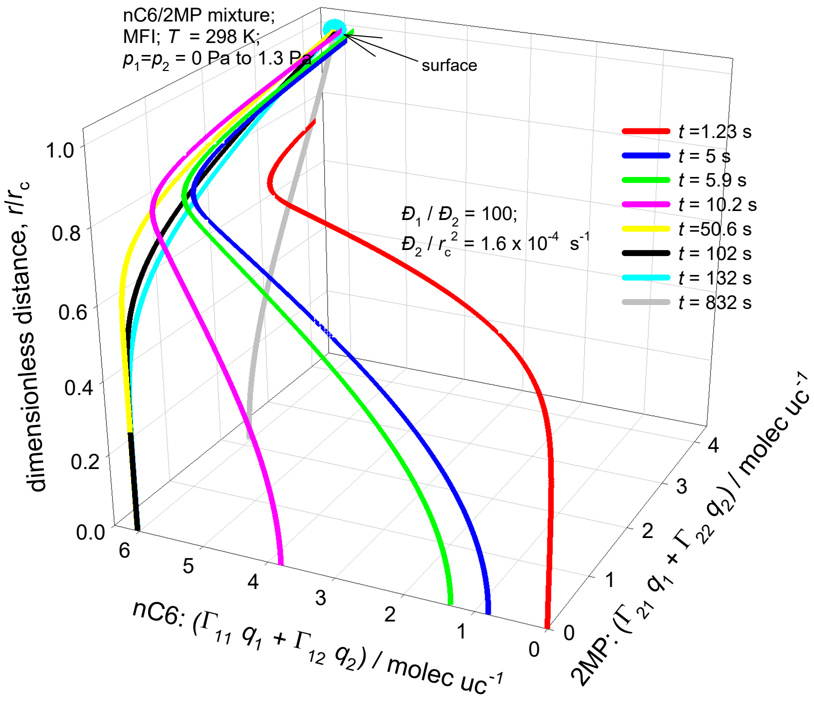

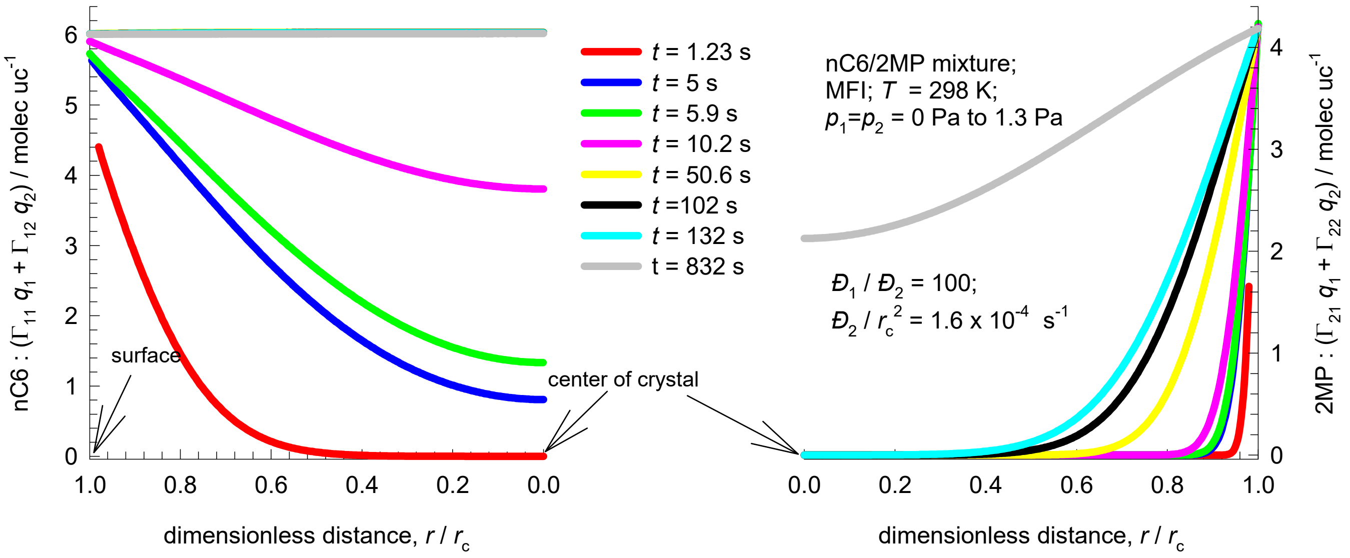

Figure S45

Transient nC4/iC4 uptake in MFI

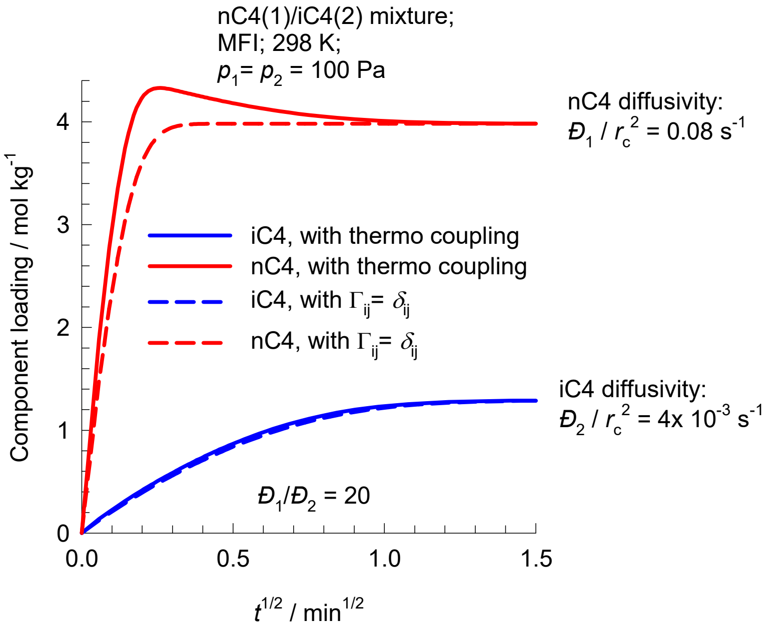

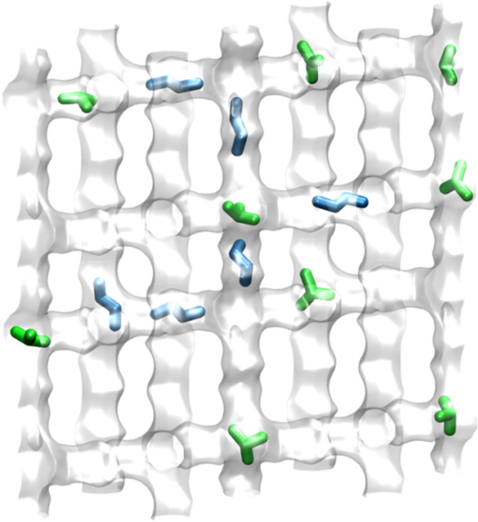

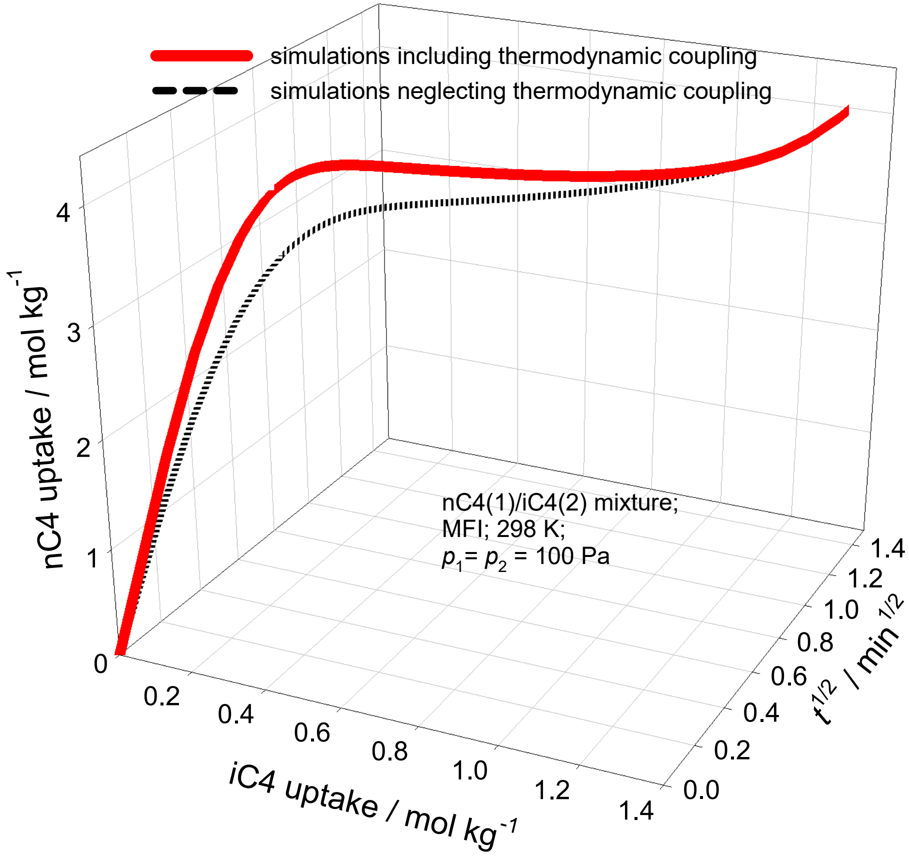

Figure S46

Transient benzene/ethylbenzene uptake in ZSM-5

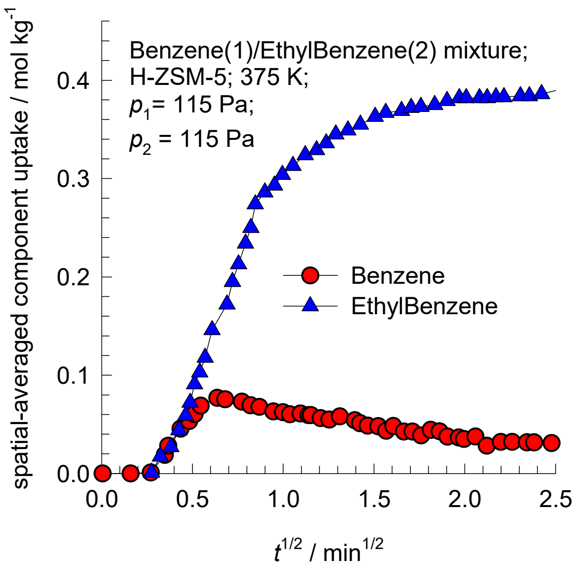

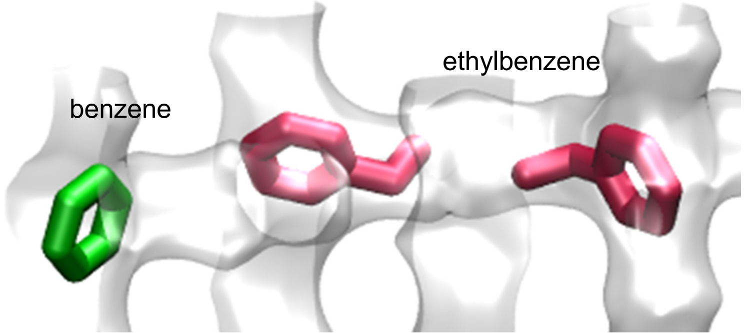

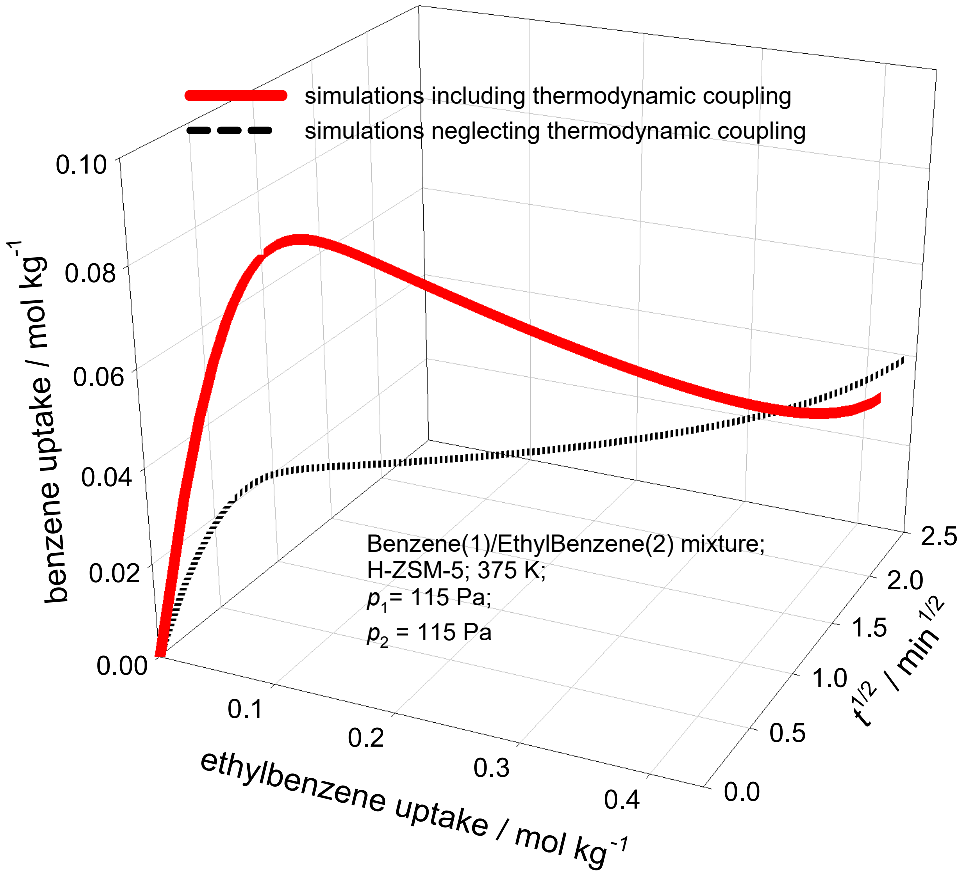

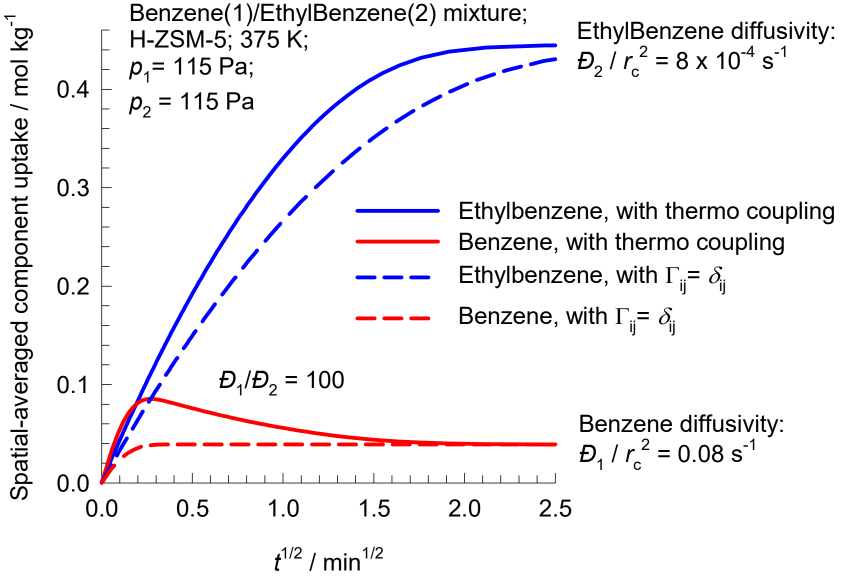

Figure S47

Transient benzene/p-xylene uptake in ZSM-5

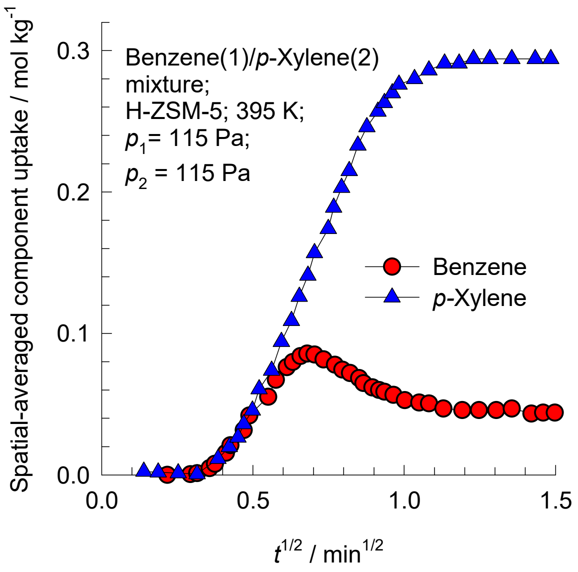

p-xylene

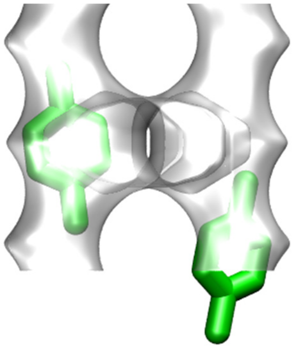

benzene

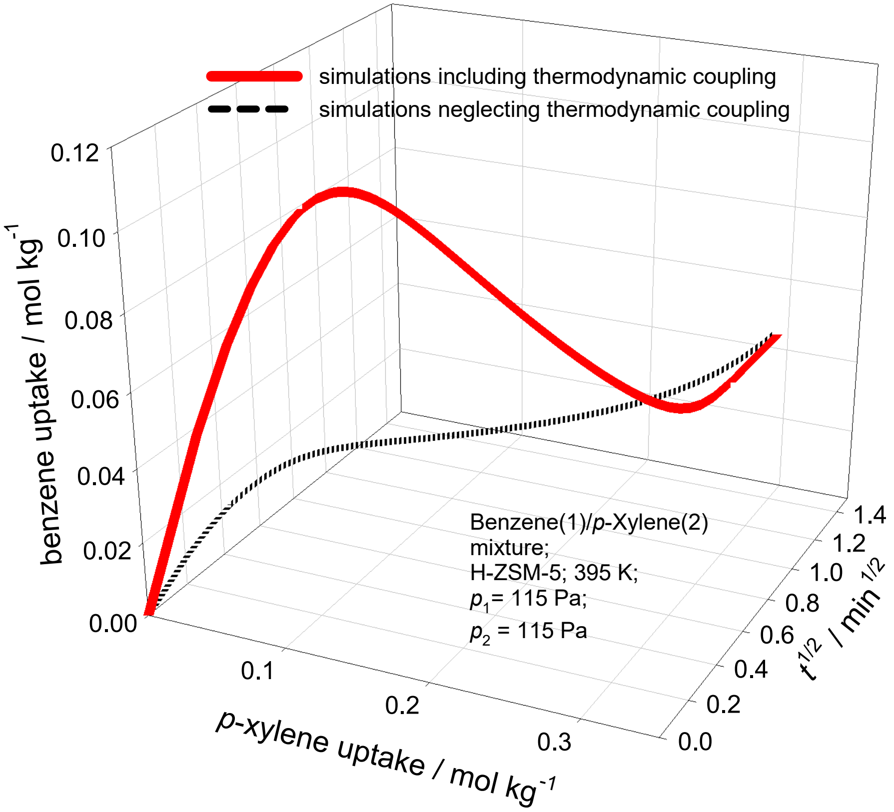

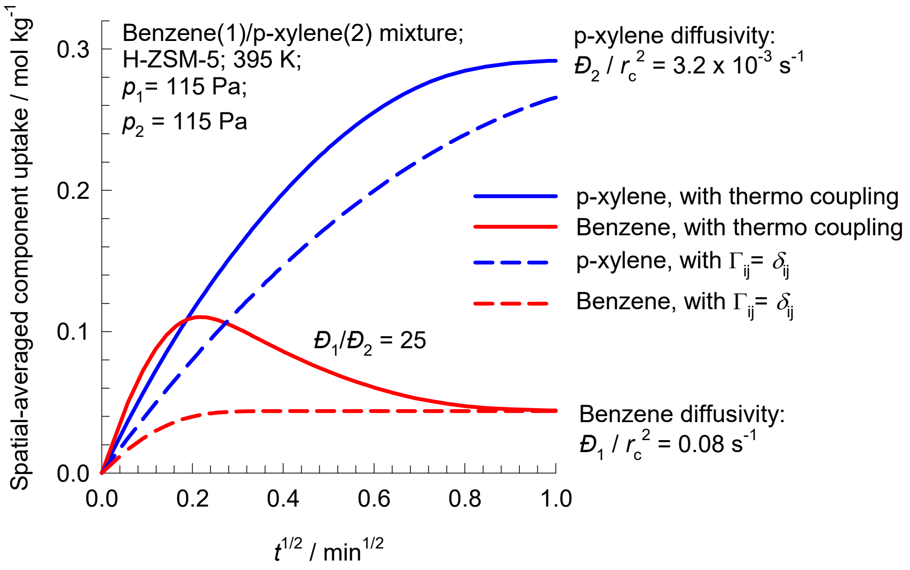

Transient n-heptane/benzene uptake in NaX

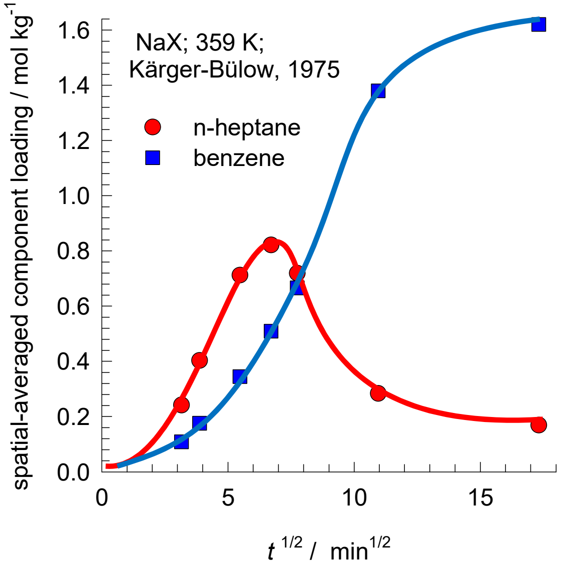

NaX zeolite

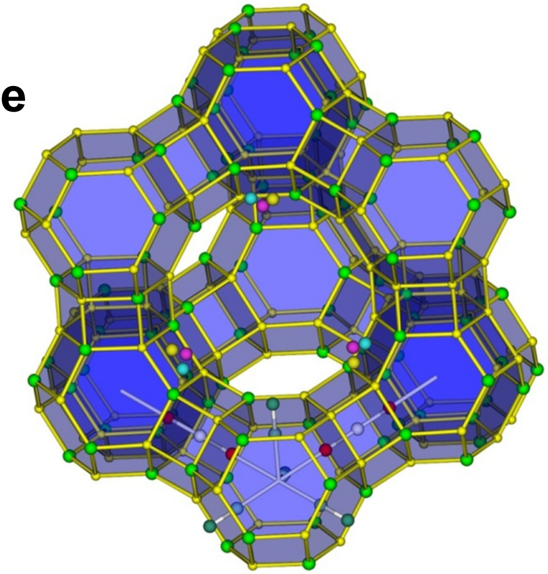

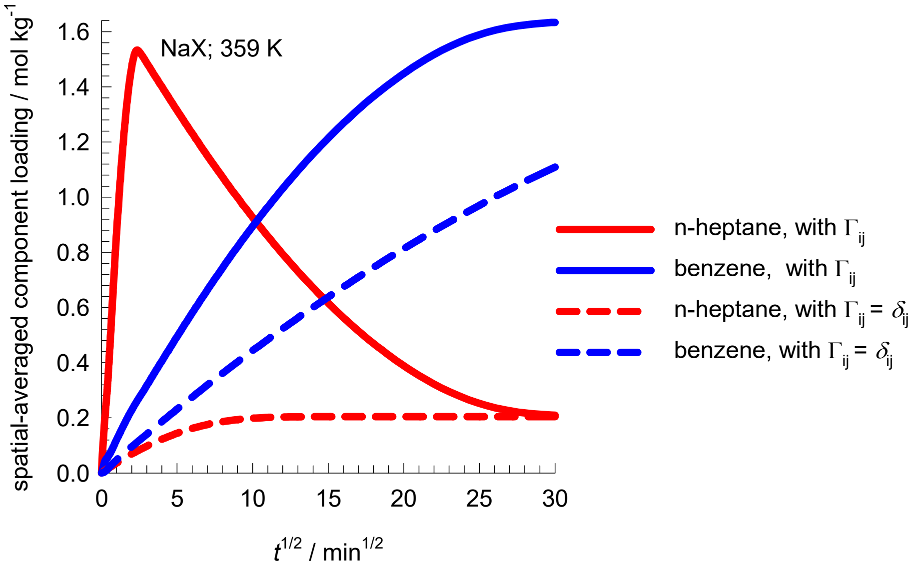

Figure S49

Transient N2/CH4 uptake in BaETS-4

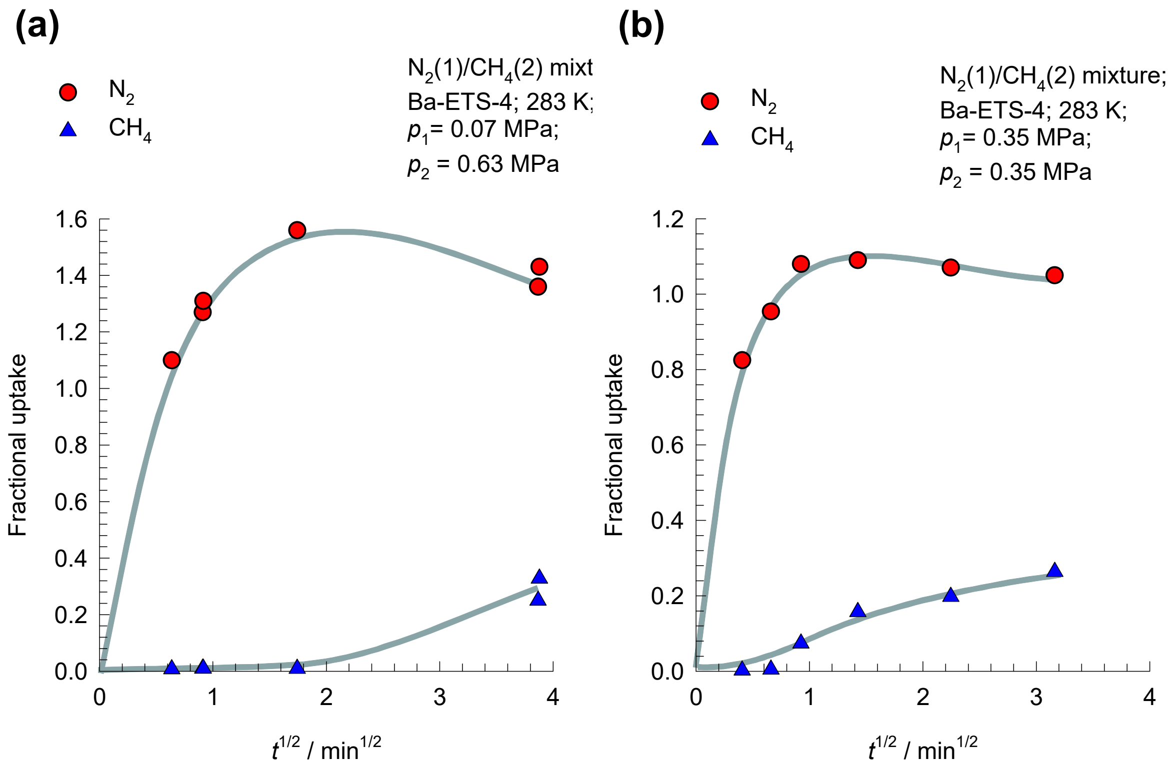

Figure S50

Transient uptake in Activated Carbon

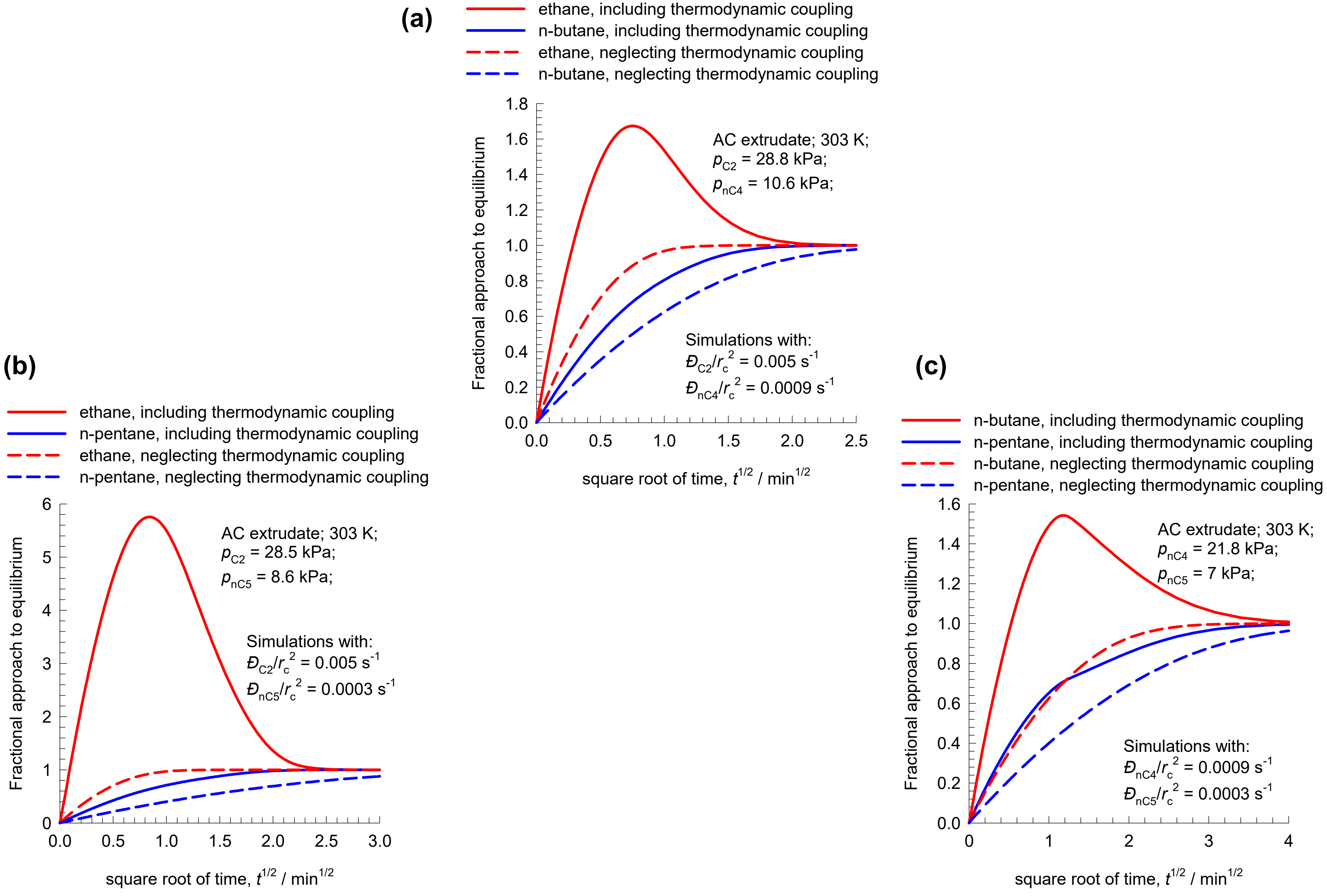

ZIF-8 pore landscapes

The ZIF-8 = Zn(methylimidazole)$_2$ structure was taken from
R. Banerjee, A. Phan, B. Wang, C. Knobler, H. Furukawa, M. O'Keeffe, O.M. Yaghi, High-Throughput Synthesis of Zeolitic Imidazolate Frameworks and Application to CO$_2$ Capture, Science 319 (2008) 939-943.

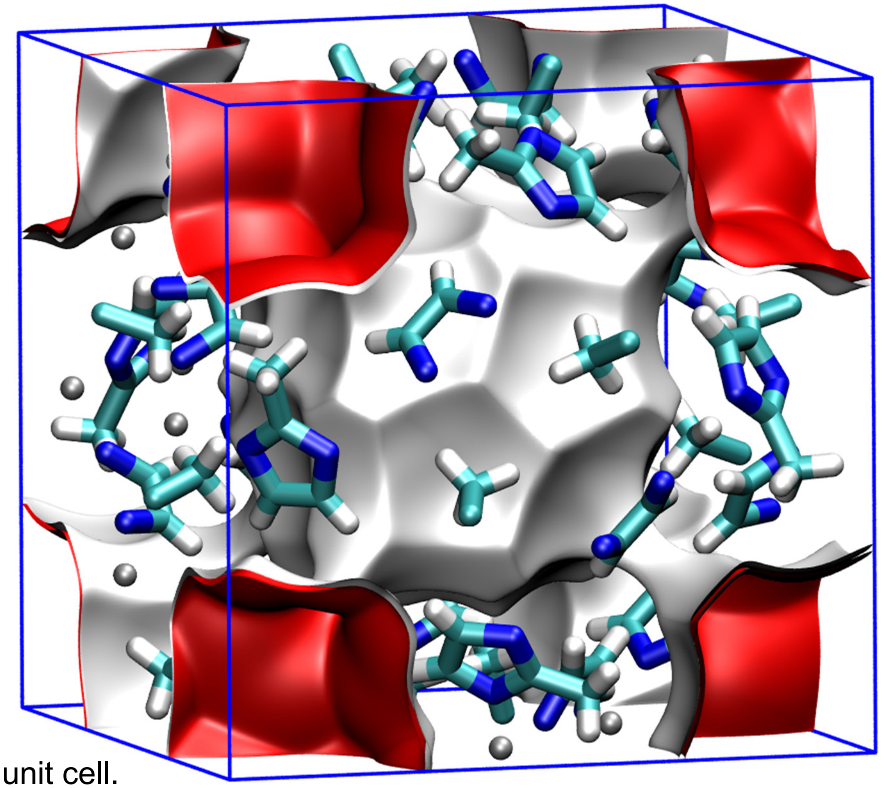

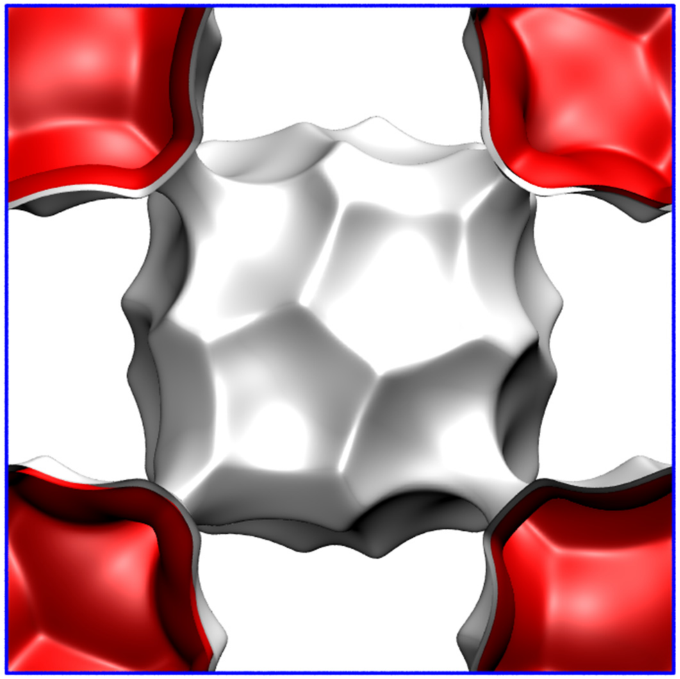

There are 2 cages per unit cell. The volume of one ZIF-8 cage is 1168 Å^3, significantly larger than that of a single cage of DDR (278 Å^3), or FAU (786 Å^3).

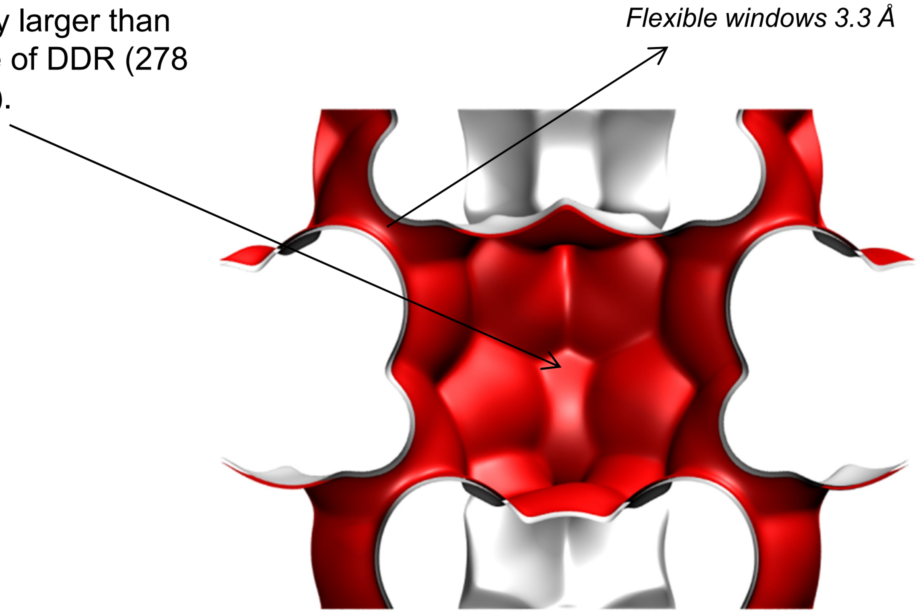

ZIF-8 dimensions

Figure S52

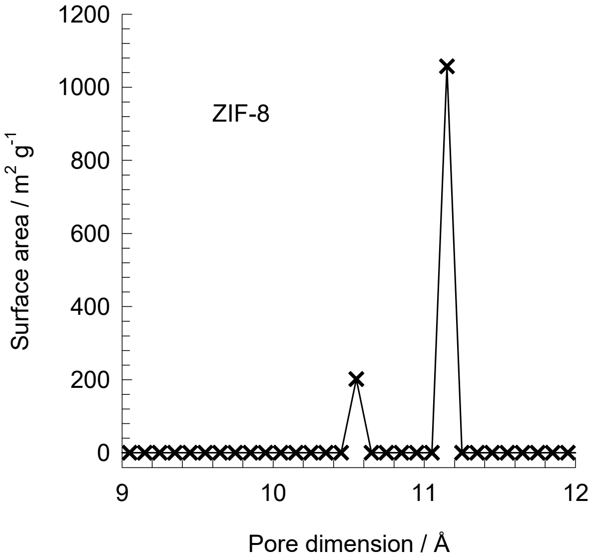

This plot of surface area versus pore dimension is determined using a combination of the DeLaunay triangulation method for pore dimension determination, and the procedure of Düren for determination of the surface area.

	ZIF-8
a /Å	16.991
b /Å	16.991
c /Å	16.991
Cell volume / Å^3	4905.201
conversion factor for [molec/uc] to [mol per kg Framework]	0.3663
conversion factor for [molec/uc] to [kmol/m^3]	0.7106
ρ [kg/m3]	924.253
MW unit cell [g/mol(framework)]	2730.182
ϕ, fractional pore volume	0.476
open space / Å^3/uc	2337.0
Pore volume / cm^3/g	0.515
Surface area /m^2/g	1164.7
DeLaunay diameter /Å	3.26

Figure S53

Propene/propane uptake in ZIF-8

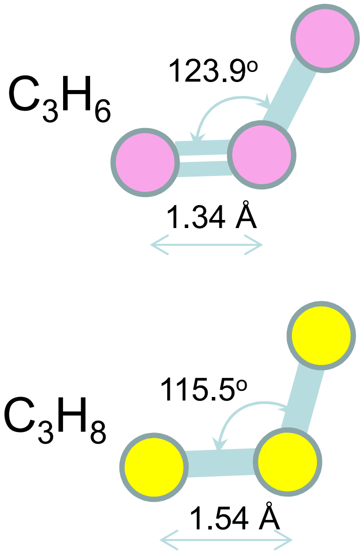

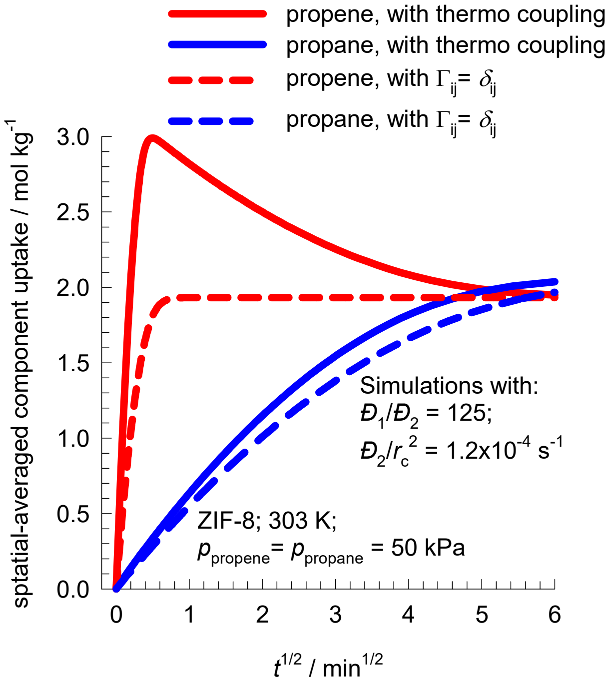

Simulations with:
$Đ_1/Đ_2 = 125$;
$Đ_2/r_c^2 = 1.2\text{x}10^{-4}$ s^{-1}

ZIF-8; 303 K;
$p_{propene} = p_{propane} = 50$ kPa

Figure S54

Propene/propane uptake in ZIF-8

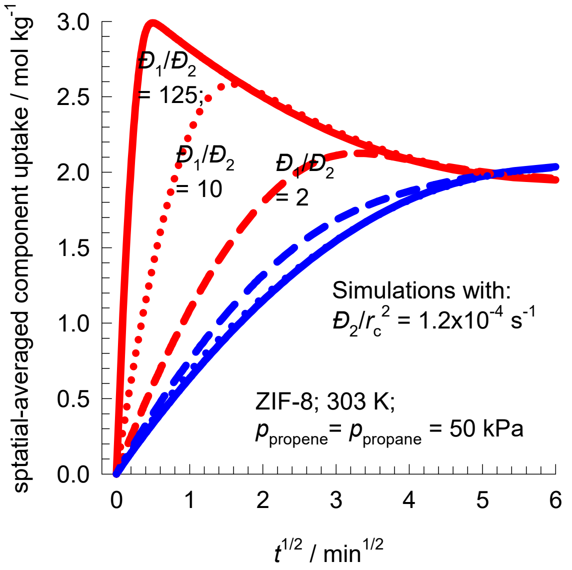

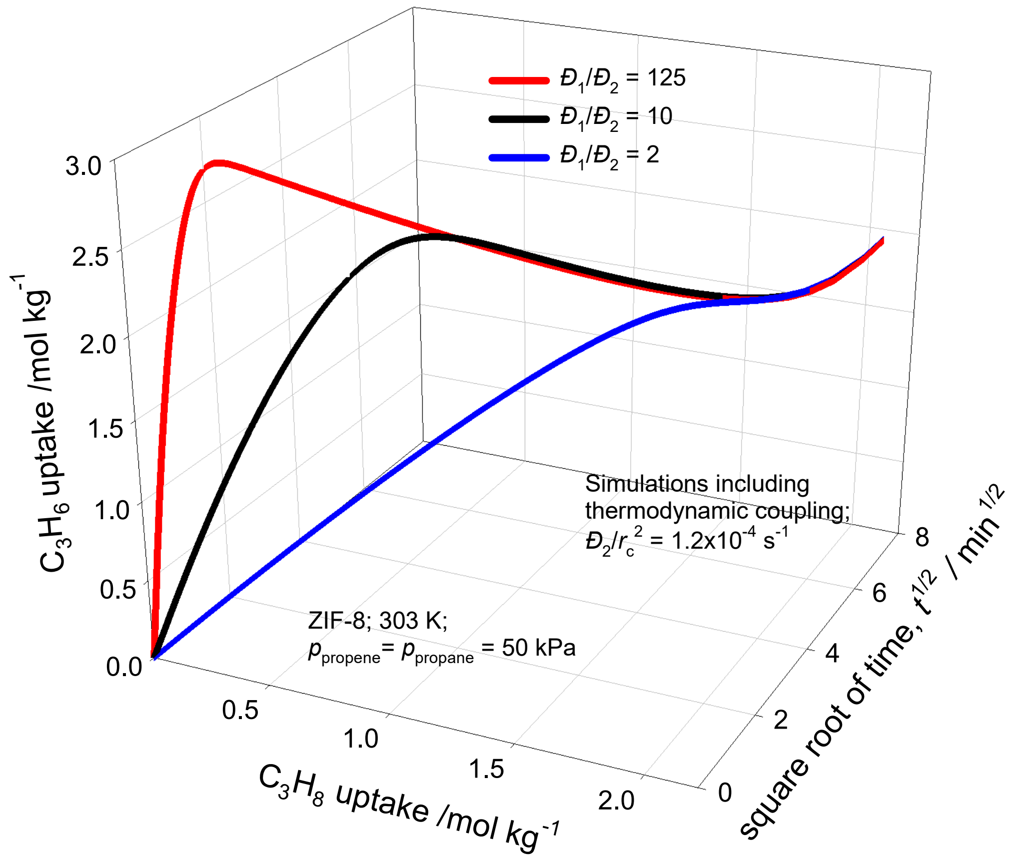

Figure S55

Propene/propane uptake in ZIF-8

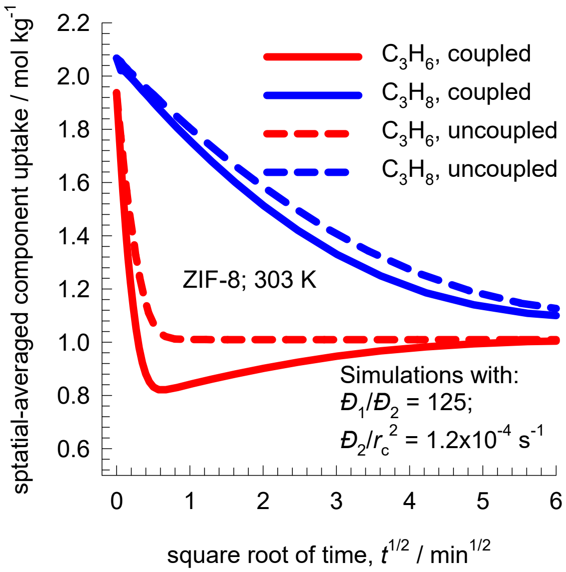

Figure S56

Transient 2MP/22DMB uptake in MFI

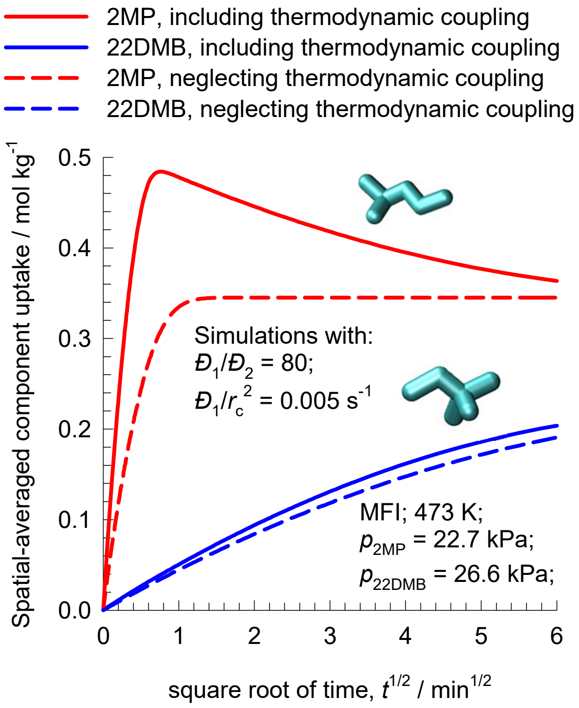

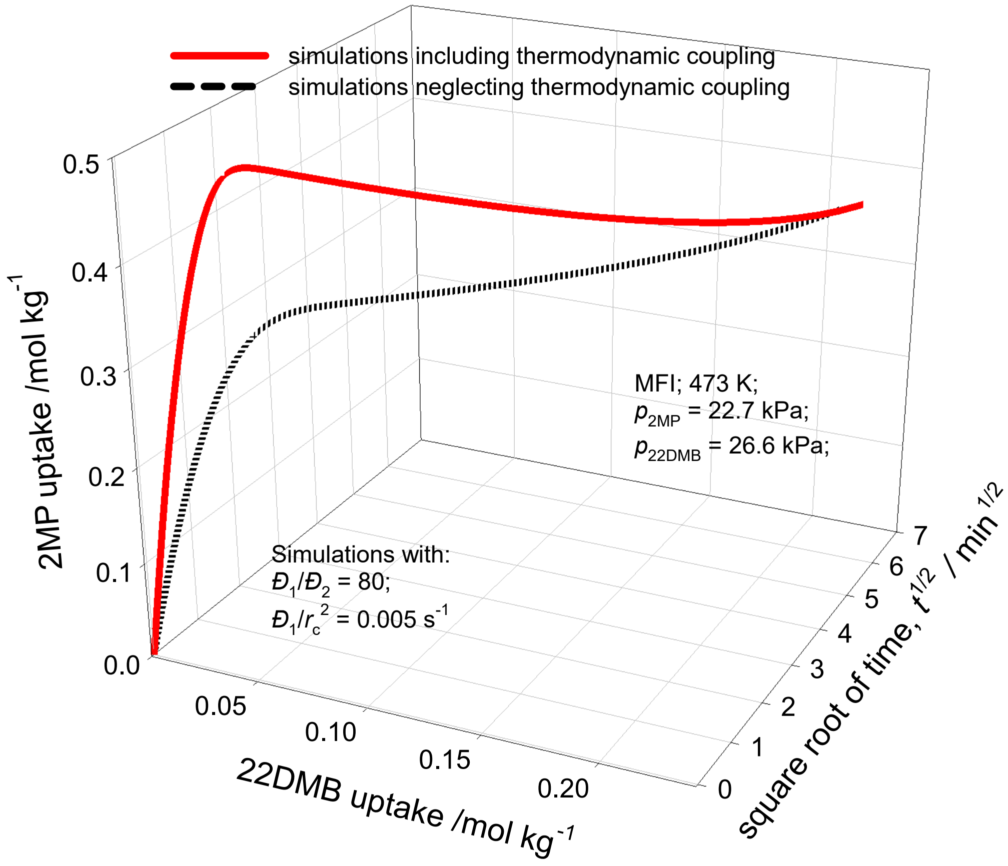

2MP/22DMB loading profiles in MFI

Figure S57

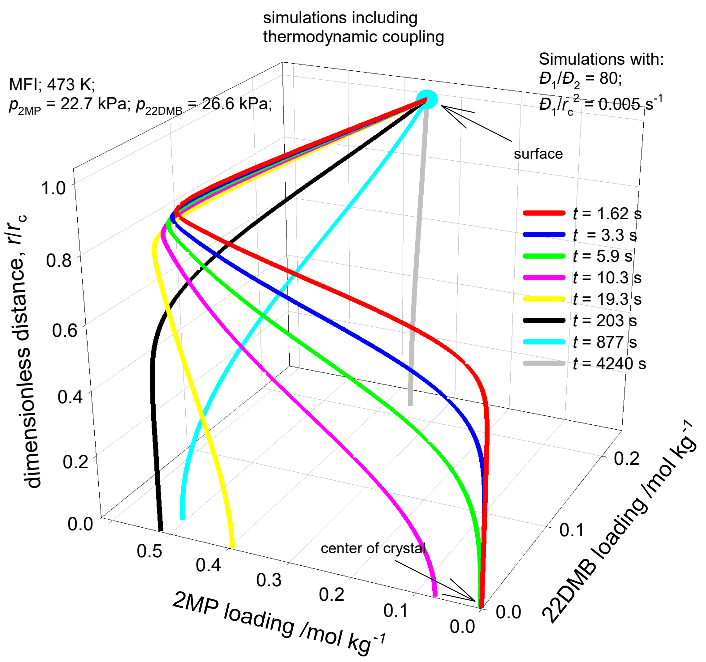

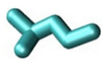

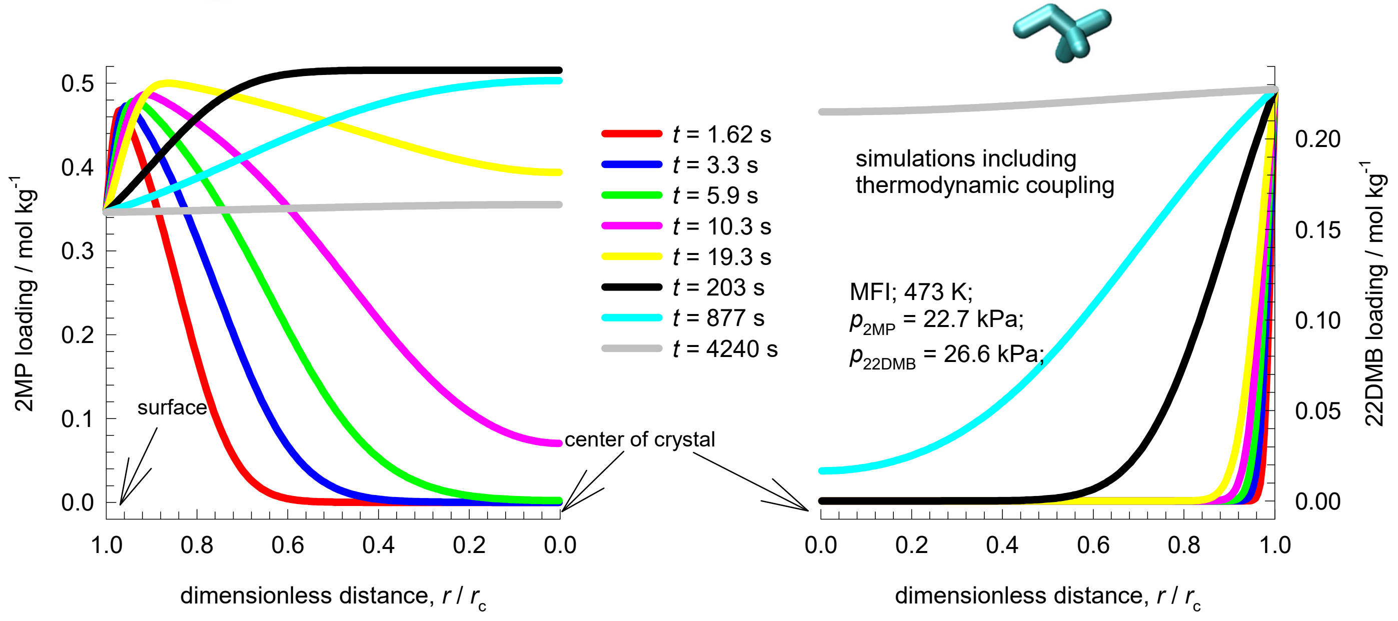

Figure S58

2MP/22DMB corrected loading profiles in MFI

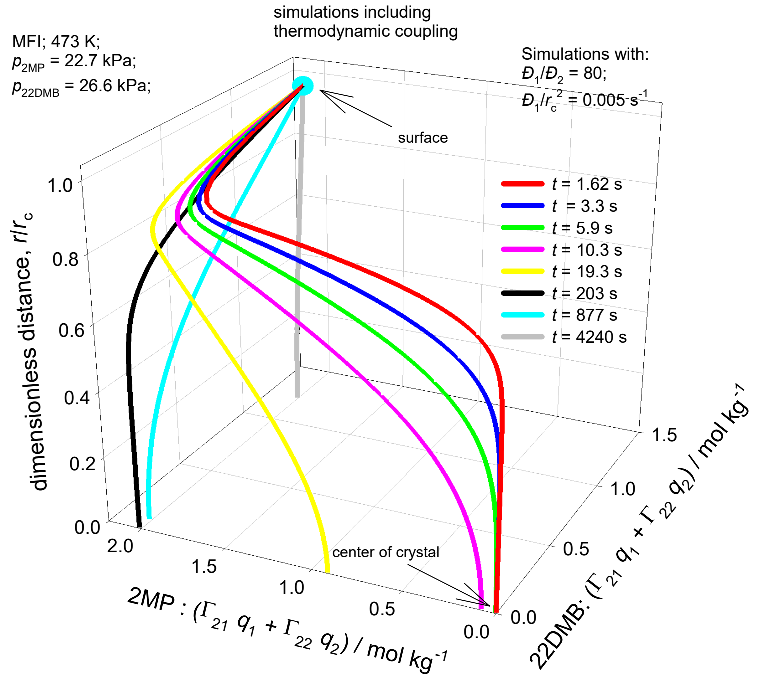

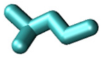

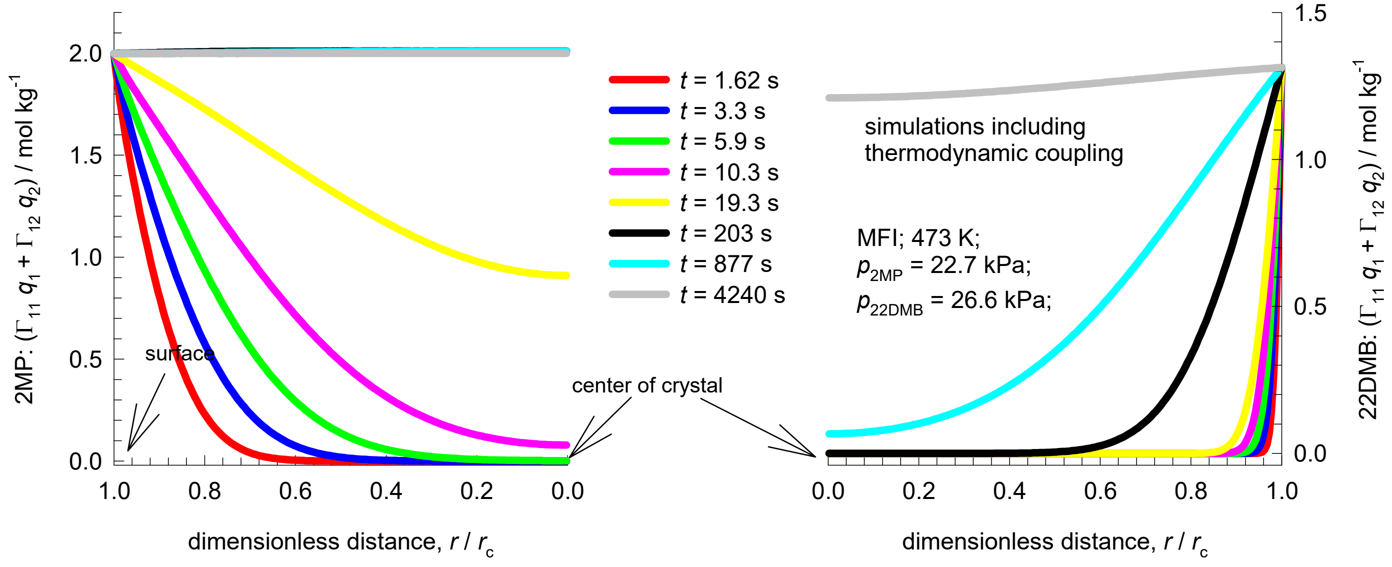

Transient 2MP/22DMB breakthrough in fixed bed of MFI extrudates

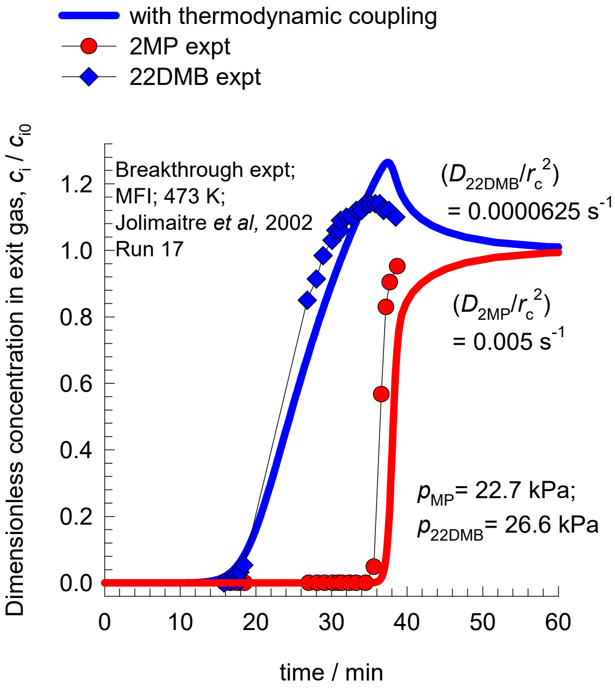

Figure S60

Transient 2MB/2MP/22DMB uptake in MFI

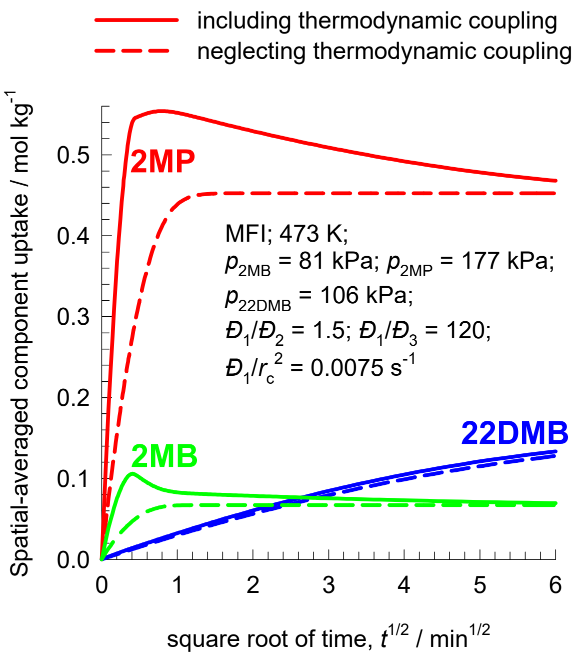

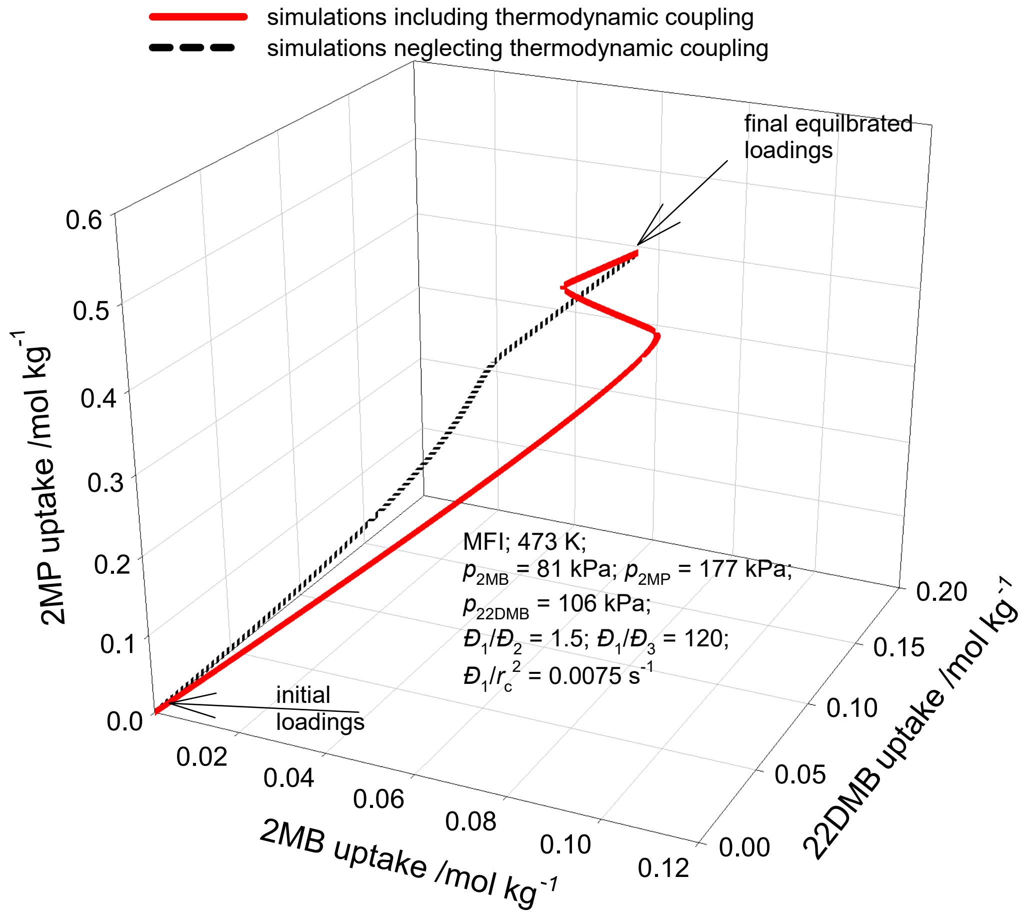

Transient 2MB/2MP/22DMB breakthrough in fixed bed of MFI extrudates

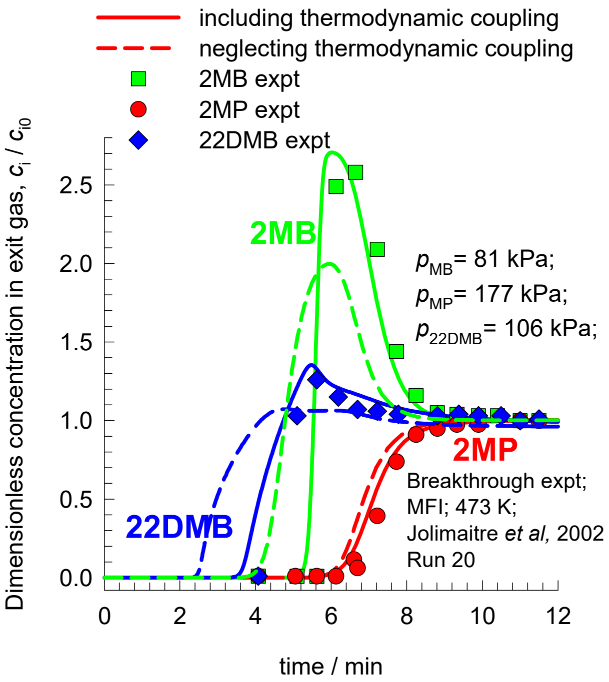

Figure S62

Transient ethanol/1-propanol uptake in SAPO-34

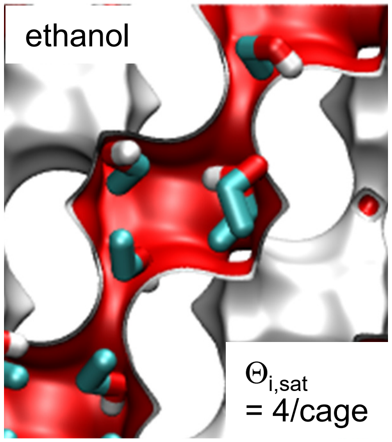

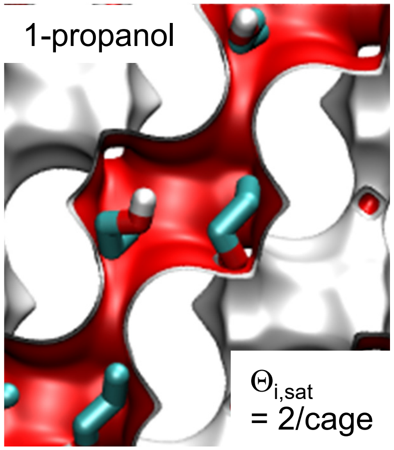

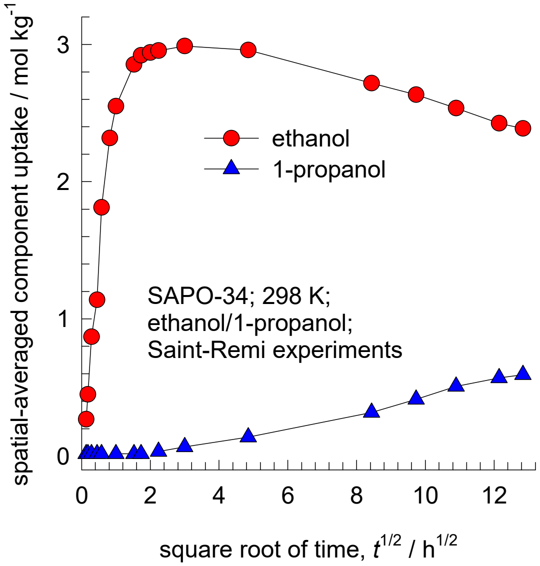

Figure S63

Transient breakthrough of 1-alcohols in SAPO-34

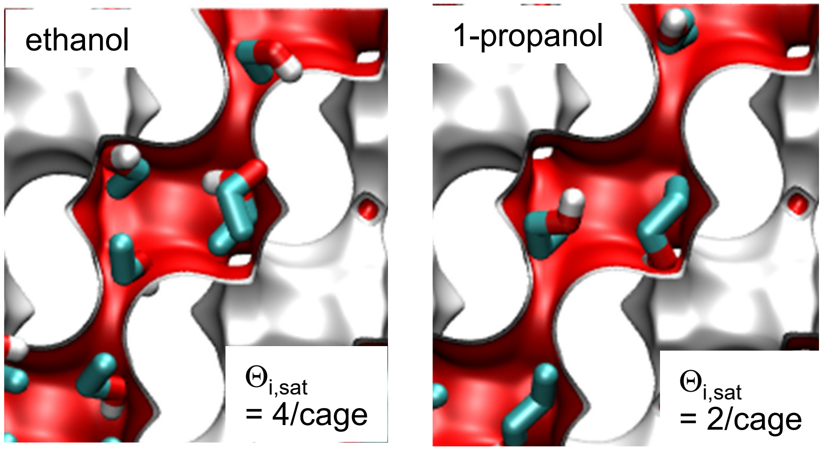

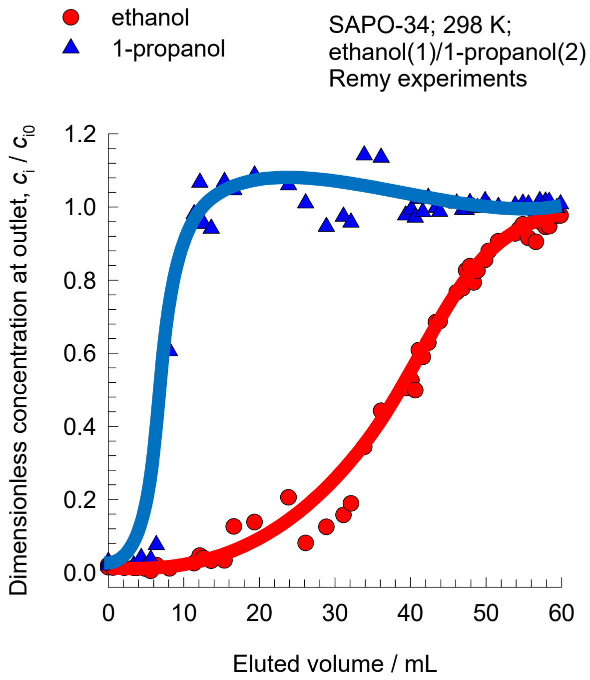

Figure S64

Transient ethanol/1-propanol uptake in CHA

(a)

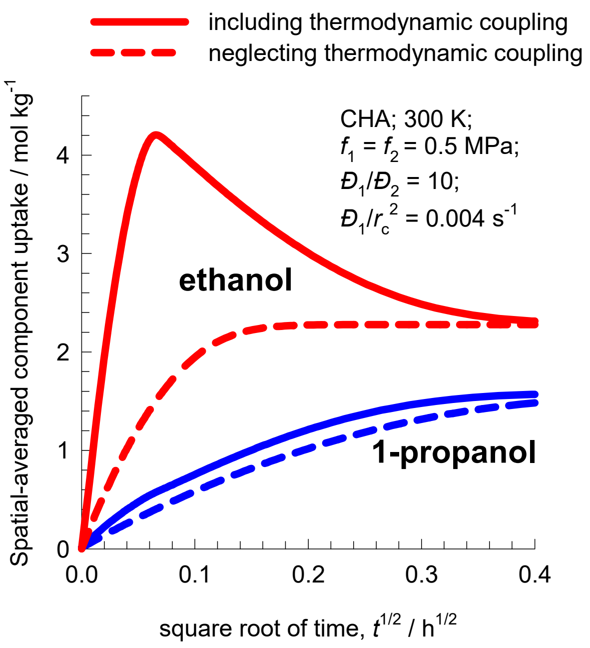

(b)

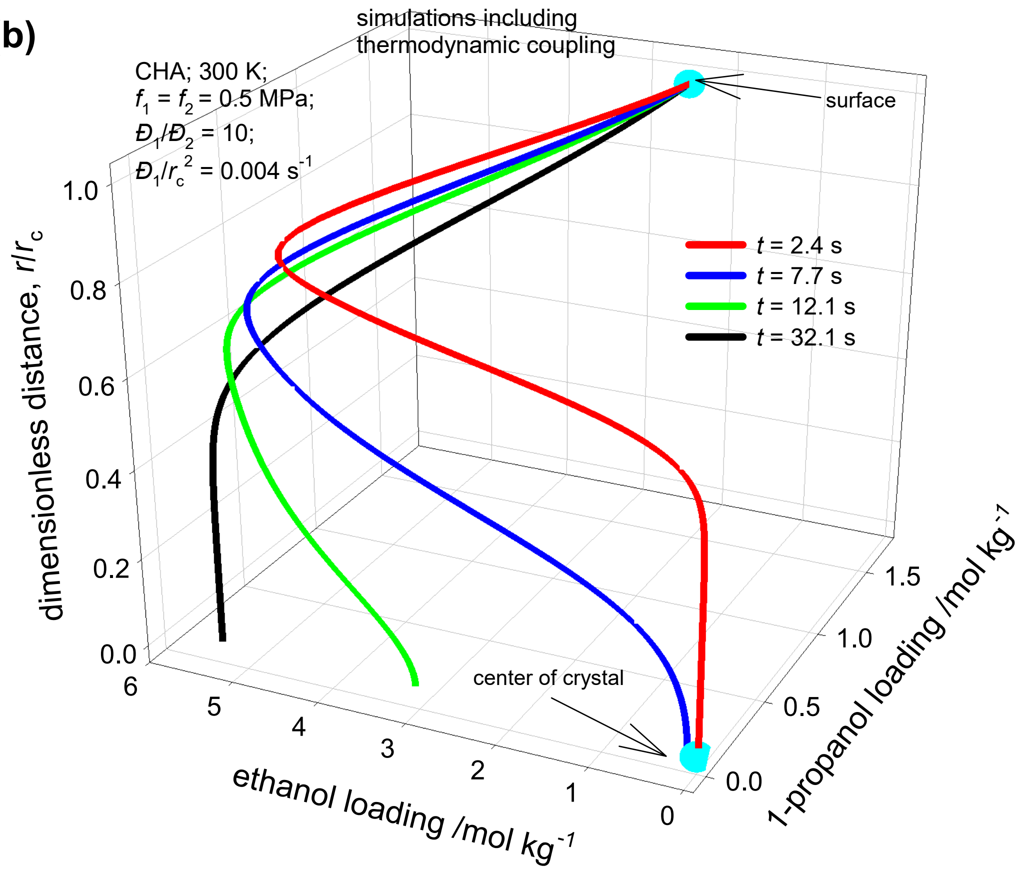

Figure S65

Transient ethanol/1-propanol breakthrough in fixed bed of CHA

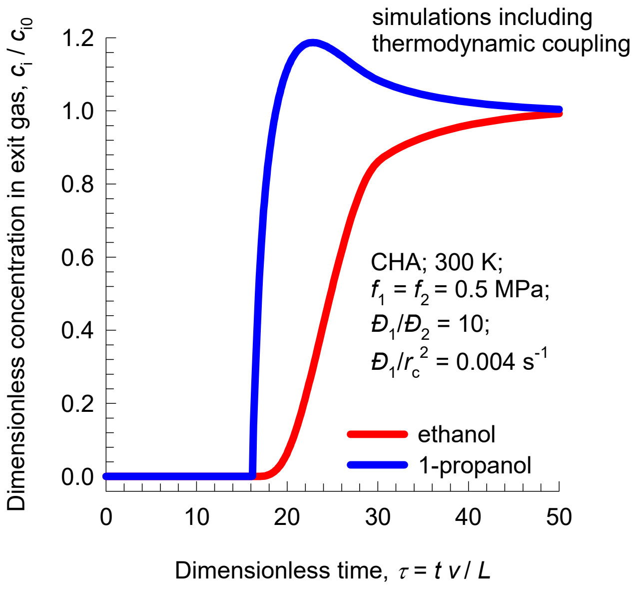

Figure S66

C_3H_6/C_3H_8 permeation across ZIF-8 membrane

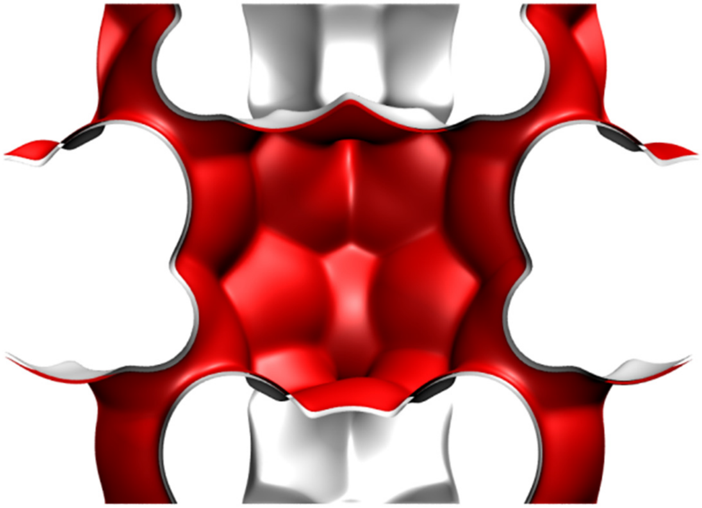

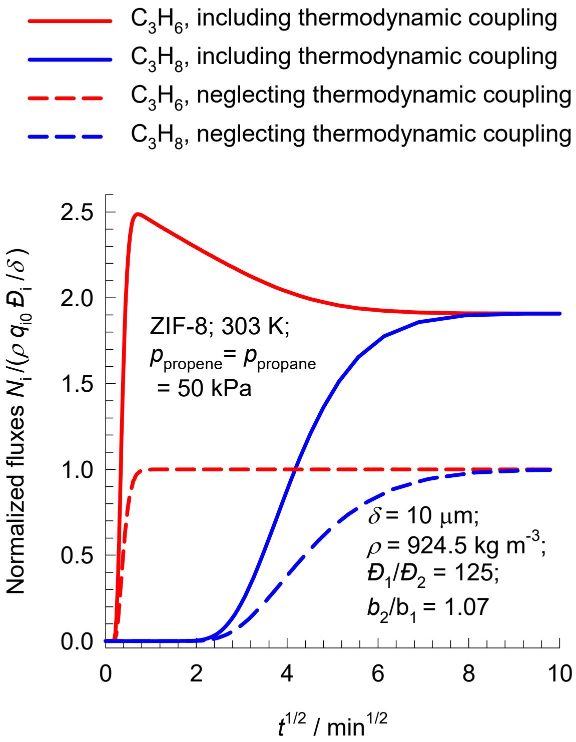

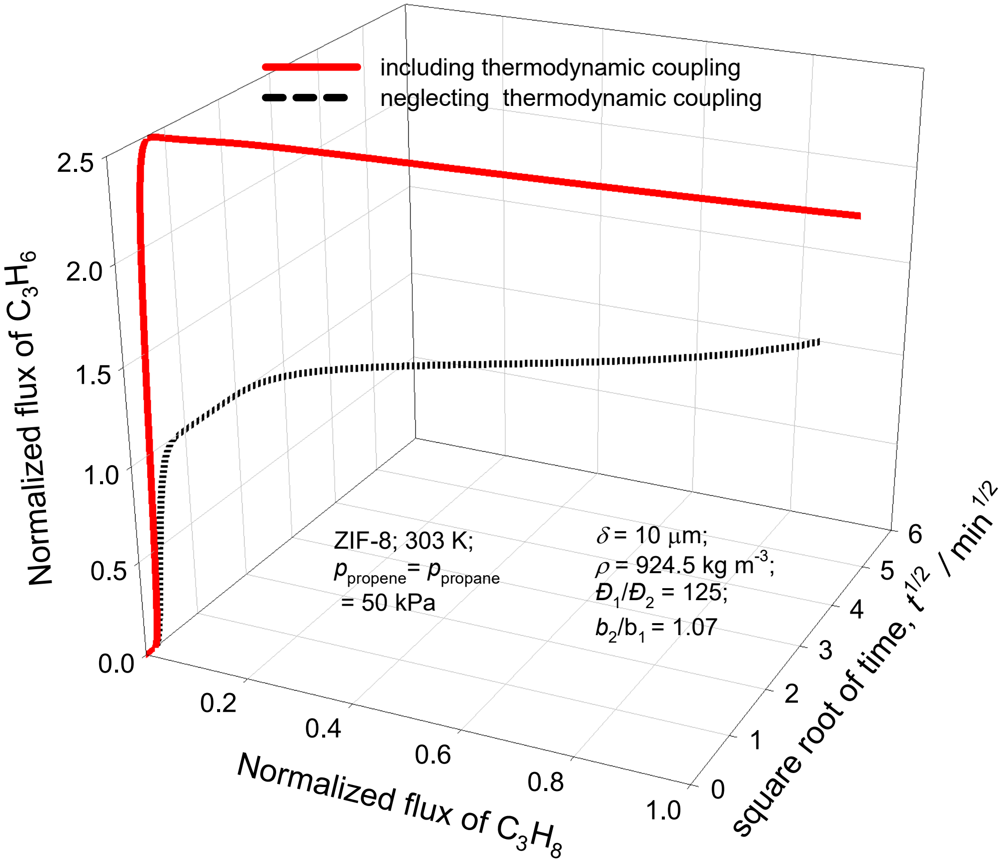

Figure S67

C_3H_6/C_3H_8 loading profiles in membrane

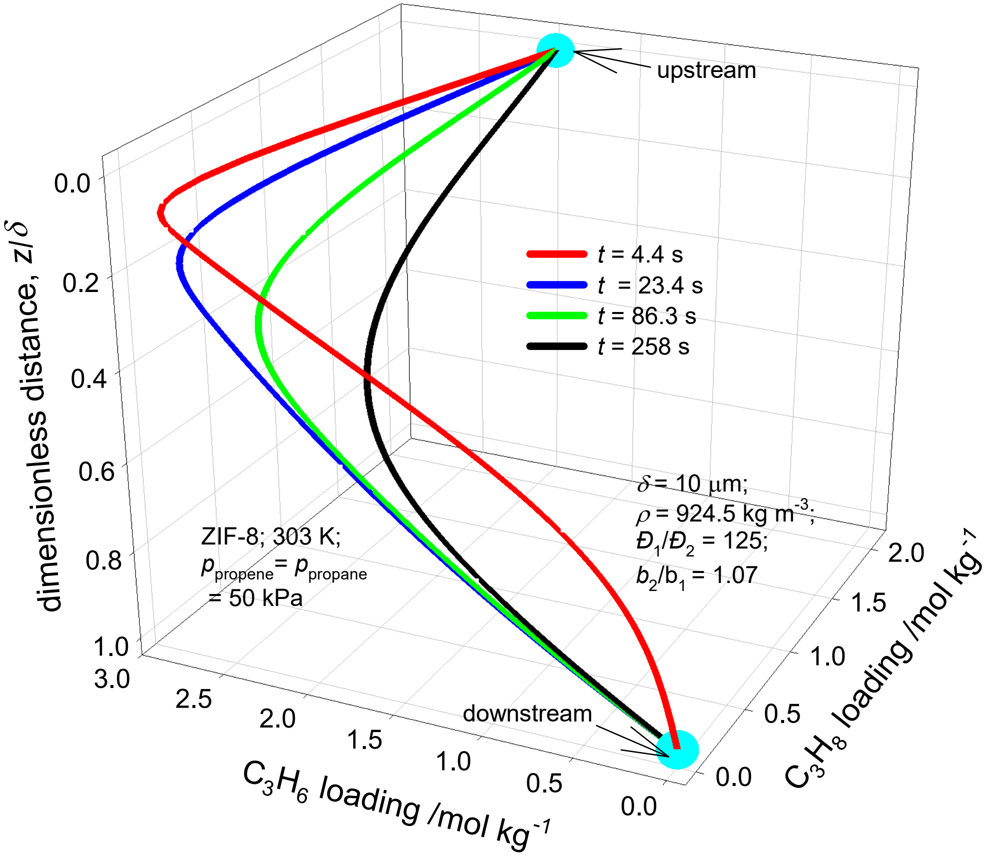

Figure S68

C_3H_6/C_3H_8 corrected loading profiles in membrane

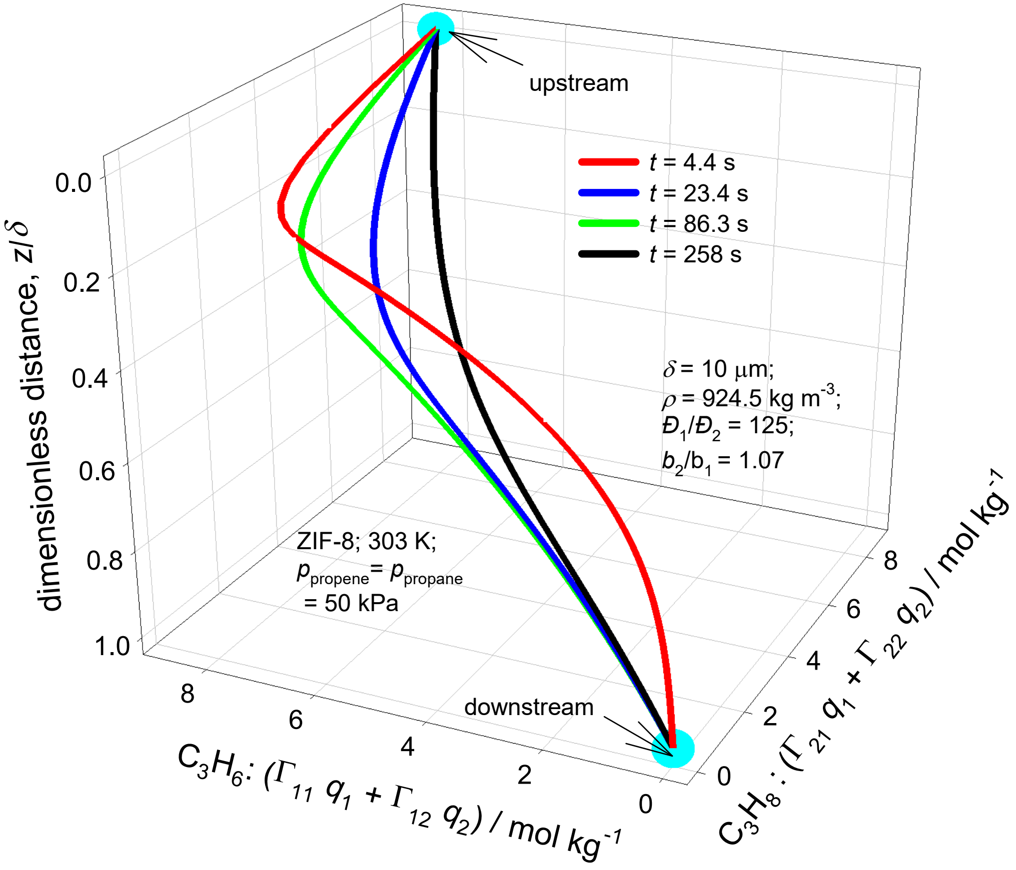

Figure S69

CH_4/nC_4H_{10} permeation: MFI membrane

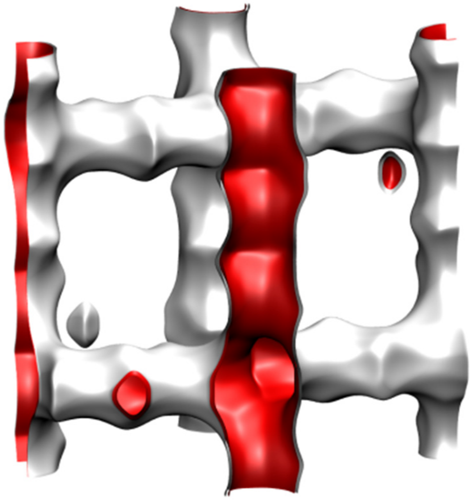

(a)

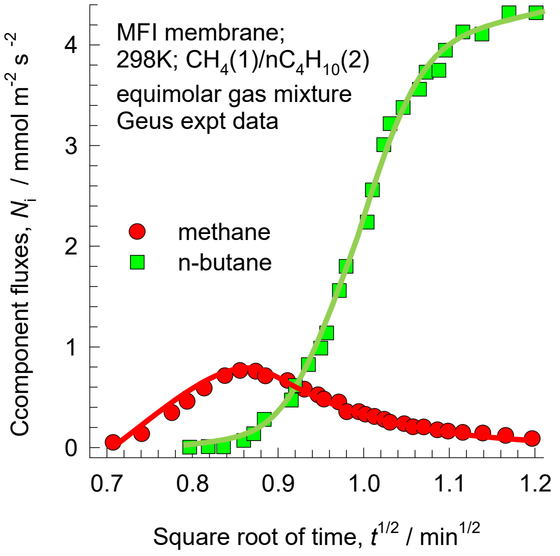

(b)

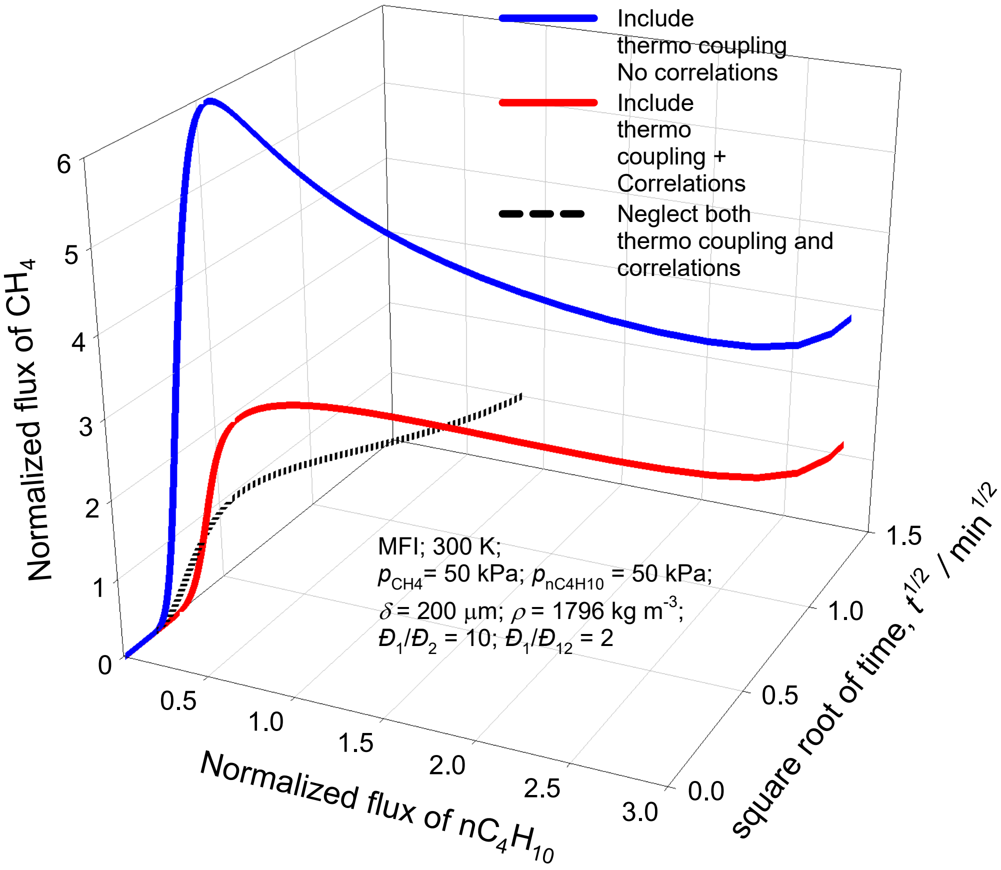

Figure S70

CH_4/nC_4H_{10} loading profiles: MFI membrane

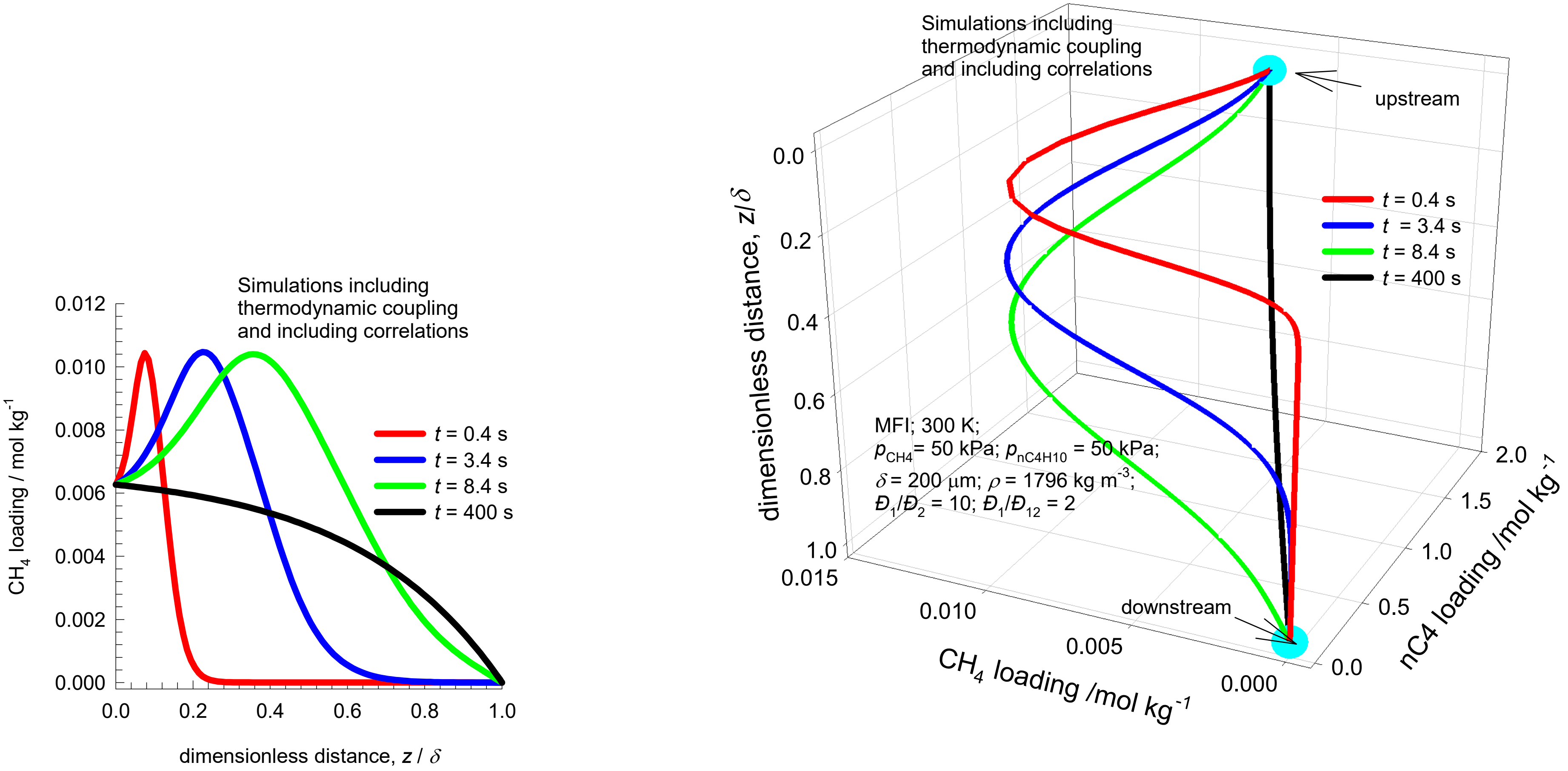

Figure S71

CH_4/nC_4H_{10} corrected loading profiles: MFI membrane

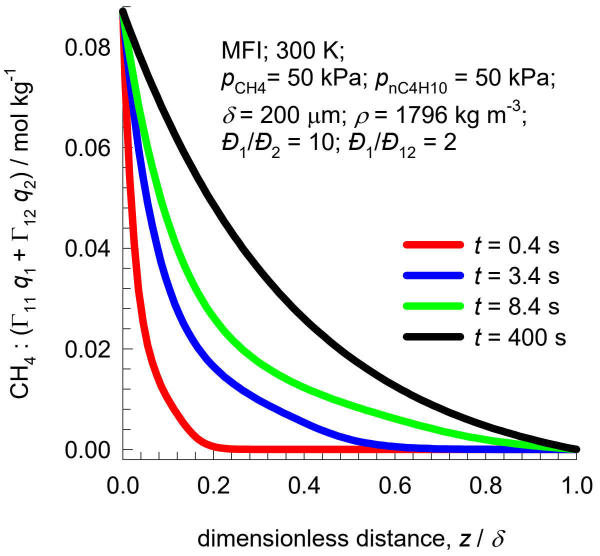

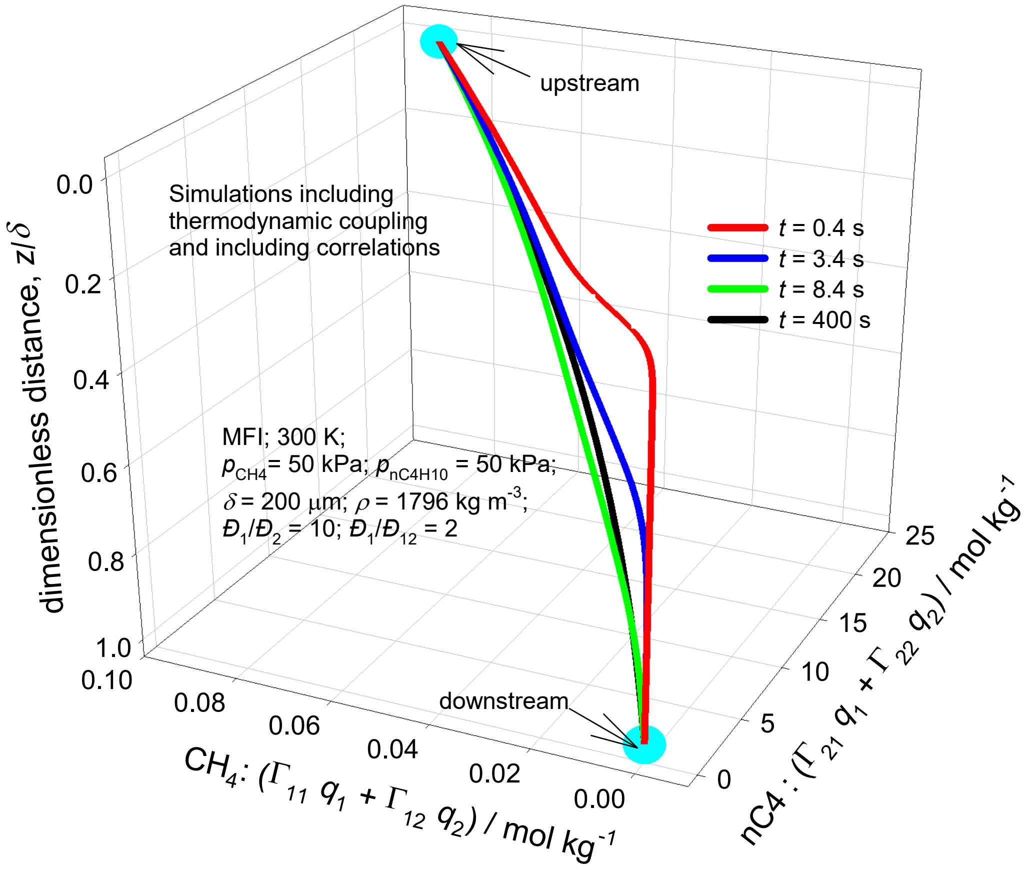

Figure S72

H_2/nC_4H_{10} permeation: MFI membrane

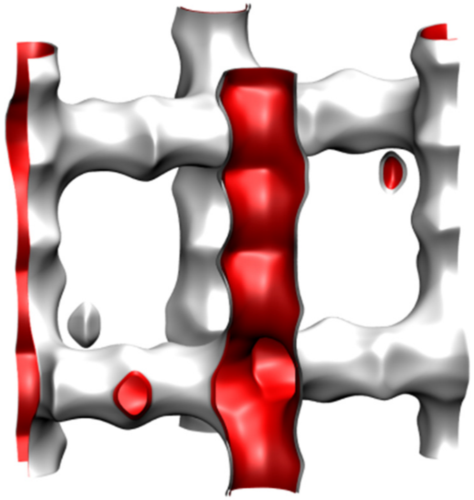

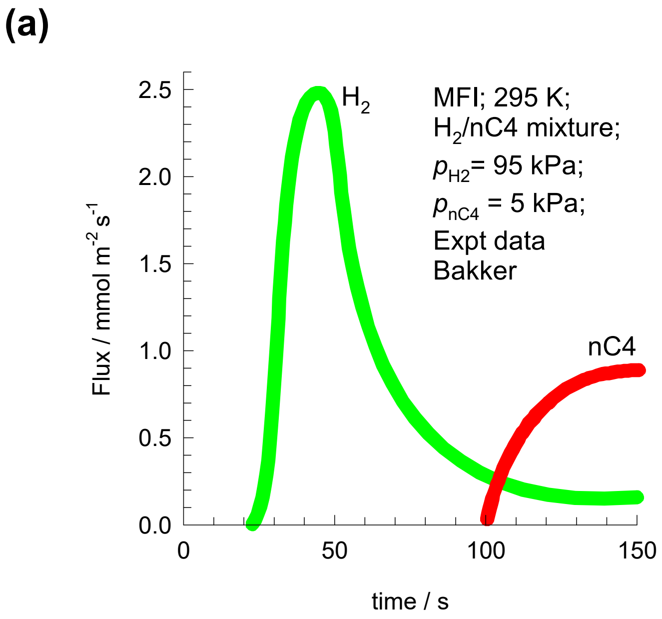

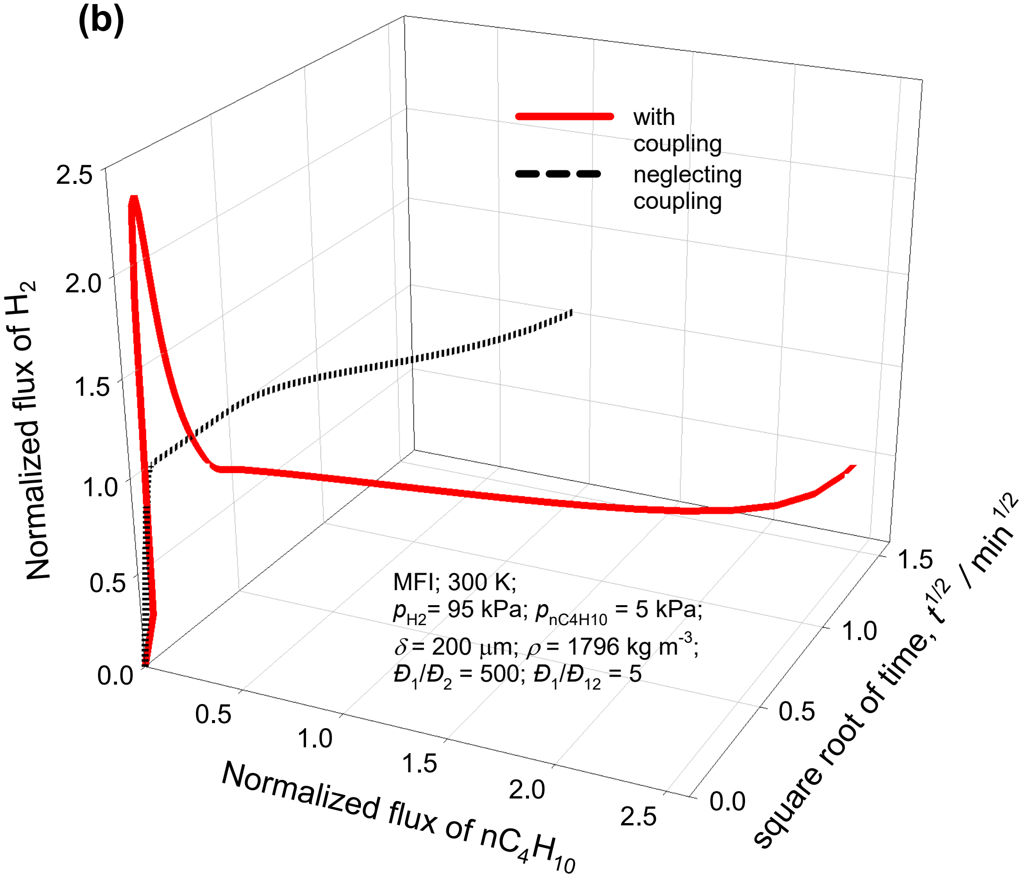

Figure S73

H_2/nC_4H_{10} loading profiles: MFI membrane

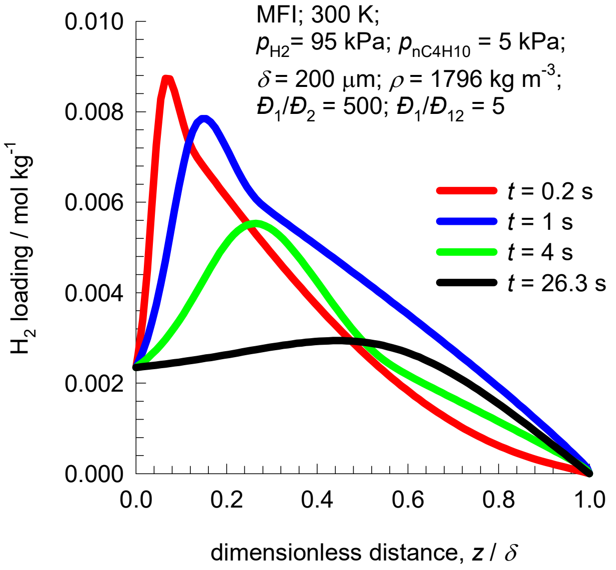

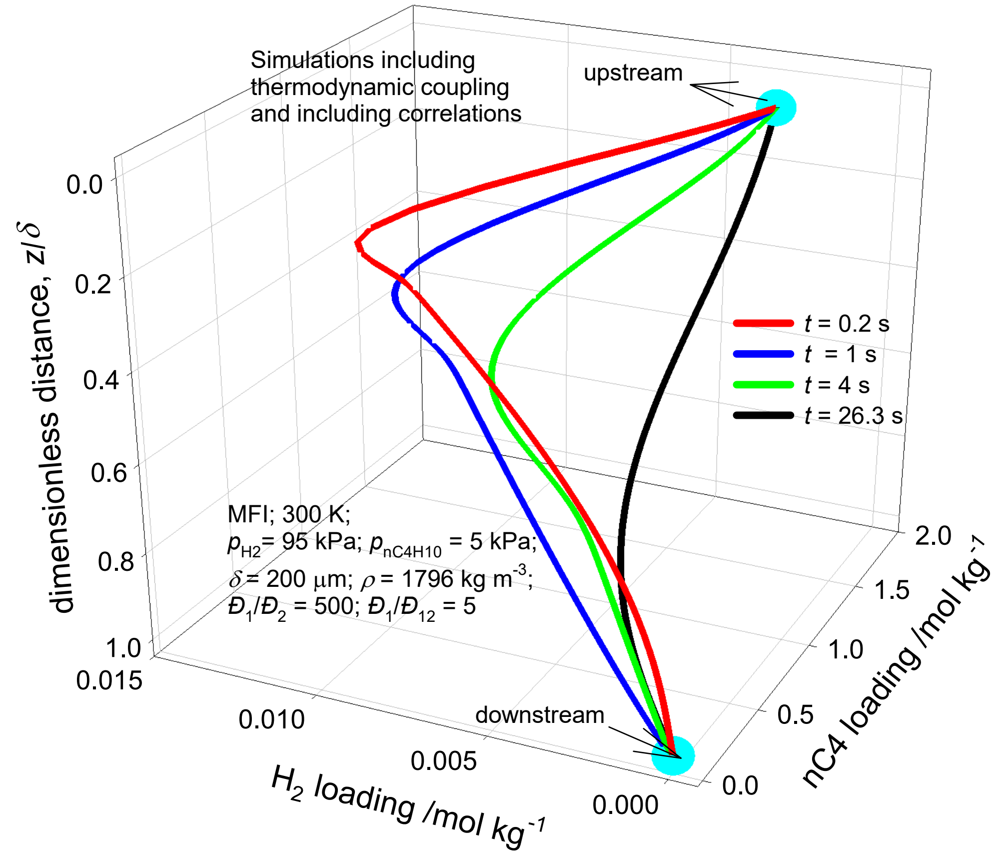

H_2/nC_4H_{10} corrected loading profiles: MFI membrane

Figure S74

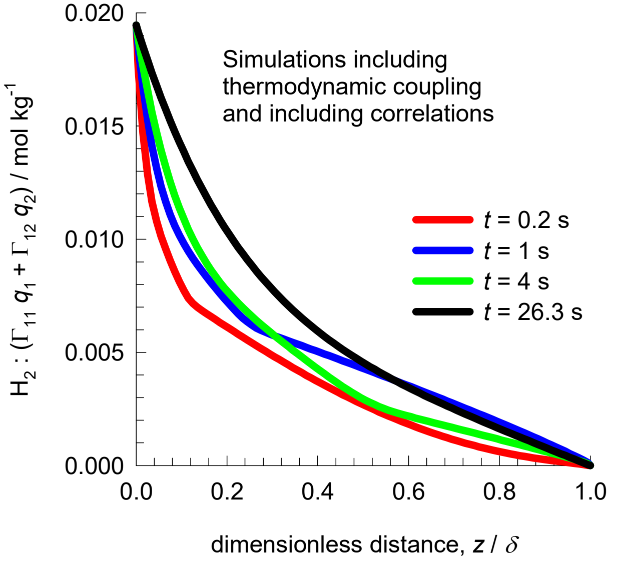

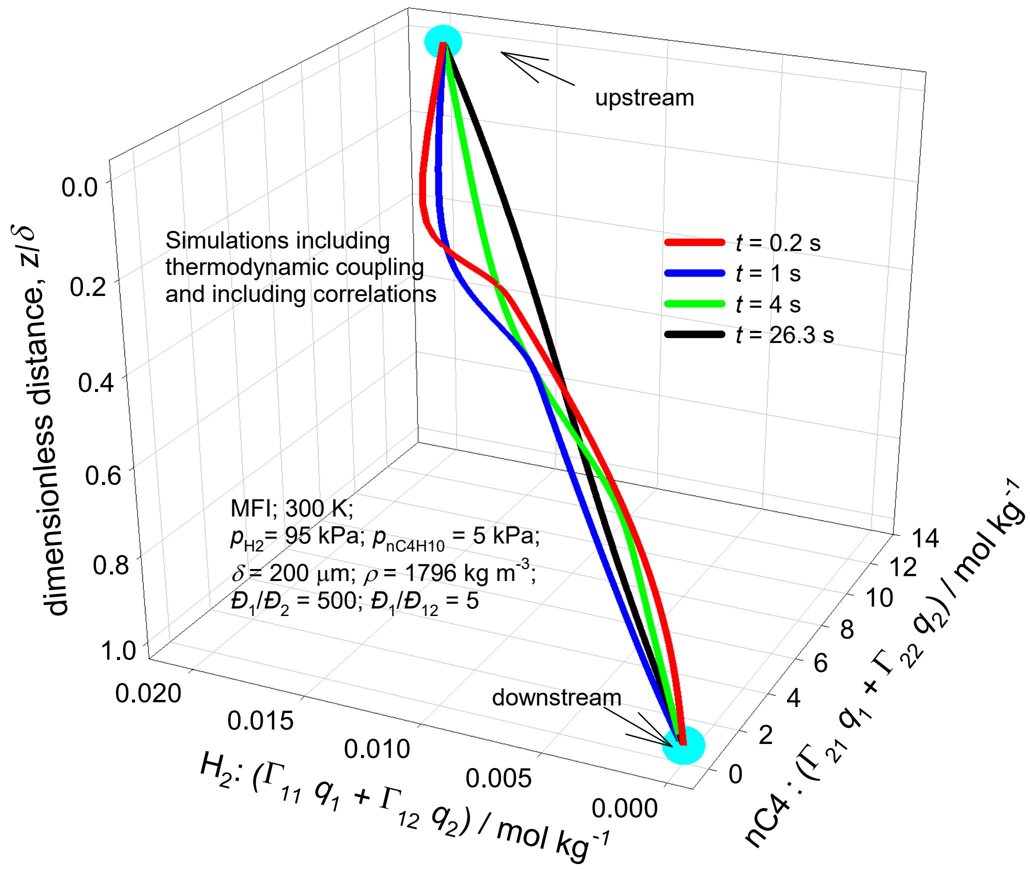

Figure S75

nC6/2MP and nC6/23DMB permeation across MFI membrane: Matsufuji

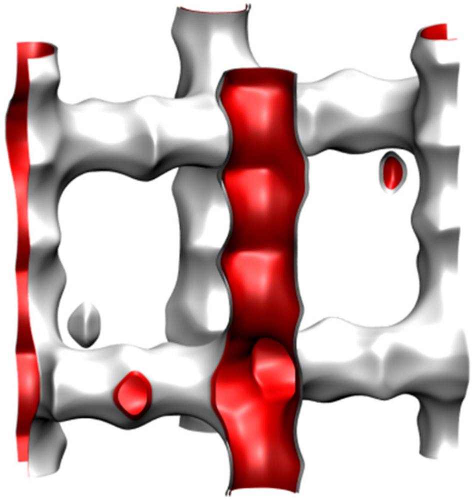

(a)

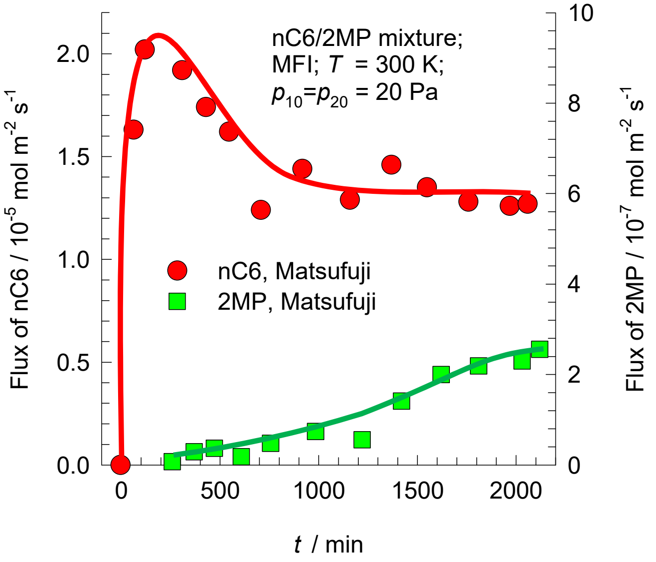

(b)

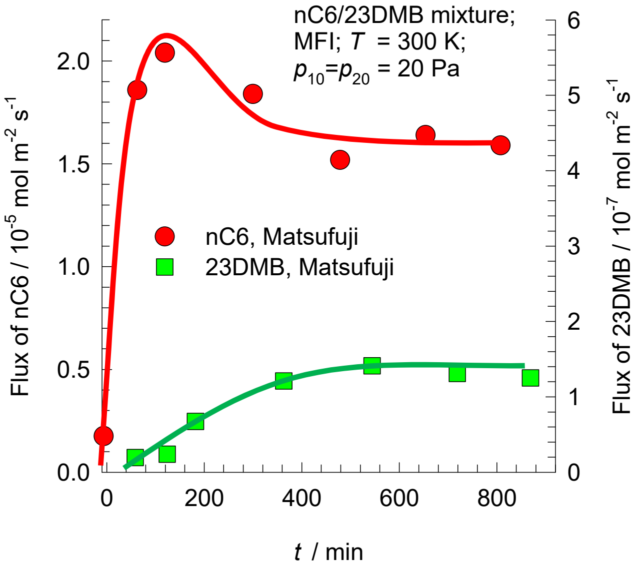

Figure S76

nC6/2MP permeation across MFI membrane

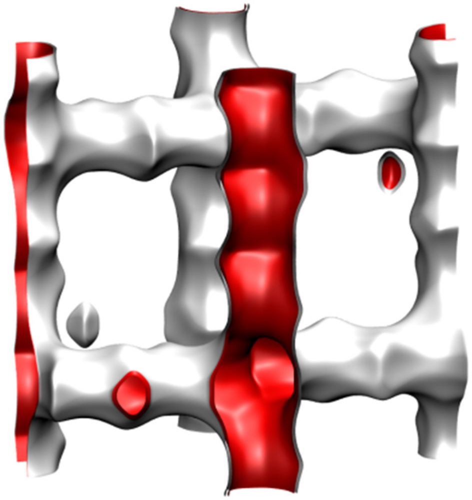

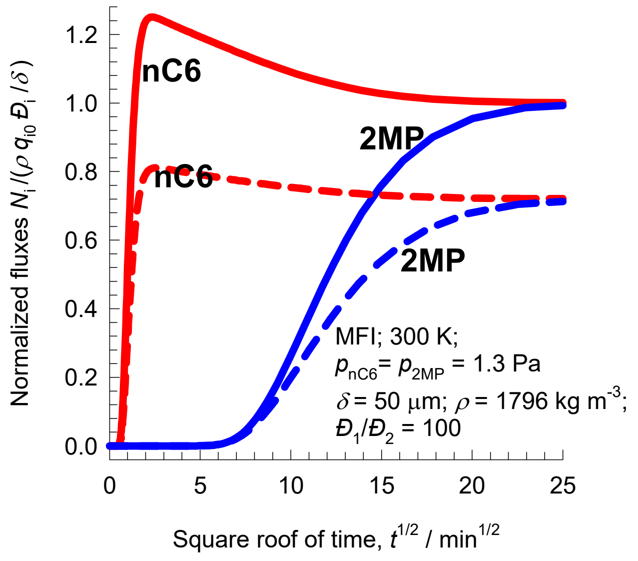

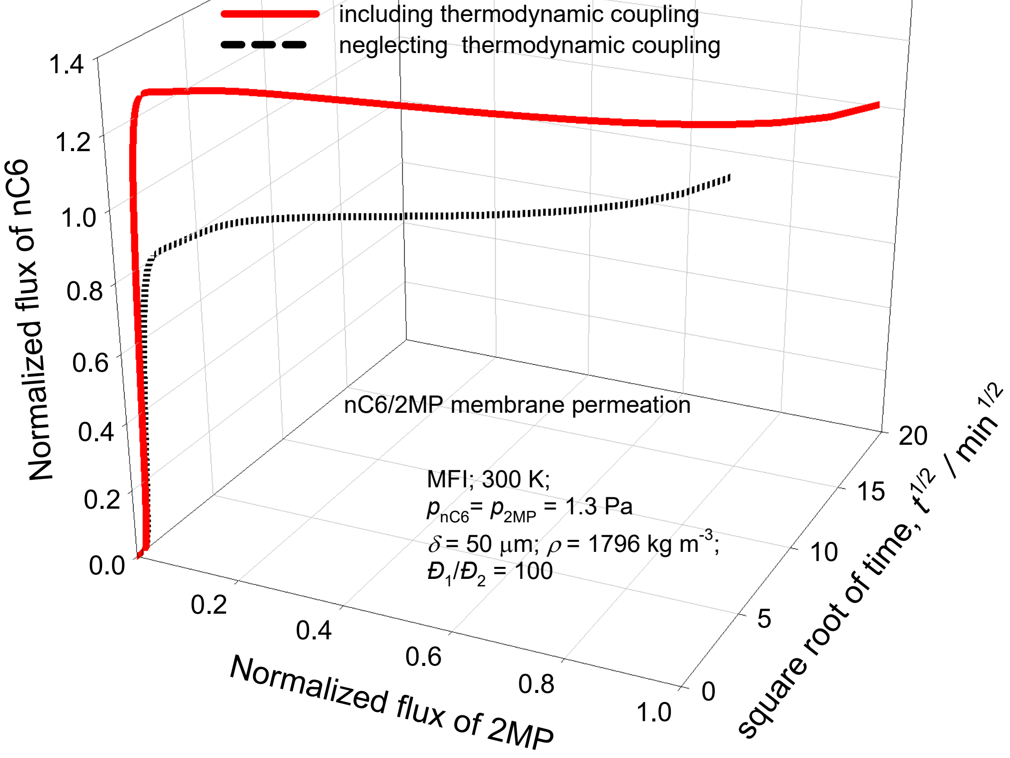

nC6/2MP loading profiles in MFI membrane

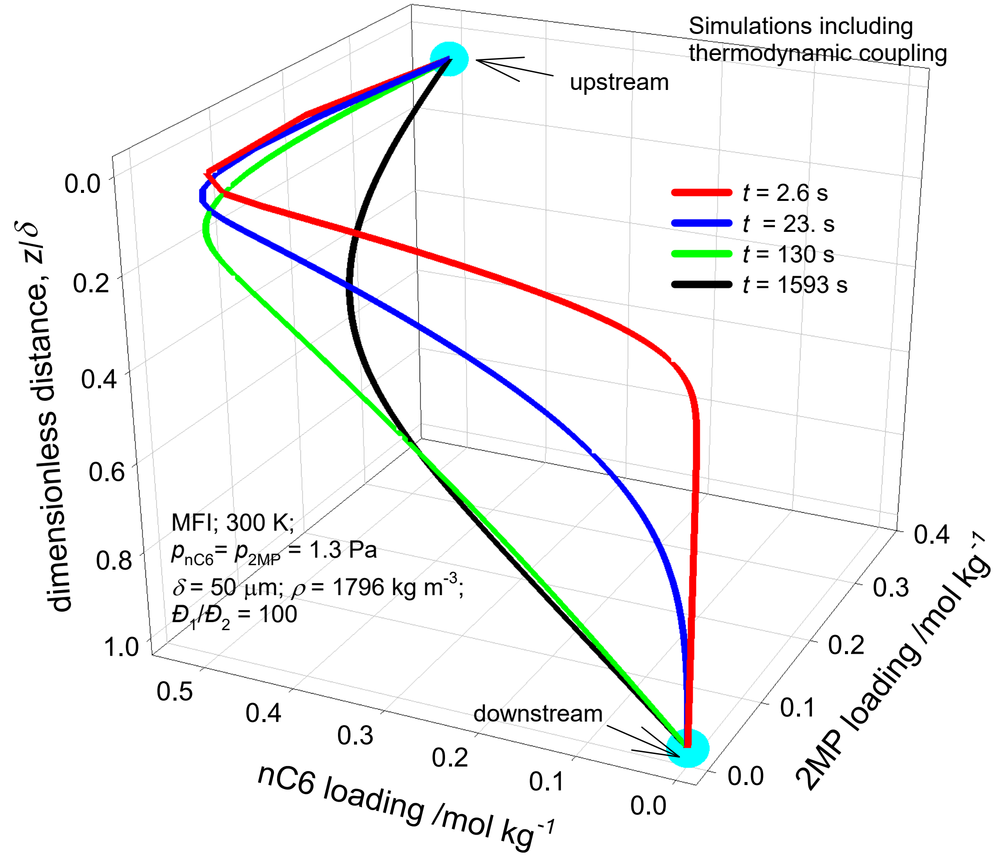

Figure S78

nC6/2MP corrected loading profiles in MFI membrane

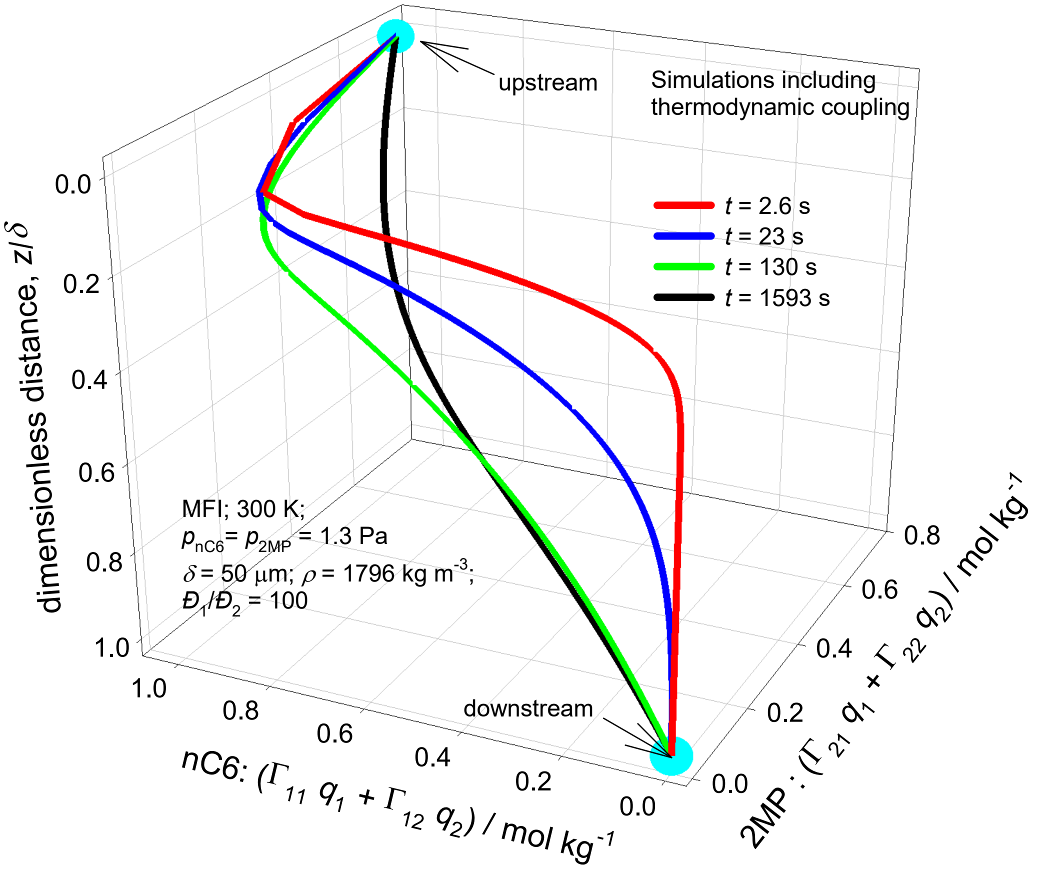

Xylenes permeation across MFI membrane

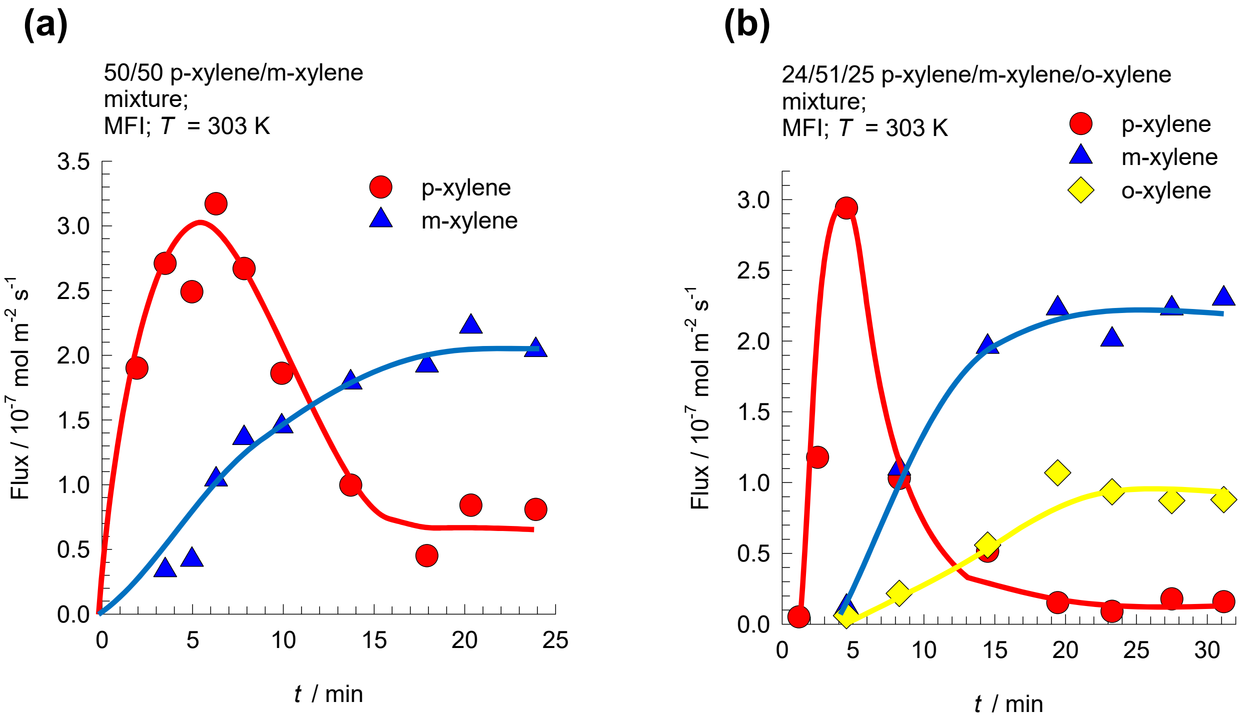

o-xylene is preferentially located at the intersections of MFI

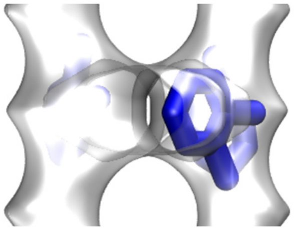

m-xylene is preferentially located at the intersections of MFI

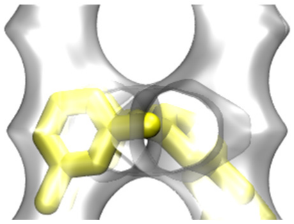

p-xylene can locate along the channels MFI

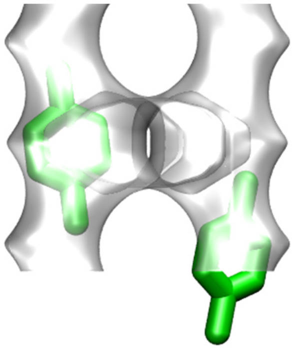

Figure S80

Xylenes permeation across MFI membrane

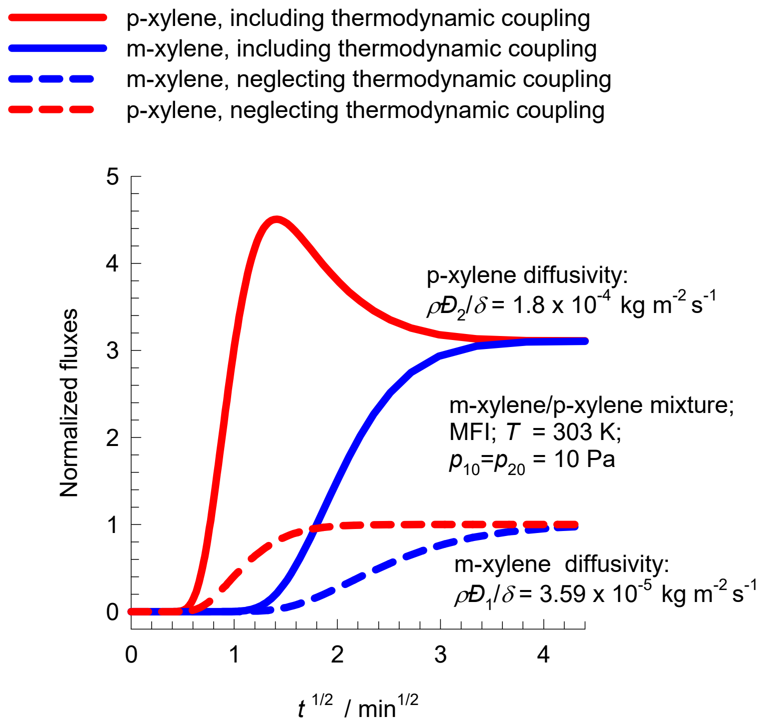

MFI membrane

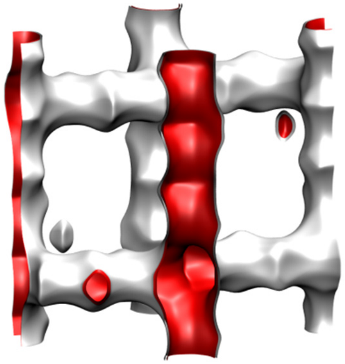

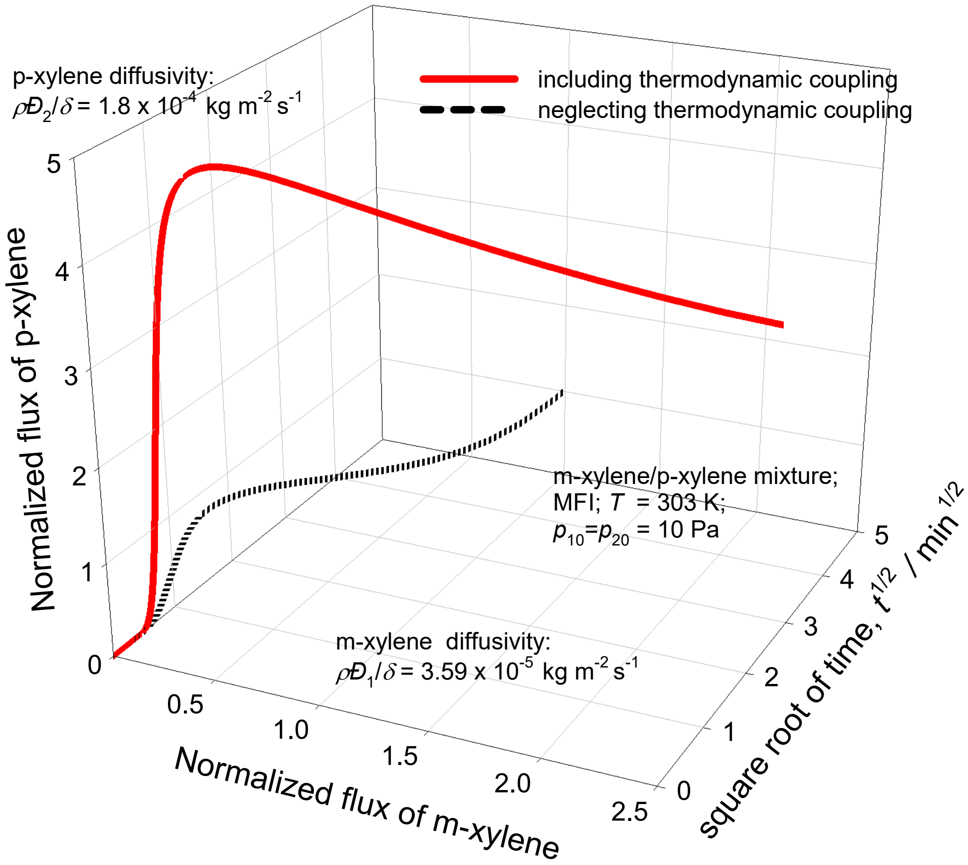

The diffusivity of p-xylene is assumed to be 5 times higher than that of m-xylene

nC4/iC4 permeation across MFI membrane

Figure S81

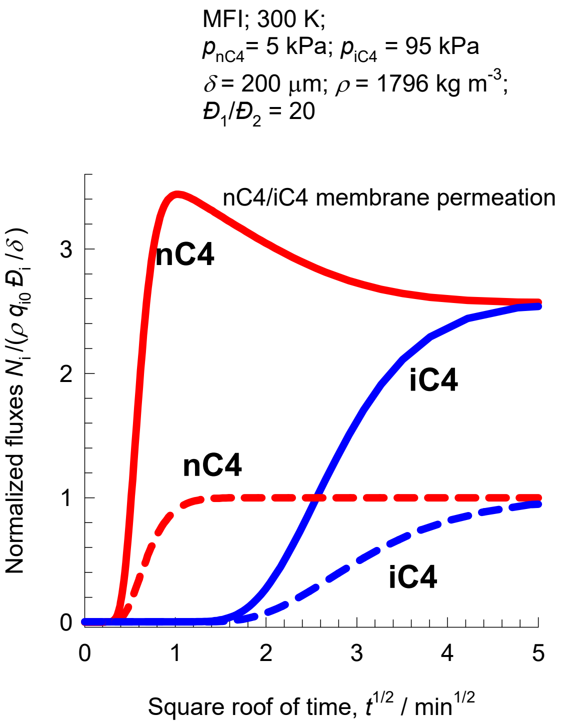

MFI membrane

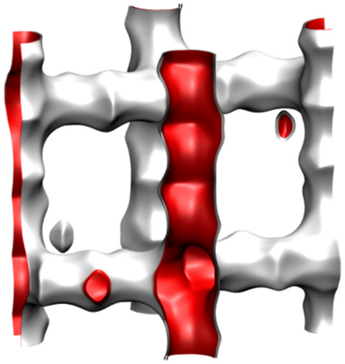

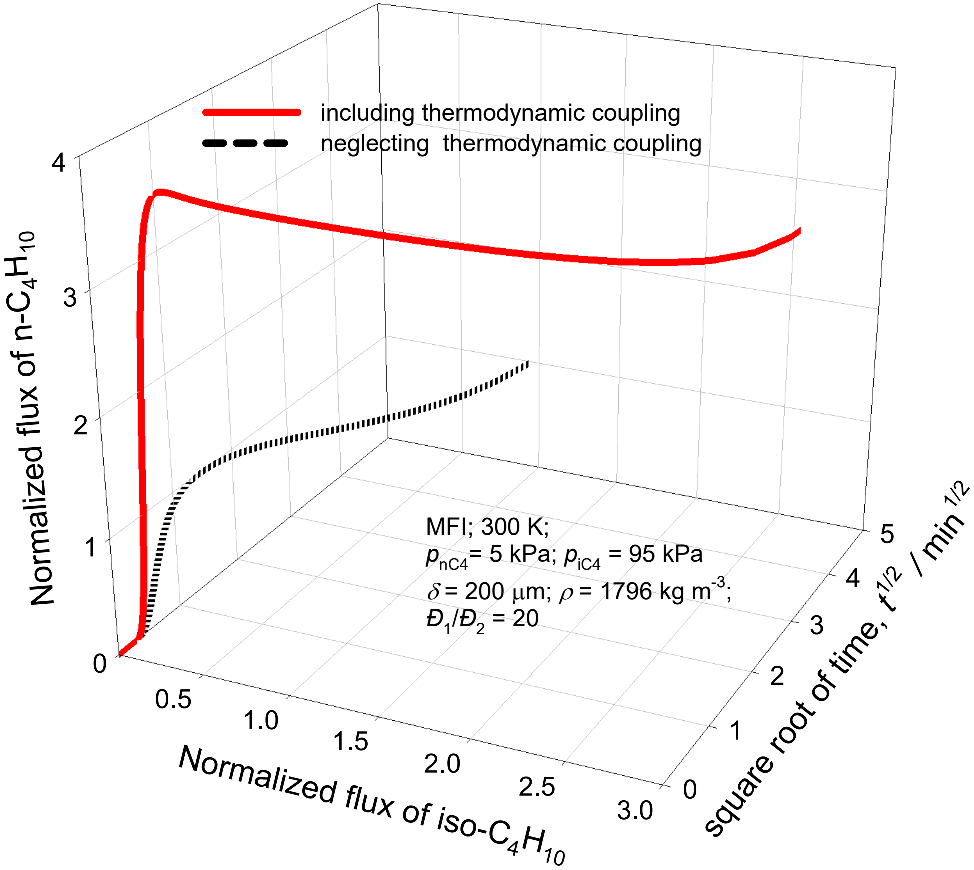

Figure S82

water/ethanol pervaporation DDR membrane

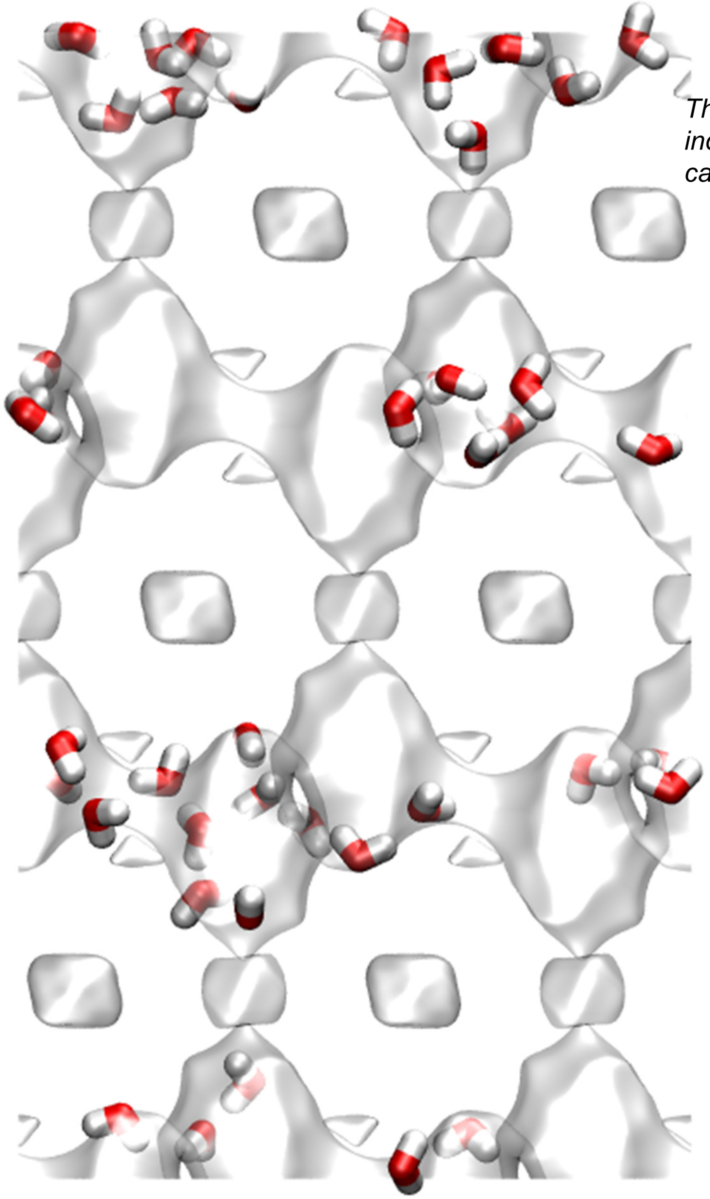

The snapshot shows some qualitative indication of clustering of water molecules caused by hydrogen bonding.

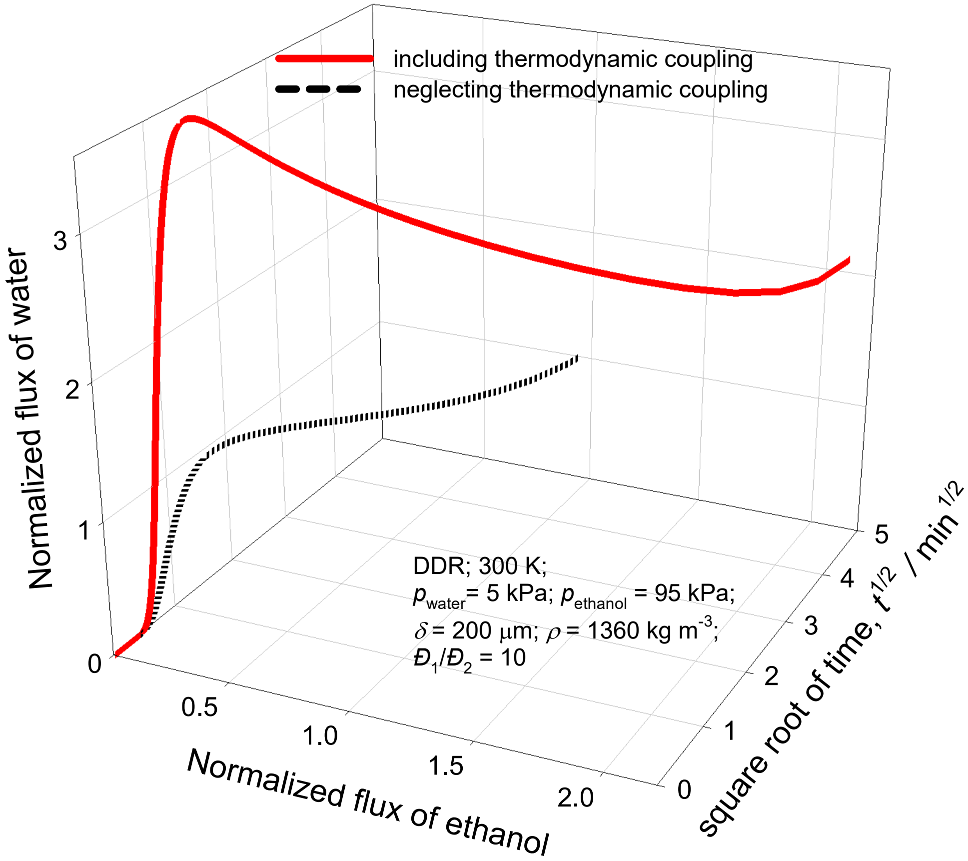

Figure S83

Water/ethanol loading profiles in DDR membrane

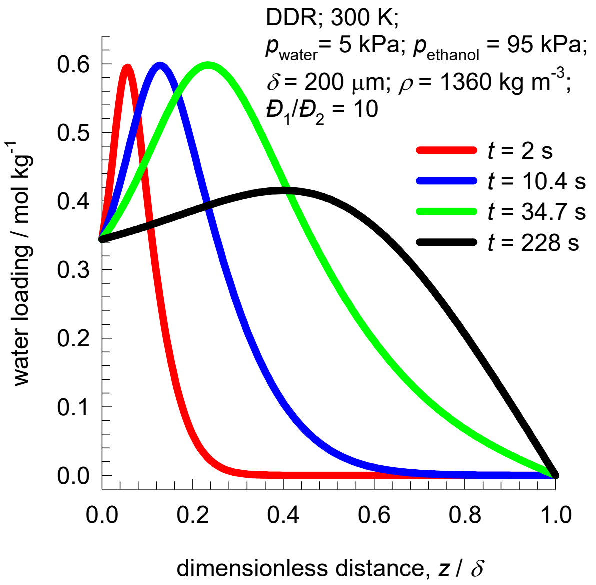

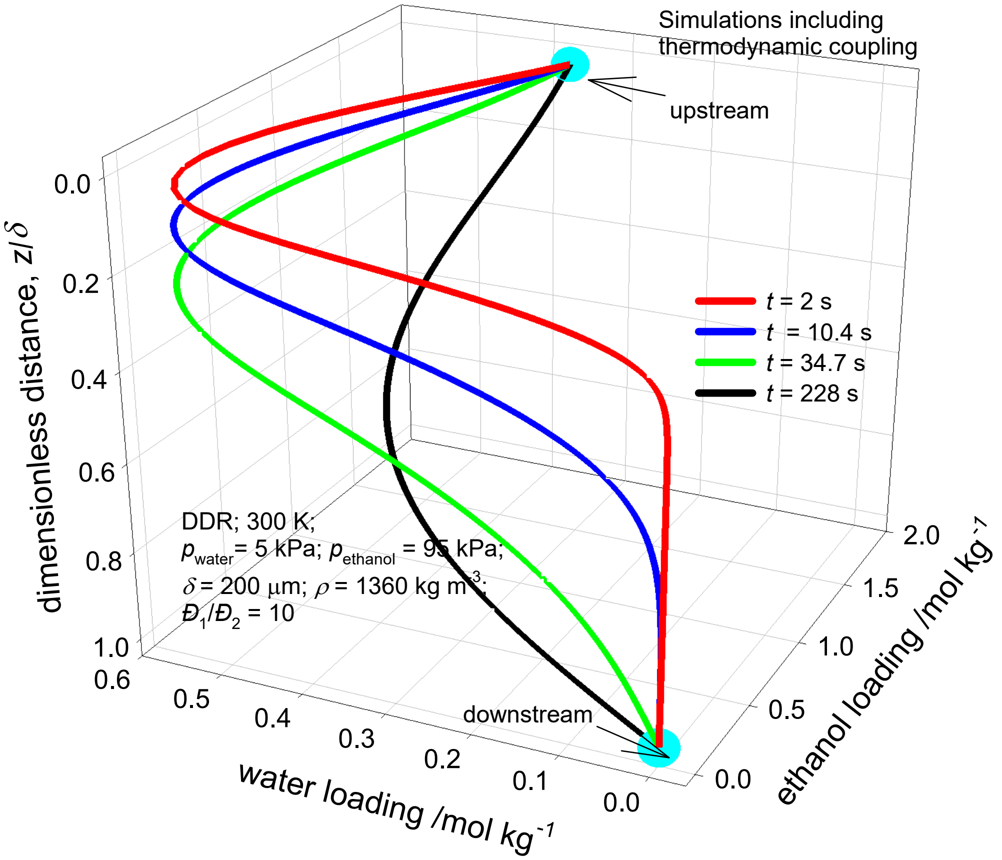

Figure S84

water/ethanol pervaporation LTA-4A membrane

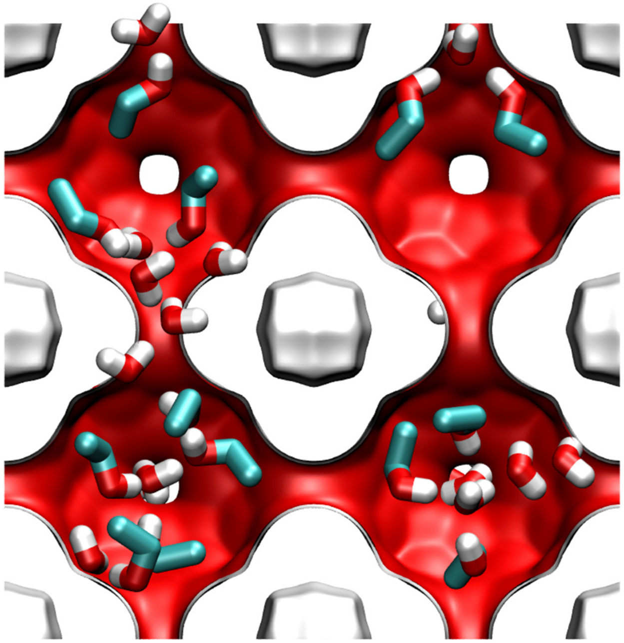

The snapshot shows water and ethanol molecules in the cages of LTA.

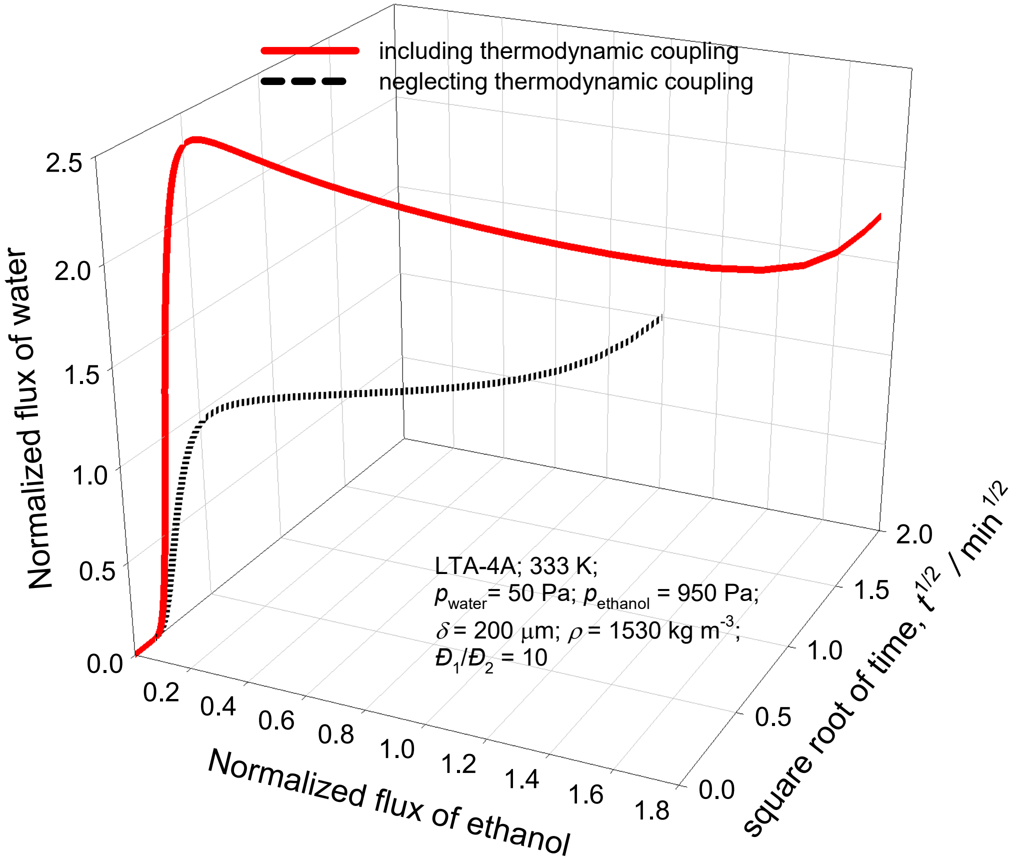

Figure S85

Water/ethanol loading profiles in LTA-4A membrane

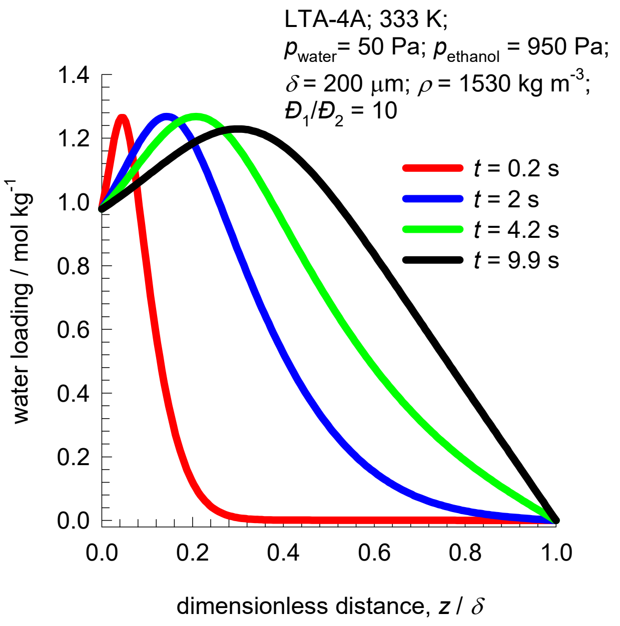
LTA-4A; 333 K;
p_{water}= 50 Pa; $p_{ethanol}$ = 950 Pa;
δ = 200 μm; ρ = 1530 kg m^{-3};
$Đ_1/Đ_2$ = 10

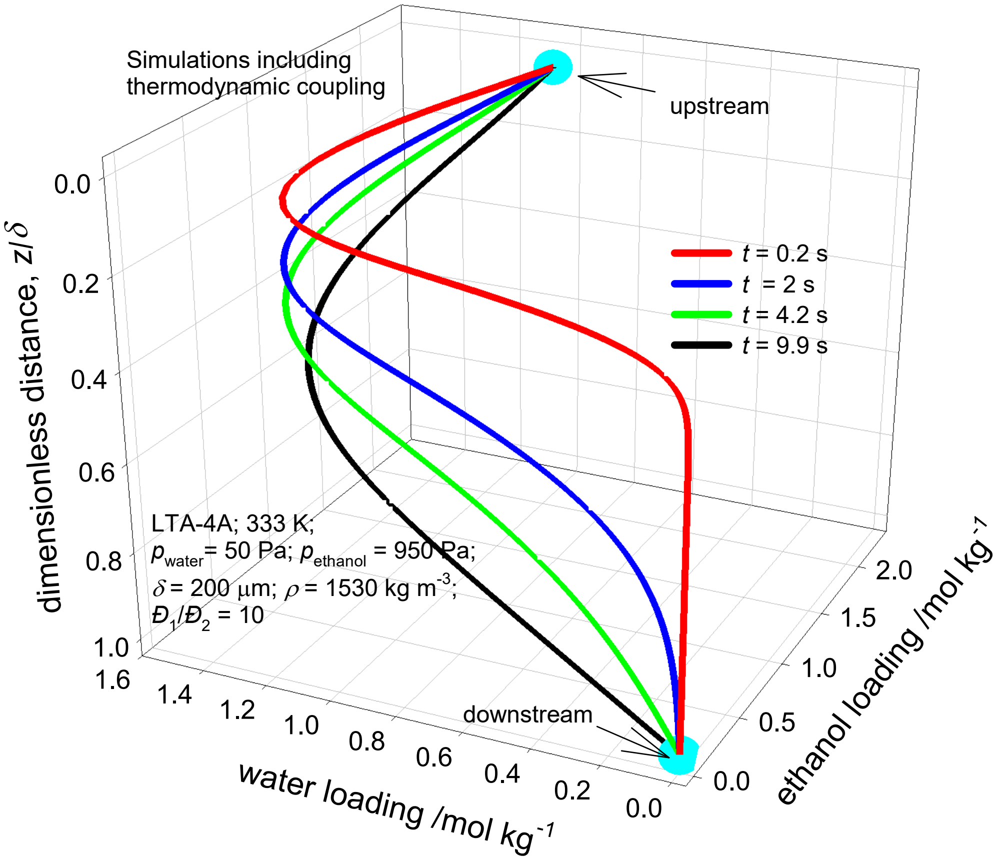
Simulations including thermodynamic coupling

upstream

downstream

LTA-4A; 333 K;
p_{water}= 50 Pa; $p_{ethanol}$ = 950 Pa;
δ = 200 μm; ρ = 1530 kg m^{-3};
$Đ_1/Đ_2$ = 10

Figure S86

Effectiveness factor for 2MP/22DMB diffusion/reaction in MFI catalyst

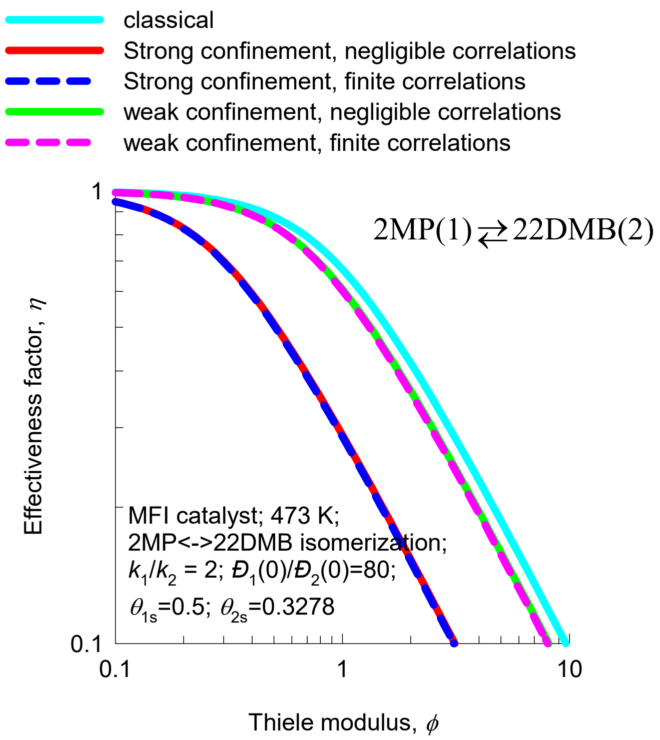

Figure S87

Transient 2MP/22DMB diffusion/reaction in MFI catalyst

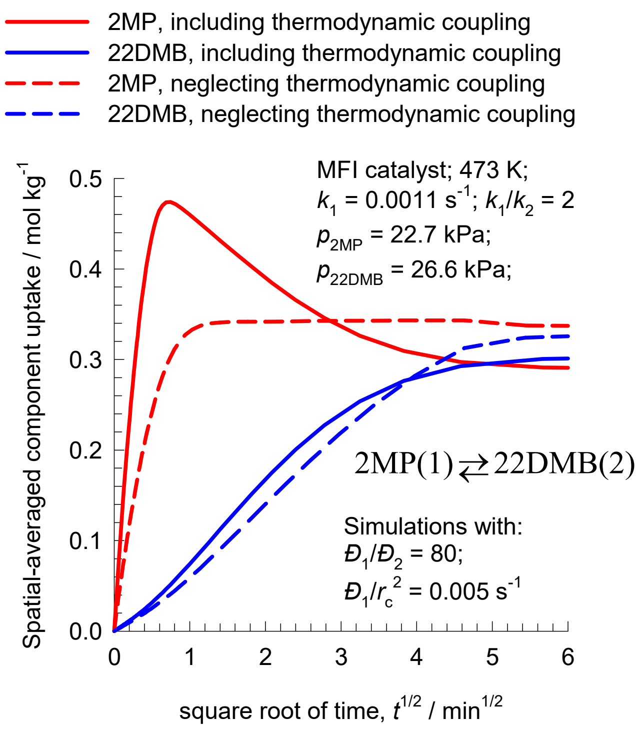

MFI catalyst; 473 K;
k_1 = 0.0011 s^{-1}; k_1/k_2 = 2
p_{2MP} = 22.7 kPa;
p_{22DMB} = 26.6 kPa;

Simulations with:
$Đ_1/Đ_2$ = 80;
$Đ_1/r_c^2$ = 0.005 s^{-1}

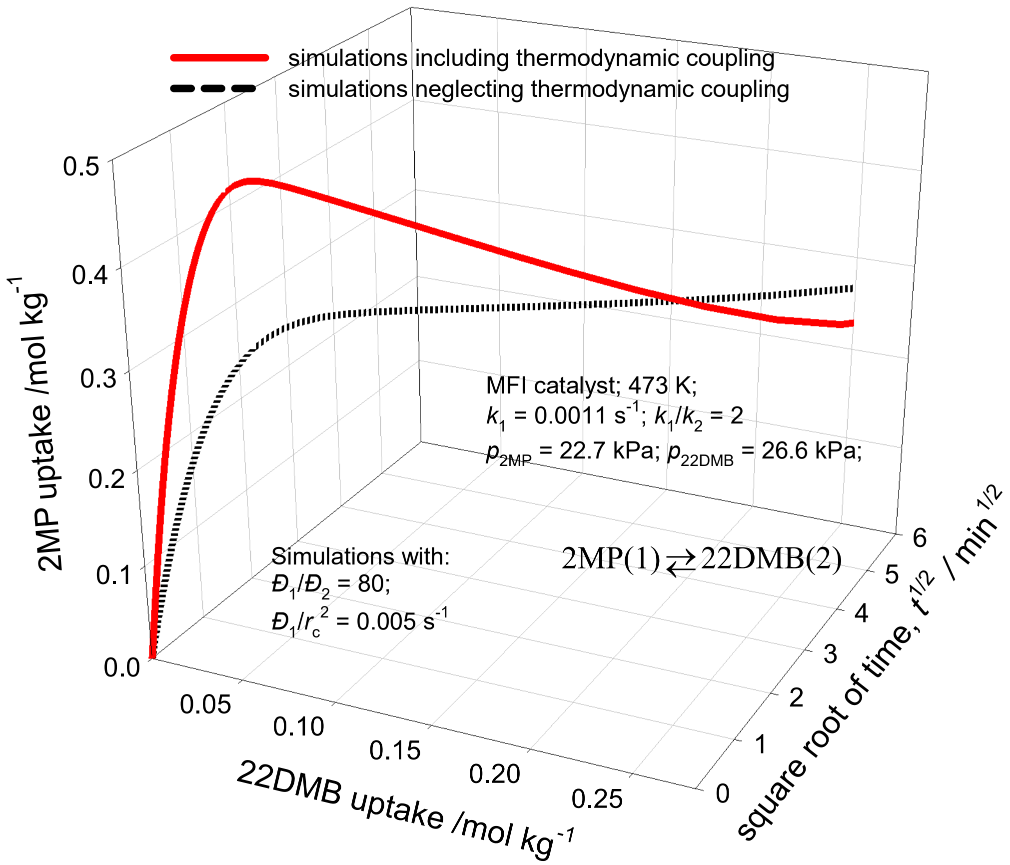

MFI catalyst; 473 K;
k_1 = 0.0011 s^{-1}; k_1/k_2 = 2
p_{2MP} = 22.7 kPa; p_{22DMB} = 26.6 kPa;

Simulations with:
$Đ_1/Đ_2$ = 80;
$Đ_1/r_c^2$ = 0.005 s^{-1}

2MP/22DMB loading profiles in MFI catalyst

Figure S88

$$2\mathrm{MP}(1) \rightleftarrows 22\mathrm{DMB}(2)$$

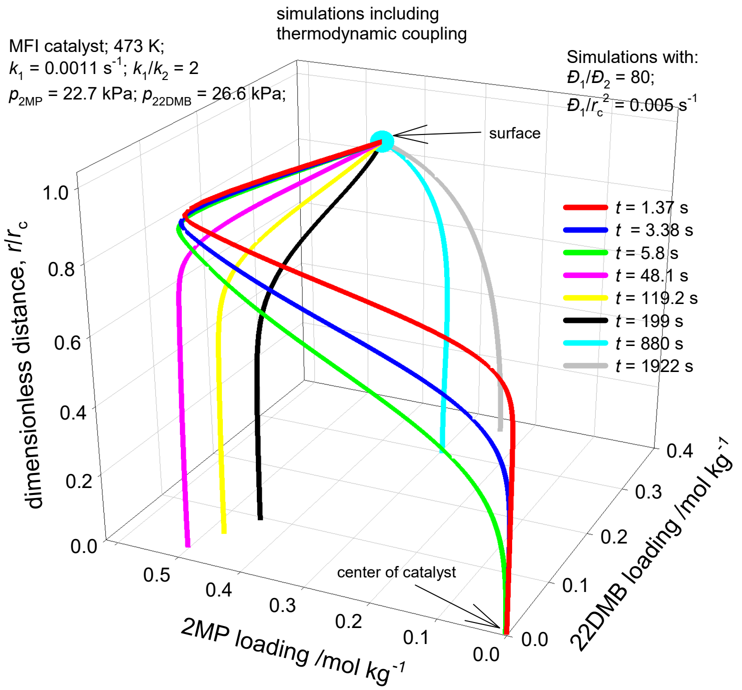

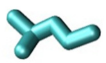

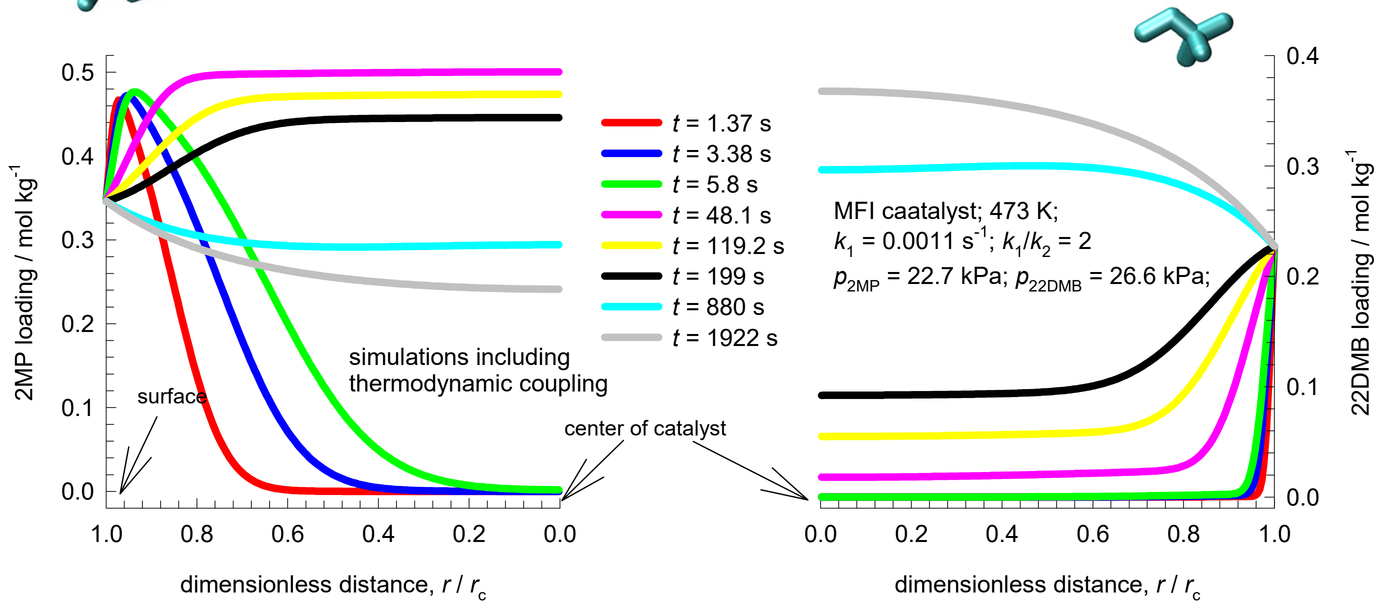

2MP/22DMB corrected loading profiles in MFI catalyst

Figure S89

$$2\mathrm{MP}(1) \rightleftarrows 22\mathrm{DMB}(2)$$

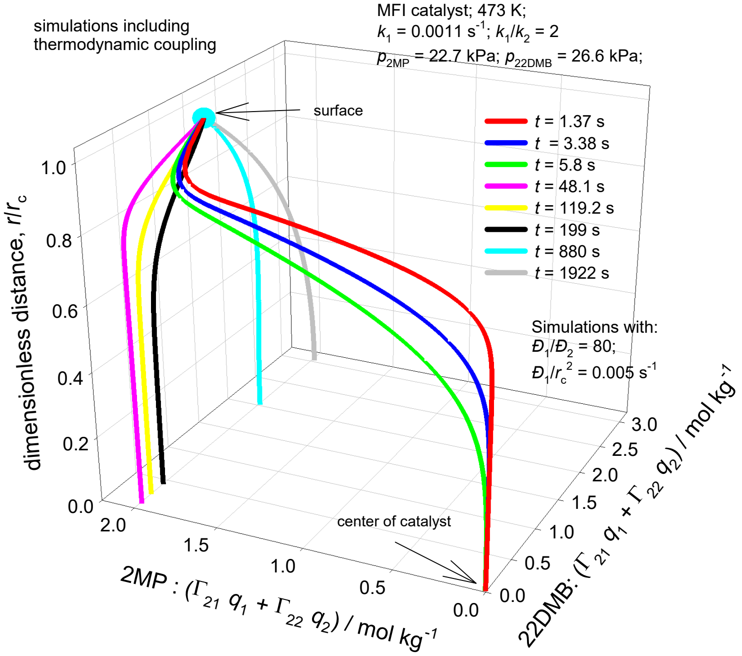

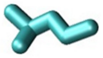

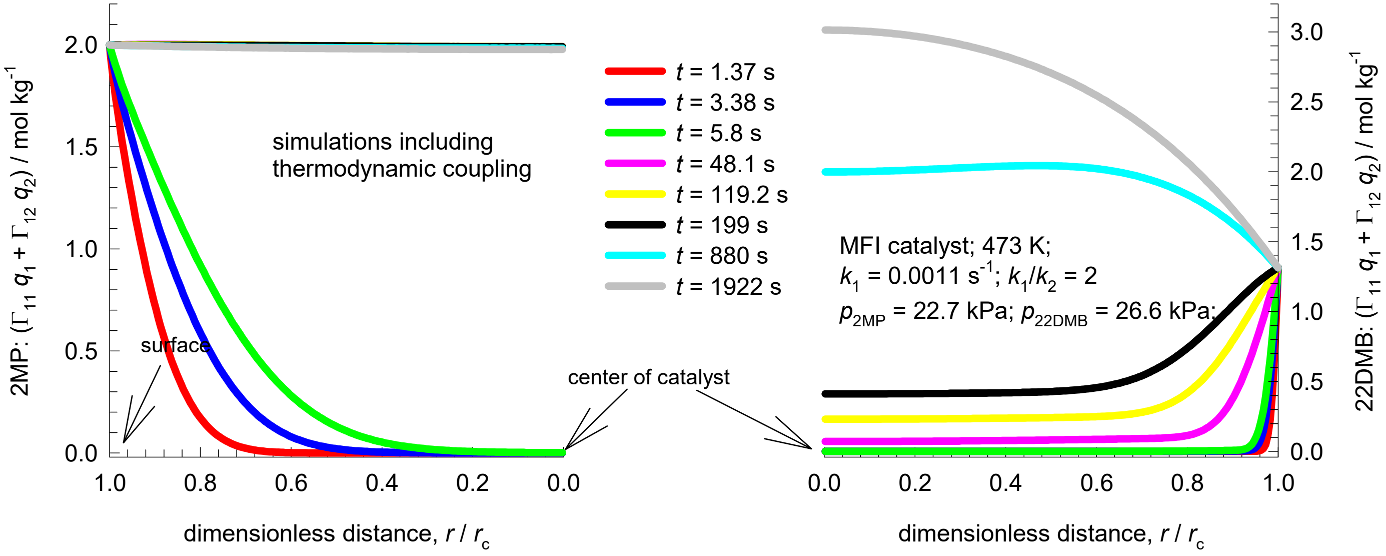

Transient 2MP/22DMB breakthrough in fixed bed MFI adsorber-reactor

$2MP(1) \rightleftarrows 22DMB(2)$

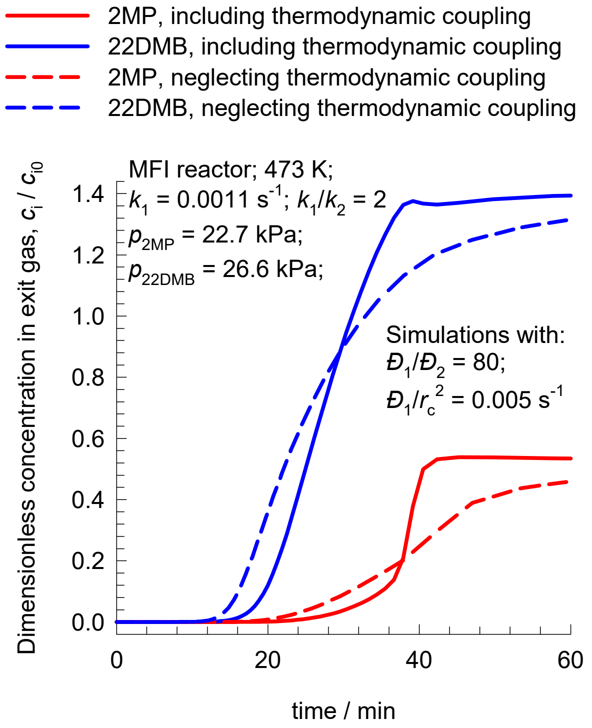

Figure S91

Transient nC6/3MP/22DMB diffusion/reaction in MFI catalyst

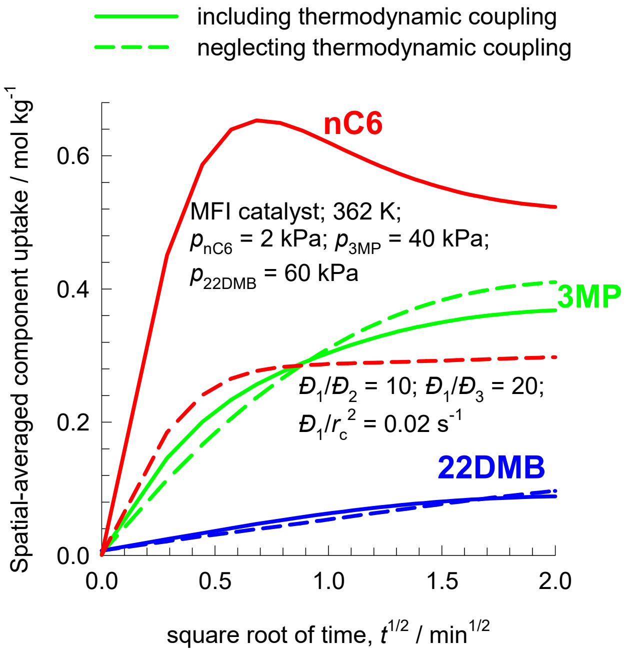

$nC6(1) \rightleftarrows 3MP(2) \rightleftarrows 22DMB(3)$

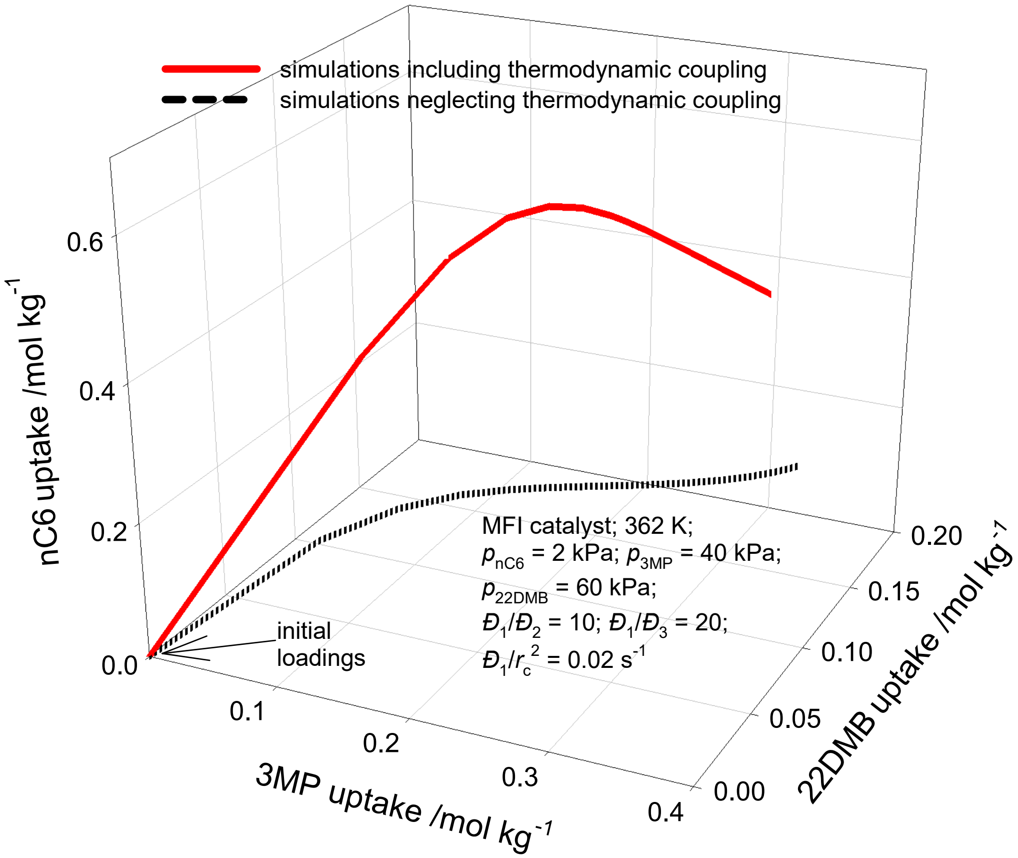

Figure S92

Transient m-X/p-X diffusion/reaction in MFI catalyst

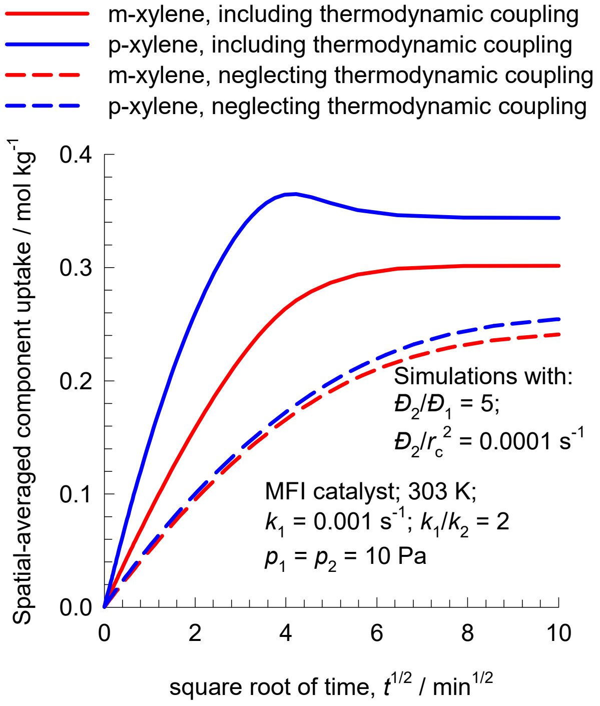

$$\text{m}-\text{xylene}(1) \rightleftarrows \text{p}-\text{xylene}(2)$$

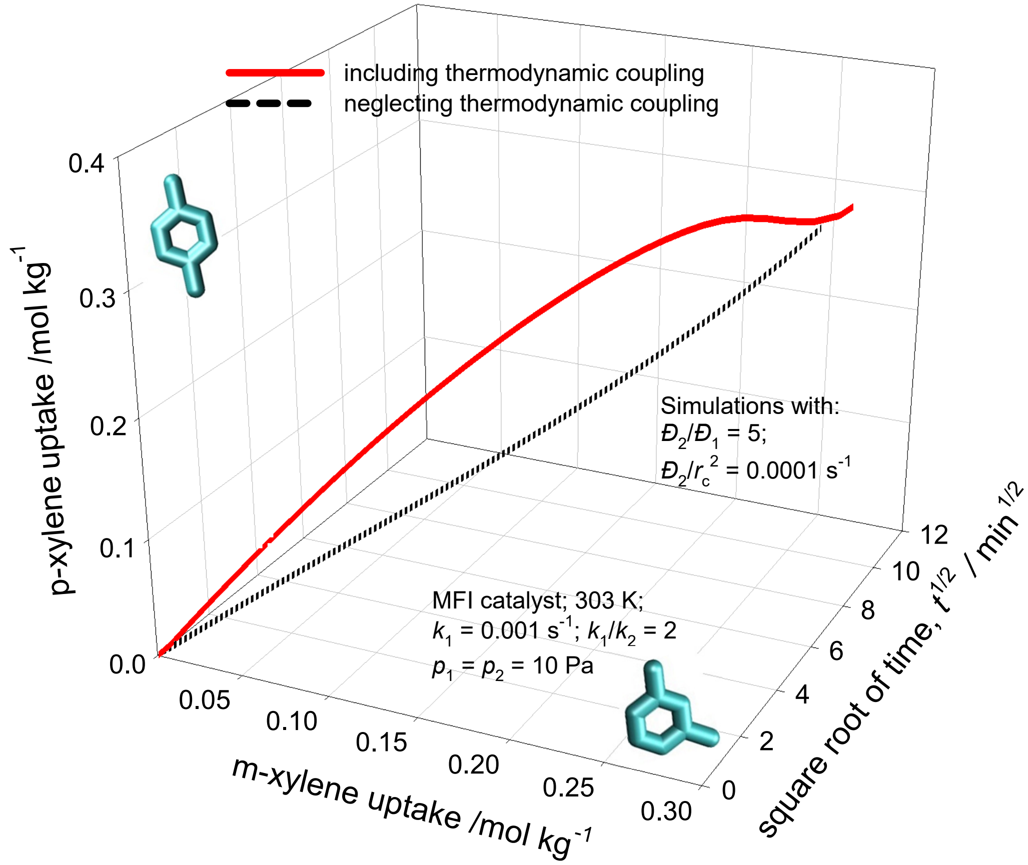

The diffusivity of p-xylene (= component 2) is assumed to be 5 times higher than that of m-xylene (= component 1)

Figure S93

Transient ethene/benzene/ethylbenzene diffusion/reaction in MFI catalyst

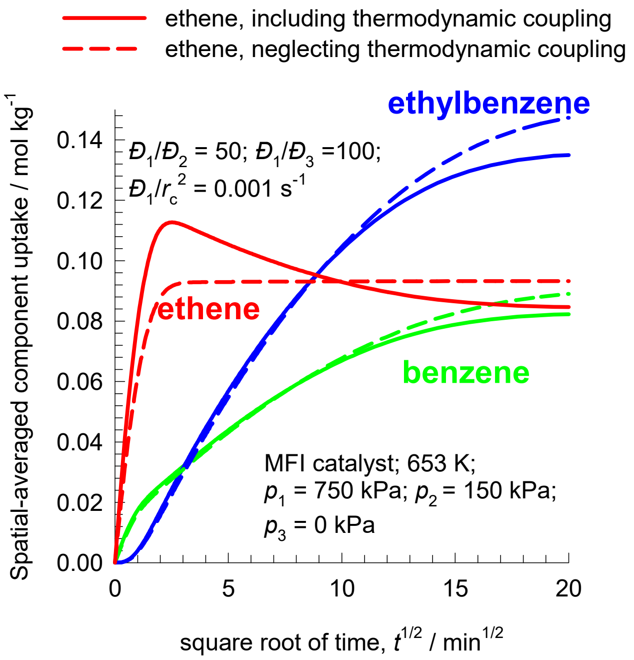

$$\text{ethene}(1) + \text{benzene}(2) \rightleftarrows \text{ethylbenzene}(3)$$

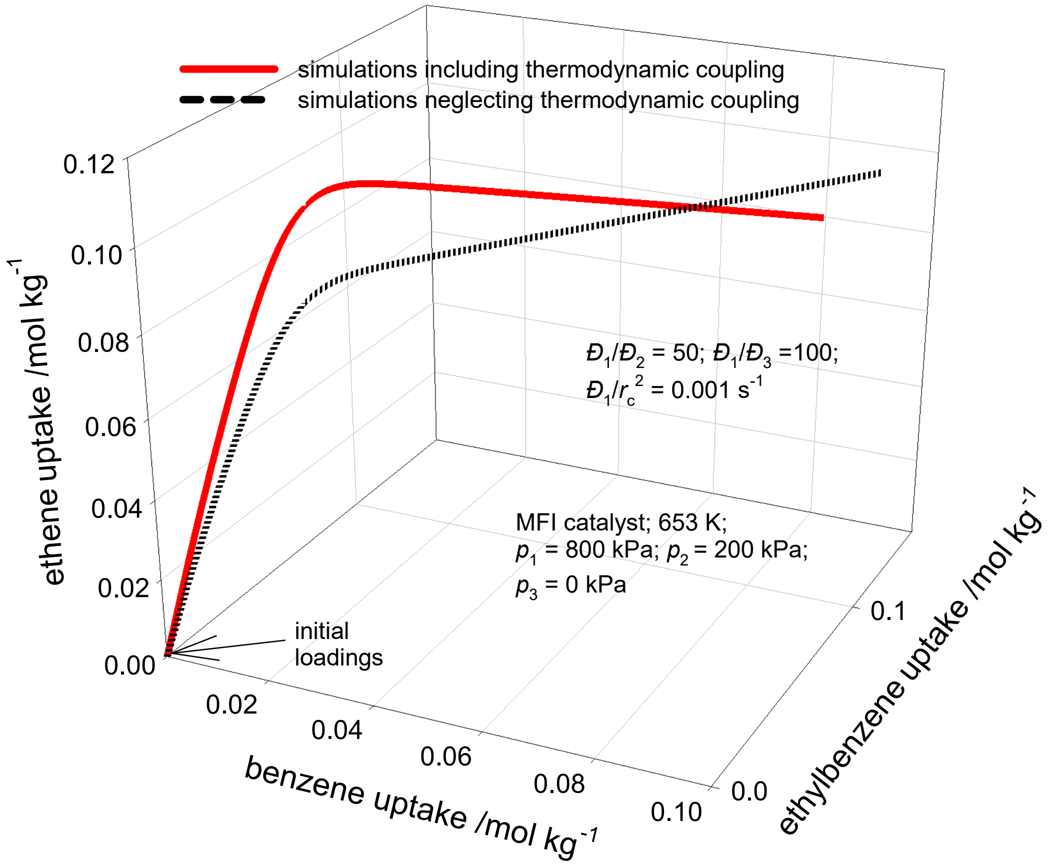

Figure S94

Transient ethane/ethene/hydrogen diffusion/reaction in MFI catalyst

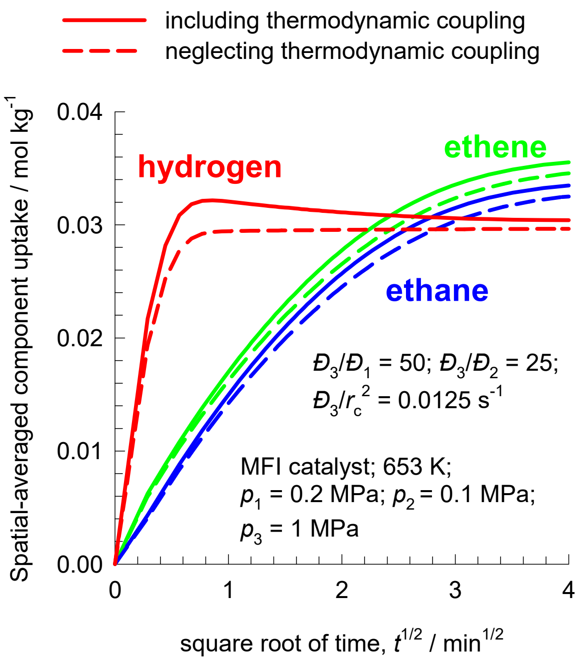

$$\text{ethane}(1) \rightleftarrows \text{ethene}(2) + \text{hydrogen}(3)$$